Massachusetts Institute of Technology

Woods Hole Oceanographic Institution

Joint Program
in Oceanography/
Applied Ocean Science
and Engineering

1930

DOCTORAL DISSERTATION

Dynamics of Global Ocean Heat Transport Variability

by

Steven Robert Jayne

June 1999

MIT/WHOI

99-05

Dynamics of Global Ocean Heat Transport Variability

by

Steven Robert Jayne

Massachusetts Institute of Technology
Cambridge, Massachusetts 02139

and

Woods Hole Oceanographic Institution
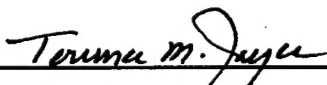Woods Hole, Massachusetts 02543

June 1999

DOCTORAL DISSERTATION

Approved for Distribution:

Terrence M. Joyce

Terrence M. Joyce, Chair
Department of Physical Oceanography

Paola Malanotte-Rizzoli
MIT Director of Joint Program

John W. Farrington
WHOI Dean of Graduate Studies

Dynamics of Global Ocean Heat Transport Variability

by

Steven Robert Jayne

S.B., Massachusetts Institute of Technology
(1994)

Submitted in partial fulfillment of the
requirements for the degree of

DOCTOR OF SCIENCE

at the

MASSACHUSETTS INSTITUTE OF TECHNOLOGY

and the

WOODS HOLE OCEANOGRAPHIC INSTITUTION
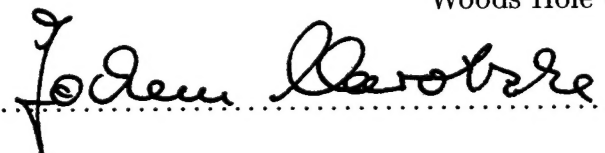
February 1999

© 1999 Steven Robert Jayne
All rights reserved.

Signature of Author . . . .
Joint Program in Physical Oceanography
Massachusetts Institute of Technology/
Woods Hole Oceanographic Institution
February 27, 1999

Certified by . . . .
Dr. Jochem Marotzke
Associate Professor
Thesis Supervisor

Accepted by . . . .
Dr. W. Brechner Owens
Chairman, Joint Committee for Physical Oceanography
Massachusetts Institute of Technology/
Woods Hole Oceanographic Institution

Dynamics of Global Ocean Heat Transport Variability
by
Steven Robert Jayne

Abstract

A state-of-the-art, high-resolution ocean general circulation model is used to estimate the time-dependent global ocean heat transport and investigate its dynamics. The north-south heat transport is the prime manifestation of the ocean's role in global climate, but understanding of its variability has been fragmentary owing to uncertainties in observational analyses, limitations in models, and the lack of a convincing mechanism. These issues are addressed in this thesis.

Technical problems associated with the forcing and sampling of the model, and the impact of high-frequency motions are discussed. Numerical schemes are suggested to remove the inertial energy to prevent aliasing when the model fields are stored for later analysis.

Globally, the cross-equatorial, seasonal heat transport fluctuations are close to $\pm 4.5 \times 10^{15}$ watts, the same amplitude as the seasonal, cross-equatorial atmospheric energy transport. The variability is concentrated within 20° of the equator and dominated by the annual cycle. The majority of it is due to wind-induced current fluctuations in which the time-varying wind drives Ekman layer mass transports that are compensated by depth-independent return flows. The temperature difference between the mass transports gives rise to the time-dependent heat transport.

The rectified eddy heat transport is calculated from the model. It is weak in the central gyres, and strong in the western boundary currents, the Antarctic Circumpolar Current, and the equatorial region. It is largely confined to the upper 1000 meters of the ocean. The rotational component of the eddy heat transport is strong in the oceanic jets, while the divergent component is strongest in the equatorial region and Antarctic Circumpolar Current. The method of estimating the eddy heat transport from an eddy diffusivity derived from mixing length arguments and altimetry data, and the climatological temperature field, is tested and shown not to reproduce the model's directly evaluated eddy heat transport. Possible reasons for the discrepancy are explored.

Thesis Supervisor: Dr. Jochem Marotzke
Associate Professor of Physical Oceanography
Department of Earth, Atmospheric, and Planetary Sciences
Massachusetts Institute of Technology

Acknowledgments

I would like to gratefully acknowledge my advisor Jochem Marotzke for guidance, encouragement and the freedom to pursue a thesis topic not necessarily what he had envisioned. I would also like to thank my thesis committee members Nelson Hogg, Paola Malanotte-Rizzoli, Breck Owens and Carl Wunsch for their advice and suggestions which helped shape this research. Bruce Warren kindly agreed to chair my thesis defense.

Special thanks are due to Robin Tokmakian and Bert Semtner from the Naval Postgraduate School, who generously provided their numerical model output. Robin gave me considerable help and advice on working with the model output and provided me with the wind stress and surface heat flux fields used to force the model. Thanks are due to Charmaine King for providing me with the gridded TOPEX/POSEIDON fields. The Scientific Computing Division at the National Center for Atmospheric Research also gave invaluable technical consulting and made the processing of over 250 gigabytes of model output and data feasible. Jim Price and Breck Owens also provided computer resources. Thanks to Alistair Adcroft for providing the Laplacian inverter, Rui Ponte for critical advice on angular momentum calculations, Mike Spall for providing comments on Chapter 2 and Mindy Hall for comments on what became Chapter 4.

I would like to thank all my friends from WHOI and MIT; I have been fortunate to have so many good friends, you have given me the moral support to get through graduate school. In particular I would like to give heartfelt thanks to David Ford, Ryan Frazier, Chris Linder, Liz Kujawinksi, Sean McKenna, Jess Rowcroft, Sarah Walsh and Joe Warren for the good times and encouragement, you all made grad school fun. I also thank my fellow PO students; Jay Austin, Derek Fong, François Primeau, Jamie Pringle, Louis St. Laurent and Judith Wells for their years of help and comradeship. I would also like to thank the folks in the Education Office for their efforts to make graduate school as painless as possible.

Finally, though it is surely an inadequate expression of my gratitude, I thank my parents for all their support. It is they who have made all this possible, and to whom

5

I can finally say, I'm done with school.

"To know the laws that govern the winds, and to know that you know them, will give you an easy mind on your voyage round the world; otherwise you may tremble at the appearance of every cloud. What is true of this in the trade-winds is much more so in the variables, where changes run more to extremes"

Joshua Slocum (1844–1909)
from *Sailing Alone Around the World*

Contents

Chapter 1

Introduction

The Earth's climate is a dynamic system and the turbulent circulations of the ocean and atmosphere participate in a complicated exchange of heat, mass, and momentum. The complexity of this system coupled with sparse observational coverage of it has made interpretation and understanding of some of the underlying processes difficult. Further, its intricacies limit our ability to predict anthropogenic impacts on climate. The ocean component of it still presents some of the largest gaps in our knowledge of the fundamental processes involved. In this thesis I approach some of the questions concerning the ocean's role in climate by addressing the role of temporal variability in the ocean's transport of heat, and in particular, the global nature of the relevant ocean dynamics will be investigated.

Estimates of the time-mean ocean heat transport show that the ocean carries the same order of magnitude of energy away from the tropics towards the poles as the atmosphere (Vonder Haar and Oort 1973; Hastenrath 1982; Carissimo et al. 1985; Peixoto and Oort 1992; Trenberth and Solomon 1994; Keith 1995). Macdonald and Wunsch (1996) made a dynamically and kinematically consistent estimate of the global transports of mass, heat, and freshwater based on an inverse model of a collection of one-time hydrographic sections. With the completion of the World Circulation Experiment (WOCE) more hydrographic sections are now available and a better estimate will be possible. Contributions to the understanding of the ocean heat transport have come from modeling studies as well (for a summary see Bryan 1991). While uncertainties still exist in estimates of the time-mean ocean heat transport, in

general it can be said that at least the sign of the ocean heat transport is known over the global ocean and quantifiable error estimates can be made.

Overall in the time-mean picture the ocean, as does the atmosphere, transports heat away from the tropics toward the polar regions, helping to balance the unequal heating of the Earth by the Sun and moderate temperatures at both extremes. The heat transport in the Atlantic Ocean is toward the north over its entire latitudinal extent, consistent with simple conceptual models for the thermohaline circulation by the global ocean (Broecker 1991). Elsewhere, in the Pacific Ocean there is poleward transport of heat away from the equator, and in the Indian Ocean there is southward heat transport over the basin's extent.

Keith (1995) concluded that the time-mean ocean heat transport calculated as the residual to close the atmospheric energy budget, has achieved the same accuracy as direct hydrographic methods. Though the uncertainties in the transports may be as large as 0.7 PW (1 PW = 10^{15} watts) and errors still remain in the partition between the ocean and atmosphere, the estimates are believed to be good enough to constrain coupled ocean-atmosphere climate models. Since the time-mean heat transport has been reasonably, though not completely addressed, it is timely to consider its time-dependent nature, which is important for several reasons. There is energetic variability in the ocean due to mesoscale eddies, wave motions, atmospherically driven transients, etc. First, the nature and magnitude of the time-dependency of the ocean heat transport is not well known and conflicting estimates of it exist and it therefore represents a large gap in our understanding. Second, it may or may not impact our ability to observe the time-mean transport. How much the rectified temporal variability contributes to the time-mean heat transport, and whether the variability significantly impacts estimates of the time-mean state made from one-time hydrographic sections, remain open questions.

Direct observation of the time-dependent heat transport by the ocean on any reasonable timescale is prohibited by the impossibility of sampling the full ocean depth over the vast range of spatial scales required. Though hydrographic surveys do provide some measure of the eddy variability along the section, it is strongly aliased in time. Therefore, estimates of the global variability have had to rely on indirect

10

approaches. These have been based on models (Bryan and Lewis 1979; Bryan 1982) or observed changes in oceanic heat storage, combined either with atmospheric and satellite observations (Oort and Vonder Haar 1976; Carissimo et al. 1985), surface flux observations (Hsiung et al. 1989) or wind-stress and surface temperatures to estimate changes in the Ekman component of the heat transport (Kraus and Levitus 1986; Levitus 1987; Adamec et al. 1993; Ghirardelli et al. 1995).

The seasonal cycle of ocean heat transport has been the subject of several investigations. This was begun by Oort and Vonder Haar (1976), who used satellite radiation data, atmospheric radiosonde data and oceanic heat storage data to study the ocean heat transport in the Northern Hemisphere. Their method calculated the ocean heat transport as the residual necessary to close the energy balance at the top of the atmosphere, after accounting for atmospheric and oceanic heat storage and atmospheric transport. They inferred a large seasonal variation in the ocean heat transport particularly in the tropics where they found that the oceans transport large amounts of heat across the equator from the summer hemisphere to the winter hemisphere. Carissimo et al. (1985) essentially updated the study of Oort and Vonder Haar (1976) using data covering the entire globe. They too found a large seasonal variation in the ocean's inferred heat transport. Peak to peak, their annual cycle of heat transport across the equator was 7.3 ± 4 PW. Over the mid-latitudes, the amplitude was smaller, but still directed northward during boreal winter (austral summer) and southward during boreal summer (austral winter). The large errorbars on this estimate are largely due to the poor quality and general lack of ocean heat storage data available at the time of their study.

Kraus and Levitus (1986) calculated the annual heat transport variations across the Tropics of Cancer and Capricorn by the Ekman heat transport and found that the amplitude of the annual cycle was the same order of magnitude as the annual mean Ekman heat transport in both the Pacific and Atlantic Oceans. This work was extended by Levitus (1987) who calculated the Ekman heat transport for all three ocean basins over their latitudinal extents using a climatological data set for the temperature (Levitus 1982) and wind stress (Hellerman and Rosenstein 1983) fields. The essential premise of these calculations is that the atmospheric wind stress drives

11

an Ekman transport in the surface layer which is accompanied by a compensating return flow which is distributed barotropically. Since the return flow is at the depth averaged temperature, which is generally colder than the surface temperature, there is a heat transport proportional to the temperature difference and the zonal wind stress. More recently Adamec et al. (1993) used wind stress values and temperatures computed from the Comprehensive Ocean-Atmosphere Data Set (COADS) to compute the Ekman heat transport. Ghirardelli et al. (1995) used satellite derived wind stress from the Special Sensor Microwave Imager (SSM/I) and sea surface temperature from the Advanced Very High Resolution Radiometer (AVHRR). All these studies qualitatively give the same picture of the annual cycle of the Ekman heat transport. Over the World Ocean the annual cycle is of order 8 petawatts peak to peak in the tropics. It is strongest in the Pacific and Indian Oceans and noticeably weaker in the Atlantic Ocean. Additionally, the phase of the annual cycle reverses in the mid-latitudes at around 20°. There are, however, some difficulties interpreting the role of the Ekman heat transport in climate processes from these studies. First, the Ekman heat transport is only one component of the total transport; changes in it may be unaffected, reinforced or completely offset by changes in other parts of the system. Second, none of these studies is applicable within a few degrees of the equator as their definition of the Ekman transport breaks down with the vanishing Coriolis parameter there. Third, none of these investigations can take into account Bryan's (1982) finding that the meridional wind plays an increasingly important role as one approaches the equator. Finally, these studies are sensitive to the assumed return flow temperature and all combine the time-dependent Ekman transports with the time-mean Ekman transport assuming that both flows have the same depth structure. The assumption that the return flow for the time-varying Ekman transport is deep and barotropic, is supported superficially by theory (Willebrand et al. 1980) and modeling studies (Bryan 1982; Böning and Herrmann 1994), but a solid dynamical argument is needed. Furthermore, there is neither a theoretical, nor an observational, nor a modeling basis to assume that the time-mean Ekman transport should be returned barotropically. In fact, Anderson et al. (1979) and Willebrand et al. (1980) clearly indicate that a time-mean forcing drives a circulation which is strongly influ-

12

enced by stratification and nonlinear effects and is generally not barotropic. More recently, Klinger and Marotzke (1999) have argued that the time-mean Ekman layer mass transport is returned at relatively shallow depths. Given a typical ocean temperature distribution, a shallower return flow translates into a warmer return flow and decreases the strength of the heat transport compared to a deep barotropic return flow. Therefore, while the time-dependent portions of the Ekman heat transports are reliable estimates, the time-mean component should be viewed with suspicion.

Global ocean general circulation models were used by Bryan and Lewis (1979), Bryan (1982) and Meehl et al. (1982) to explore heat transport variability. Bryan and Lewis found a significant seasonally varying heat transport, whose structure and amplitude was similar to that found by Hsiung et al. (1989). Meehl et al. (1982) added a seasonally varying, surface heat flux forcing to a similar ocean model and used a wind stress field which had both a semiannual harmonic and an annual harmonic. Their results were similar to those of Bryan and Lewis (1979) for the seasonally varying heat transport, with the addition of a semi-annual signal in the heat transport due to the different forcing fields. Lau (1978) also found a large annual cycle in the ocean heat transport, but did not directly attribute it to the seasonal wind stress cycle. Bryan (1982) found that while the zonal wind stress seasonal cycle forced an ocean heat transport from the summer hemisphere to the winter hemisphere, the seasonal cycle in the meridional wind acted to suppress the heat transport seasonal cycle in the tropics. This was particularly true close to the equator where a meridional surface layer transport can be driven directly by the meridional wind, owing to the Coriolis parameter going to zero there. Bryan's (1982) seminal explanation of the physics behind the seasonally varying Ekman flows, which are the major source of ocean heat transport variability, seems to have been largely ignored outside of the ocean modeling community. More recently, models of various resolutions have been applied to basin-scale studies. Böning and Herrmann (1994) and Yu and Malanotte-Rizzoli (1998) have examined the Atlantic Ocean, while McCreary et al. (1993), Wacongne and Pacanowski (1996), Garternicht and Schott (1997) and Lee and Marotzke (1998) looked at the Indian Ocean. These studies all found strong annual cycles in the ocean heat transport and confirmed the importance of the wind on the ocean heat transport

13

variability. The Pacific Ocean has not been investigated and there have been no recent model studies of the global, time-dependent ocean heat transport with high resolution since Bryan (1982) and Meehl et al. (1982). Further, all the above works use monthly wind stress fields and it is unknown whether higher frequency wind stress fields will introduce high frequency ocean heat transport oscillations.

The most recent global estimate of the time-mean and seasonal cycle of ocean heat transport was made by Hsiung et al. (1989) using ocean heat storage data calculated from the Master Oceanographic Observations Data Set (MOODS). They closed their energy budget at the ocean surface with fluxes computed using the bulk formulae. The ocean heat transport was calculated as the residual needed to close the energy budget in the ocean after accounting for surface fluxes and storage terms. This work expanded that of Lamb and Bunker (1982) in the Atlantic to cover the Pacific and Indian Oceans as well. Their estimate of the annual cycle of heat transport across the equator by the ocean had a peak to peak amplitude of 4.4 ± 1.4 PW. Overall, the picture of the annual cycle they presented was consistent with that of Bryan (1982). However, they found the annual cycle lagged several months behind that of Carissimo et al. (1985). Hsiung et al.'s (1989) seasonal cycle reversed sign in mid-latitudes, as in the studies of Ekman heat transport discussed above, as well as in those of Bryan and Lewis (1979) and Bryan (1982). Therefore, from previous studies there appears to be a large seasonal cycle driven by the seasonal cycle of wind stress. However, there is disagreement about both its magnitude and dynamics. The global studies by Hsiung et al. (1989), Bryan (1982) and Levitus (1987) give a generally consistent picture of the seasonal heat cycle, though differing in details. In contrast, the study of Carissimo et al. (1985), stands out as significantly different from the other estimates, most likely because their data was not sufficiently precise to resolve the seasonal cycle in ocean heat transport.

There are additional consequences of the ocean heat transport variability to be considered. One of the uses for hydrographic surveys, either single lines or large international programs such as the World Ocean Circulation Experiment (WOCE), is that the annual-mean ocean heat transport at a latitude can be estimated by a one-time ocean section. These estimates of heat transport rely on the method used by

14

Hall and Bryden (1982) or on global inversions of hydrographic data (Macdonald and Wunsch 1996). However, if there is strong ocean variability, the estimate of the heat transport may be badly corrupted. Hall and Bryden (1982) assessed the potential error introduced by eddy noise on their estimate of the heat transport at 24°N and found that it could be as large as 25% of the total and was the largest error in their estimate. Additionally, seasonal biases may corrupt estimates of heat transport owing to the predominance of summer time oceanographic field work, particularly at high latitudes. Therefore, it is important that the ocean heat transport variability be quantified and its impact on hydrographic heat transport estimates be evaluated.

Finally, the time-varying circulations themselves can contribute to the mean ocean heat transport by rectification. This process is the subject of considerable interest and debate. Coarse resolution models do not resolve the transport processes associated with the oceanic mesoscale field. Therefore, significant effort has been spent developing a parameterization of the mesoscale eddy field (*e.g.* Gent and McWilliams 1990; Holloway 1992; Griffies 1998). However, the role of the oceanic mesoscale eddy field in climate processes has been only marginally addressed observationally. Stammer (1998) used altimetry data from the TOPEX/POSEIDON satellite to estimate mixing length scales over the global ocean, and combined them with a climatological temperature field to estimate the eddy heat transport by the ocean. He found that over large areas of the ocean gyres the eddy heat transport was small. But, in several places the eddy heat transport was significant: the western boundary currents, the equatorial regions and the Antarctic Circumpolar Current. Wunsch (1999) using a compilation of current meter data came to a similar conclusion. However, the question of whether mixing length scales are even appropriate to parameterize the effects of the ocean mesoscale eddy field has not been addressed using direct ocean measurements, though analyses of atmospheric data suggest they work in the atmosphere (Kushner and Held 1998).

Enhanced computational capability over the past 20 years has allowed ocean general circulation models to use significantly higher resolution than Bryan and Lewis (1979) used in their global ocean model with approximately 2.5° resolution to look at the seasonal variation in poleward heat transport. Resolution has increased by over

an order of magnitude from that in Bryan and Lewis's (1979) calculations. Additionally, more accurate and higher frequency wind stress fields are now produced by the meteorological centers such as the European Centre for Medium-Range Weather Forecasting (ECMWF) and the National Centers for Environmental Prediction (NCEP) and improved fields of surface heat and freshwater flux are available (Barnier et al. 1995). These factors taken together make current numerical model simulations more realistic than their predecessors.

This thesis addresses the dynamics of the time-dependent ocean heat transport through the use of a state-of-the-art ocean general circulation model. Specifically, output from the Parallel Ocean Climate Model from the Naval Postgraduate School is used (the POCM_4B run was discussed by Stammer et al. (1996) and McClean et al. (1997)). The model is a primitive equation, level model (Semtner and Chervin 1992). It has an average resolution of 1/4° in the horizontal direction, and 20 levels in the vertical. It uses realistic topography and extends over a domain from 75°S to 65°N. The model output is available at 3-day intervals throughout the model run. The output was instantaneously sampled from the model and not averaged or filtered, creating temporal aliasing problems (Jayne and Tokmakian 1997; and Chapter 2 of this thesis). The ability of this particular numerical simulation to represent the true variability of the ocean has been addressed by Stammer et al. (1996) and McClean et al. (1997).

Using a high-resolution global ocean general circulation model allows insight into the nature and magnitude of the seasonal cycle of the ocean heat transport. The behavior of higher frequency oscillations can be examined as well. It is also possible to determine the magnitudes of the variability induced by mechanisms other than the Ekman heat transport. Though the use of a numerical model suffers from the model's dependencies and deficiencies, it does let us test dynamical theories for the physical mechanisms that drive the ocean heat transports inferred by Carissimo et al. (1985) and Hsiung et al. (1989). It will also permit an examination of the frequency range higher than the seasonal cycle which heretofore has not been addressed by other modeling studies. Furthermore it allows a more complete picture of the total heat transport variability than can be garnered from examining only the Ekman

16

contribution to the heat transport and allows us to check the consistency of the assumptions that go into the estimates of the Ekman heat transport. It allows an assessment of the contribution of mesoscale eddies to the time-mean heat transport and their impact on one-time hydrographic sections. Most important, it gives a global picture of all these processes that has been heretofore lacking.

Bearing in mind that the model which I have chosen to analyze is not a perfect representation of the ocean and may have significant errors, it is still useful for elucidating the physical mechanisms which lead to heat transport variability in the ocean. Chapter 2 of this thesis addresses the appropriate forcing and sampling of ocean models in which high-frequency motions are present. The nature of aliasing of the high-frequency phenomena given varying sampling methods is discussed and schemes are provided that will remove the aliased energy from the model fields stored for later analysis. A reader who is uninterested in the technical details of this problem may skip this chapter. A complete theory for the role of variable wind stress in forcing fluctuating ocean heat transport has been lacking. While some of the underlying dynamics have been discussed in previous studies, they have never been put together in a cohesive argument. Chapter 3 examines the dynamics allowing temporal variations in wind stress to lead to large variations in the ocean heat transport. These arguments are illustrated with a conceptual model and a homogeneous, shallow-water model with full topography and wind forcing. A detailed description of the time-dependent nature of the ocean heat transport as seen in the Parallel Ocean Climate Model is described in Chapter 4. The time variations in the heat transport are broken down into components due to velocity variations, temperature variations and the covariation of temperature and velocity. Additionally, the heat transport is decomposed into dynamical components, separating the Ekman, gyre and baroclinic contributions to the heat transport variability and allowing an analysis of the impact of the temporal variability on estimates of the time-mean heat transport from hydrographic sections. Finally, the rectified eddy heat transport from the POCM is discussed. A comparison with an analysis derived from TOPEX/POSEIDON data (Stammer 1998) is made and the validity of using a mixing length hypothesis to derive the eddy heat transport is tested.

Chapter 2

Forcing and Sampling of Ocean General Circulation Models: Impact of High Frequency Motions

Steven R. Jayne and Robin Tokmakian [1]

2.1 Introduction

Inertial oscillations arise as simple solutions to the momentum equations for a rotating fluid. In the ocean, these motions are known to be energetic and it should therefore not be surprising that they are significant in numerical models of the ocean driven by realistic, high-frequency forcing. Long time series of realistic wind stress fields are now available 4 times per day for forcing ocean general circulation models (OGCM) and therefore the effects of associated inertial oscillations present in the models on model diagnostics need to be addressed. Two problems arise with respect to inertial oscillations in OGCMs. First, the temporal approximation form of the wind stress forcing can excite zonal bands of large amplitude oscillations. For example if wind fields are not changed smoothly in time but are updated every 3 days, the step function resonantly forces the inertial oscillations at specific latitudes. Secondly, most analyses of OGCM output for climate research or process studies are unconcerned

---

about processes at timescales that are as short as the inertial period. However, if the prognostic fields are sampled at any interval greater than half the inertial period, instantaneous sampling will alias inertial oscillations into lower frequencies that vary with latitude.

Recent analysis of high resolution primitive equation models (Parallel Ocean Climate Model (POCM) with $1/4°$ resolution (Semtner and Chervin 1992; Stammer et al. 1996) and Los Alamos Parallel Ocean Project (POP11) with $1/6°$ resolution (Dukowicz and Smith 1994; Fu and Smith 1996)) as well as lower resolution OGCMs (e.g. the global MIT model with $1°$ resolution (Marshall et al. 1997a; Marshall et al. 1997b)) all show unrealistic features in the output velocity fields (u and v) subsampled every 3 days and the associated diagnosed field of eddy kinetic energy (EKE) which result from the aliasing of inertial oscillations generated by the high-frequency wind stress forcing fields. To understand and to remove this unrealistic signal from future model runs, we have analyzed the sensitivity of the model inertial motions and the model output on the temporal forcing and the sampling period. Both aspects are addressed in this chapter. To do so, the temporal forcing was changed from uninterpolated step functions to a linear interpolant of the data. The sampling scheme is modified to filter out oscillations at frequencies higher than the Nyquist frequency prior to the model fields being saved to output.

Tests are performed using the $1/4°$ resolution POCM. The version of the model is the same as described by Stammer et al. (1996). It is a primitive equation model on a Mercator grid (nominal resolution of $1/4°$) with 20 levels in the vertical. The model's surface momentum is forced with realistic wind stress fields derived from the twice-daily European Centre for Medium-Range Weather Forecasting (ECMWF) 10 m wind fields. The resulting wind stress fields are interpolated in space using bi-cubic spline fits onto the model grid. The changes of the present runs relative to the standard run discussed by Stammer et al. (1996) are related to 1) the temporal wind forcing and 2) the sampling of the prognostic variables, which are summarized in Table 1. All runs were initiated from the same point in time, February 23, 1993, defined by the date of the ECMWF wind stress fields and the initial prognostic 3-D model fields from the run of POCM 4_B. Sampling of POCM 4_B was instantaneous

Table 2.1: Summary of test runs with varying forcing periods, functional forms, and sampling periods.

Test number	Wind forcing	Interpolation	Sampling
Original (POCM_4B)	3 day	no	3-day snapshot
1	3 day	no	hourly
2	3 day	linear	hourly
3	1 day	linear	hourly

snapshots of the model's prognostic variables (velocities, temperature, salinity and sea surface elevation) every 3 days. The model time step is 1/2 hour. In this study, the model's prognostic variables were also sampled hourly along several lines, meridional and zonal, to determine the differences resulting from how each run was being forced. For POCM 4_B and test 1, the wind stress fields were held constant over a 3 day period, whereas for tests 2 and 3 the wind stress fields were linearly interpolated to each time step. Section 2 focuses on the forcing problem and section 3 discusses the possible remedies to remove the aliasing in the sampled fields.

2.2 Changes in the forcing of the model

Inertial oscillations are a well studied phenomenon in the ocean (Fu 1981; Gill 1982). A simple model of inertial oscillations can be found by a reduction of the momentum equations:

$$
\begin{aligned}
\frac{\partial u}{\partial t} - fv &= \tau_x(t) - ru \\
\frac{\partial v}{\partial t} + fu &= \tau_y(t) - rv,
\end{aligned}
\tag{2.1}
$$

where u is the zonal component of velocity and v is the meridional component of velocity, $f = 2\Omega \sin(\phi)$ is the Coriolis parameter in which Ω is the angular rotation rate of the Earth and ϕ is the latitude, τ_x and τ_y are the zonal and meridional components of the wind stress, respectively, and r is the decay timescale for a linear dissipation. This coupled set of differential equations can be solved to give:

$$
u + iv = e^{-ift}e^{-rt} \int e^{ift}e^{rt}[\tau_x(t) + i\tau_y(t)]\, \mathrm{d}t,
\tag{2.2}
$$

21

where $i = \sqrt{-1}$. This solution has a strong resonance at the frequency $-f$ which is limited only by the presence of dissipation so any energy in the forcing at that frequency will excite inertial oscillations of significant amplitude. In a statistical sense, the amplitude response of the inertial oscillations can be understood by knowing the characteristics of the rotary spectrum for the forcing function, $\tau(t)$. The spectral response, $S_{u+iv}(\omega)$, of (2.2) is given by:

$$S_{u+iv}(\omega) = \frac{S_\tau(\omega)}{(\omega + f - ir)^2},$$

(2.3)

where ω is the angular frequency and $S_\tau(\omega)$ is the power spectrum of the wind forcing (Priestley 1981).

In the real world, the wind stress varies on all timescales and $S_\tau(\omega)$ is a continuous function. However, the available high-frequency wind stress data sets are provided at best only 4 times a day as compared to model time steps of about an hour. What is the most appropriate method to interpolate the provided wind fields to the model time steps in such a way as to best preserve the real high-frequency wind stress spectrum? Three methods are possible: 1) a wind stress field kept constant over an observation period (series of step functions), 2) a wind field linearly interpolated between observation time points and 3) a cubic spline interpolation (or other higher-order method, such as Hermite interpolation) of the wind forcing. At frequencies lower than the Nyquist frequency of the wind stress data, the power spectrum of the forcing is determined by the data. However, at frequencies higher than the Nyquist frequency of the data, the power spectrum is dominated by the auto-correlation behavior of the functional form used for the interpolation. If the available data have a Nyquist period that is order days, then the inertial frequency for latitudes away from the equator will lie in the portion of the power spectrum that is determined by the interpolation and accordingly the forcing of inertial oscillations will be a function of the interpolation scheme. If one is not interested in inertial motions, the interpolation method therefore should be chosen carefully so that its high-frequency characteristics are smooth and continuous to avoid artificial high-frequency motions. However, there may be issues related to mixed-layer-physics parameterizations where the inertial energy is needed (Large et al. 1994).

Since most high-frequency wind stress data sets will require some form of interpolation to be used as forcing in an OGCM, it is necessary to discuss the implications of various methods. The two methods discussed here are 1) keeping the wind stress constant over a data period since it is relevant to the available POCM output and 2) the more commonly used linear interpolation. In order to establish a notational framework, we first denote a sequence of indices for the forcing functions; where $i = 0, 1, 2, \ldots$ are the times when we have data available and $j = 0, 1, 2, \ldots$ are the model time steps that we are interpolating the original data to. If the model wind stress is simply updated once per 3 days without any interpolation, the forcing function is written:

$$\tau_i^j = a_i \tag{2.4}$$

for all $j = 0, 1, 2, \ldots$ where the a_i are simply the values of the wind stress read in from the data files. If we make the assumption that the a_i are uncorrelated, then the power spectrum of the wind forcing at frequencies higher than the Nyquist frequency of the data can be found analytically by taking the Fourier transform of the auto-correlation of the interpolant (Bracewell 1986). For the case of the series of step functions, the power spectrum is given by:

$$S_\tau(\omega) \propto \frac{1 - \cos(\omega h)}{(\omega h)^2} = \text{sinc}^2\left(\frac{\omega h}{2}\right), \tag{2.5}$$

where $h = 3$ days. The more advanced technique of linearly interpolating to each time step between the available data is denoted by:

$$\tau_i^j = a_i + b_i(j\Delta t), \tag{2.6}$$

where $b_i = (a_{i+1} - a_i)/h$, where a_i is again the wind stress read in from the data files for that day, and a_{i+1} is the wind stress for the third day following, $\Delta t = 1/2$ hour and again $h = 3$ days. This form of the forcing has the power spectrum

$$S_\tau(\omega) \propto \frac{3 - 4\cos(\omega h) + \cos(2\omega h)}{(\omega h)^4} = \text{sinc}^4\left(\frac{\omega h}{2}\right). \tag{2.7}$$

It can be seen that both of these methods have zeros in the power spectrum at $\omega h = 2\pi, 4\pi, 6\pi, \ldots$ which, still assuming that $h = 3$ days, correspond to periods

of 3 days, 1.5 days, 1 day, etc. Any motions at these periods will be only weakly forced compared with motions with frequencies at $\omega h \approx 3\pi, 5\pi, 7\pi, \ldots$ (periods of 2 days, 1.2 days, 0.86 days, etc.) which are located at local maxima of both the forcing functions' spectra. If the zeros correspond to the period of the inertial oscillations at a given latitude, there will be a marked decrease in the amplitude of the inertial oscillations at that latitude since there is much less energy in the forcing to drive them. On the other hand if the inertial period is at a local maximum in the power spectrum of the forcing function the inertial oscillations will be forced much more strongly. Moreover, between the zeros in the power spectrum, the peaks fall off at a rate of ω^{-2} for the uninterpolated forcing and ω^{-4} for the linearly interpolated forcing. This should result in a noticeable depletion in the strength of the inertial oscillations at the latitude where their frequency is higher than the Nyquist frequency of the data and a more general weakening in the high-frequency energy in the model overall.

These effects can be seen in two different ways in the hourly sampled model data. First, we can consider the power spectrum of the velocity at a single point in the ocean as a function of frequency. If the velocities in the surface layer are strongly coupled to the forcing function at high frequencies, it is expected that the shape of the spectrum for the velocities will be strongly influenced by the shape of the forcing spectrum. Figure 2.1 shows the power spectrum of the u component of velocity sampled every hour for the surface layer at 30°N, 200°E for the 3 different forcing tests. Most noticeable is the deficit of energy at frequencies corresponding to 3 days and 1.5 days and peaks of energy at 2 days and 1.2 days when the forcing function is derived from the once-per-3-day data in both the uninterpolated and linearly interpolated methods. The comparison at higher frequencies becomes more difficult owing to the noisiness of the spectrum and to the strong spectral peak from the inertial oscillations. At 30°N the peak in the spectrum due to the inertial oscillations corresponds to approximately 1 day, where a spectral gap from the forcing is expected. But, the energy in the higher frequencies does indeed show an overall weakening of almost an order of magnitude when the linear interpolant is used. This is consistent with the analytic forms derived above. When the wind stress forcing is derived from daily data instead of data every 3 days, the spectrum fills out at periods of longer than 2 days, but now shows a

24

depletion at the 1-day period, again consistent with the previous arguments if $h = 1$ day.
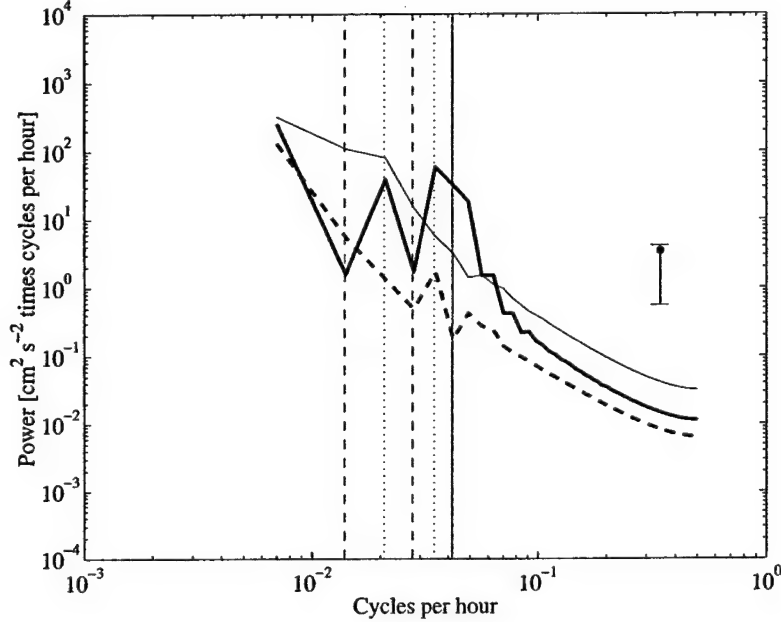
Figure 2.1: Frequency spectra of the u component of velocity at 30°N, 200°E in the North Pacific for tests 1 with once per 3 days uninterpolated forcing (thin solid line), test 2 with once per 3 days linearly interpolated forcing (dashed line) and test 3 with once per day linearly interpolated forcing (heavy solid line). Vertical dashed lines are at the expected minima (3 days and 1.5 days) and dotted lines are the expected maxima (2 days and 1.2 days). The thin solid vertical line is at the inertial frequency.

The second way to compare these analytic arguments to the model results is to consider the amplitude of the inertial oscillations as a function of latitude. Since the frequency of the inertial oscillations increases with increasing latitude, the inertial oscillations will be forced by varying energy according to (2.5) and (2.7), and therefore we expect to see minima in the amplitude of the inertial oscillations where $S_\tau(\omega)$ is small and maxima where it is large. At most latitudes the inertial oscillations dominate the EKE in the hourly sampled data, so we use the EKE as a proxy for the strength of inertial oscillations. Figure 2.2 shows the EKE as a function of latitude for the three tests. Figure 2.2a compares the uninterpolated forcing (test 1) with the linearly interpolated forcing (test 2). The EKE from test 1 shows bands

of sharp peaks alternating with bands of low energy. The bands of low energy correspond directly to latitudes where the forcing spectra have minima, namely where $\omega h = fh = 2\pi, 4\pi, 6\pi, \ldots$ corresponding to:

$$\phi = \operatorname{asin}\left(\frac{2n\pi}{2\Omega h}\right) \qquad \text{for } n = 1, 2, 3, \ldots, \tag{2.8}$$

which for once-per-3-day data ($h = 3$ days) occur at the latitudes 9.6°, 19.4°, 29.9°, 41.7° and 56.2°. The most noticeable effect from the change to linear interpolation is the significant decrease in strength of the EKE away from the equator when the linear interpolation is used. This is driven by the faster decay of wind stress energy at high frequencies using the linear interpolation method instead of the uninterpolated method. The change to using daily wind stress values with linear interpolation (Fig. 2.2b) increases the energy at most latitudes, but there a minimum still occurs at the latitude of 29.9° where $fh = 2\pi$ for $h = 1$ day. Better methods would be either real forcing fields every time step or a spline fit applied to the original data to interpolate to each time step. Both of these solutions, however, are logistically difficult to implement. This leads directly to the next section on how to remedy the problems shown.

2.3 Solutions to aliasing of the inertial frequencies

In POCM, prognostic fields are saved to storage every 3 model days, whereas the inertial period varies with latitude from 1/2 a day at the poles to infinitely long at the equator. Therefore, the saved model record only resolves the inertial oscillations where their period is greater than 6 days corresponding to within about 5°of the equator. At higher latitudes where the sampling does not resolve the inertial oscillations, they are aliased in time, so that they impersonate oscillations with much longer periods. The aliasing frequencies follow from:

$$\omega = f - \frac{2n\pi}{\Delta t} \tag{2.9}$$

with $\Delta t = 3$ day sampling period, and $n = 0, 1, 2, \ldots$ such that $|\omega| \leq \pi/\Delta t$. Because f varies meridionally, the aliased frequency is also a function of latitude. Shown

26
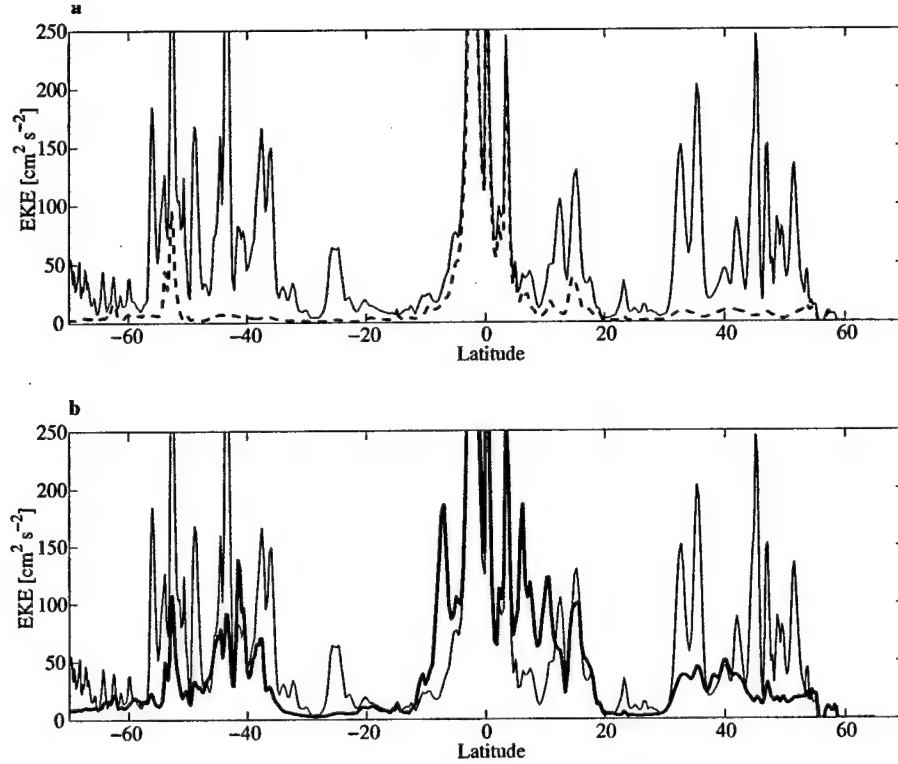
Figure 2.2: EKE along 200°E for forcing with (a) once per 3 days uninterpolated wind stress (thin solid line) and with once per 3 days linearly interpolated forcing (dashed line) and (b) once per day linearly interpolated forcing (heavy solid line). EKE is in cm^2s^{-2}.

in Fig. 2.3 is the true period of inertial oscillations and their aliased period as a function of latitude for sampling periods (Δt) of once per day and once per 3 days. The latitudes at which the aliased period of the inertial motions go to infinity (the frequency, $\omega = 0$) follow from (2.8), substituting Δt for h and are at 9.6°, 19.4°, 29.9°, 41.7° and 56.2°. At these latitudes, the inertial oscillations are aliased into the time mean. In between these latitudes there are broad bands where the period of the inertial oscillations is aliased to a period longer than the Nyquist frequency of the output data.

It is impossible to eliminate aliasing due to the subsampling of the model; however, one can reduce the amplitude of the aliased inertial oscillation signal in the true EKE by saving filtered estimates of the prognostic variables instead of using instantaneous dumps of the variables every three days. An ideal filtering scheme would remove from

27

Figure 2.3: The true period of inertial oscillations (dashed) and their aliased period (solid) as a function latitude for sampling at (a) once per day and (b) once per 3 days.

the output all oscillations at frequencies higher than the Nyquist frequency of the output data. However, such filtering schemes would require knowledge of the entire

time history of the model to make a filtered estimate at any given time point, which is not realistic in an OGCM because of memory and/or disk storage requirements. But filters can be applied to the model during the run which only requi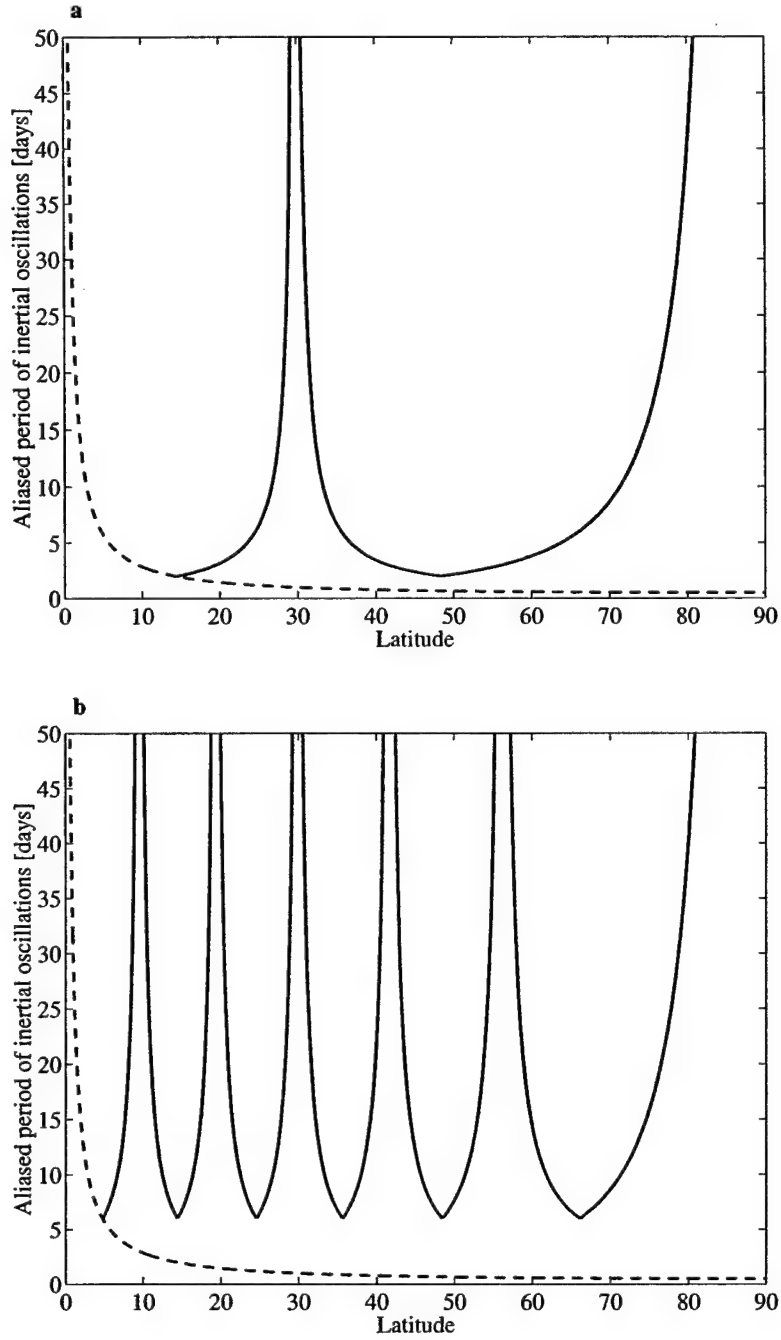re knowledge from single timesteps over the output period. There is an extensive literature on the design and use of filters (Priestley 1981). Among the host of possible choices, the running average (or boxcar filter) and Hamming filter are commonly used and easy to implement. Note that a low pass filter (> 9 days) applied to the POCM 4_B output will remove much of the spurious eddy energy associated with the inertial motions, but not where it was aliased into the mean fields.

2.3.1 Average fields

The running average requires only summing the variables in time over a given period and dividing by the number of time points included in the sum. If the period is chosen to be significantly greater than the period of the inertial oscillations, inertial energy will be removed from the output. A comparison of the zonally averaged EKE as a function of latitude for the original run with the result of tests 2 and 3 averaged over 3 day periods is shown in Fig. 2.4. The dominant feature to recognize is the removal of the large peaks in the EKE associated with the inclusion of the inertial oscillations in lower-frequency time-dependent motions. In the thin bands of low EKE in the unfiltered estimate near $9.6°$, $19.4°$, $29.9°$, $41.7°$ and $56.2°$, the inertial oscillations do not contribute to the EKE, since their aliased period is very long. In the filtered estimate, however, the inertial oscillations are removed from the output before the EKE calculation. Therefore, at these latitudes there is very little difference between the filtered and unfiltered estimates of EKE. The minor differences between tests 2 and 3 are real effects of the higher-frequency forcing used in test 3.

2.3.2 Hamming filter

The boxcar filter is the simplest filter to implement, requiring only that the model save the mean of the prognostic variables every three days. However, unless the length of the boxcar filter is much greater than the period of the oscillations which are to be
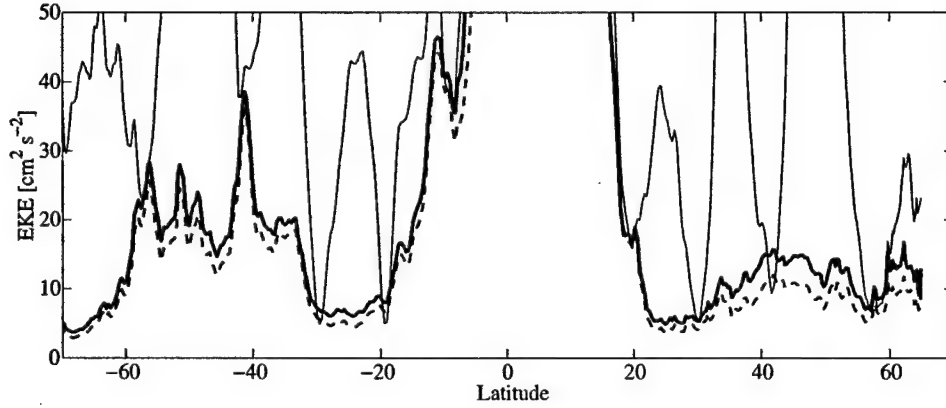
Figure 2.4: (a) Zonal average EKE for April 1993 for the original run which used once per 3 days uninterpolated forcing and once per 3 days instantaneous sampling (thin solid line), test 2 with used once per 3 days linearly interpolated forcing and 3 day averaged samples (dashed line) and test 3 with once per day linearly interpolated forcing and 3 day averaged samples (heavy solid line). EKE is in cm^2s^{-2}.

removed, or there is an integral number of complete oscillations within the period of the filtering, the boxcar filter can only weakly damp their amplitude because of the significant side lobes in the frequency domain of the boxcar filter. It is well known that tapering the sides of the filter in the time domain reduces the amplitude of the side lobes in the frequency domain. An excellent candidate for this application is the Hamming filter since it minimizes the side lobes in the frequency domain (Priestly 1981). The Hamming filter would be implemented in a similar fashion as the boxcar filter, except that, a weighting coefficient used for each time step is changed at each time step. The coefficients are given by the formula:

$$w(k) = 0.54 - 0.46 \cos\left(\frac{2\pi k}{n-1}\right), \qquad 0 \leq k \leq n-1, \tag{2.10}$$

where n is the number of time steps in 3 days. We can compare the effectiveness of the boxcar and Hamming filters at damping an oscillation at the inertial frequency as a function of latitude. Figure 2.5 shows the damping coefficient of the filtered inertial oscillation as a function of latitude for the boxcar and Hamming filters. For a sampling period of 3 days, the filtered inertial energy poleward of $\pm 19°$ is less than 1% of its original magnitude, whereas over a similar range, the boxcar filter is about an order of magnitude less effective.

30

Eddy Kinetic Energy – No averaging

Eddy Kinetic Energy – 3 day averages
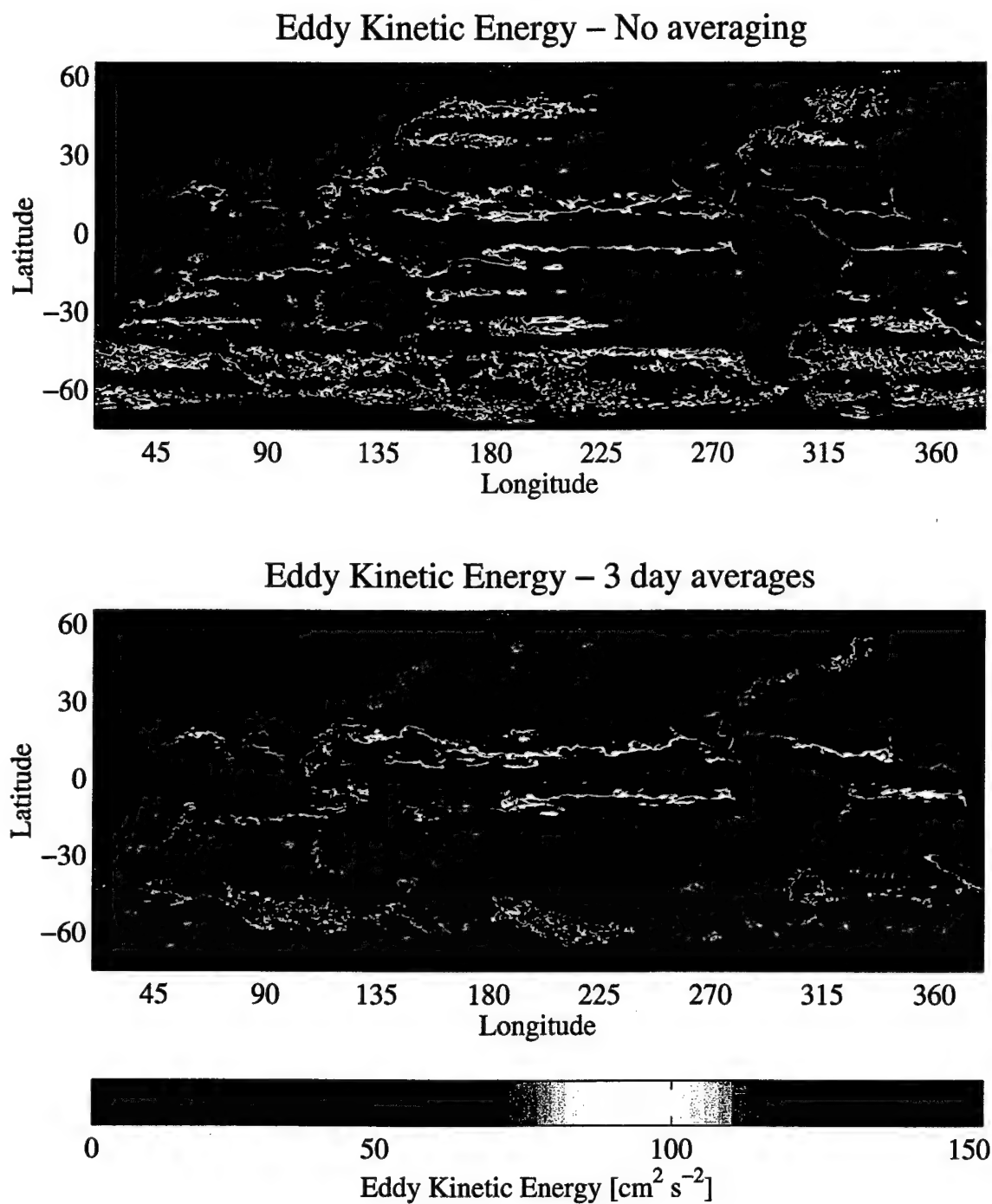
Figure 2.4: cont. (b) EKE calculated over 6 months from March through August 1993 for the original run (upper panel) showing aliased inertial oscillations and test 3 (lower panel) where the inertial oscillations have been removed by a 3-day boxcar filter.
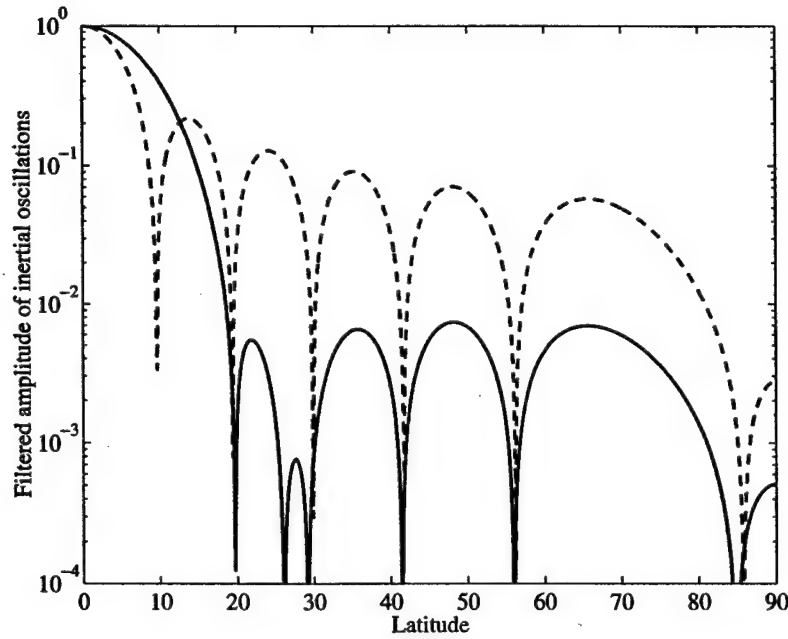
Figure 2.5: Damping response coefficient for inertial oscillations as a function of latitude for a Hamming filter (solid line) and a boxcar filter (dashed line).

The inertial oscillations present in the model affect not only the velocity fields and eddy kinetic energy, but also higher-order products. The meridional heat transport is very sensitive to the aliasing induced by the inertial oscillations because in the model they carry a large amount of heat in the surface layer. It has a very large amplitude oscillation at the inertial frequency as can be seen in Fig. 2.6a. The heat transport across 25°N in the Atlantic Ocean calculated from hourly output from test case 1 shows an oscillation at the inertial frequency with an amplitude of about 1 Petawatt. Overlaying an arbitrary 3-day subsampling on it clearly gives a much different picture from what the full time series shows from hourly sampling. In Fig. 2.6b, the response in the zonal heat transport at 25°N with the boxcar filter is compared to that derived from a Hamming filter with a width of 3 days. The Hamming filter (solid line) damps out the inertial oscillations much more effectively than the boxcar filter (dashed line). From these considerations, it appears that the Hamming filter is the most appropriate to use to remove the inertial oscillations from the model records.
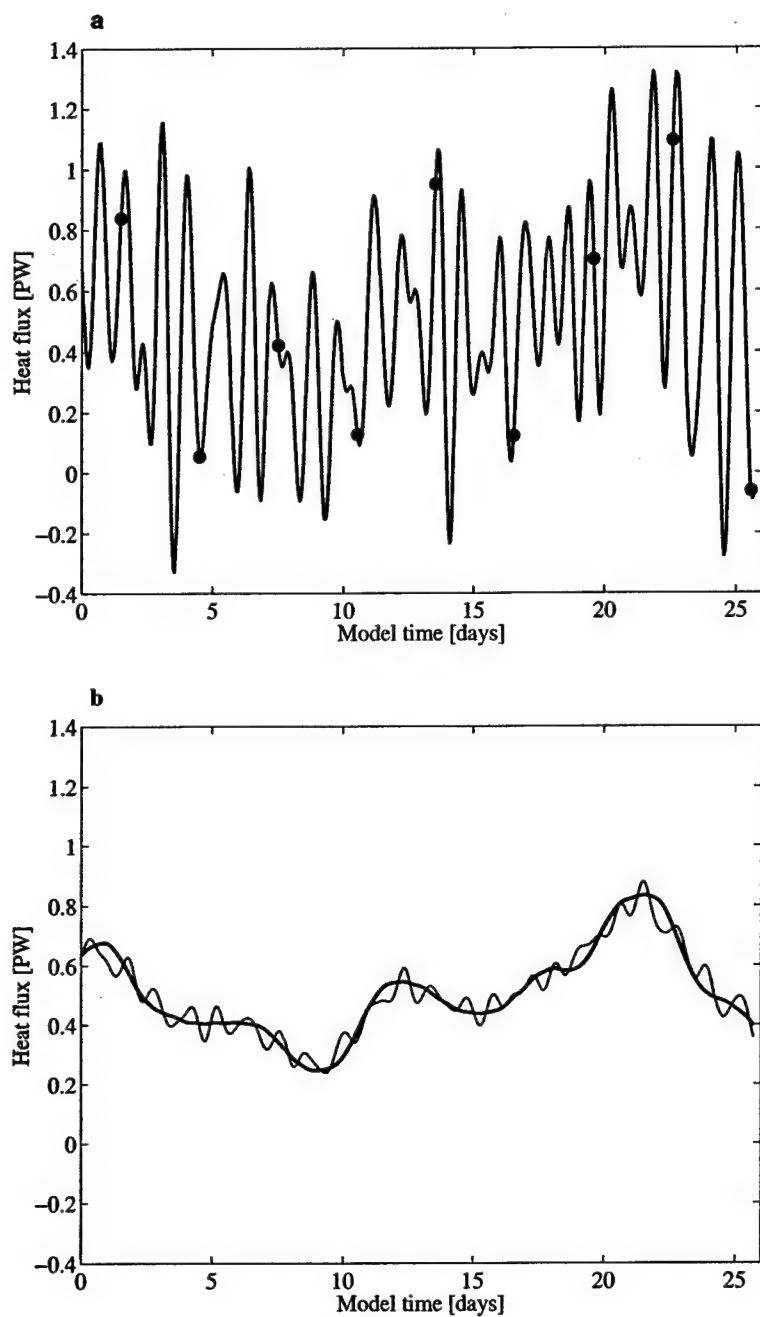
Figure 2.6: (a) Unfiltered heat transport time series at 25°N in the Atlantic with the dots representing arbitrary once-per-3-days sampling. (b) Same results but using a 3-day running boxcar filter (thin solid line) and a 3 day running Hamming filter (heavy solid line) on the heat transport data.

2.4 Conclusions

This chapter has discussed how high-frequency forcing and associated sampling in models introduces aliased signals due to inertial oscillations into the sampled prognostic fields. It has been shown that inertial motions are aliased into longer-period motions whose frequency depends on the latitude and sampling rate. At some combinations of latitude and subsampling period, the inertial motions can be aliased into the mean fields. The method used to perform the temporal interpolation of the wind stress fields can cause the high-frequency power spectrum to be distorted. For an investigator wishing to study high-frequency motions, such as inertial oscillations, these arguments indicate that it would be best to examine the model state at a very high frequency and force the model with high-frequency fields. However, for an investigator studying the general circulation of the ocean, we recommend that some type of filtering prior to saving fields for later analysis be incorporated in the model run to remove the inertial oscillations. We also suggest that even when new forcing fields are read in every day, they need to be interpolated to every time step to remove steps in the forcing of the model.

2.5   Appendix: Derivation of interpolation spectra

The power spectra for the interpolation functions used in this chapter require some derivation. In order to have a framework in which to discuss them, the following indices are defined according to the following time line:
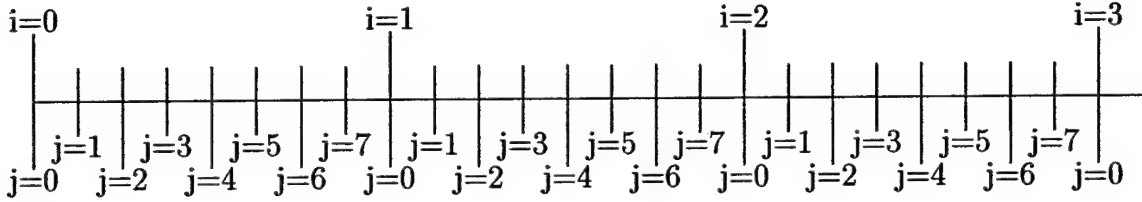
where $i = 0, 1, 2, 3 \ldots$ are the time points where the data are provided, namely once every 3 days in this case, and $j = 0, 1, 2, 3 \ldots$ are the time steps to which the data are being interpolated. Here for illustration purposes, there are 8 time steps per day. In practice, there are 48 time steps per day (one time step $= 1/2$ hour) so $j = 0, 1, 2, 3 \ldots 143$ if one is interpolating the once per day wind fields. (If one is interpolating the once per day winds fields then $j = 0, 1, 2 \ldots 47$.)

In the original method of using the wind stress without any interpolation:

$$\tau_i^j = a_i \tag{2.11}$$

for all j, where a_i is simply the wind stress read in from the data files. In this case the interpolated function itself is not continuous in time, it has discontinuities at every update. The method is visualized in Fig. 2.7 with synthetic data.

If the a_i are uncorrelated, so that: $\langle a_k a_l \rangle = \delta_{k,l}$, where $\delta_{k,l}$ is the Kronecker delta function, then the autocorrelation function for this interpolant is:

$$\rho(\tau) = \begin{cases} 1 - \dfrac{\tau}{h} & 0 \leq \tau \leq h \\[2mm] 0 & \tau \geq h \end{cases} \tag{2.12}$$

where ρ is the correlation coefficient, τ is the time lag and h is the time between the original data points. It is an even function, so negative time lags are equivalent to positive time lags. Assuming the original data have a standard deviation of 1, then
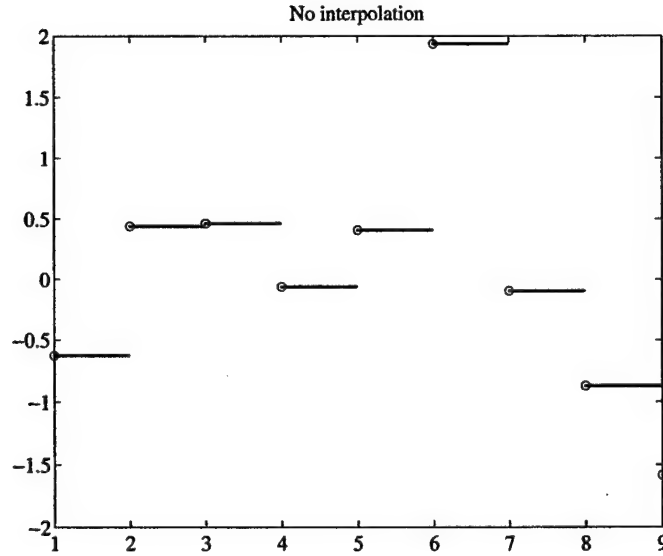
Figure 2.7: No interpolation between data points

the interpolated function also has a standard deviation of 1 (given by the square-root of the zero lag of the auto-correlation function). The Fourier transform of the auto-correlation function gives the power spectrum:

$$S(\omega) \propto \frac{2[1 - \cos(\omega h)]}{(\omega h)^2} = \text{sinc}^2\left(\frac{\omega h}{2}\right). \tag{2.13}$$

This power spectrum falls off like ω^{-2}, but it has zero variance lines every $\omega h = n\pi$, $n = 1, 2, 3, \ldots$ which can cause undesirable depleted energy bands.

Following the same notation, the linear interpolation method would be denoted:

$$\tau_i^j = a_i + b_i(j\Delta t) \tag{2.14}$$

where $b_i = (a_{i+1} - a_i)/h$, where a_i is again the wind stress read in from the data files for that day, and a_{i+1} is the wind stress for the next day and h = 3 days (for the case of interpolating 3 day averaged winds). Using this method the interpolated function is now continuous in time, but its first derivative has offsets between at the data points. Figure 2.8 illustrates this method.

Again, assuming the a_i are uncorrelated, the autocorrelation is:

36
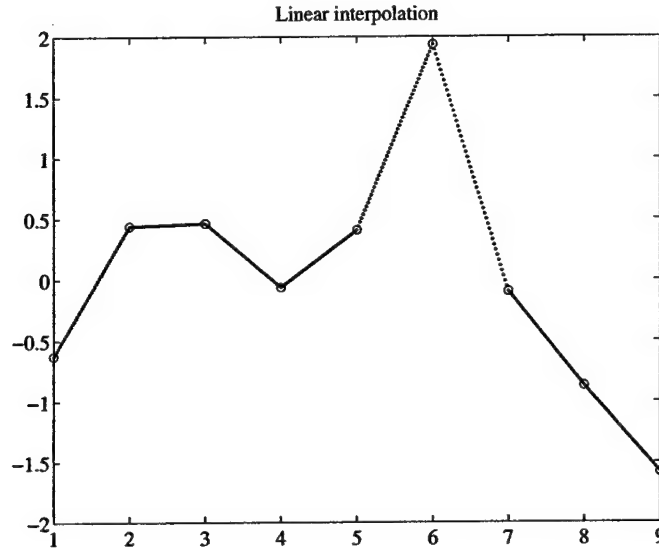
Figure 2.8: Linear interpolation between data points

$$\rho(\tau) = \begin{cases} \dfrac{\tau^3}{2h^3} - \dfrac{\tau^2}{h^2} + \dfrac{2}{3} & 0 \leq \tau \leq h \\[2ex] \dfrac{-\tau^3}{6h^3} + \dfrac{\tau^2}{h^2} - \dfrac{2\tau}{h} + \dfrac{4}{3} & h \leq \tau \leq 2h \\[2ex] 0 & \tau \geq 2h. \end{cases} \tag{2.15}$$

Again it is an even function and assuming the original data have a standard deviation of 1, then the interpolated function has a standard deviation of $\sqrt{2/3} \approx 0.816$. So the interpolated function has 82% of the total variance of the original data. This issue and methods to alleviate it were addressed by Killworth (1996). The power spectrum is:

$$S(\omega) \propto \frac{2[3 - 4\cos(\omega h) + \cos(2\omega h)]}{(\omega h)^4} = \text{sinc}^4\left(\frac{\omega h}{2}\right). \tag{2.16}$$

What has been gained using this method is that the power spectrum at high frequencies falls off much faster, like ω^{-4}, and the number and position of the zero energy bands have not changed.

Still using two data points a_i and a_{i+1} one can write the following interpolation method using a cosine function:

$$\tau_i^j = \frac{a_i - a_{i+1}}{2} \cos\left(\frac{j\Delta t\pi}{h}\right) + \frac{a_i + a_{i+1}}{2} \tag{2.17}$$

37
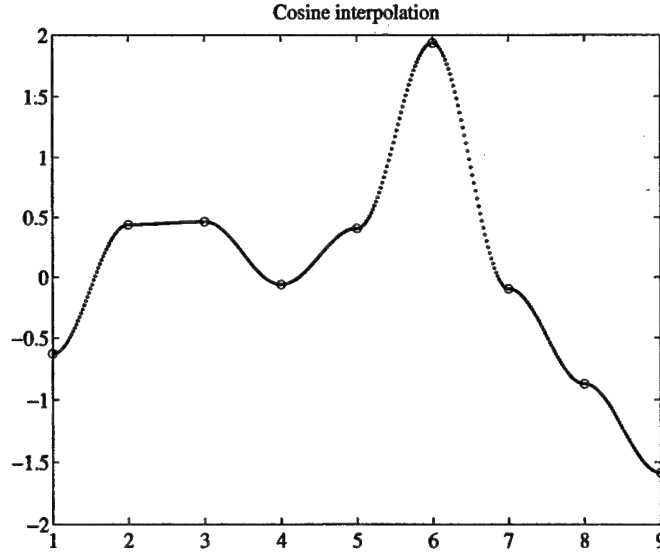
Figure 2.9: Cosine interpolation between data points

which is both continuous and has a continuous first derivative since its slope goes to zero at the ends of each interval. This achieves the goal of not having discontinuities in the function or its first derivative, but it is a bit artificial in that its derivative does go to zero at the ends of each interval.

Its autocorrelation function is given by:

$$\rho(\tau) = \begin{cases} \dfrac{3}{8\pi}\sin\left(\pi\dfrac{\tau}{h}\right) + \dfrac{1}{4}\left(1 - \dfrac{\tau}{2h}\right)\cos\left(\pi\dfrac{\tau}{h}\right) + \dfrac{1}{4}\left(2 - \dfrac{\tau}{h}\right) & 0 \le \tau \le 2h \\ \\ 0 & \tau \ge 2h \end{cases} \tag{2.18}$$

which gives a power spectrum of the form:

$$S(\omega) \propto \frac{\pi^4}{2}\frac{1 - \cos{(2\omega h)}}{(\omega h)^2[(\omega h)^2 - \pi^2]^2} = \pi^4\frac{\mathrm{sinc}^2(\omega h)}{[(\omega h)^2 - \pi^2]^2} \tag{2.19}$$

The interpolated function has a standard deviation of $\sqrt{3/4} \approx 0.866$. The power spectrum at high frequencies now drops off like ω^{-6}, but the number of zero energy bands has doubled.

It is possible to use more data points in the interpolation. A three-point method can be written using quadratic interpolants, matching the function and the first derivative at each interval, but it is very unstable with wild oscillations between the data points. There are spline methods, but they require a global inversion of

38

the data to find the coefficients. Though they can be made into local calculations once one of the coefficients is known, they are unsuitable for a numerical model that would be started and stopped many times during a single run as the coefficients would have to be stored and reread or recalculated at each restart. However, a local interpolation can be formed using four data points. The method of Hermite polynomial interpolation uses both the value of the function and its derivative at each data point. However, in general only the value of the function at each time point is known, but the derivative can be approximated using finite-difference methods. Using this method, the interpolated function is continuous as are its first and second derivatives. The form of the interpolant function is chosen to be a cubic:

$$\tau_i^j = a_i + b_i(j\Delta t) + c_i(j\Delta t)^2 + d_i(j\Delta t)^3 \tag{2.20}$$

The function at $j = 0$ is:

$$\tau_i(0) = a_i \tag{2.21}$$

The time derivative at $j = 0$ is:

$$\tau_i'(0) = b_i \approx \frac{a_{i+1} - a_{i-1}}{2h} \tag{2.22}$$

The function at $j\Delta t = h$ is:

$$\tau_i(h) = a_i + b_i h + c_i h^2 + d_i h^3 = a_{i+1} \tag{2.23}$$

The time derivative at $j\Delta t = h$ is:

$$\tau_i'(h) = b_i + 2c_i h + 3d_i h^2 \approx \frac{a_{i+2} - a_i}{2h} \tag{2.24}$$

Solving these equations gives the formulae for the coefficients:

$$
\begin{aligned}
b_i &= \frac{1}{2h}(a_{i+1} - a_{i-1}) \\
c_i &= \frac{1}{2h^2}(2a_{i-1} - 5a_i + 4a_{i+1} - a_{i+2}) \\
d_i &= \frac{1}{2h^3}(-a_{i-1} + 3a_i - 3a_{i+1} + a_{i+2})
\end{aligned}
\tag{2.25}
$$
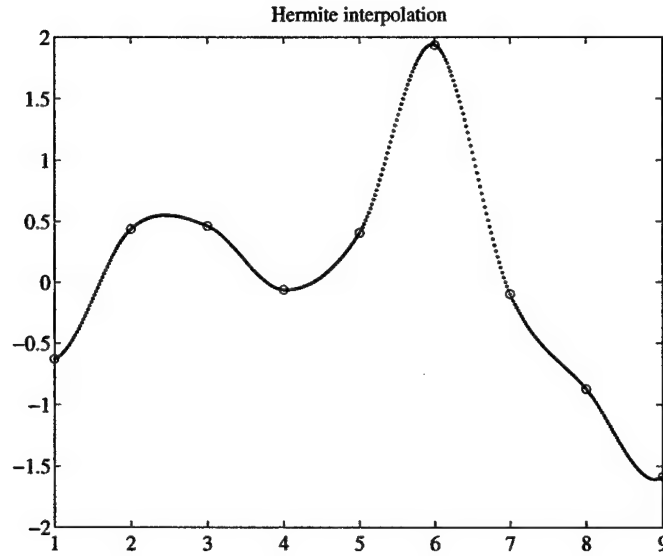
Figure 2.10: Hermite interpolation between data points

The above equations are written for interior points; suitable expressions can be derived for the boundary values using the one-sided difference formulae for the derivatives there. The method gives an interpolant that is shown in Fig. 2.10 for the synthetic data. The autocorrelation function for this function can be found to be:

$$\rho(\tau) =$$

$$
\begin{cases}
\dfrac{57}{70} - \dfrac{7\tau^2}{6h^2} + \dfrac{2\tau^4}{3h^4} - \dfrac{\tau^5}{24h^5} - \dfrac{5\tau^6}{24h^6} + \dfrac{\tau^7}{16h^7} & 0 \le \tau \le h \\[2ex]
\dfrac{107}{140} + \dfrac{\tau}{6h} - \dfrac{23\tau^2}{20h^2} - \dfrac{5\tau^3}{6h^3} + \dfrac{9\tau^4}{4h^4} - \dfrac{169\tau^5}{120h^5} + \dfrac{3\tau^6}{8h^6} - \dfrac{3\tau^7}{80h^7} & h \le \tau \le 2h \\[2ex]
\dfrac{107}{140} + \dfrac{17\tau}{6h} - \dfrac{113\tau^2}{12h^2} + \dfrac{59\tau^3}{6h^3} - \dfrac{61\tau^4}{12h^4} + \dfrac{57\tau^5}{40h^5} - \dfrac{5\tau^6}{24h^6} + \dfrac{\tau^7}{80h^7} & 2h \le \tau \le 3h \\[2ex]
\dfrac{128}{35} - \dfrac{32\tau}{3h} + \dfrac{176\tau^2}{15h^2} - \dfrac{20\tau^3}{3h^3} + \dfrac{13\tau^4}{6h^4} - \dfrac{49\tau^5}{120h^5} + \dfrac{\tau^6}{24h^6} - \dfrac{\tau^7}{560h^7} & 3h \le \tau \le 4h \\[2ex]
0 & \tau \ge 4h. \quad (2.26)
\end{cases}
$$

The interpolated function has a standard deviation of $\sqrt{57/70} \approx 0.902$ relative to the original data's standard deviation of 1. The power spectrum can be found, it is quite complicated:

40

$$S(\omega) \propto [630 + 10(\omega h)^2 - 1008\cos{(\omega h)} + 504\cos{(2\omega h)} - 144\cos{(3\omega h)} + 18\cos{(4\omega h)}$$
$$- 168(\omega h)\sin{(\omega h)} + 168(\omega h)\sin{(2\omega h)} - 72(\omega h)\sin{(3\omega h)} + 12(\omega h)\sin{(4\omega h)}$$
$$- 8(\omega h)^2\cos{(\omega h)} - 8(\omega h)^2\cos{(2\omega h)} + 8(\omega h)^2\cos{(3\omega h)} - 2(\omega h)^2\cos{(4\omega h)}]/(\omega h)^8$$

$$(2.27)$$

The power spectra for the four interpolation methods are compared in Fig. 2.11, where the solid line is the power spectrum for a series of step functions, the thin dashed line is that of linear interpolation, the heavy dashed line is the cosine interpolant's power spectrum and the heavy line is the power spectrum for the four-point method discussed above. The dotted black vertical line is at the Nyquist frequency of the original data. At frequencies lower than the Nyquist, the power spectrum is determined by the data and at frequencies above the Nyquist, the power spectrum is determined by the form of the interpolant. The four-point Hermite method has the most rapid decay of energy at the high frequencies. The cosine interpolation has a significant lobe of energy after the first zero band; that may make it less desirable than the four-point method. The linear interpolation decays more slowly than the cosine product and finally the power spectrum with no interpolation decays very slowly. It would therefore appear that the four-point method is the best method, of those discussed, at removing the high-frequency energy put in by the interpolation method.
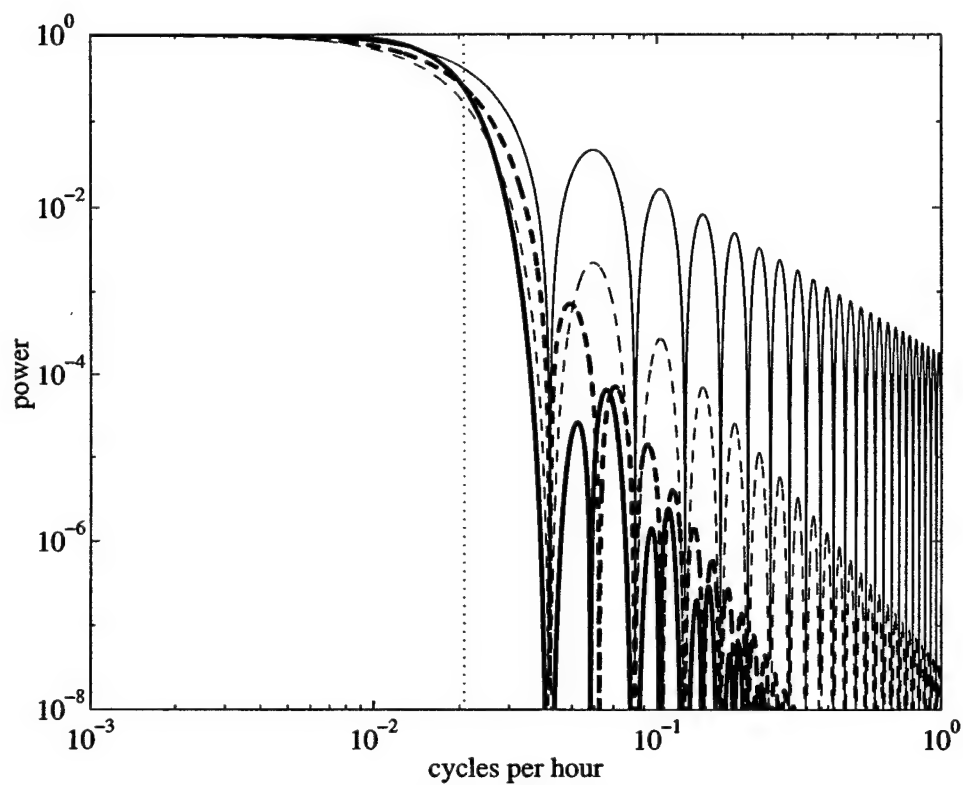
Figure 2.11: Power spectra from theoretical arguments. The thin solid line is the no interpolation case, the thin dashed line is for linear interpolation, the heavy dashed line is for cosine interpolation, and the heavy solid line is for Hermite interpolation.

Chapter 3

The Dynamics of Wind-Induced Heat Transport Variability

3.1 Introduction

A complete theory for the role of variable wind stress in forcing fluctuating ocean heat transport has been lacking. While some of the underlying dynamics have been discussed in previous studies, they have never been put together in a cohesive argument. The first studies to examine the issue were those of Bryan and Lewis (1979) and Bryan (1982) in a series of numerical modeling experiments. They were attempting to reproduce the observations of Oort and Vonder Haar (1976) who had found a large seasonal cycle in the ocean heat transport implied from satellite measurements. As the amplitude of the annual cycle of heat transport was found to be at least the same order of magnitude as the time-mean, it was desirable to identify the physical mechanism responsible for the ocean heat transport cycle. Bryan (1982) discussed and expanded upon the results from the first study of the ocean's heat transport using a global ocean general circulation model forced with observed wind fields (Bryan and Lewis 1979) and provided some dynamical arguments that were largely lacking in the earlier work. In his seminal discussion, Bryan (1982) argued that changes in the zonally integrated wind stress leads directly to changes in the Ekman mass transport, and associated with the variable Ekman flow is a compensating deep flow. The resulting meridional overturning circulation lead to a time-dependent heat transport as the Ekman layer transports water warmer than that of the compensating deep flow.

However, there was only weak theoretical underpinning for his arguments. Furthermore, he combined the time-mean response together with the time-varying response in his analysis, making interpretation difficult and obscuring the fact that the dominant physics which determines the mean flow is different from that which determines the time-varying flow.

Some aspects of the ocean response to variable forcing were explained by Willebrand et al. (1980). They provided a theoretical basis for the response of the ocean to forcing on large spatial scales at time scales longer than a day. However, their work did not directly address ocean heat transport. They used a one-layer shallow water model and arguments based on quasi-geostrophy which explicitly exclude the dynamics that will be shown to be responsible for the seasonally varying ocean heat transport. The wind stress applied to the ocean by the atmosphere can be broken into two components: the time-mean part and the fluctuating part. The time-mean wind stress drives an ocean circulation with western boundary currents whose dynamics are strongly controlled by stratification and nonlinear/advective effects. Willebrand et al. (1980) showed that the fluctuating part of the wind stress drives ocean variability that is governed by simpler physics: namely the linear, barotropic response should dominate in latitudes away from the equator [see also Gill and Niiler (1973) and Philander (1978)]. Furthermore, despite claims to the contrary (Bryden et al. 1991), there is observational evidence of deep ocean currents forced directly by time-varying wind stress fields (Koblinsky and Niiler 1982; Niiler and Koblinsky 1985; Brink 1989; Koblinsky et al. 1989; Luther et al. 1990; Samelson 1990; Chave et al. 1992; Niiler et al. 1993). There is also observational evidence of large-scale wind forcing of sea-surface height fluctuations (Fu and Davidson 1995; Chao and Fu 1995; Fu and Smith 1996; Fukumori et al. 1998).

The work of Willebrand et al. (1980) is only applicable to the middle- and high-latitude oceans. A connection to the low latitudes and in particular the equator will need to be made. Some work on this problem was done by Schopf (1980), who used an idealized model of the ocean to discuss the role of variable wind forcing in the tropical ocean heat transport. He isolated the heat transport mechanism and found that it could be described by a simple linear model in which the Ekman transport was the

44

mechanism by which heat was transported across the equator. Directly on the equator where the Ekman transport becomes meaningless since the Coriolis parameter is zero there, he argued that by continuity, the pressure force directly drives the seasonally-varying flow across the equator. The addition of gravity and planetary waves to the model did not significantly change the dynamics. However, Schopf's (1980) work was done on a one-hemisphere model, and his boundary conditions required that the flow be symmetric about the equator. Therefore, it is worthwhile to examine whether his findings apply to a global model.

Finally, the relationship of the "Ekman heat transport" to the total ocean heat transport and a discussion of the physics underlying it is needed. Introduced by Bryan (1962) in his analysis of early modeling work, it was adapted for use with observational data by Kraus and Levitus (1986) and then later by Levitus (1987), Adamec et al. (1993) and Ghirardelli et al. (1995). The original Kraus and Levitus paper gives a definition of the Ekman heat transport as the following integral across coast-to-coast zonal section:

$$ H(t) = \int \rho_0 \, c_p \, \frac{\tau_\lambda}{f \, \rho_0} [T_{Ekman} - \frac{1}{H} \int_{-H}^{0} \theta(z) \, dz] \, a \cos \phi \, d\lambda \tag{3.1} $$

where c_p is the specific heat of seawater, f is the Coriolis parameter, $T(x)$ is the temperature of the surface Ekman layer, $\theta(z)$ is the potential temperature, $\tau_\lambda(x)$ is the zonal wind stress, and a is the radius of the earth. Simply put, this equation expresses the heat transport as the integral of the Ekman mass flux times the difference between the Ekman layer temperature and the section averaged potential temperature. It implies that for any given section the mass transport in the Ekman layer is compensated by a return flow distributed uniformly across the depth and zonal extent of the section. It further suggests that the fluctuating wind stress elicits the same response as the time-mean wind stress. But they only provided a passing reference to observational evidence and no theoretical support to show that the above equation should hold. None of the subsequent authors have expanded on the theoretical basis for using this equation. Therefore, (3.1) could simply be regarded as a definition,

with no relation to any real phenomenon necessarily implied, but that would render it of questionable utility for saying anything about the ocean. On the other hand, it could be that (3.1) is appropriate under some circumstances and needs to be placed in a proper theoretical framework.

This chapter evaluates the theoretical arguments for using an equation of form (3.1) and determines when, where and how it is appropriate to use it to describe the ocean. In many respects the trio of studies by Willebrand et al. (1980), Schopf (1980), and Bryan (1982) provides the pieces for a dynamical picture of the driving of the seasonal ocean heat transport by the seasonally varying wind. However, these arguments have never been gathered together in a cohesive theory and one need only look at the confusion that still exists in the current literature to see that the ocean's response to the seasonal wind field is still not well understood. For example, Garternicht and Schott (1997) were able to correlate the heat transport fluctuations to the wind stress variations, but they did not provide a detailed dynamical explanation of the mechanism by which the changes in the wind stress lead to variability in the ocean's heat transport. Most recently, Kobayashi and Imasato (1998) diagnosed the seasonal variability of the heat transport using the observed wind stress and hydrographic data. However, they provided no dynamical justification for their calculation. Also, while there have been studies of how the ocean responds to the time varying wind stress, they have been largely theoretical and have not dealt specifically with the ocean heat transport. One that does (Schopf 1980) uses an idealized basin and wind stress pattern and does not give a complete picture of the response. Finally, the global nature of the heat transport variability has not been visited since the work of Bryan (1982) as more recent investigations have explored individual basins: Böning and Herrmann (1994) and Yu and Malanotte-Rizzoli (1998) in the Atlantic Ocean, and Wacongne and Pacanowski (1996), Garternicht and Schott (1997) and Lee and Marotzke (1998) in the Indian Ocean. It is the intent of this chapter to connect the arguments about the seasonal cycle of heat transport to a more dynamical description based on angular momentum considerations and observations. A simple dynamical balance will be examined to determine whether it holds for realistic models, and its implications for the ocean heat transport will be discussed. From this, an extension

46

from seasonal cycles to higher frequencies will follow. Finally, the implications for the ocean's transport of heat will be discussed. Two numerical models will be used in the discussion; the Parallel Ocean Climate Model (POCM) from the Naval Postgraduate School (Semtner and Chervin 1992; Stammer et al. 1996; McClean et al. 1997) and a homogeneous shallow water model.

3.2 The model

The numerical simulation output from run 4_B of the Parallel Ocean Climate Model (POCM) from the Naval Postgraduate School (Semtner and Chervin 1988; Semtner and Chervin 1992; Stammer et al. 1996; McClean et al. 1997) is used to calculate ocean heat transport at three day intervals. The POCM is a primitive-equation, level model with the traditional Boussinesq and hydrostatic approximations and uses the free surface formulation of Killworth et al. (1991). The configuration is for the global ocean between 75°S and 65°N, with realistic topography. The Mediterranean and other marginal seas are not included. Restoring sponge layers at the mouth of the Strait of Gibraltar, north of 58°N and south of 68°S are used to simulate water mass formation outside the model domain. Its average grid spacing of 1/4° permits the nominal resolution of the ocean's mesoscale eddy field. The model was forced with 3-day averages of the 10-meter wind stress fields from the European Centre for Medium-Range Weather Forecasting (ECMWF) for the period between 1987–1996. The previous run of the model (POCM 4_A) was forced with 3-day averages of the wind stress computed from the ECMWF 1000-mbar winds. It was found that deriving the wind stress from the 1000-mbar winds instead of the 10-meter winds overestimated the magnitude of the sea-surface wind stress by about 50% (Mestas-Nuñez et al. 1994) and resulted in a simulated circulation that was too vigorous (Stammer et al. 1996). The monthly surface heat fluxes were derived from ECMWF analyses by Barnier et al. (1995). The surface layer temperatures and salinities were also restored to the Levitus et al. (1994) climatology on a monthly timescale using the Haney (1971) scheme. The 4_B model run was initialized from the previous 1/4° 4_A run which had been integrated for 4 years. It in turn had been interpolated and equilibrated

47

from a previous 1/2° resolution run of 33 years duration which was started from an initial temperature and salinity distribution given by Levitus (1982).

This particular model simulation was chosen because of its relative ease of accessibility and because several studies have discussed its realism at simulating the observed ocean (Stammer et al. 1996, McClean et al. 1997). These studies consistently found that the model underestimates the observed ocean variability. Stammer et al. (1996) compared the numerical model to sea-surface-height observations from the TOPEX/POSEIDON satellite altimeter as well as to hydrographic data obtained during the WOCE program. They found that model simulation's variability was too weak compared to the observations by a factor of 2–4 over a large spectral range of periods and wavelengths. McClean et al. (1997) compared the 1/4° resolution simulation to TOPEX/POSEIDON altimetry as well as to the 1/6° resolution run of a similar model (the Parallel Ocean Program from Los Alamos National Laboratory). They looked specifically at the mesoscale variability simulated by the models and measured by the altimeter and found that globally the 1/4° model had about 50% of the variability measured by the altimeter and the higher resolution model had about 60% of the variability. They discussed reasons for the under-estimation of the variability and suggested that higher resolution calculations and improved forcing fields would result in more realistic simulations of the ocean. Fu and Smith (1996) also assessed the realism of the 1/6° resolution model and found that while its variability was deficient on the mesoscale, it was more realistic on the largest spatial scales and at the seasonal cycle. While this means that any conclusions drawn from the model have to be considered to be biased estimates of the true ocean variability, it is still feasible to use the model to identify physical mechanisms that drive variability and examine the nature of the variability.

3.3   The seasonal cycle in meridional overturning

The motivation for this discussion comes from examining the volume transports across oceanic sections. In particular, in the POCM as in most other models, there is a near perfect compensation between the deviations from the time-mean Ekman transport

across a section and the deviations from the time-mean barotropic transport. Figure 3.1 shows the balance between the two at 30°N in the Pacific Ocean. The correlation coefficient between the time-varying Ekman transport and the time-varying barotropic transport is -0.9873 ± 0.0011 (the estimated error was found using the bootstrap technique). The Ekman transport here is calculated as the sum of the shear velocities in the the upper 100 m of the model (top four model layers) relative the velocity at 117.5 m (the fifth model layer) below which the wind stress shear did not appear to penetrate. The barotropic transport is then taken as the vertical integral of the velocity over the full ocean depth after the Ekman velocity has been removed.

What dynamics create this compensation? In a model that has the rigid-lid approximation imposed, this compensation must be perfect. That is, there can be no net transport across a closed oceanic section, and therefore the barotropic transport must equal the Ekman transport. In a numerical model with a free surface, as in the true ocean, it is less clear that the Ekman transport must equal the barotropic transport as accumulations of mass through closed oceanic sections can lead to free surface displacements. Why the compensation persists is a key question in explaining the role of the time-varying wind forcing the heat transport fluctuations and will be addressed here.

The meridional overturning streamfunctions are another way to examine the structure of the flow. The meridional transport streamfunction from the POCM for the time-mean circulation is shown in Fig. 3.2. For the individual basins, the streamfunction is not drawn south of 37° S (the Cape of Good Hope on Africa), since it is not defined there. The POCM represents the gross features of the circulation seen in previous numerical modeling studies and from observations from hydrography; however significant quantitative differences do exist. In particular, there is strong upwelling along the equator in the Pacific and Atlantic Oceans. The Indian Ocean has a weaker mean upwelling and it is displaced south of the equator. In the Pacific and Indian Oceans and the South Atlantic Ocean, the surface flows associated with the time-mean Ekman transport are returned at depths above 500 m, whereas in the North Atlantic Ocean the Ekman circulation connects to the thermohaline circulation cell and is subducted with it. There is northward flow of deep water from the Southern
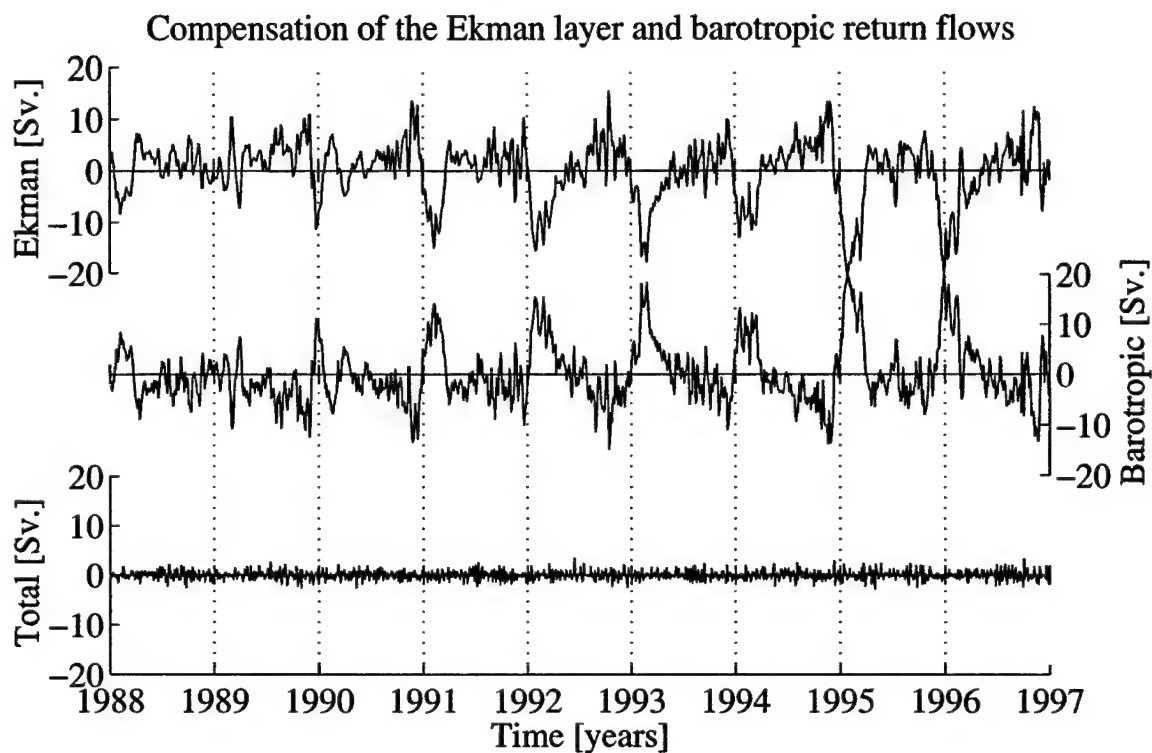
Figure 3.1: Deviations from the time-mean Ekman transport compared to deviations from the time-mean barotropic transport at 30° in the Pacific Ocean showing a high degree of compensation, the sum of the two is shown in the bottom panel.

Ocean into all the basins associated with the abyssal circulation of bottom water. In the Pacific Ocean 10 Sv (1 Sv = 1 Sverdrup = 10^6 m^3 s^{-1}) of deep water flow northward, in agreement with an estimate from Macdonald and Wunsch (1996) of 10 ± 6 Sv of deep water flowing north across 43°S. In the Indian Ocean, a much weaker northward deep water flow of 4.7 Sv is found, which is very much less than the estimates from hydrography of 27 Sv (Toole and Warren 1993), 16.5 ± 5 Sv (Macdonald 1995) and 11.6 ± 2.6 Sv (Robbins and Toole 1997). The estimate is consistent with previous modeling studies (Semtner and Chervin 1992; Garternicht and Schott 1997; Lee and Marotzke 1998). On the other hand, the POCM has northward flow extending all the way to the bottom which is not the case for Lee and Marotzke (1998). The reasons for the weak deep inflow in the model's Indian Ocean are not clear, but may be related to the smoothness of the climatology used to initialize the model (Robbins and Toole 1997). Initial results from current meters deployed at 20°S in the Indian Ocean indicate the deep inflow is weaker than expected (Warren personal communication), leaving open to question the character of the deep Indian Ocean circulation. Near the surface there is a time-mean flow of about 8 Sv. from the Pacific Ocean into the Indian Ocean through the Indonesian Archipelago at 6°S, which is discussed in more detail later in this chapter. In the Atlantic Ocean, the deep water formed in the North Atlantic dominates the picture with a total overturning strength of 21.6 Sv of southward flow which is consistent with the Macdonald's estimate of 27 ± 7 Sv at 47°N.

The seasonal cycle of the overturning streamfunction can be represented by the mean conditions in January minus the mean conditions in July, averaged over the last 9 years of the model run (1988-1996). Figure 3.3 shows that the seasonal patterns differ radically from the time-mean overturning circulation. In the time-mean overturning circulations, the return flow to balance the surface Ekman transport is highly baroclinic with reversals of the flow at depth. The seasonal varying component on the other hand is largely depth independent, with the return flow for the surface currents showing no deep reversals. The Pacific Ocean displays the strongest difference, with the time-mean overturning being essentially anti-symmetric about the equator and the seasonally varying overturning being nearly symmetric about the equator. Though

51
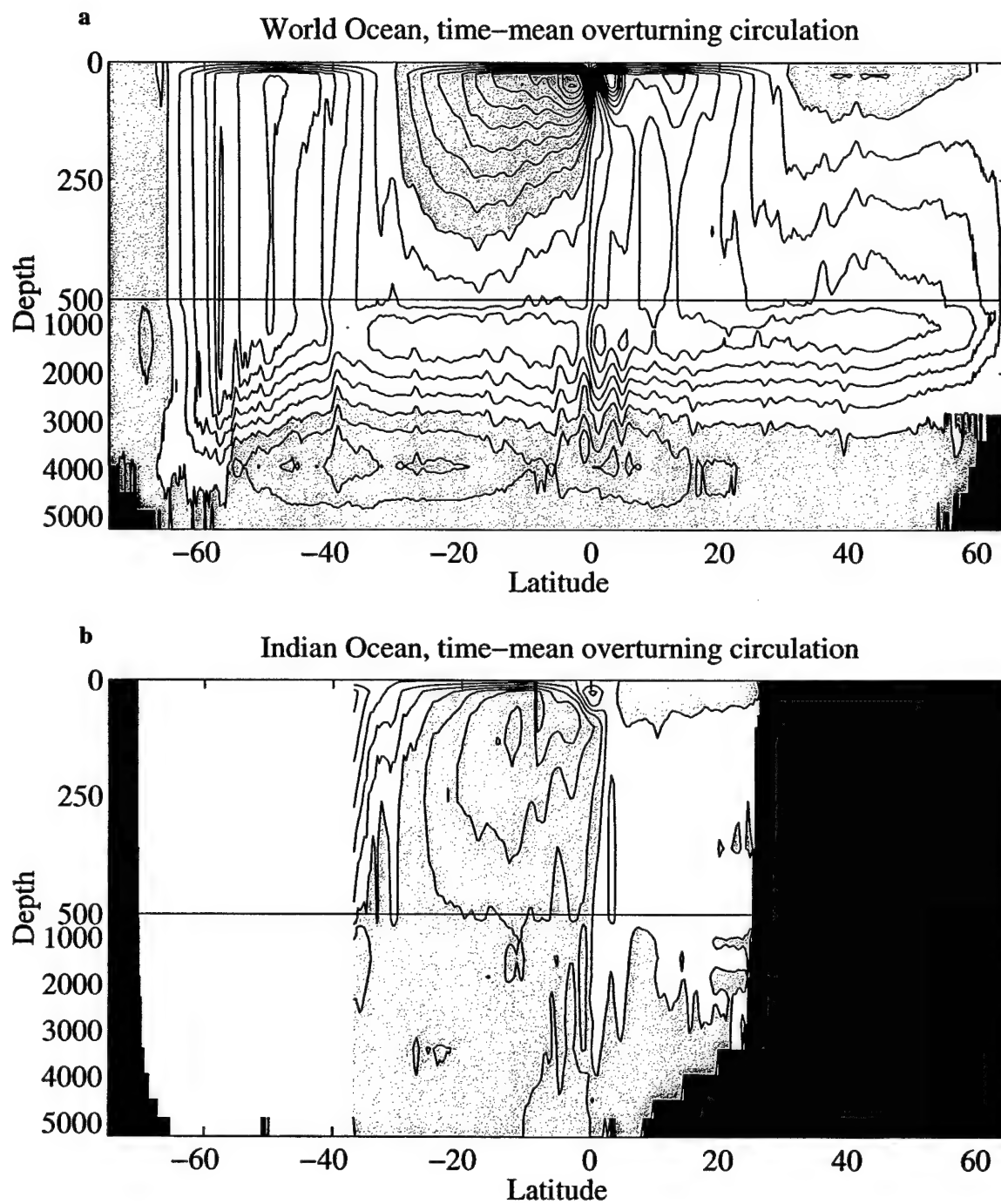
Figure 3.2: Time-mean overturning circulation for (a) the World Ocean and (b) the Indian Ocean. Contour interval for World Ocean in 5 Sv and contour interval for Indian Ocean is 2.5 Sv. Negative values of the streamfunction are shaded gray and indicate counterclockwise overturning.

c

Pacific Ocean, time–mean overturning circulation

d

Atlantic Ocean, time–mean overturning circulation
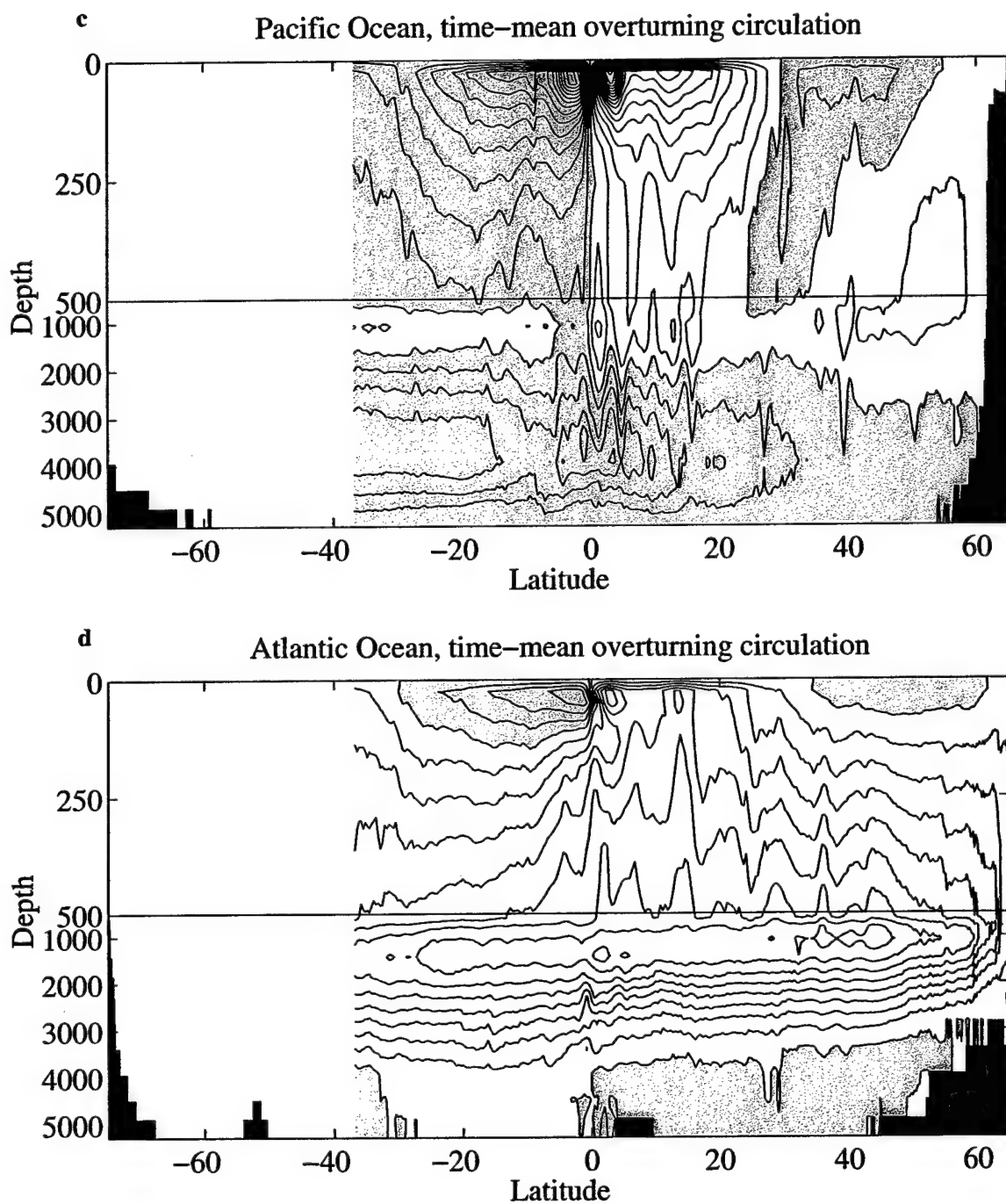
Figure 3.2: cont. Time-mean overturning circulation for (c) the Pacific Ocean and (d) the Atlantic Ocean. Contour interval for both is 2.5 Sv. Negative values of the streamfunction are shaded gray and indicate counterclockwise overturning.

Figure 3.3: Seasonal (January - July) overturning circulation for (a) the World Ocean and (b) the Indian Ocean. Contour interval for World Ocean in 5 Sv and contour interval for Indian Ocean is 2.5 Sv. Negative values of the streamfunction are shaded gray and indicate counterclockwise overturning in January.

c Pacific Ocean, seasonal overturning circulation

d Atlantic Ocean, seasonal overturning circulation

Figure 3.3: cont. Seasonal (January - July) overturning circulation for (c) the Pacific Ocean and (d) the Atlantic Ocean. Contour interval for both is 2.5 Sv. Negative values of the streamfunction are shaded gray and indicate counterclockwise overturning in January.

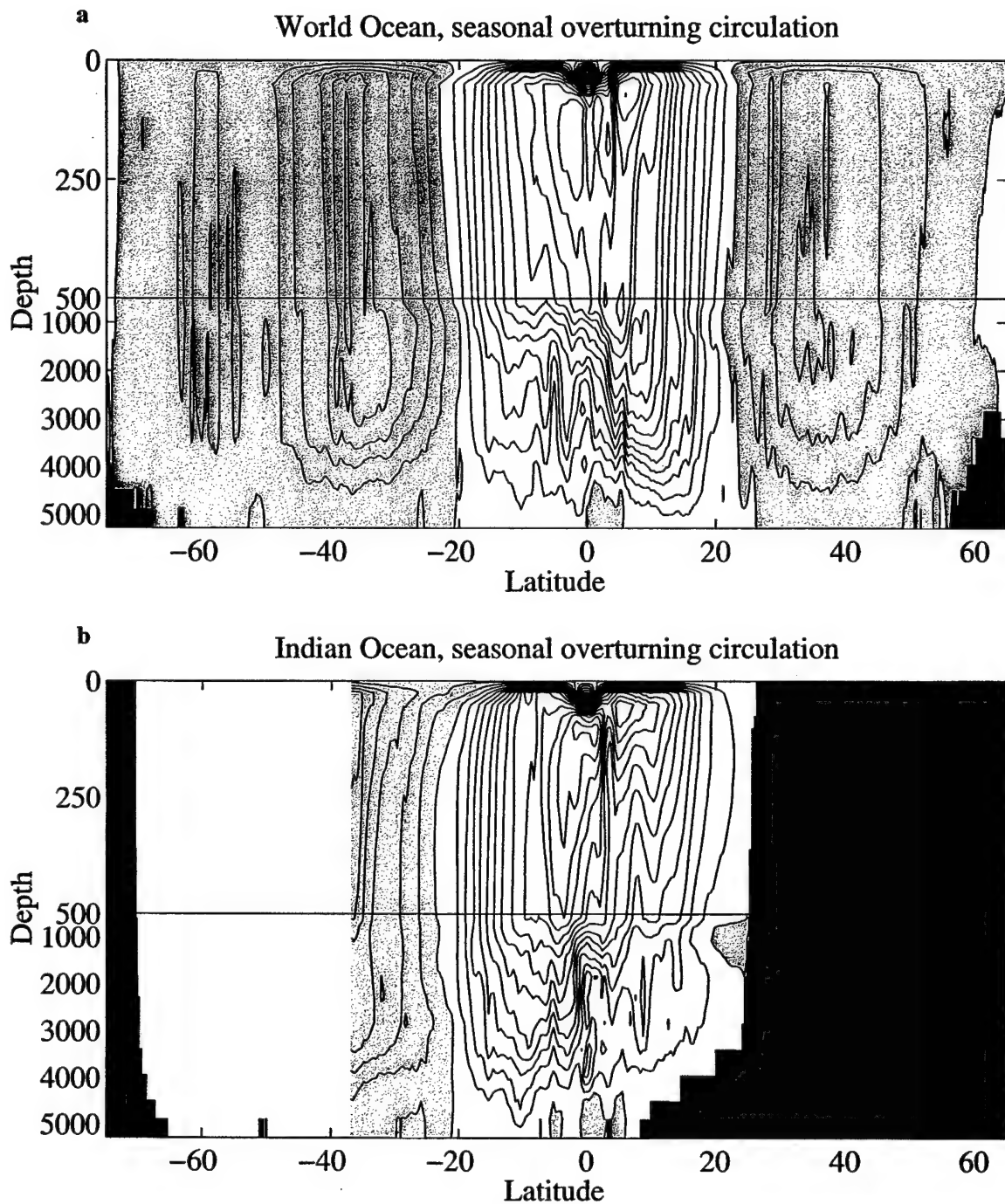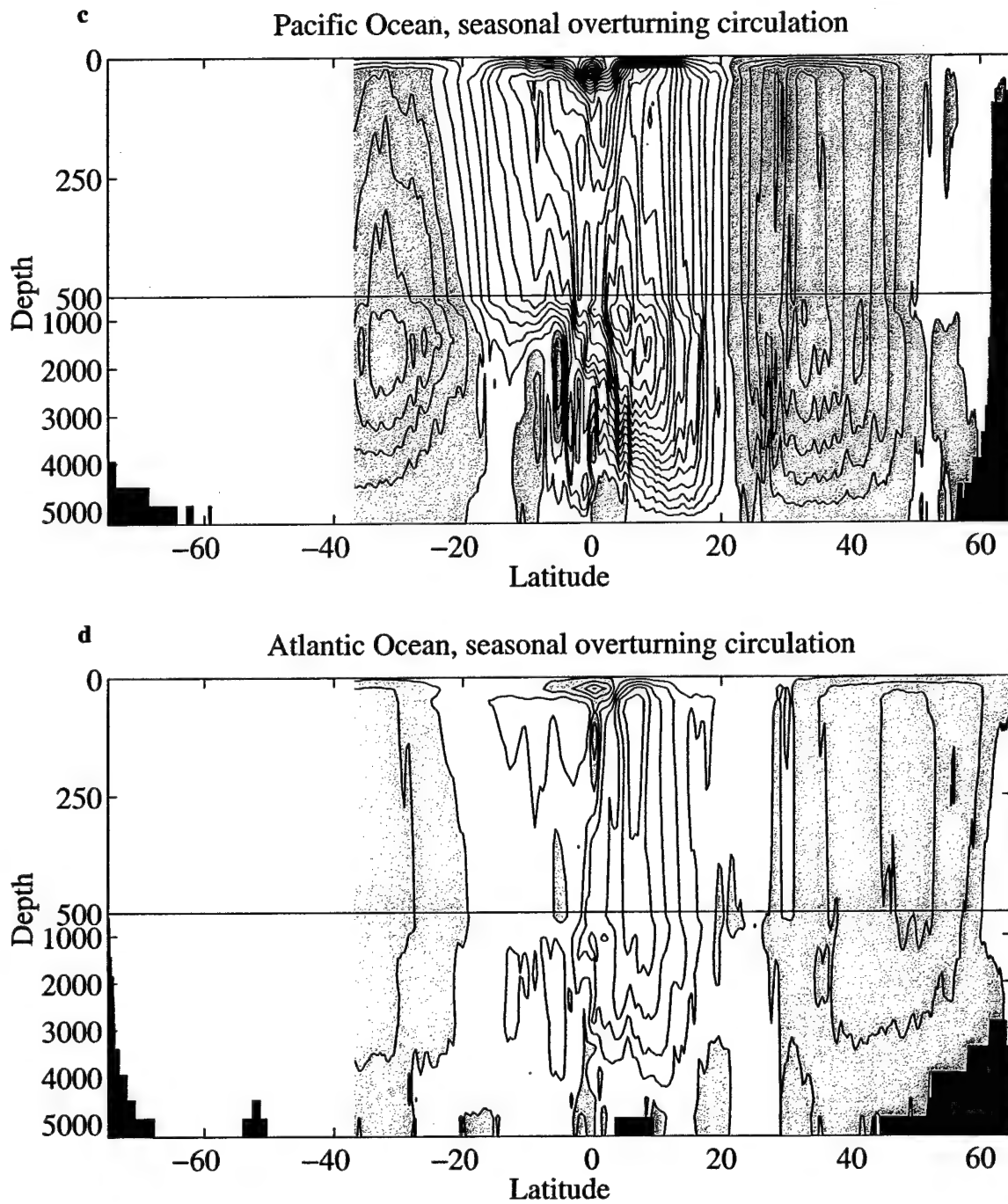55

structural differences between the time-mean and seasonal overturning circulations have been noted before, they have never been satisfactorily given a dynamical explanation and they are rarely presented separately; rather they are usually presented as January conditions and August conditions, which obfuscates the differences between the time-mean and time-varying components [*e.g.* Bryan 1982; Böning and Herrmann 1994; Wacongne and Pacanowski 1996; Garternicht and Schott 1997; though see Lee and Marotzke 1998 for an exception. The amplitude of the seasonal cycle of the overturning circulation in the equatorial region is about 50 Sv for the world total, which is comprised of 20 Sv in the Indian Ocean, 25 Sv in the Pacific Ocean and 5 Sv in the Atlantic Ocean. The actual velocities associated with these seasonal overturning circulations are quite small; the deep horizontal velocities are of order 10^{-3} m s^{-1}, and the vertical velocities are of order 10^{-6} m s^{-1} leading to seasonal displacements of 20 km in the horizontal and 20 m in depth. The Ekman layer horizontal velocities are obviously much larger, of order 0.1 m s^{-1}.

3.4 The seasonal wind field

Before the model simulations and dynamics are discussed further, the general nature of the time-varying wind should be examined. The seasonal wind stress field (annual cycle represented by January conditions minus July conditions averaged over the year 1988-1996) is summarized in Fig. 3.4. The characteristics of the variable wind stress field have been discussed before (Hellerman 1967; Vinnichenko 1970; Willebrand 1978; Hellerman and Rosenstein 1983). The zonal integral of the seasonally varying zonal wind stress (January – July) is shown in Fig. 3.5. Perhaps the most surprising feature of the variable wind field is that the integral of the zonal wind stress component is anti-symmetric across the equator, which was noted by Schopf (1980). However, this particular aspect of the seasonal wind cycle and its implications for the Ekman transport across the equator do not appear to have been addressed much in the literature, either atmospheric or oceanographic. Hence, even though the Coriolis parameter goes to zero on the equator, the seasonal variation in the Ekman transport is well behaved. Since the Coriolis parameter and the seasonally-varying part of the

56

wind stress are anti-symmetric about the equator, the Ekman transport, which is given by their ratio, will be symmetric across the equator. The seasonal cycle of the zonal wind goes to zero at $\pm 20°$ and is of opposite sign poleward of that. This leads to a reversal of the direction of the Ekman transport, and a convergence (divergence) there in the winter (summer) hemisphere. Comparing the ocean basins, the seasonal cycle of the zonal wind is weakest in the Atlantic, where it is noticeably weaker south of the equator compared to north of it. This accounts for the marked asymmetry of the meridional overturning circulation in the Atlantic seen in Fig. 3.3. In the Indian Ocean there is a particularly strong seasonal cycle in the meridional wind associated with the monsoonal system there.

Seasonal cycle of the wind stress (January – July)
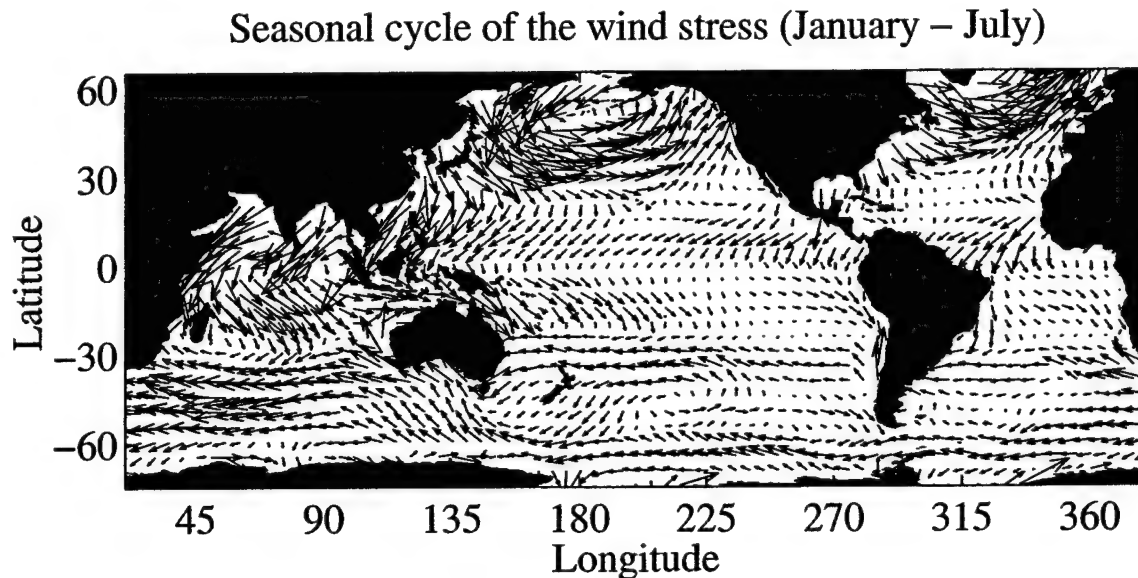
Figure 3.4: Annual cycle of the zonal integral of the zonal wind stress (January - July)

Since there is a paucity of literature addressing the seasonal cycle of the zonal wind in the tropics, a further discussion is warranted. The tropical atmospheric circulation on the largest spatial scales is dominated by the Hadley cell. The dynamics of this circulation have been addressed beginning with Halley (1686) and Hadley (1735). In more recent times Gill (1980) proposed a relatively simple model for the atmospheric circulation to illustrate how the tropical atmosphere responds to localized diabatic
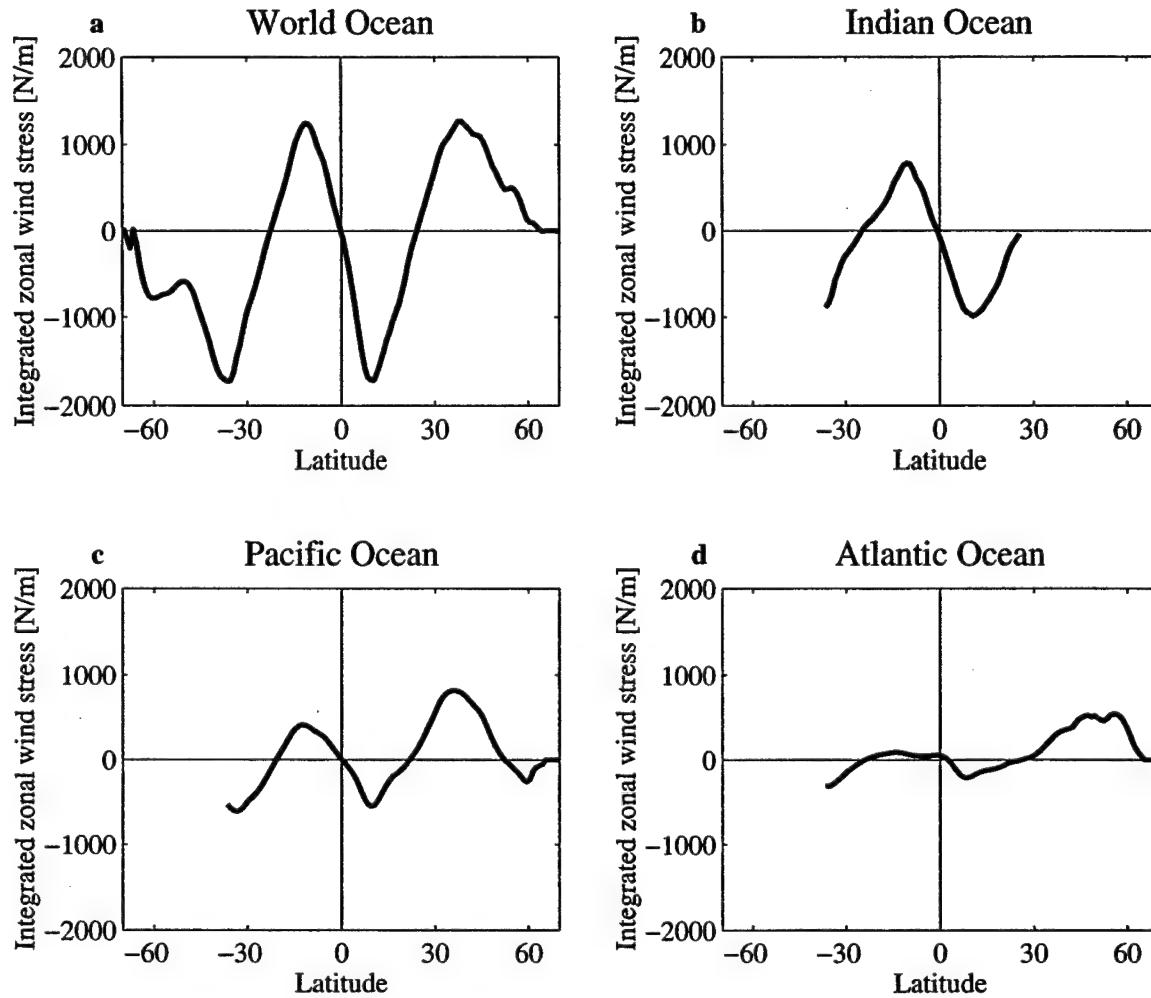
Figure 3.5: Annual cycle of the zonally integrated zonal wind stress (January - July) for (a) the World Ocean, (b) the Indian Ocean, (c) the Pacific Ocean and (d) the Atlantic Ocean.

heating. The circulation that results from the seasonal cycle of heating produces a seasonally-varying zonal wind which is anti-symmetric across the equator, while the time-mean wind is symmetric across the equator. The reader is referred to Gill (1980) for details, but in summary, he found solutions to the shallow-water equations on an equatorial beta-plane with diabatic heating. The time-mean behavior is given by heating localized along the equator and an atmospheric circulation that is symmetric about it. The January and July conditions are represented by the time-mean solution together with an anti-symmetric component in which the maximum heating is in the summer hemisphere. These solutions are summarized in Fig. 3.6 showing the
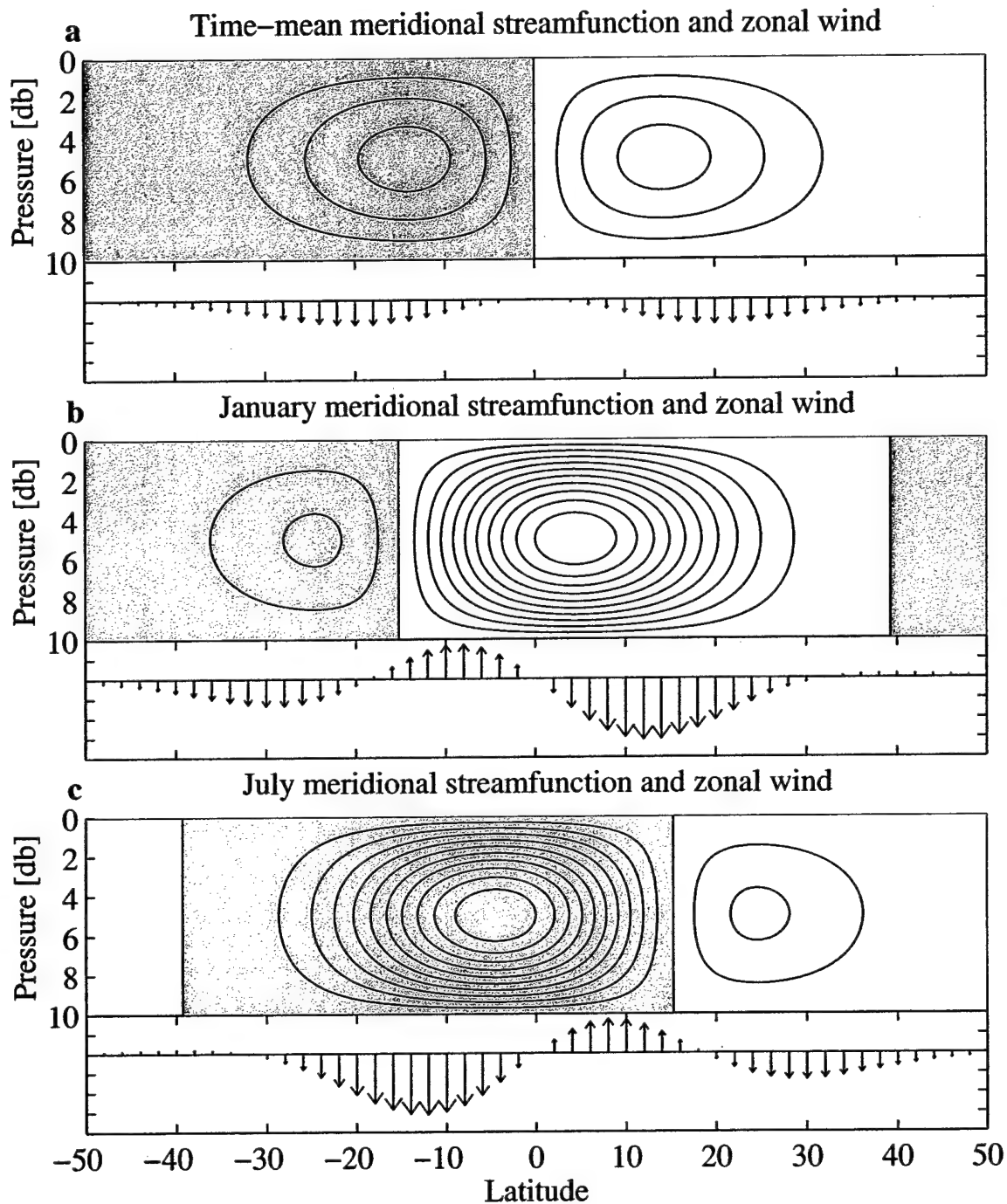
Figure 3.6: (a) The zonally-averaged meridional streamfunction (upper panel) and the zonally-averaged zonal wind (lower panel) for the time-mean tropical atmospheric circulation, (b) The same, but for January conditions, and (c) The same, but for July conditions. Negative values of the streamfunction are shaded gray and indicate counterclockwise overturning. Solutions from Gill (1980).

Predicted seasonal cycle of the zonal wind
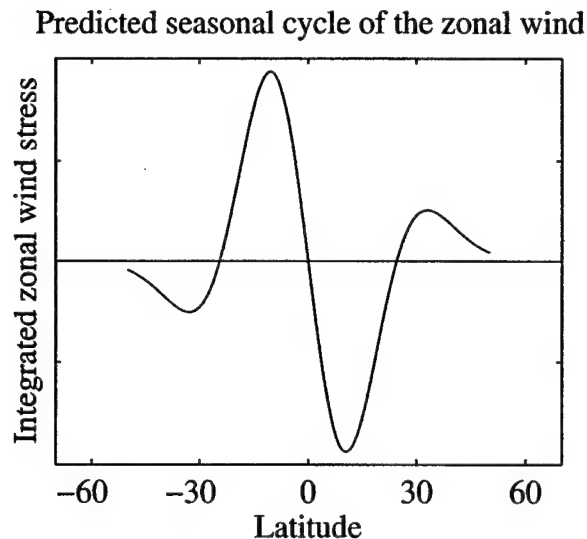
Figure 3.7: Annual cycle of the zonal integral of the zonal wind stress (January - July) predicted by Gill's (1980) model.

zonally-averaged meridional streamfunction together with the surface zonal wind for the time-mean conditions as well as the January and July conditions. Differencing the January and July conditions gives the zonal wind profile in Fig. 3.7, which is anti-symmetric across the equator and in remarkable agreement with Fig. 3.5. In the wind-stress climatology, the zero-crossing of the seasonal cycle occurs at about 23°S and 25°N; in Gill's (1980) model, it occurs at about 24° (both north and south), assuming a deformation radius of 10° at the equator. Therefore, Gill's (1980) model readily explains the observed characteristics of the seasonal wind field.

The evidence so far points to a seasonal overturning circulation driven by the wind stress creating an Ekman layer at the surface. But what of the return flow? In the papers by Kraus and Levitus (1986), Levitus (1987), Adamec et al. (1993) and Ghirardelli et al. (1995), in the Eulerian view, the return flow for the Ekman layer has been assumed to be depth independent. But is this correct and if so, what are the dynamical balances associated with it?

3.5   Linear homogeneous shallow water model

As a first step beyond simple Ekman dynamics, it is appropriate to work with a model with a more complete set of physics, but not so complicated as an ocean general circulation model (OGCM). It is also instructive to isolate the ocean response to the fluctuating wind from the eddies introduced by unstable boundary currents and baroclinic instability. Therefore, a model with intermediate complexity is introduced to complement the simple Ekman model and full OGCM. Willebrand et al. (1980) showed that the ocean's response, away from the equator, to large-scale atmospheric disturbances on timescales of a day to a year is largely linear and barotropic, and concluded that it was unnecessary to use a full OGCM to understand the response. The model developed here is barotropic, as was the one used by Willebrand et al. (1980), but the nonlinear terms are neglected since they were shown to be small by Willebrand et al. (1980) and Anderson and Corry (1985). The most important difference from Willebrand et al. (1980) is that the present model separates the Ekman layer dynamics from the barotropic mode. This is important, since combining both the wind stress forcing and the pressure forcing into a single one-layer momentum equation seriously distorts the vertical velocity profile for even the simplest wind forced barotropic response. The model is given by the following set of equations:

$$\frac{\partial U_E}{\partial t} - fV_E = \frac{\tau_\lambda}{\rho_0} - \frac{U_E}{r_E} \tag{3.2}$$

$$\frac{\partial V_E}{\partial t} + fU_E = \frac{\tau_\phi}{\rho_0} - \frac{V_E}{r_E} \tag{3.3}$$

$$W_E = -\frac{1}{a\cos\phi}\frac{\partial U_E}{\partial \lambda} - \frac{1}{a\cos\phi}\frac{\partial\left(\cos\phi V_E\right)}{\partial\phi} \tag{3.4}$$

$$\frac{\partial U_I}{\partial t} - fV_I = -\frac{gH}{a\cos\phi}\frac{\partial\eta}{\partial\lambda} - AH\nabla^4\left(\frac{U_I}{H}\right) \tag{3.5}$$

61

$$\frac{\partial V_I}{\partial t} + fU_I = -\frac{gH}{a}\frac{\partial \eta}{\partial \phi} - AH\nabla^4\left(\frac{V_I}{H}\right) \tag{3.6}$$

$$W_I = -\frac{1}{a\cos\phi}\frac{\partial U_I}{\partial \lambda} - \frac{1}{a\cos\phi}\frac{\partial\left(\cos\phi V_I\right)}{\partial \phi} \tag{3.7}$$

$$\frac{\partial \eta}{\partial t} = W_E + W_I \tag{3.8}$$

where (U_E, V_E) is the Ekman layer transport, (U_I, V_I) is the interior transport, λ, ϕ are the zonal and meridional directions, $(\tau_\lambda, \tau_\phi)$ is the fluctuating part of the wind stress, ρ_0 is the reference density taken to be 1025 kg m^{-3}, a is the radius of the Earth, $f = 2\Omega\sin(\phi)$ is the Coriolis parameter, g is gravity, $H = H(\lambda, \phi)$ is the ocean depth, η is the ocean's free surface height, r_E is the Ekman layer decay timescale, A is the coefficient of biharmonic friction for the interior and W_E, W_I are the vertical mass fluxes from the Ekman layer and interior respectively. The lateral boundary conditions are that $U = 0, V = 0$ and $\nabla^2 U = 0, \nabla^2 V = 0$. The shallow water model was configured to use the same topography grid as the POCM, as well as the same wind-stress fields. The model therefore has the same resolution of 1/4° as the POCM does. It was implemented using the free surface scheme (with the tidal option) of Killworth et al. (1991). It was forced with only the fluctuating component of the wind stress used in the POCM 4_B run, as defined as the deviations from the time-mean wind stress between 1988 and 1996. The Ekman layer frictional timescale was set to be $r_E = 30$ days, and the biharmonic friction on the barotropic velocities was set to be the same as the biharmonic friction used in the momentum equations of POCM, $A = 1.1 \times 10^{12}\cos^{2.25}(\phi)$ m^4 s^{-1}. The model results were found to be relatively insensitive to the friction used, indicating it does not play a significant role. The exception is at the equator where the Ekman layer decay timescale plays the most important role in determining the circulation there. Using only the variable part of the wind stress field also obviates the need for a spin-up, though for a homogeneous ocean the spin-up time is very fast, order 10 days (Anderson et al. 1979).

3.5.1 Free surface height deviations

As a first look at the model results, the homogeneous response of the sea surface due to time-dependent wind forcing can be examined and compared to observations of the sea surface height variability and other numerical model results. The satellite altimeter TOPEX/POSEIDON has the highest accuracy of any altimeter to date and for the first time permits an observational investigation of where the ocean does actually respond to the large-scale atmospheric forcing of the kind discussed by Willebrand et al. (1980). Fu and Davidson (1995) addressed this question by comparing the data from TOPEX/POSEIDON to a quasi-geostrophic, barotropic vorticity model forced with observed wind stress fields. They found that only in a few places in the global ocean, namely the northeastern Pacific and in the Antarctic Circumpolar Current, is there a significant barotropic sea level response to the time-dependent wind forcing. The results were later supported by Chao and Fu (1995), Fu and Smith (1996) and Fukumori et al. (1998), who all used more sophisticated primitive equation models. Does the linear homogeneous shallow water presented here provide consistent results?

The sea-surface heights measured by the satellite altimeter TOPEX/POSEIDON were gridded onto a 2° grid for cycles 11 − 156; these were then averaged over 10° boxes with a moving box-car filter. From these smoothed fields the variance for the 20 − 150 day periods was computed using Thompson's multitaper method (Thompson 1982; Park et al. 1987; Percival and Walden 1993; Lees and Park 1995). The sea-surface heights from the Parallel Ocean Climate Model (POCM) and the homogeneous shallow-water model were also averaged in time and space to 2° resolution and time periods corresponding to the TOPEX/POSEIDON repeat cycles. The sea-surface height variance was then computed using the same method as was used with the altimeter fields.

As can be seen in Fig. 3.8, the only areas in the shallow water model with significant sea-surface variability are in the northern Pacific and the Antarctic Circumpolar Current, in agreement with the results of Fu and Davidson (1995), Fu and Smith (1996), Chao and Fu (1995) and Fukumori et al. (1998). It supports the conclusion that in these particular areas, there is a significant sea-surface-height signature due

a TOPEX/POSEIDON: Large scale 20 − 150 day variability

b Parallel Ocean Climate Model

Standard deviation of sea surface height [cm]
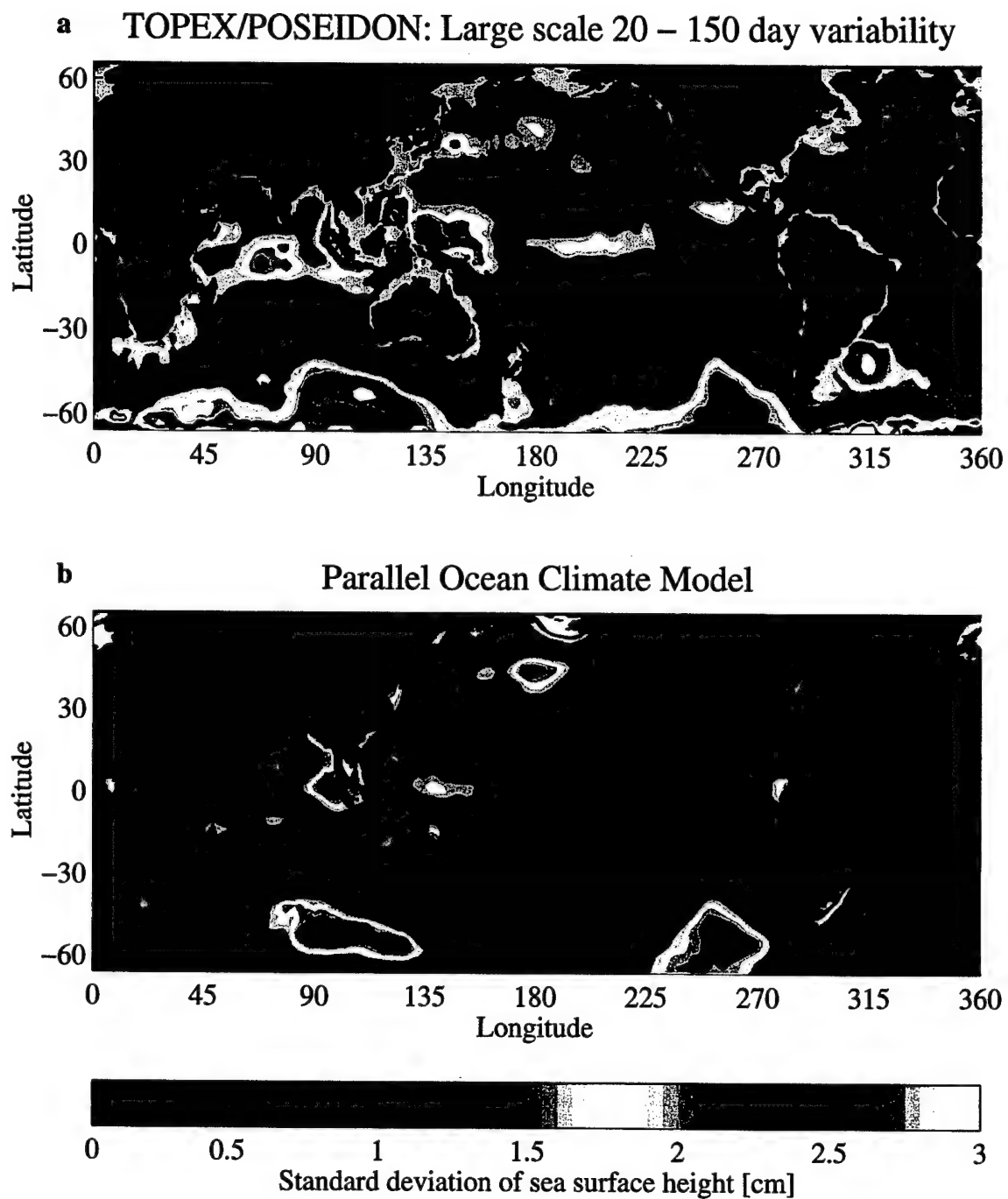
Figure 3.8: Standard deviation of sea surface height from (a) TOPEX/POSEIDON and (b) the POCM, for periods between 20 − 150 days, smoothed over 10° boxes.

c Linear homogeneous shallow water model

d Shallow water model, with a flat bottom

Standard deviation of sea surface height [cm]
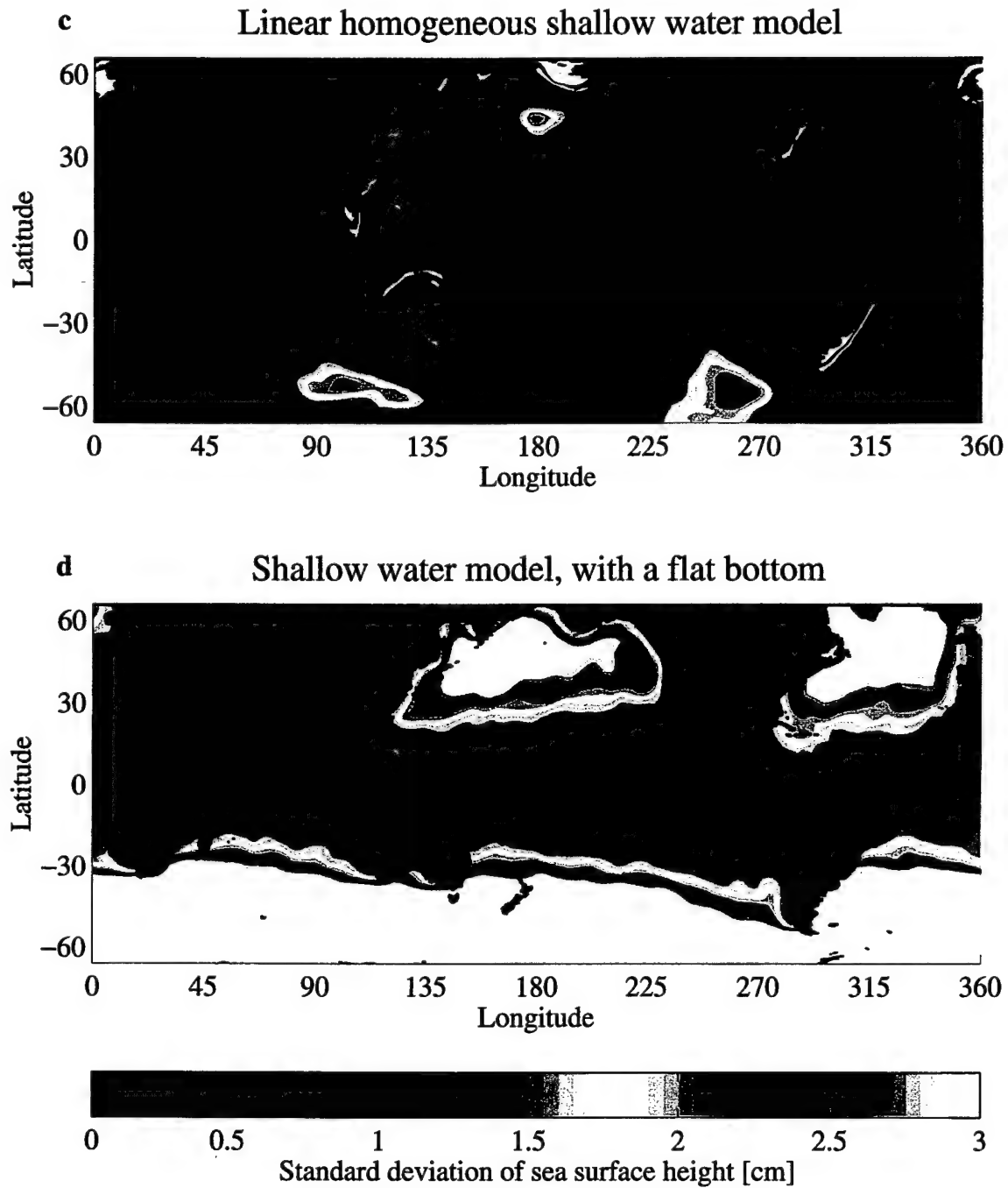
Figure 3.8: cont. Standard deviation of sea surface height from (c) the homogeneous shallow water model and (d) the homogeneous shallow water model, with a flat bottom of 4000 m, for periods between 20 – 150 days, smoothed over 10° boxes.

65
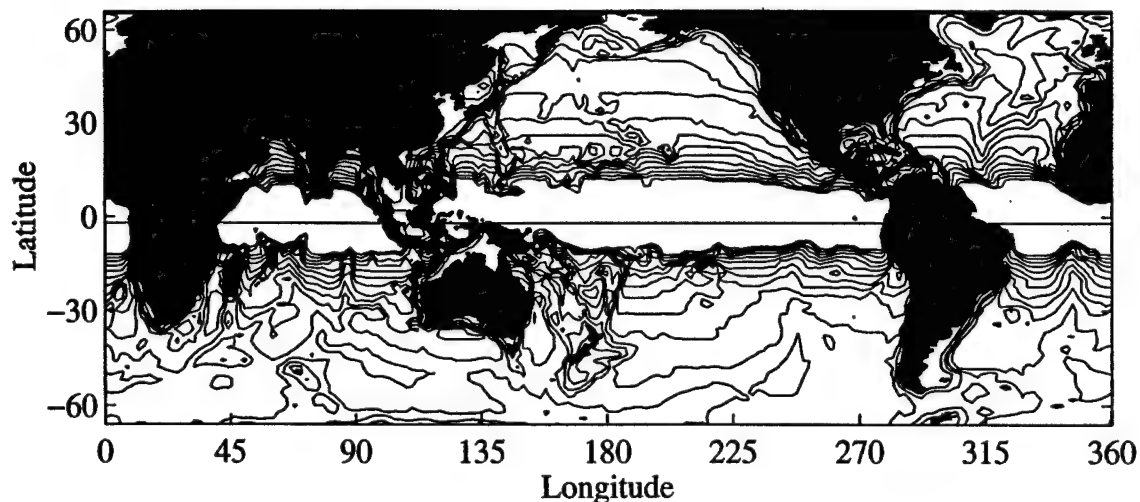
Figure 3.9: Contours of f/H, where the depth, H, has been smoothed over 10° boxes as was done for Fig. 3.8.

to the homogeneous ocean response to the fluctuating wind. However, it is not a priori clear what is controlling the distribution of the sea-surface height variation: the structure of the wind stress fields or the structure of the topography. To explore this problem more, the shallow water model was rerun with the same wind fields but with a flat-bottomed ocean of depth 4000 m, therefore removing the topography as a constraint. Shown in Fig. 3.8d, the sea-surface-height variability has a strongly different character. The Southern Ocean and subpolar North Pacific and North Atlantic are filled with strong sea level variability, indicating that in the absence of topography, the wind field alone does not determine the observed distribution of sea-surface-height variability in these places and that topography is the key constraint. The areas in the Southern Ocean are areas of closed f/H contours, confirming topographic control there. The area of high variability in all of the models' Northern Pacific Ocean does not correspond to closed f/H contours but instead to an area of significant variation in the wind-stress curl, is not as strong in the TOPEX/POSEIDON data. Overall, the wind-driven, sea-surface-height variability is controlled by the topography in the Southern Ocean and the wind stress in the North Pacific. Questions regarding this problem will likely receive more attention when data are obtained from the Gravity Recovery and Climate Experiment (GRACE) satellite to be launched in a few years.

3.6 Meridional overturning

To compare the behavior of the POCM to the homogeneous shallow water model, the velocity fields from their integrations were used to compute meridional overturning streamfunctions. Following Lee and Marotzke (1998), the meridional velocity fields from the POCM were broken into three separate dynamical contributions according to:

$$
\begin{aligned}
v(x,y,z) \;=\; & \frac{1}{H} \int_{-H}^{0} v(x,y,z)\,\mathrm{d}z \\
+ \; & \left[v_e(x,y,z) - \frac{1}{H} \int_{-H}^{0} v_e(x,y,z)\,\mathrm{d}z \right] \\
+ \; & v_{sh}(x,y,z)
\end{aligned}
\tag{3.9}
$$

where $H = H(x,y)$ is the ocean depth. The three components are in the order they appear in (3.9): 1) The contribution to the meridional velocity due to the external mode (or barotropic gyre circulation) flowing over varying topography. Essentially it is the flow that is governed by Sverdrup relation taking into account time dependence, bottom topography and frictional effects. 2) The surface Ekman flow (v_e) minus its vertical average to represent its barotropic compensation. The Ekman component of velocity, v_e is taken here to be the shear velocity in the four surface layers referenced to velocity at the fifth model layer (117.5 m). Note that the vertical integral of this term is zero and hence the barotropic velocities associated with it are not part of the first term. 3) The vertical shear flow (v_{sh}) which is generally associated with thermal wind shear balanced by zonal density gradients, as well as smaller contributions from the ageostrophic shear from frictional and nonlinear effects. The velocities from the shallow water model were used to compute a meridional overturning streamfunction as well. Finally, the meridional velocity arising from the Ekman layer driven by the zonal wind with an associated depth-averaged compensating flow was estimated from:

$$
v_e(x,y,z) = \frac{\delta_{1,k}}{h} \frac{\tau_\lambda(x,y)}{f\rho_0} - \frac{1}{H} \frac{\tau_\lambda(x,y)}{f\rho_0}
\tag{3.10}
$$

where h is the thickness of the POCM surface model layer (25 m) and $\delta_{i,j}$ is the Kronecker delta function.
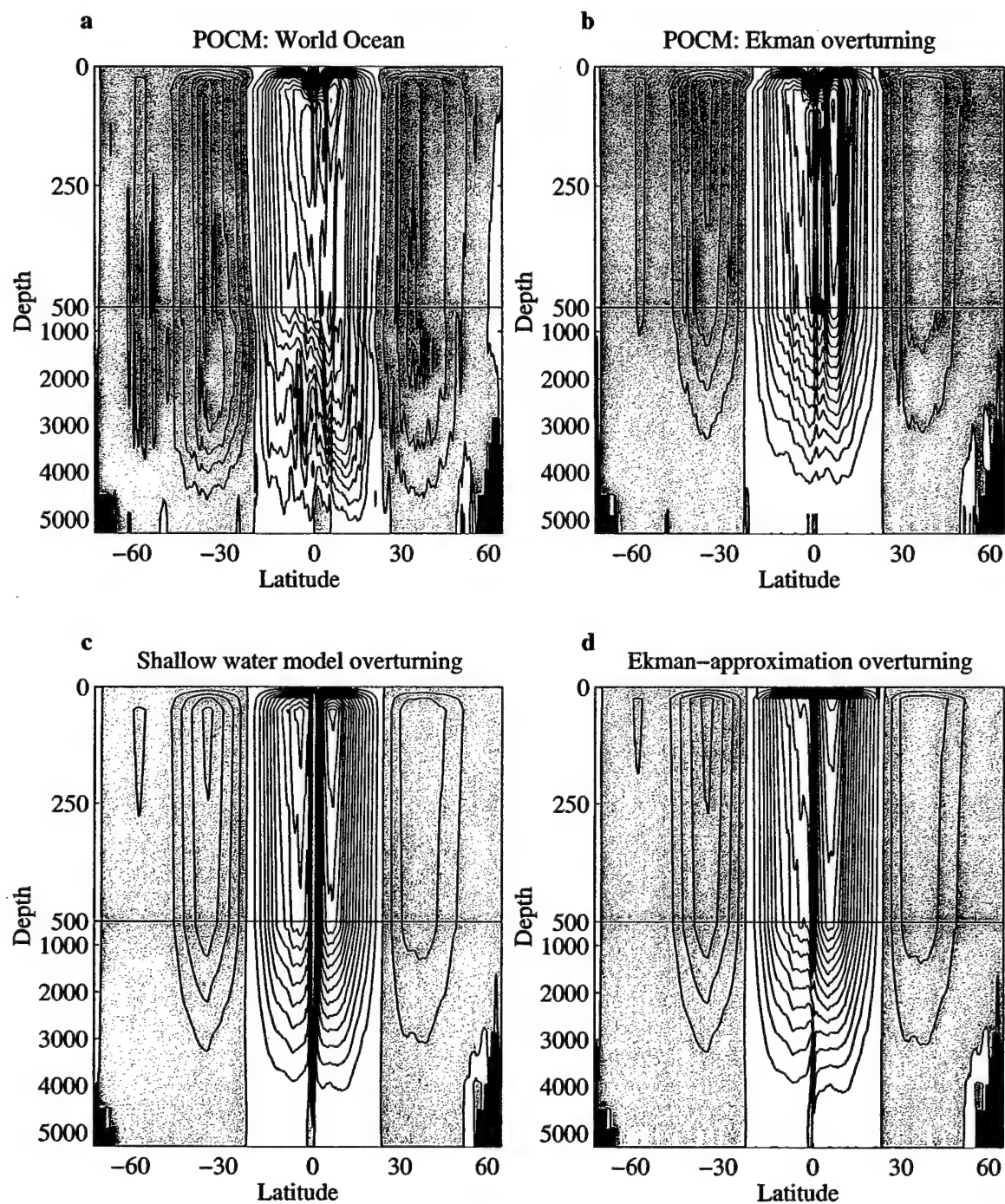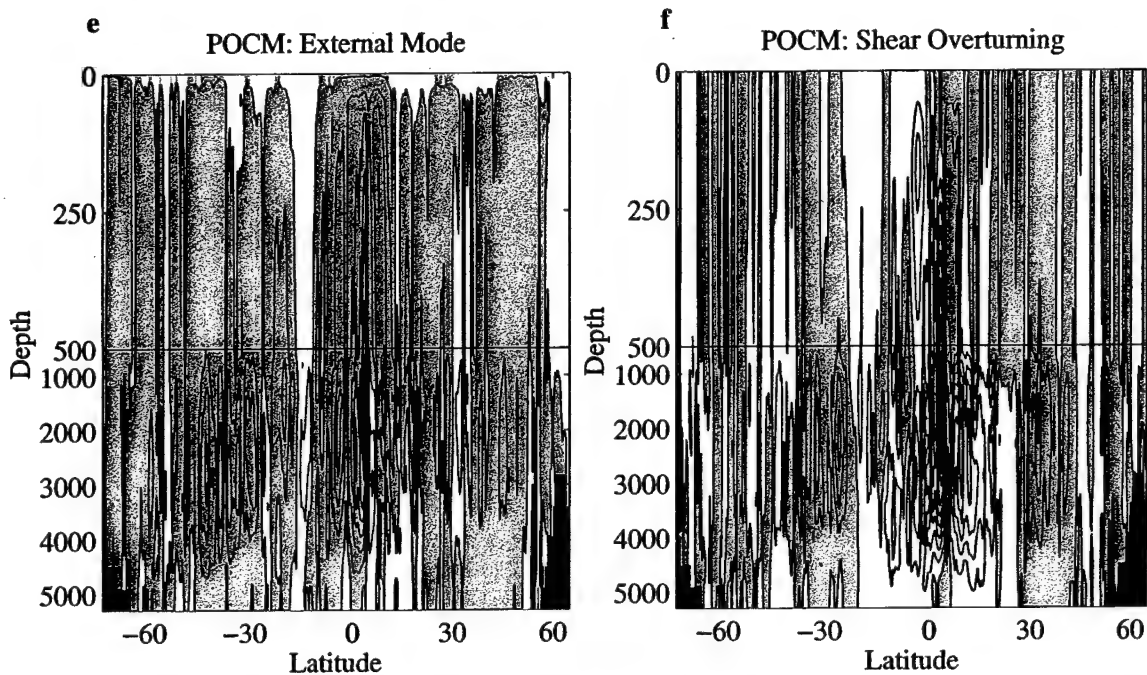
Figure 3.10: Seasonal (January - July) overturning circulation for the World Ocean from (a) POCM, (b) the "Ekman only" part of the POCM circulation from (3.9), (c) the homogeneous shallow water model and (d) the Ekman contribution alone from (3.10), (e) the external mode contribution to the overturning and (f) the shear overturning. Contour interval is 5 Sv. Negative values of the streamfunction are shaded gray and indicate counter-clockwise overturning.

The seasonal overturning circulations are shown in Fig. 3.10. The results from the intermediate model and Ekman approximation correspond well both in magnitude and spatial structure to those from the full numerical model (POCM). The exception is at the equator, where the shallow water model does not have the vertical resolution necessary to represent the shear between the surface layers permitted by the vanishing Coriolis parameter. On the equator, in the simplified model, there appears a narrow counter-rotating cell over the full ocean depth instead of being confined to the upper 25 m as in the full POCM. Overall, the similarity between the two model results suggests that the simplified model contains the dominant physical processes. The overturning owing to the external mode and shear velocities (Figs. 3.10e and 3.10f) have smaller amplitudes and are much noiser, suggesting their contributions to the seasonal cycle of heat transport are small and that this decomposition is probably

69
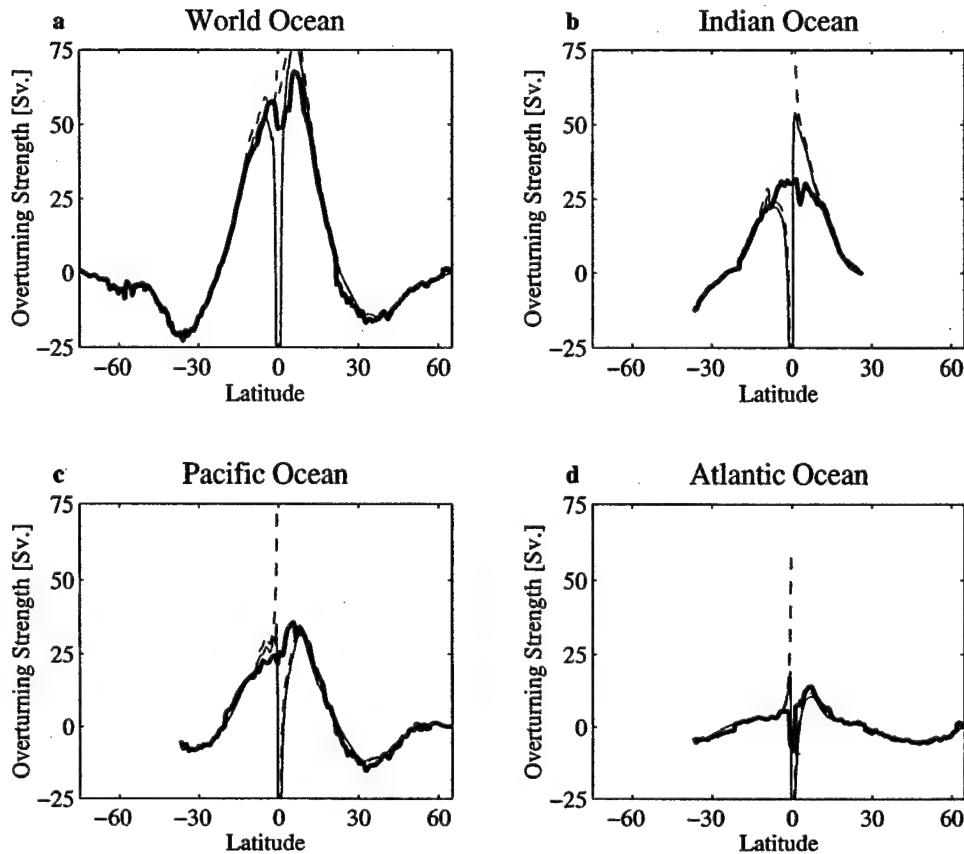
Figure 3.11: The maximum overturning amplitude for each basin as a function of latitude for (a) the World Ocean, (b) the Indian Ocean, (c) the Pacific Ocean and (d) the Atlantic Ocean. The POCM value is given by the heavy solid line, the thin solid line is for the homogeneous linear shallow water model and the dashed line is for the estimate derived solely from the wind stress.

not a useful way to probe their dynamics.

The equatorial surface circulation is apparently directly driven by the seasonal cycle of the meridional wind, since the meridional wind stress can directly drive a meridional circulation on the equator. Therefore, the counter flow also does not appear in the circulation derived from the Ekman-approximation using only the zonal wind stress and (3.10). The magnitude of the seasonal meridional overturning circulation was also computed for the separate ocean basins and is shown in Fig. 3.11. The agreement is good between the estimates in all of the basins, the exception again being the equatorial region, particularly in the Indian Ocean, where the meridional wind cycle is very strong.

3.7 Adjustment to variable wind stress

While some of the investigations of the ocean's seasonal cycle have mentioned a theoretical basis for their work, none have proffered an actual mechanism for the seasonal cycle in the overturning. In particular, the often cited work of Willebrand et al. (1980) argues that the ocean response to basin-scale forcing on the timescale of a year should be largely barotropic. However, the connection to the seasonal overturning circulation is not obvious, and moreover the models used by Willebrand et al. (1980) explicitly excluded the physics that drives the ocean heat transport.

Expanding the work of Philander (1978) on the structure of forced oceanic waves, Willebrand et al. (1980) discussed the ocean response to forcing at large spatial scales, not only by atmospheric wind stress disturbances, but also by surface pressure forcing and a surface mass flux, over timescales from the inertial period to a year. They based their conclusions on the theoretical vertical trapping scale, z_e, of the ocean's forced wave response which satisfies (their equation (2)):

$$\int_{-z_e}^{0} \left[\left(\|\vec{k}\|^2 + \frac{\beta k_1}{\omega} \right) \frac{N^2(z)}{f^2 - \omega^2} \right]^{1/2} \mathrm{d}z = 1. \tag{3.11}$$

where β is the meridional derivative of the Coriolis parameter, f is the Coriolis parameter, and N is the Brunt-Väisälä frequency, ω is the forcing frequency and $\vec{k} = (k_1, k_2)$ is the wavenumber of the forcing. In the limits of $\omega \to f$ and $\omega \to 0$, the ocean response becomes strongly surface trapped, that is, z_e is much less than the ocean depth. This is also the case for small-wavelength forcing, $k \ll 2\pi/100$ km. However, the trapping depth increases with increasing horizontal spatial scale and for periods between the time-mean and inertial. Away from the equator, for spatial scales larger than 100 km and between periods of 1 day and 300 days, the trapping depth is larger than 5000 m. For the largest spatial scales (the ocean basin scale), the frequency of the forcing can be as low as a year and the trapping depth would still be larger than 5000 m. The trapping depth increases with latitude away from the equator and increases for larger basin widths, but it is only a weak function of these two parameters. The theory says that some aspect of the ocean response should be barotropic, but what

then is the mechanism by which this happens? Specifically, how does the quasi-geostrophic theory of Willebrand et al. apply to the seasonal overturning circulations which are largely driven by non-geostrophic Ekman dynamics?

A complementary argument for the barotropic compensation of Ekman mass transports caused by large-scale wind stress fluctuations comes from Ponte and Rosen (1994) in the context of angular momentum dynamics. Angular momentum, though less used in the ocean as a diagnostic of ocean circulation than vorticity and energy, nevertheless provides an excellent basis for a discussion of variable wind forced motions. Following a lull after Munk and MacDonald (1960), interest in the angular momentum balance of the ocean has been revived owing to its geophysical impact on the rotation rate of the Earth and hence the measured length of the day (Ponte 1990; Ponte and Rosen 1994; Bryan 1997; Marcus et al. 1998), as well as its role as an excitation source for polar motions (Ponte et al. 1998). In studies of the Earth's angular momentum balance, it has been observed that on time scales as short as 2 weeks, there is a high correlation between the atmospheric angular momentum changes and the observed changes in the length of the Earth's day (Rosen et al. 1990) and polar motion (Ponte et al. 1998). (At timescales shorter than 2 weeks, the Earth rotation data was not of sufficient quality to make a meaningful comparison.) These results imply that the momentum imparted to the ocean by wind stress is passed through to the solid earth faster than within two weeks. Fast barotropic dynamics must mediate the ocean's response to the fluctuating wind stress; how does this occur?

In the deep ocean external gravity waves are fast; in water 4000 m deep, they can travel 17,000 km per day. Therefore, they permit an adjustment to the wind stress across the ocean basin on timescales as short as one day. The barotropic adjustment is most readily explained with the following thought experiment. In a northern hemisphere basin, a zonal wind from east to west is turned on. Within an inertial period, this results in an Ekman transport to the right of the wind, in this case northward. This piles up water in the northern part of the basin while removing it from the southern part. This creates a meridional pressure gradient, which drives a flow to its right, east to west. This in turn piles water up along the western edge of the basin, creating a zonal pressure gradient directed from west to east. Finally,

72

this zonal pressure gradient drives a geostrophic flow from the north to the south, balancing the Ekman transport and reducing the north-south pressure gradient. In equilibrium, the Ekman transport associated with the wind stress is balanced by the geostrophic transport due to the zonal pressure gradient. Equivalently, the angular momentum imparted by the wind stress is taken up by the zonal walls, consistent with the observational analyses by Rosen et al. (1990) and Ponte et al. (1998), mentioned in the preceeding paragraph. This thought experiment is summarized in the cartoon in Fig. 3.12. As the period of the wind stress fluctuation becomes longer, the Ekman layer convergences can begin to couple to the slower internal gravity waves, allowing the ocean response to become baroclinic. However, at basin scales, this only happens at timescales of longer than a year.
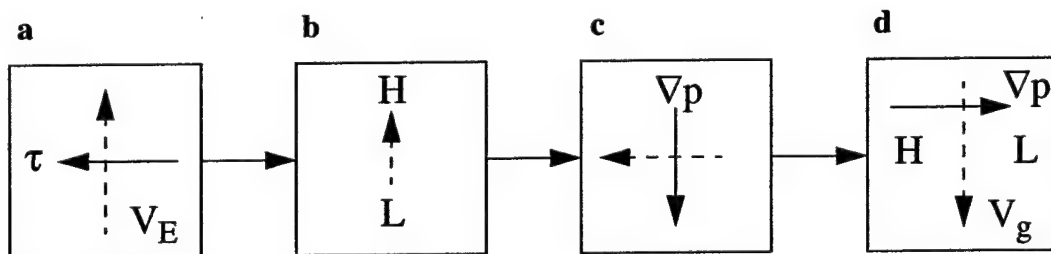
Figure 3.12: Cartoon of a thought experiment; forces are represented as solid lines, and transports are represented as dashed lines. Highs and Lows of surface elevation are represented as H and L respectively, the wind stress is denoted by τ and the pressure gradient by ∇p. (a) The zonal wind stress is turned causing an Ekman flow to the North, (b) the Ekman transport creates a high pressure in the north and low pressure to the south, (c) the north-south pressure gradient drives a geostrophic flow to the west, creating (d) a high pressure in the western part of the basin and low pressure on the eastern side of the basin, which drives a geostrophic flow to the south, whose transport compensates the Ekman layer mass transport.

Further confirmation of the correspondence between angular momentum and mass transport balances comes from analyses of OGCM runs. Using the $1/2°$ run of the POCM (Semtner and Chervin 1992), Ponte and Rosen (1994) demonstrated that for any given zonal ocean section, the annual cycle of the wind stress torque was balanced by a pressure torque due to a pressure gradient across the section. However, owing to the way the model simulation they used was archived, the surface pressure

was not available and they were forced to calculate their pressure gradient from the velocity fields using geostrophy, potentially biasing their result. But, Bryan (1997) confirmed that this balance was valid with a direct calculation of the pressure torque in his model. Using the more recent POCM simulation, the pressure gradient was directly calculable. To examine this in the POCM, we consider the section at 30°N in the Pacific that was presented in Fig. 3.1 where it was demonstrated that there is very strong compensation between the Ekman mass transport and the barotropic transport. Now, the torque balance is considered. The wind torque on a zonal section of the ocean, at a latitude, ϕ, is:

$$T_w = \int_{\lambda_e}^{\lambda_w} \tau_\lambda \, a^2 \, \cos^2 \phi \, d\lambda \tag{3.12}$$

where τ_λ is the zonal wind and a is the radius of the Earth. The pressure torque on the ocean is given by:

$$T_p \;=\; \iint_{-H}^{\eta} \frac{\partial p}{a \, \cos \phi \, \partial \lambda} \, a^2 \, \cos^2 \phi \, dz \, d\lambda = \iint_{-H}^{\eta} \frac{\partial p}{\partial \lambda} \, a \, \cos \phi \, dz \, d\lambda \tag{3.13}$$

It is possible to break the pressure torque into two parts, the "baroclinic" torque corresponding to the first term on the right hand side of (3.14), owing to density deviations producing baroclinic pressure gradients (T_p^ρ), and the second owing to the free surface pressure gradients (T_p^η) represented by the second term on the right hand side of (3.14). One obtains:

$$T_p = \iint_{-H}^{0} \int_{-z}^{0} g \frac{\partial \rho(z')}{\partial \lambda} a \, \cos \phi \, dz' \, dz \, d\lambda + \int g \, \rho_0 \, H \frac{\partial \eta}{\partial \lambda} a \, \cos \phi \, d\lambda, \tag{3.14}$$

where ρ is the density, g is the gravitational constant, H is the ocean depth, and η is the free surface height. Apart from a metric term, the quantities in (3.12) and (3.13) are simply related to the integrated wind stress force and pressure force acting

74

on a zonal ocean section. If geostrophy and Ekman dynamics are assumed, then it immediately follows that the balance between the wind troque and pressure torque implies a compensation between the Ekman mass transport across a section and net geostrophic mass transport across the section. The balance between the wind torque and pressure torque then is:

$$T_p^\rho + T_p^\eta = T_w. \tag{3.15}$$

If the the fluctuating wind stress and the pressure are in balance, then they should be highly correlated. A measure of this is the normalized correlation:

$$C = \frac{\langle T_p' T_w' \rangle}{\langle T_w' T_w' \rangle} \tag{3.16}$$

If the ocean's response to changes in the wind forcing occurs through a barotropic adjustment, the correlation between the wind torque and the surface component of the pressure torque should be high. In contrast, if the adjustment were trapped to a shallow surface layer, as implied by Bryden et al. (1991) who assumed that the seasonal response should be confined to the upper 700 m of the ocean, then the correlation between the wind torque and the baroclinic component of the pressure torque would be positive, and the correlation with the surface pressure gradient would be negative. For a sample section at 30°N in the Pacific Ocean in the POCM, the normalized correlation was 0.77 ± 0.24. The error estimate was based on breaking the time-series into year-long sections and calculating the normalized correlation on them. By individual components, the surface pressure term's normalized correlation with the wind stress was 0.85, whereas the baroclinic pressure term's normalized correlation was -0.08, indicating that the wind stress is in fact balanced by the barotropic pressure gradient there, and the response is not confined to the upper 700 m as was assumed by Bryden et al. (1991). The maximum correlation between the wind stress and the pressure gradient occurred with no time lag; however, the POCM simulation

75

was archived at 3-day intervals. If the adjustment of the ocean to the wind stress was much shorter than 3 days, it would be unresolvable by the temporal sampling of the POCM's output. The correlation between the wind stress and the pressure gradient was also computed for the same region from the linear homogeneous shallow water model. The shallow water model only has the barotropic pressure gradient. The normalized correlation between the surface pressure and the wind stress was 0.91 ± 0.03. The shallow water model was sampled at half-hour intervals at this section so that the time lag between the wind stress and pressure response might be resolved. The maximum correlation between the wind and the pressure gradient was found to occur with the pressure gradient lagging the wind stress by 1.03 ± 0.29 days, indicating that the balance between the wind and pressure is achieved very rapidly.

3.7.1 The equator

The arguments given above hold over most of the ocean, but, the equator requires special discussion. Near the equator, as the Coriolis parameter goes to zero, the vertical trapping scale of forced motion according to (3.11) becomes very small. However, the argument of Willebrand et al. (1980) is based on quasi-geostrophy which is not valid near the equator. Schopf (1980), in a very idealized study, specifically discussed the role of Ekman flow in the cross-equatorial heat transport, which he found to be unidirectional across the equator. His explanation for this was that at the equator, though the Coriolis force vanishes, the flow is carried across the equator by continuity and direct pressure driving. In Schopf's one-hemisphere model the meridional flow was required to be symmetric across the equator by the boundary condition at the equator, namely that $\frac{\partial v}{\partial \phi} = 0$, where v is the meridional velocity and ϕ is the latitude. However, in the global model used here, that requirement is not explicitly imposed. Rather, it is created by the anti-symmetry of the seasonally varying zonal winds about the equator, which implies that the seasonally varying, meridional Ekman transport – where it is defined – is symmetric about the equator. By continuity, any deviation in the flow from symmetry close to the equator would tend to pile water up on one side or the other; but with the vanishing Coriolis parameter there, nothing could support the pressure gradient and the water would be pushed directly down the pressure

76

gradient.

Looking back at Fig. 3.3, it is observed that within ±4° of the equator, there is a very shallow circulation trapped at the surface which is directly driven by the meridional wind. It is largest in the Indian Ocean where the seasonal cycle of the cross-equatorial meridional wind is the strongest. It is also present in the Pacific Ocean and to a much smaller extent in the Atlantic Ocean. Figure 3.13 shows an expanded view of the POCM's seasonal equatorial circulation in the Indian Ocean. This "roll" circulation was discussed in the study of the Indian Ocean by Wacongne and Pacanowski (1996) who found that it was frictionally driven in the downwind direction. Furthermore, they stated that it did not affect the meridional heat transport as it was simply recirculating water of the same temperature. This circulation feature can also be seen in the model based studies by Garternicht and Schott (1997) and Lee and Marotzke (1998). The strong vertical shear needed by this flow can only occur near the equator since thermal wind does not apply there. Figure 3.14, a cartoon of the equatorial circulation, summarizes the findings of Schopf and Wacongne and Pacanowski.
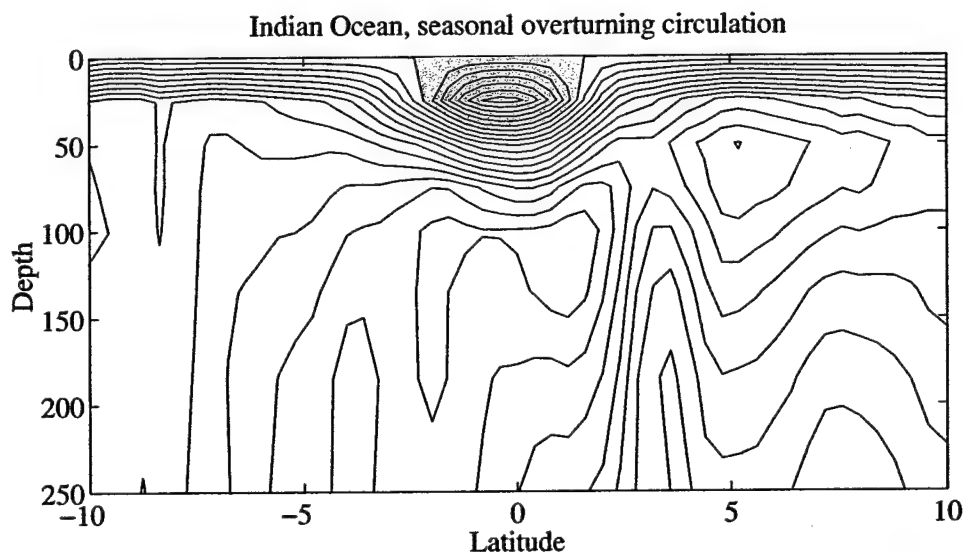

Figure 3.13: Closeup of seasonal equatorial circulation in the Indian Ocean. Contour interval is 2.5 Sv. Negative values of the streamfunction are shaded gray.
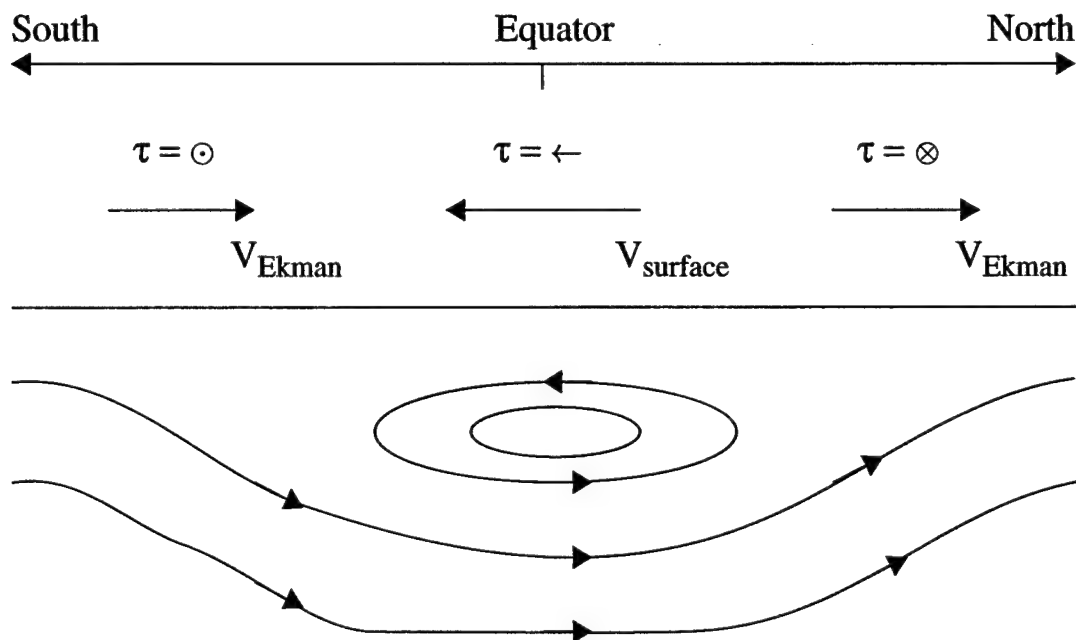
Figure 3.14: Schematic of near surface circulation for cross-equatorial flow, where the wind stress, τ, is denoted by $\otimes$ being into the page (east to west), $\odot$ being out of the page (west to east), and $\leftarrow$ being north to south.

3.7.2 A summary of the ocean's response to time-varying wind stress

All of the components of a complete theory of the role of wind forcing in driving heat transport variations can now be brought together. An oscillation in the zonal integral over the basin width of the zonal wind stress drives a corresponding change in the integrated northward Ekman mass transport across that section. This response of the Ekman transport to the variable wind occurs quickly, on the timescale of an inertial period. The change in the mass transport across the zonal section creates a pressure imbalance which through geostrophy and a series of gravity waves adjusts the pressure gradient to drive a barotropic flow back across the section, balancing the initial change in the Ekman transport. Hence, there is no net flow across the section. The response is essentially the combination of the wind stress leading to an Ekman mass transport, coupled with a compensating flow governed by barotropic dynamics of the kind discussed by Willebrand et al. (1980). Near the equator, where the Coriolis parameter goes to zero, the symmetry of the flow field around the equator and

78

continuity creates a pressure gradient to directly drive the flow across the equator. The temperature difference between the Ekman layer and the section averaged temperature coupled with the opposite directions of the flows creates a heat transport across the section. The depth independence of the time-varying flow means that it will not appear in velocity fields computed from density fields taken from one-time hydrographic surveys. An important conclusion of this is that estimates of the time-mean ocean circulation from hydrographic surveys will not be contaminated by the aliasing of this signal, as long as the time-mean wind stress is used in the calculation.

3.8   Implications for heat transport

We finally turn our attention to the heat transport. In this chapter only the average seasonal cycle will be discussed. A detailed description of the heat transport variations will be given in Chapter 4. Throughout this discussion I will refer to the energy transport implied by the integral of the product $\rho c_p \theta v$ over the area of a zonal ocean section as the northward "heat transport", where ρ is the *in-situ* density, c_p the specific heat per unit mass of water at constant pressure, θ is the potential temperature and v is the northward velocity. Warren (1999) points out that this is actually the internal energy transport, or more accurately the transport of enthalpy plus potential energy, and would be more appropriately referred to as such. However, by convention the vernacular terminology of heat transport shall be used. The heat transport will be considered in the Eulerian framework in which the fluid parcels do not necessarily change their physical properties during an oscillation. Rather, parcels of differing temperatures are exchanged across the section. This is opposed to the Lagrangian view of the heat transport, in which the fluid parcels themselves undergo a diabatic transformation along their trajectory to create a heat transport.

Using the output from POCM, the ocean heat transport across latitude lines was calculated every 3 days for the period 1988-1996. The heat transport for a Boussinesq, incompressible fluid is:

$$F(t) = \rho_0 c_p \iint_{-H(x)}^{0} v\,\theta\,dz\,dx - \frac{\rho_0 c_p}{A} \iint_{-H(x)}^{0} v\,dz\,dx \iint_{-H(x)}^{0} \theta\,dz\,dx, \quad (3.17)$$

where $F(t)$ is the heat transport, x is the zonal coordinate, z is the depth coordinate and t is time, ρ_0 is the density of sea water, here set to be 1025 kg m^{-3} and c_p is the specific heat of seawater, 3994 J (kg°C)$^{-1}$. $v(x, z, t)$ and $\theta(x, z, t)$ are the model meridional velocity and model temperature, respectively, A is the area of the section, and $H(x)$ is the ocean depth.

Like the real ocean, this numerical model has a free surface, so at any given time there may be a non-zero mass transport through a section. This presents a conceptual and practical problem as the prescription of the heat or energy transport requires zero net mass transport through the chosen boundary to eliminate arbitrary reference state constraints. The net movement of water across a zonal section does not necessarily represent a climatologically important energy transport, as it may simply move back across the section at a later time. The second term in (3.17) accounts for the instantaneous, non-zero net mass transport across the section and recovers the temperature scale independence for the heat transport calculation. This term has negligible overall effect on the estimate of the heat transport if the time mean mass transport across the section is nearly zero and the time dependent portion of the section integrated mass transport is uncorrelated with the mean zonal temperature deviations. This adjustment has a maximum root-mean-square amplitude of 4×10^{13} watts near the equator, compared with the heat transport which has a root-mean-square variability of 4×10^{15} watts there. Therefore, it is a small part of the much larger signal, and will not be discussed further. There is, however, a particular area of the ocean where the definition of heat transport in (3.17) is still not sufficient: the latitudes south of the Indo-Pacific throughflow.

3.8.1 Indo-Pacific throughflow

The Indo-Pacific throughflow region presents a special problem when discussing heat transports. As was discussed above, if the time-mean net mass transport across a

section is small, then the effect is also small and can be easily accounted for. However, for the Indian and Pacific Oceans south of the Indo-Pacific throughflow there exists a significant time-mean mass transport from one ocean basin to another around Australia. For zonal sections in the Indian and Pacific Oceans south of the throughflow, the time-mean mass transport is not zero and calculating individual basin heat transports is meaningless. However, it is still desirable to discuss each basin's heat transport independently and not combined as has been done previously (*e.g.* Semtner and Chervin 1992). Therefore a systematic method must be used to account for the net mass transport and its associated temperature transport. Zhang and Marotzke (1999) provide a method for this whereby the influence of the throughflow can be separated from the heat transport in the rest of the basin. Their method involves an additional term to (3.17) for all sections south of the throughflow. The additional term effectively accounts for the local warming (or cooling) of the water which has entered into the basin from the Indo-Pacific throughflow and makes the calculation of the heat transport independent of temperature scale again. For zonal sections affected by the Indo-Pacific throughflow in the Indian Ocean, (3.17) becomes:

$$
\begin{aligned}
F(t) &= \rho_0 C_p \iint_{-H(x)}^{0} v\,\theta \mathrm{d}z\,\mathrm{d}x - \frac{\rho_0 C_p}{A} \iint_{-H(x)}^{0} v\,\mathrm{d}z\,\mathrm{d}x \iint_{-H(x)}^{0} \theta\,\mathrm{d}z\,\mathrm{d}x \\
&+ \rho_0 C_p M_{ITF}\theta_{ITF}
\end{aligned}
\tag{3.18}
$$

where θ_{ITF} is the section mean temperature of the throughflow transport and M_{ITF} is the mass transport across the throughflow. The sign of the correction term is reversed for Pacific Ocean sections. In the POCM, there are 4 gaps in the Indo-Pacific throughflow region. Therefore the flow through all of them must be accounted for individually, this is done for each time point and for all latitudes south of the throughflow.

A thorough discussion of the Indonesian throughflow based on observations and model analysis of the 1/6° Los Alamos model is given by Gordon and McClean (1999). Since these models are so similar in design and forcing, only a brief discussion of the
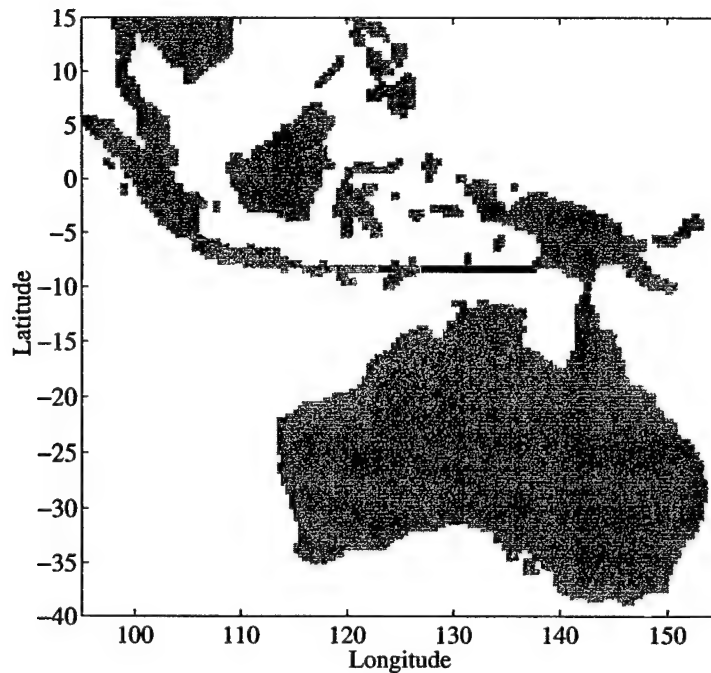
Figure 3.15: Geographical view of the Indonesian throughflow for POCM 1/4° resolution model. The 4 gaps which the throughflow was calculated are shown in black.

throughflow will be given. In the time mean, the POCM 4_B transports 7.8 Sv from the Pacific Ocean to the Indian Ocean in the throughflow, though the flow is strongly time-dependent and has a variance of 5.0 Sv. The majority of the flow in the POCM passes through the gap south of the Banda Sea. This transport estimate is within the limits of observations of the throughflow as summarized by Godfrey (1996), though given the significant variability in the throughflow transports, scattered instantaneous estimates are suspect. The throughflow also has a highly time-dependent heat transport with a mean of 0.67 PW from the Pacific Ocean into the Indian Ocean and a variance of 0.58 PW. The average of the POCM's time-dependent transport compares well with model estimates from Hirst and Godfrey (1993) of 0.63 PW and from Gordon and McClean of 0.66 PW. Of the 0.67 PW of heat transport into the Indian Ocean, 0.31 PW is contributed by baroclinic transport (again mostly across the gap south of the Banda Sea) and 0.36 PW is attributed to a net cooling of the 7.8 Sv of mass transport from 13.7°C to 2.4°C on its trip around Australia.

3.8.2 Seasonal heat transport variations

The time-dependent meridional overturning circulation has implications for the ocean heat transport. As it has been shown the wind stress drives a surface flow which is compensated by a depth-independent flow. Over most of the ocean the temperature of the surface Ekman layer will be higher than the depth averaged temperature. This combination of the time-varying overturning circulation with the vertical temperature structure results in a time varying ocean heat transport. This is summarized in the cartoon in Fig. 3.16.
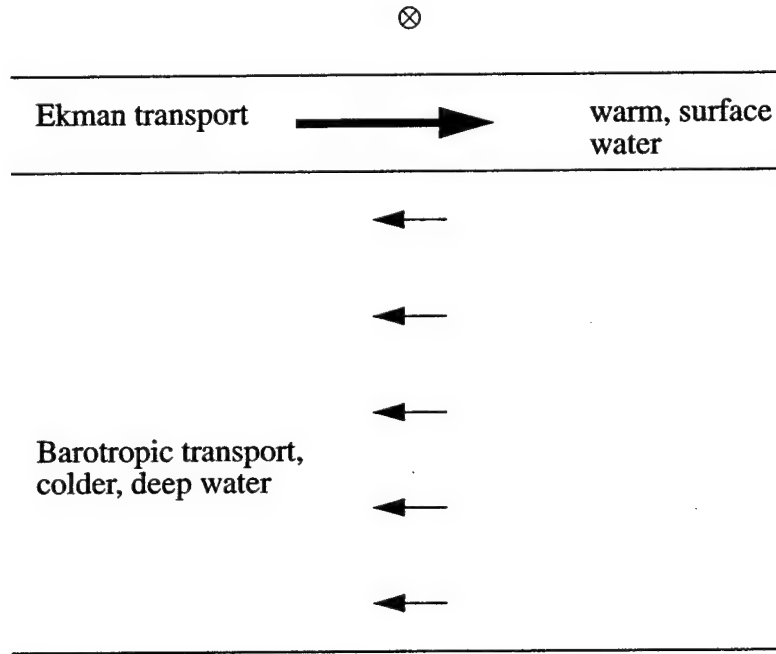
Figure 3.16: Schematic of overturning circulation, where the wind stress, is denoted by $\otimes$ being into the page (east to west) driving a warm surface Ekman layer transport to the north with a compensating depth independent flow transporting cold water to the south, resulting in a positive northward heat transport.

The definition of the Ekman heat transport given by Kraus and Levitus (1986) is:

$$H(t) = \int \rho_0 \, c_p \, \frac{\tau_\lambda}{f \, \rho_0} [T_{Ekman} - \frac{1}{H} \int_{-H}^{0} \theta(z) \, dz] \, a \cos \phi \, d\lambda \qquad (3.19)$$

where c_p is the specific heat of seawater, ρ_0 is the density, f is the Coriolis parameter,

τ_λ is the zonal wind, T_{Ekman} is the temperature of the Ekman layer, $\theta(z)$ is the potential temperature, a is the radius of the earth, λ is the zonal coordinate, and z is the depth. This equation relates the Ekman mass transport and the temperature difference between the Ekman layer and the section average. It assumes that the net mass transport by the Ekman layer across a zonal section is balanced by a flow which is distributed uniformly over the zonal section. Indeed, Kraus and Levitus (1986) and succeeding writers, such as Levitus (1987), Adamec et al. (1993), and Ghirardelli et al. (1995), all assumed that this equation held over all timescales. Adamec et al. (1993) and Ghirardelli et al. (1995) also made the further assumption the local Ekman transport was returned locally at the same longitude, but this is not necessary. However, as it has been discussed, the Ekman mass transport is balanced by a depth-independent flow only for the time-varying component. Klinger and Marotzke (1999) have shown that the time-mean Ekman mass transport is returned at shallow depths, and relatively warm temperatures, within the main thermocline. Therefore, the heat transport by the time-mean flow would not be well represented by the assumption that its return flow was barotropic. In order to separate out the components of the heat transport, a decomposition of (3.19) is made.

$$F_{Ek}(t) = \quad - \frac{c_p}{f} \int (\overline{T} - [\theta]) \overline{\tau_\lambda}\, a \cos\phi\, d\lambda - \frac{c_p}{f} \int (\overline{T} - [\theta]) \tau'_\lambda\, a \cos\phi\, d\lambda$$
$$- \frac{c_p}{f} \int T' \overline{\tau_\lambda}\, a \cos\phi\, d\lambda - \frac{c_p}{f} \int T' \tau'_\lambda\, a \cos\phi\, d\lambda. \qquad (3.20)$$

where the overline represents the time-mean and the prime variations from it. The assumption has been made that the section averaged temperature, $[\theta]$, is nearly constant over the seasonal cycle. The first term represents the expected heat transport due to the time-mean wind stress fields and the time-mean ocean temperatures. However, since there is strong reason to believe that the return flow for the time-mean Ekman mass transport is not barotropic, this is not an appropriate computation and this term will be discussed no further. However, the time-varying terms will be evaluated.

First, the time-varying part due to velocity variations alone is considered. A simple estimate from data can be made of the annual cycle in the Ekman heat transport based

on the climatology of ocean temperature (Levitus et al. 1994) and monthly-averaged wind stress fields derived from the same fields used to force the POCM simulation.The portion of the Ekman heat transport variability due to the temporal variation in the Ekman layer mass transport alone is related to the second term of (3.20):

$$F_v'(t) = -\frac{c_p}{f} \int (\overline{T} - [\theta]) \tau'_\lambda \, a \cos \phi \, d\lambda.$$

(3.21)

Figure 3.17 shows a comparison of the average annual cycle of the heat transport in POCM due to velocity variations compared to the Ekman heat transport variations due to wind stress variability. The seasonal cycle is again taken as January conditions minus July conditions averaged over the last 9 years of the model simulation (1988 – 1997). The agreement between the heat transport variability in POCM due to velocity variations and this simple calculation show overall good agreement, which shows that the time-dependent ocean heat transport is essentially given by the time-varying part of the Ekman heat transport. The poorest agreement is in the tropical Indian Ocean, where the seasonal cycle of the meridional winds probably play a role. This is not an unexpected result given Bryan's (1982) arguments that the meridional wind tends to suppress the heat transport there. It is difficult to add the meridional wind to the calculation given in (3.20), except in some *ad hoc* fashion.

Next, we consider the heat transport fluctuations due to temperature variations. The third term of (3.20) relates changes in the Ekman layer temperature to changes in the Ekman layer heat transport:

$$F_T'(t) = -\frac{c_p}{f} \int T' \overline{\tau_\lambda} \, a \cos \phi \, d\lambda.$$

(3.22)

Here the assumption is made that only the temperature variability in the Ekman surface layer is the important factor in driving the variability. The return flow for the time-mean Ekman transport is presumed to be deep enough that its temperature does not vary strongly on timescales shorter than the seasonal. As a result, for this

85

Figure 3.17: Comparison of annual cycle of heat transport induced by velocity anomalies for the World Ocean from (a) the POCM and (b) climatology from (3.21). The annual cycle (January - July) from the POCM (heavy line) versus climatology (thin line) for (c) the World Ocean, (d) the Indian Ocean, (e) the Pacific Ocean and (f) the Atlantic Ocean. Contour interval for (a) and (b) is 0.5 PW.

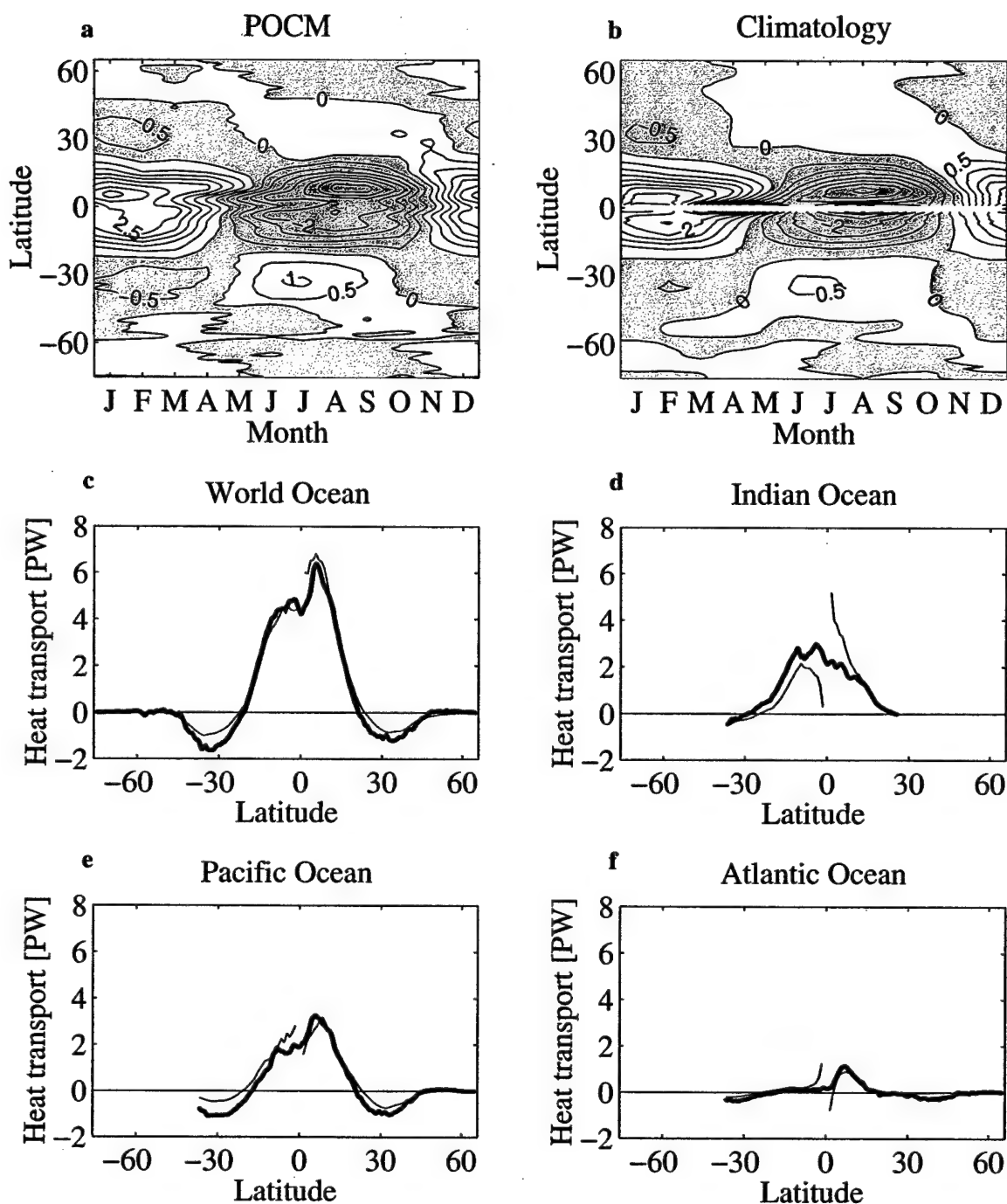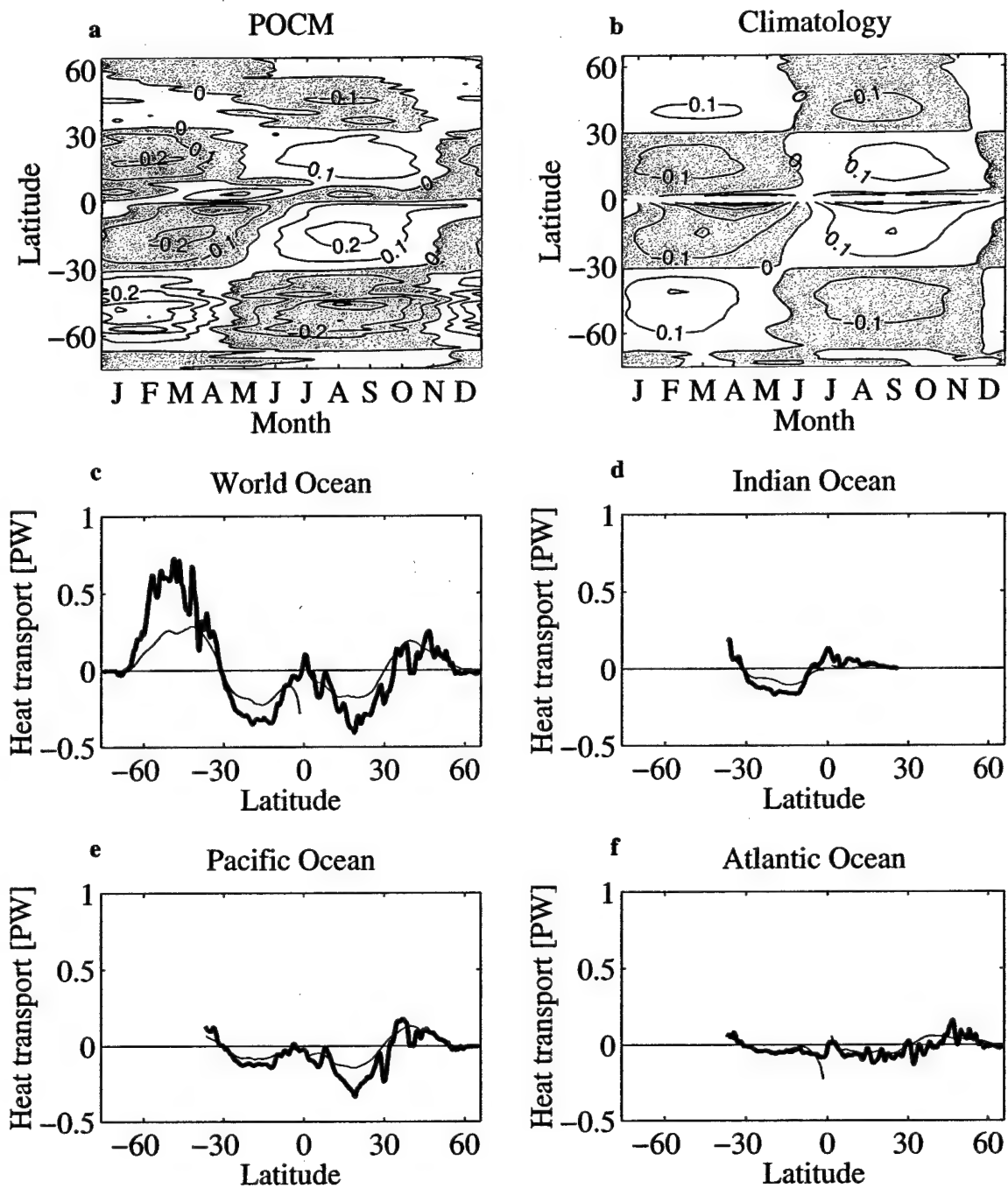Figure 3.18: Comparison of annual cycle of heat transport induced by temperature anomalies for the World Ocean from (a) the POCM and (b) climatology from (3.22). The annual cycle (January - July) from the POCM (heavy line) versus climatology (thin line) for (c) the World Ocean, (d) the Indian Ocean, (e) the Pacific Ocean and (f) the Atlantic Ocean. Contour interval for (a) and (b) is 0.1 PW.

87

term, no specification of the return flow temperature needs to be made, since it does not contribute to the Ekman heat transport variability. Hence, the question of the exact structure of the Ekman layer's return flow is avoided. Figure 3.18 compares the estimate from the climatological data using (3.22) and the output from POCM. The agreement is reasonably good. Of particular note is the seasonal cycle of heat transport in the southernmost latitudes due to temperature variations in the surface layer. This was not seen before in the results of Bryan and Lewis (1979) and Bryan (1982) as their model did not include this variability because of a lack of time-varying thermal forcing.

Finally, the heat transport variability due to covarying temperature and velocity is considered. Here it appears that the semi-annual cycle dominates, which should be expected from the covariance of two out-of-phase annual cycles. Again using climatology the simple estimate for heat transport variations due to covariations in the Ekman layer temperature and Ekman layer transport, the fourth term of (3.20) is:

$$F'_{vT}(t) = -\frac{c_p}{f} \int T' \tau'_\lambda \, a \cos \phi \, d\lambda. \tag{3.23}$$

Figure 3.19 shows a comparison of the average semi-annual cycle of the heat transport in POCM due to covarying velocity and temperature variations in the POCM compared to the Ekman heat transport variations due to wind stress variability. The agreement between the heat transport variability in POCM due to velocity and temperature variations and this simple calculation show overall good agreement.

In summary, the annual cycle of heat transport in the POCM is well reproduced by the simple Ekman heat transport equation. The annual cycle of the Ekman heat transport appears to be dominated by velocity variations in the surface Ekman layer. The temperature variability in the Ekman layer appear to play a weaker, but still significant role. The heat transport variations due to covarying Ekman layer transports and temperatures play the smallest role of all.

88

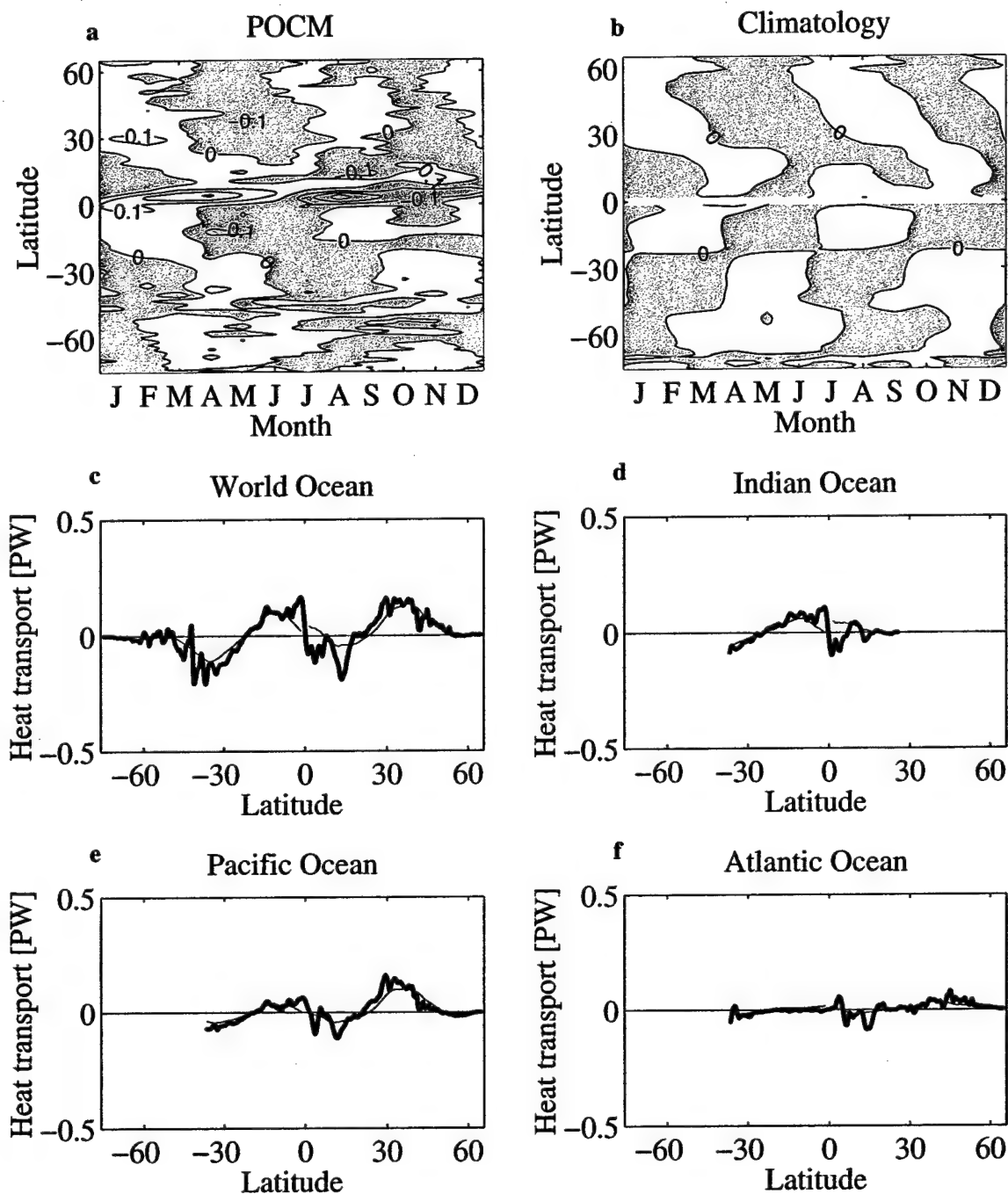Figure 3.19: Comparison of semi-annual cycle induced by covarying anomalies for the World Ocean from (a) the POCM and (b) climatology from (3.23). The semi-annual cycle ((January + July)/2 - (April + October)/2) from the POCM (heavy line) versus climatology (thin line) for (c) the World Ocean, (d) the Indian Ocean, (e) the Pacific Ocean and (f) the Atlantic Ocean. Contour interval for (a) and (b) is 0.1 PW.

89

3.8.3 The tropics

Additional discussion of tropics is in order as the dynamical picture there is not intuitively obvious. The area is schematized in Fig. 3.20 for the January and July anomalies from the time-mean circulation for the atmosphere and ocean. In January (northern hemisphere winter) the area of maximum heating is in the southern hemisphere. In July the anomaly circulation is reversed as the latitude of maximum heating moves into the northern hemisphere. The resulting anomaly in the atmospheric circulation has a net energy transport from the summer hemisphere into the winter hemisphere. The sensible and latent heat transports are directed from the winter hemisphere into the summer hemisphere, but the potential energy is directed from the summer hemisphere into the winter hemisphere and overcompensates for the sensible and latent heat transports so that the net atmospheric energy transport is from the summer hemisphere into the winter hemisphere (Peixoto and Oort 1992). Meanwhile, the ocean's heat transport anomaly is directed from the summer hemisphere into the winter hemisphere. So in total, the atmosphere and ocean together undergo a combined seasonal cycle of ± 4.5 PW, with nearly equal contributions from the atmosphere and ocean.

3.8.4 Error estimates

It is important to consider the error in the model estimation of the heat transport. Errors in a numerical model may come from any number of places including missing model physics, errors in the boundary conditions, errors in the forcing fields and deficiencies in the numerical methods used. It is beyond the scope of this work to do a thorough error analysis of the POCM. However, some attempt should be made to investigate it. Since the seasonal cycle of the wind dominates the dynamics of the ocean heat transport variability and the wind stress fields are some of the least well known fields, an estimate of their uncertainty can give some estimate of uncertainty in the heat transport. Even this simple proposition is difficult though. No formal error estimate is available for the wind stress data used in this study. An examination of older wind stress climatologies, *e.g.* Hellerman and Rosenstein (1983), shows that

a Deviation from time–mean of meridional streamfunction in January

b Deviation from time–mean of meridional streamfunction in July
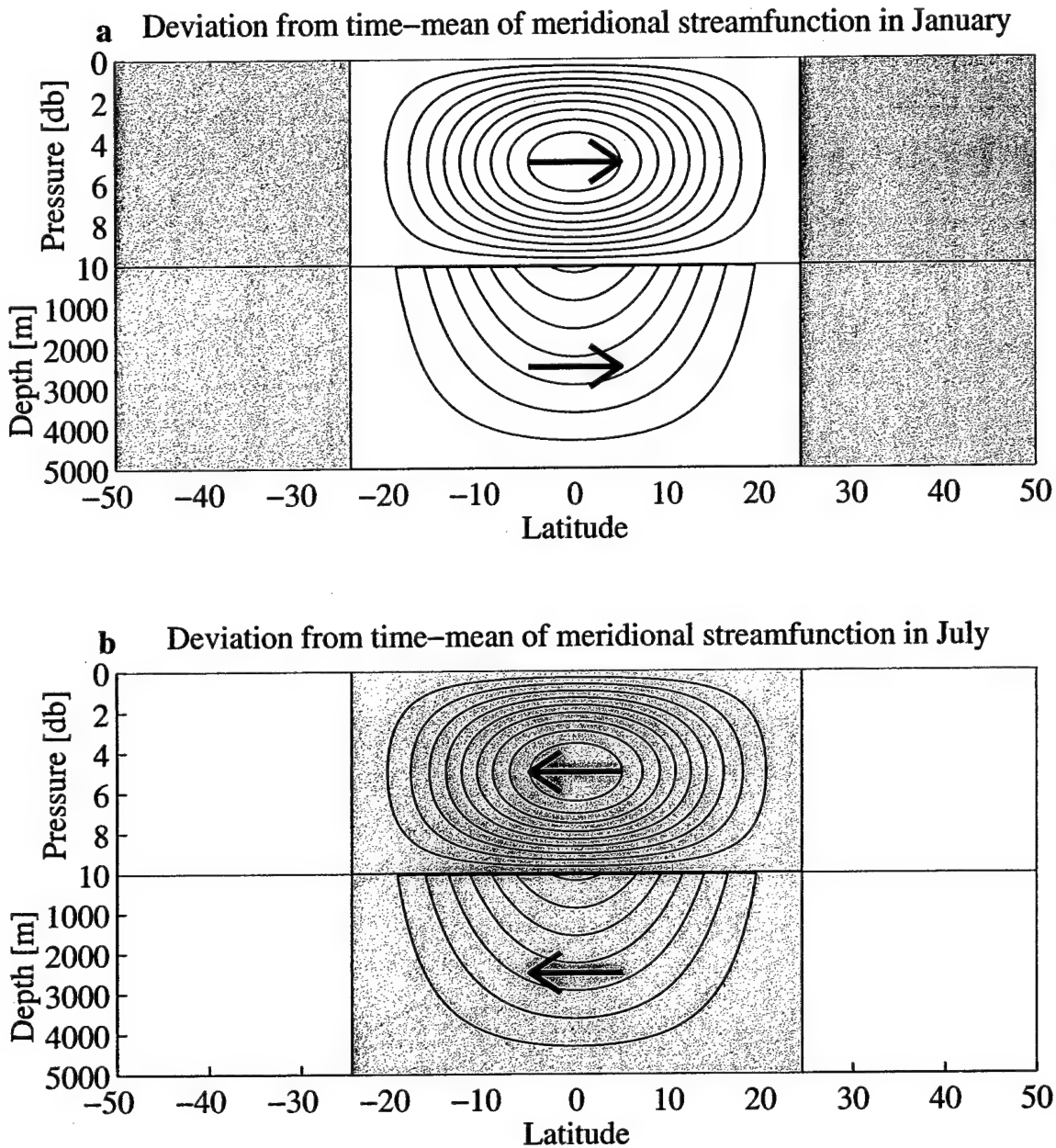
Figure 3.20: (a) The zonally-averaged meridional streamfunction for the atmosphere (upperhalf of the panel) and the zonally-averaged meridional streamfunction for the ocean (lower panel) for the January anomaly from the time-mean of the tropical atmospheric ocean circulation, (b) The same, but for July anomaly. The arrow indicates the direction of the total atmospheric energy transport and ocean heat transport. Negative values of the streamfunction are shaded gray and indicate counterclockwise overturning.

91

the error in individual wind stress values is a complex function of space, mostly due to the geographical coverage of the observing stations. Furthermore, the quantity of interest is an integral quantity of the wind stress field. The errors in the wind are surely wavenumber dependent with the longer waves being more well resolved by the sampling network. Therefore, perhaps the best that can be done is to compare the estimates derived from two different wind stress fields as a proxy for the error. The two wind stress climatologies used here were created from observations over different time periods and hence can be considered independent. The first is the ECMWF wind stress fields used in the POCM run, and the second is the Hellerman and Rosenstein wind stress climatology. Figure 3.21 shows the heat transport derived from (3.20) using the climatologies and the Levitus et al. (1994) temperature climatology.

The estimates agree surprising well in their spatial distribution and magnitude. Nonetheless, there are some important differences. Overall, the difference between the two estimates is roughly 1 PW. The Hellerman and Rosenstein climatology gives a larger magnitude for the annual cycle that the newer ECMWF climatology. This is particularly true near the equator where the smallness of the Coriolis parameter amplifies differences between them and the uncertainty is at least 2 PW.

3.9 Discussion and conclusions

It has been shown that the meridional overturning circulation driven by the seasonal wind field has a strong impact on the ocean heat transport. In particular, a simple relation between the time-varying wind stress and the heat transport has been examined. A dynamical argument has been put forth to explain the fundamental physics relating the wind stress to the heat transport. Variations in the zonal wind stress field drive overturning circulations that transport surface water across the equator from the summer hemisphere to the winter hemisphere. This transport of water is balanced by a depth-independent return flow. In the mid-latitudes poleward of about 20°, the seasonal cycle changes phase and drives a cycle of transport carrying surface waters equatorward in the winter hemisphere and poleward in the summer hemisphere. This "Ekman" component of the time-dependent overturning circulation has a strong im-
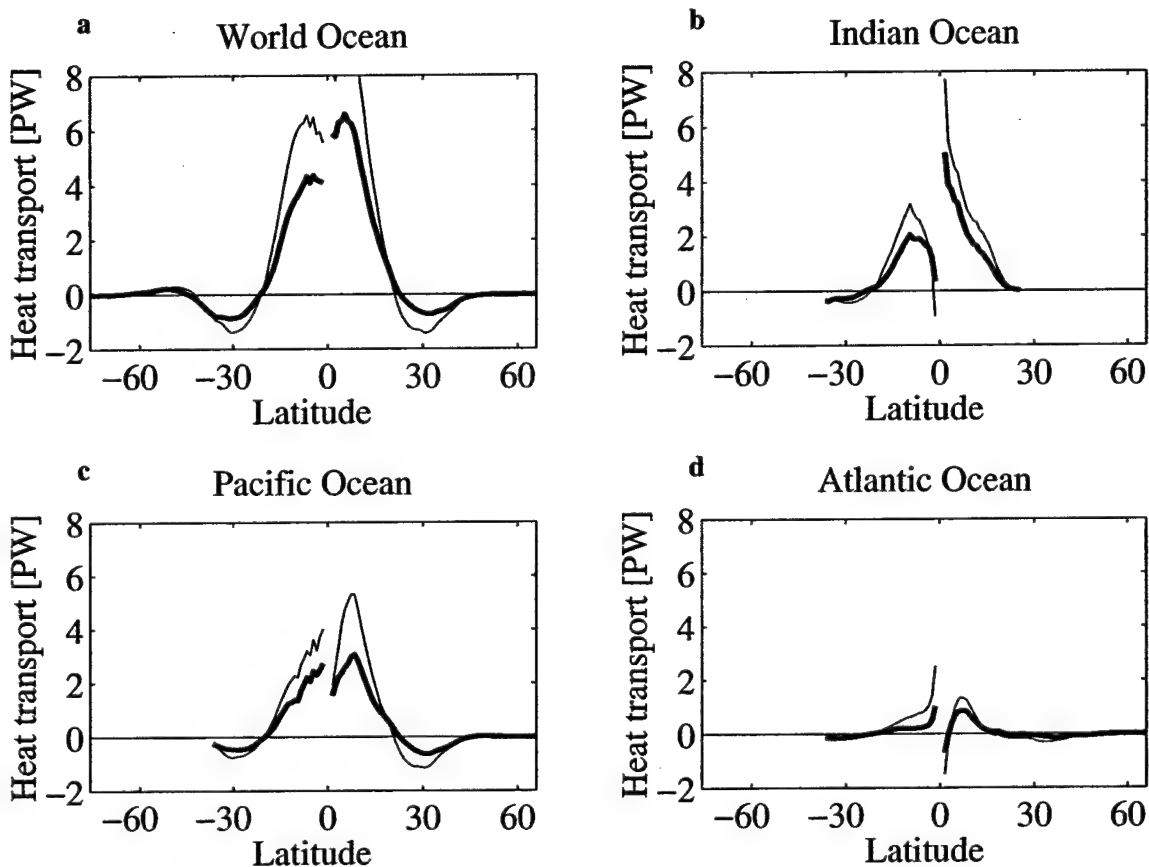
Figure 3.21: Comparison of Ekman heat transport predicted from the ECMWF (heavy line) versus Hellerman and Rosenstein climatology (thin line) for (a) the World Ocean, (b) the Indian Ocean, (c) the Pacific Ocean and (d) the Atlantic Ocean.

pact on the ocean heat transport, but its depth-independent nature means that it does not affect estimates of the time-mean heat transport made by hydrographic surveys (Böning and Herrmann 1994). At the equator, the atmosphere and ocean carry approximately the same amount of energy in their seasonal cycles and the combined energy transport undergoes a cycle of ±4.5 PW.

The annual cycle of heat transport is sensitive to the wind stress fields, with the zonal winds playing the dominant role. Ultimately, the ocean's response to the fluctuating wind stress will be dependent on the spatial and temporal characteristics of the wind field and the spatial characteristics of the bottom topography and stratification. But to first order, the coherent wind-stress fluctuations drive an overturning

circulation whose character is a surface Ekman flow in conjunction with a depth-independent return flow. In conclusion, the fluctuating wind stress plays the critical role in determining the time-dependent ocean heat transport. Therefore, high-quality wind stress fields are of first order importance in making estimates of the fluctuating heat transport.

Chapter 4

Ocean Heat Transport Variability

4.1 Introduction

In this chapter I present, for the first time, a description of the global characteristics of the high-frequency, time-varying ocean heat transport from a state of the art ocean general circulation model (the POCM described in the previous chapter). Though the goal of this work is to examine the time-varying heat transport, in order to place it in the context of the larger climate system, a comparison is made between the POCM's time-mean heat transport and estimates made from oceanographic data (Macdonald and Wunsch 1996) and atmospheric data (Trenberth and Solomon 1994). Though a few studies have addressed the variability of the heat transport across single zonal sections, notably the work of Molinari et al. (1990) work at 26.5°N in the Atlantic and the study by Wilkin et al. (1995) at 24°N in the Pacific, very little work has been done on the global context of the time-varying heat transport. To begin, the seasonal cycle of the ocean heat transport from the model is compared to previous global estimates from models (Bryan and Lewis 1979; Bryan 1982) and observational data (Carissimo et al. 1985; Hsiung et al. 1989). Then, I discuss the time-varying heat transport by examining three different decompositions of it. The first is a breakdown of the the heat transport by ocean basin, the second is a decomposition of its temporal components, and the third is an examination of its dynamical components. These three were chosen from the near-infinite number of possible decompositions for their ability to illustrate key features of the high-frequency ocean heat transport variability:

namely, that the three ocean basins have unique characteristics while sharing some similarities; that the variability of the total heat transport is dominated by velocity variability rather than temperature variability, implying that a certain set of physics is dominant over others; and that one dynamical mode of the ocean accounts for the majority of the variability. Individually, these decompositions are not new, as they have been applied to single basin models before; what is new is that all three are applied to a single global OGCM in addition to having high-frequency variability beyond the annual and semi-annual cycles. The seasonal heat balance of the model is examined to understand the impact of the time-varying heat transport on the local heat budget. This is done on a global scale, as well as for individual ocean basins.

The global distribution of the rectified eddy heat transport is considered and several new analyses are applied to it in order to begin to understand its characteristics. This process is the subject of considerable interest and debate. Coarse resolution models do not resolve the transport processes associated with the oceanic mesoscale field. Therefore, significant effort has been spent on the parameterization of the impacts of the mesoscale eddy field (*e.g.* Gent and McWilliams 1990; Holloway 1992; Griffies 1998). However, the role of the oceanic mesoscale eddy field in climate processes has been only marginally addressed observationally (Bryden 1979; Bryden and Heath 1985; Bryden and Brady 1989; Stammer 1998; Wunsch 1999). To gain insight into its characteristics, it is examined by basin, by depth interval and by dynamical component. Then the vector distribution of the rectified eddy transport is considered. Following the suggestion of Marshall and Shutts (1981) it is separated into its rotational and divergent parts with the Gulf Stream as an example. The rotational component can not transport heat across latitude circles and does not contribute to the poleward transport of heat by the oceans, whereas the divergent component of the heat transport does affect the local heat balance and does transport heat northward. It is shown that for a coherent meandering jet, the rotational eddy heat transport dominates and it is not necessarily down gradient, leading one to doubt the validity of claims that current-meter data show down-gradient temperature transport. A comparison of the model's northward eddy heat transport and a global estimate derived from TOPEX/POSEIDON data (Stammer 1998) is made. The basic technique used

by Stammer (1998) is tested and thereby the assumptions that were used in calculating it are evaluated. And lastly, the eddy heat transport at a few selected locations is examined by using its cospectrum for an indication of what part of the frequency spectrum is contributing to the rectified heat transport.

4.2 Time-mean heat transport

Before considering the heat transport variability, the annual-mean heat transport from observations and by the model should be discussed so that the variability may be placed in its proper context. Several global estimates of the annual-mean ocean heat transport have been made. Macdonald and Wunsch (1996) computed a global estimate from an inverse model of ocean hydrographic sections. Trenberth and Solomon (1994) and Keith (1995) computed a global heat budget from top-of-the-atmosphere radiation data and atmospheric analyses from ECMWF to calculate the atmosphere and ocean heat transports. Historically, there have been inconsistencies between data-derived estimates of the ocean heat transport from atmospheric analyses and more direct measures from hydrographic surveys, though the work of Keith (1995) suggests that the estimates from the methods are now consistent within the uncertainty inherent in them.

A summary of results from Trenberth and Solomon (1994) and Macdonald and Wunsch (1996) is shown in Fig. 4.1 together with the time-mean heat transport from the POCM calculated using (3.17) and (3.18). In the Northern Hemisphere, the model estimate of the annual-mean heat transport is consistent with Macdonald and Wunsch's analysis and inconsistent with the Trenberth and Solomon estimate. The agreement between the POCM and Macdonald and Wunsch in the Atlantic Ocean is good for all but one section in the South Atlantic. On the other hand, in the Southern Hemisphere, the model does not transport enough heat southward to be consistent with either estimate. The model's 0.7 PW southward transport at 30°S in the combined Pacific and Indian Oceans is only half the 1.4 PW estimated by Trenberth and Solomon (1994), Macdonald (1995) and Keith (1995). Because of the strong northward heat transport in the Atlantic and the weak southward heat
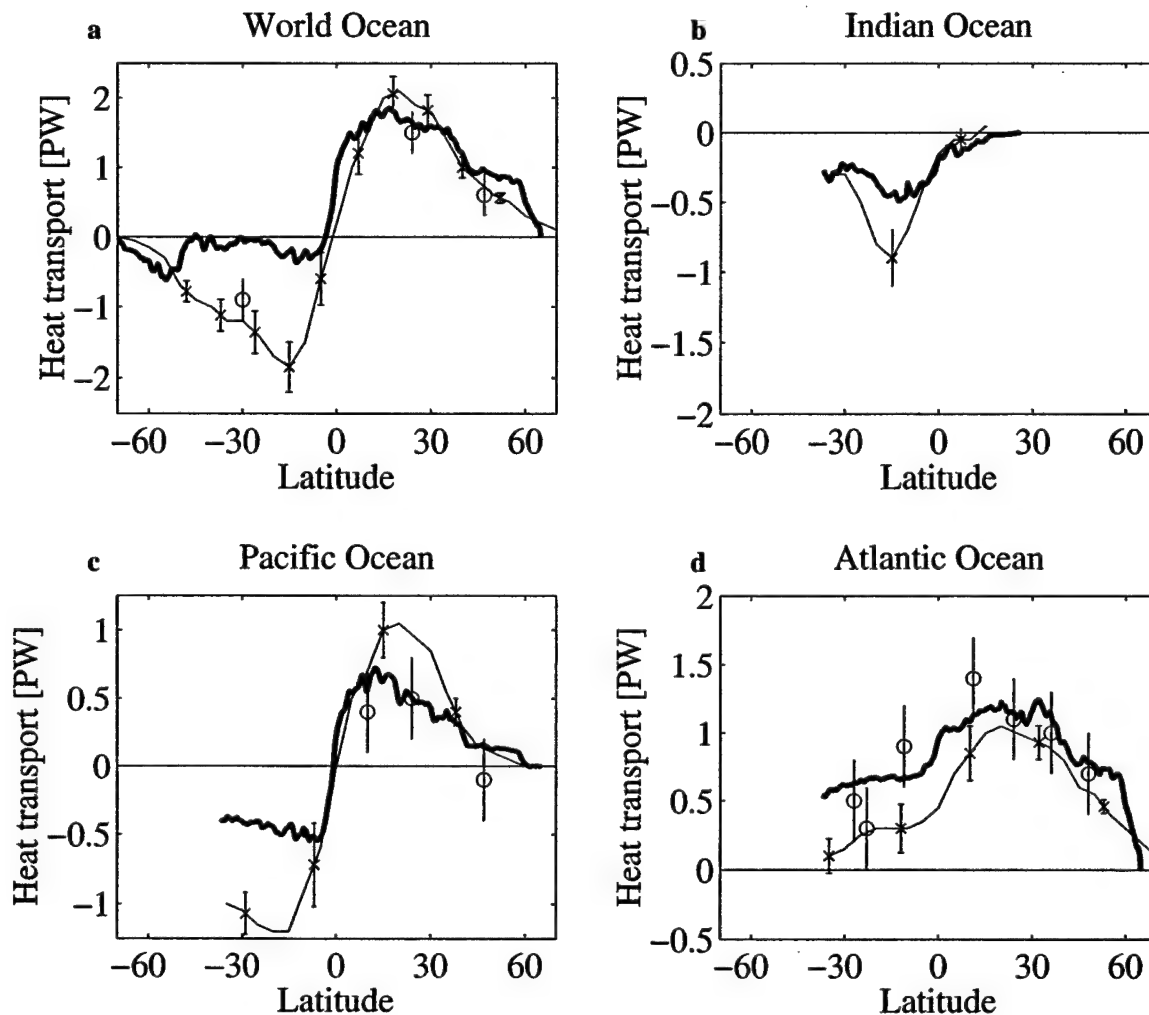
97

Figure 4.1: Time-mean heat transport for the (a) World Ocean, (b) Indian Ocean, (c) Pacific Ocean and (d) Atlantic Ocean. Heat transport from POCM is plotted with the heavy line, the estimate of Trenberth and Solomon (1994) is plotted with the thin line, with errorbars given by x's. The heat transport estimates from Macdonald and Wunsch (1996) are plotted with o's with errorbars.

transports by the Pacific and Indian Oceans, over much of the Southern Hemisphere the POCM is carrying very little heat poleward. This finding is similar to that of Macdonald (1995) who showed that the previous 1/2° version of the POCM also had a combined Pacific and Indian Ocean heat transport that was too weak (Semtner and Chervin 1992; Macdonald and Wunsch 1996). The reasons for this model deficiency are not clear; however, the model has improved between the 1/2° run and the 1/4° run, since in the 1/2° model, in the global total, there was actually northward heat

transport over portions of the Southern Hemisphere (Semtner and Chervin 1992).
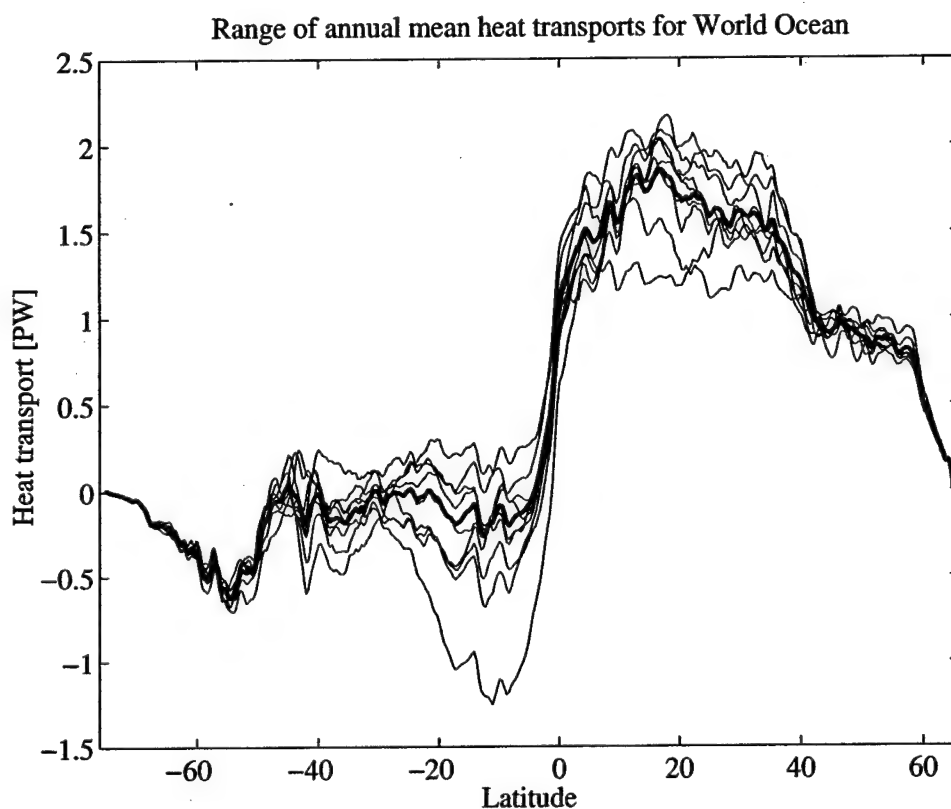

Figure 4.2: Annual mean heat transport for each year between 1988–1996 (thin solid lines) and mean of annual means (heavy solid lines).

The difference between the time-mean and annual-mean should be briefly mentioned. The term "annual-mean" is often used when discussing the heat transport averaged over the seasonal cycle. However, this terminology can be misleading as the mean heat transport over a single year can fluctuate from year to year. It would be more appropriate to refer to the time-mean heat transport over some period. As an example of this, the annual-mean heat transport for the global ocean was calculated from the model for each calendar year from 1988–1996 to obtain an estimate of the variability of the annual-means compared to the overall time-mean for the same period. The results are shown in Fig. 4.2. There is large scatter in the annual estimates around the time-mean, with a variance of 0.2 PW at the equator ranging up to 0.4 PW at $\pm 20°$. The one particularly anomalous year is 1996, the last year of the run.

However, there is no significant secular drift in the estimates. Given this large inter-annual variability, how valid is an annual-mean estimate? The variability is largely from wind-driven changes in the Ekman overturning, and not the result of water mass redistributions within the model. Therefore, to avoid confusion over terminology, the time-mean is used throughout this discussion, and is the average over the last 9 years of the model run (1988–1996).

4.3 Comparison of the annual cycle with previous model results and observational evidence

Before the details of the high-frequency heat transport variability are discussed, a comparison with some of the previous estimates of the seasonal cycle of ocean heat transport is in order. The annual cycle of heat transport has been investigated using several methods as discussed in the introduction. Here the estimates of Bryan and Lewis (1979), Carissimo et al. (1985) and Hsiung et al. (1989) are compared and discussed.

Bryan and Lewis (1979) used a numerical model of the global ocean, forced with monthly averaged wind stresses from Hellerman (1967), and with restoring to time-mean temperature fields of Levitus and Oort (1977). Their annual cycle in heat transport, taken as the January minus July transports, is shown in Fig. 4.3, contrasted with the same annual cycle of heat transport from the POCM 4_B run. The estimates are remarkably similar given that the POCM simulation was forced with higher quality and higher frequency wind stresses in addition to time varying thermal forcing in POCM. There are, however, differences. POCM has a larger amplitude annual cycle, particularly in the tropics north of the equator. While the Bryan and Lewis (1979) estimate is nearly symmetric about the equator, the POCM is less so. In addition, POCM has a decrease in the heat transport annual cycle at the equator which is not present in the Bryan and Lewis (1979) model. This double peak in the world total in the POCM arises from the Pacific and Atlantic having their peak annual cycle at 7°N while the Indian Ocean has its peak at 4°S. Presumably its appearance is due to differences and improvements in the wind stress fields used by the POCM. Also,

100

the POCM simulation has a significant seasonal cycle at the southernmost latitudes where Bryan and Lewis (1979) have none. It will be seen later that this is an effect of the time varying thermal forcing that was absent in the Bryan and Lewis (1979) work.
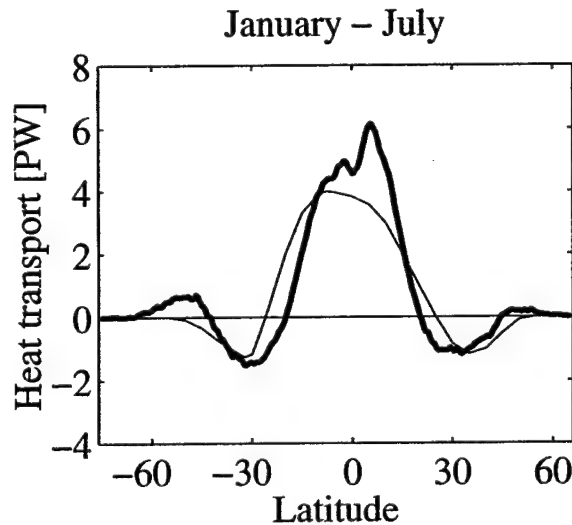

Figure 4.3: Annual cycle of ocean heat transport for the World Ocean from POCM (heavy line) and numerical model of Bryan and Lewis (thin line) for January minus July.

Carissimo et al. (1985) used satellite derived net radiation balances, atmospheric transports and ocean heat storages to estimate the ocean heat transport as a residual. Their annual cycle, as measured by the difference in the season of December, January and February minus the season of June, July and August, is presented in Fig. 4.4. The seasonal difference between boreal spring (March, April and May) and boreal autumn (September, October and November) is plotted as well. There are large differences between the POCM heat transport and the Carissimo et al. (1985) estimate. While the POCM annual cycle changes sign in the mid-latitudes and then again at high-latitudes, the Carissimo et al. (1985) estimate does not, and is of the same sign over the whole latitudinal extent. However, it is difficult to say what differences are significant as the estimated error of Carissimo et al. (1985) is ±3 PW, which may still be too small given that their estimate is inconsistent with observations by Hsiung et al. (1989), Bryden et al. (1991), and Trenberth and Solomon (1994).
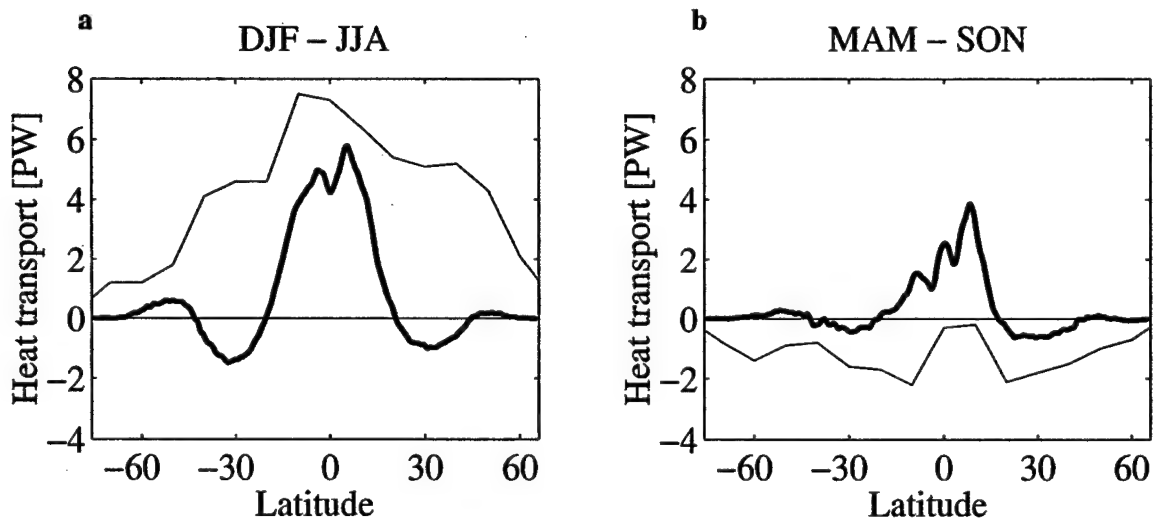
Figure 4.4: Annual cycle of ocean heat transport for the World Ocean from POCM (heavy line) and estimate of Carissimo et al. (thin line) for (a) average of December, January and February (DJF) minus June, July and August (JJA) and (b) average of March, April and May (MAM) minus September, October and November (SON).

Hsiung et al. (1989) expanded the work of Lamb and Bunker (1982) to include the Pacific and Indian Oceans as well as the Atlantic Ocean. For their estimate of the heat transport, Hsiung et al. (1989) used ocean heat-storage observations combined with ocean surface heat fluxes derived from the bulk formulae to calculate the ocean heat transport as the residual. They estimated monthly values of the heat transport for each of the three basins between 50°N and 20°S. Errors in their data analysis tended to accumulate as they integrated from north to south so that the transports near the equator were unreliable and compared poorly with other estimates of the transport (*e.g.* Philander and Pacanowski 1986; Böning and Herrmann 1994). Therefore, a comparison of the divergence of the POCM results heat transport to their more robust estimate of the divergence is made in Fig. 4.5. This allows two things; first, any systematic errors are removed by the differentiation, and second, it allows, for the first time, the presentation of the annual cycle of divergence for the world ocean heat transport from POCM, which is of general interest for its more direct relevance to climate. The estimate of Hsiung et al. (1989) and the estimate derived from POCM are generally of similar character. In agreement with the Bryan and Lewis estimate,

102

the annual cycle of Hsiung et al. (1989) changes sign in the mid-latitudes. The range of the error bars on Hsiung et al.'s (1989) estimate are ± 25–50 W m^{-2}. Overall then, the two estimates are consistent, while the extrema in the POCM estimate are of larger magnitude than those in the coarser resolution climatology.
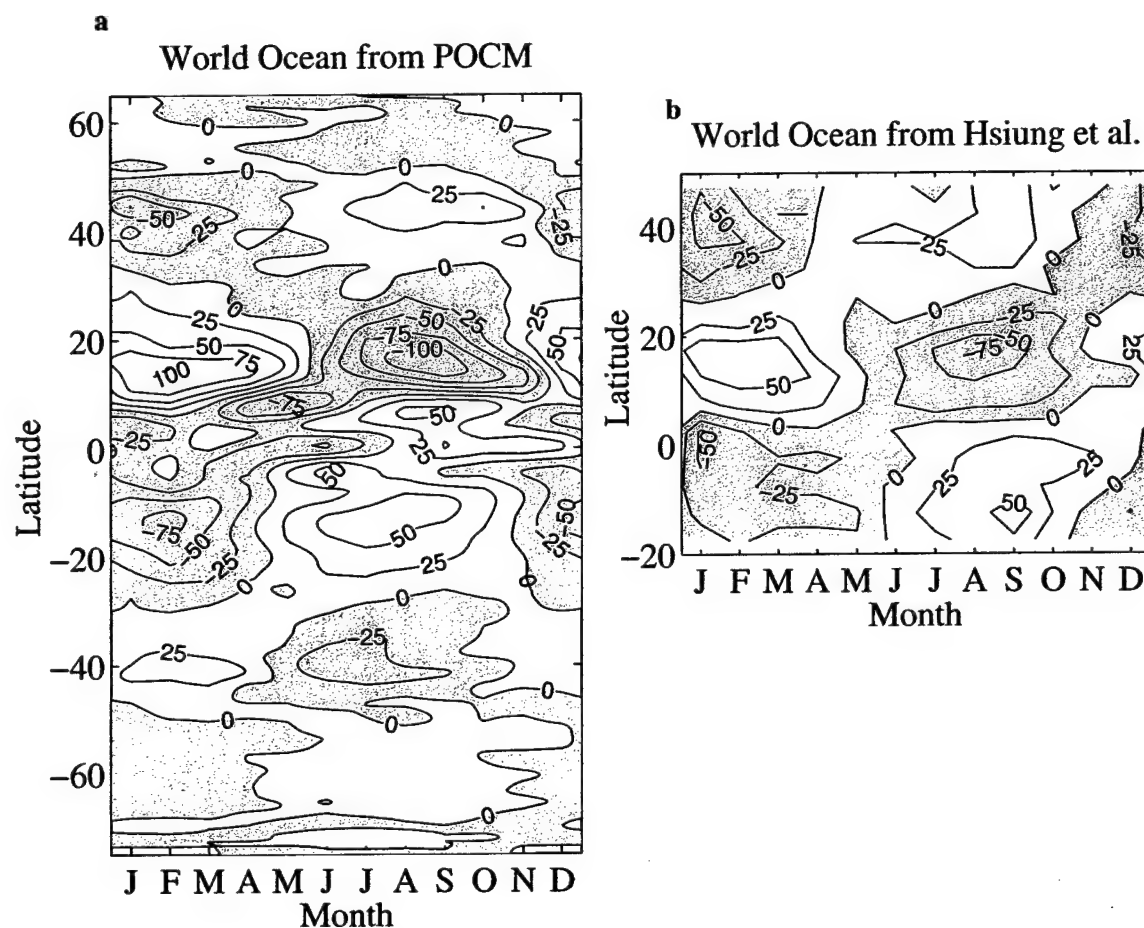

Figure 4.5: Annual cycle of the divergence of the advective ocean heat transport (time-mean removed) for the (a) World Ocean from POCM and (b) Hsiung et al. The contour interval is 25 W m^{-2}, gray shading indicates negative fluxes.

4.4 Basin heat transport variability

To begin the investigation of the full temporal variability of heat transport in POCM, the heat transport for each basin was calculated using (3.17) and (3.18). The time-mean heat transport was then removed and the time-series at each latitude was filtered in time using a simple triangle filter of half-width 4.5 days to reduce the amplitude of aliased inertial oscillations (Jayne and Tokmakian 1997; and Chapter 2 of this thesis). The annual cycles are summarized in Fig. 4.6 and the Hovmöller diagrams of the heat transport anomaly as a function of latitude and time are presented for the World Ocean (Fig. 4.7a), the Pacific Ocean (Fig. 4.7b), the Atlantic Ocean (Fig. 4.7c) and the Indian Ocean (Fig. 4.7d).

Numerous features in Fig. 4.7 merit discussion. First and foremost, the variability is dominated by a large annual cycle in heat transport found in all of the ocean basins. The largest signal is confined to within 20° of the equator and is in phase across the equator. For the world ocean total, the annual cycle near the equator has an amplitude of nearly 6 PW peak-to-peak. This is composed of annual cycles in the Indian Ocean of 2.6 PW peak-to-peak, 3 PW peak-to-peak in the Pacific Ocean, and a much weaker annual cycle in the Atlantic Ocean of about 1 PW. The Indian Ocean's annual cycle has a peak at 5°S, while the Atlantic and Pacific Ocean's peak amplitudes are at 7°N. It is clear comparing Fig. 4.6 to Fig. 4.1 that the seasonal heat transport variability is much larger than the time mean signal. The ocean response to the seasonal cycle in the atmospheric wind stress is to transport heat from the summer hemisphere to the winter hemisphere, in phase with the total energy transport by the atmosphere's Hadley cell (Peixoto and Oort 1992). Superimposed on the annual cycle are both higher frequency oscillations and interannual variations which are coherent over large meridional extents. There are weaker opposite-sign heat transports in the subtropical gyres, which further enhance a mid-latitude heat transport convergence in the winter hemisphere and a net divergence in the summer hemisphere relative to the time-mean.

To examine the relative distribution of variability, power spectra of the heat transport time-series were computed at the equator for the three basins and the combined
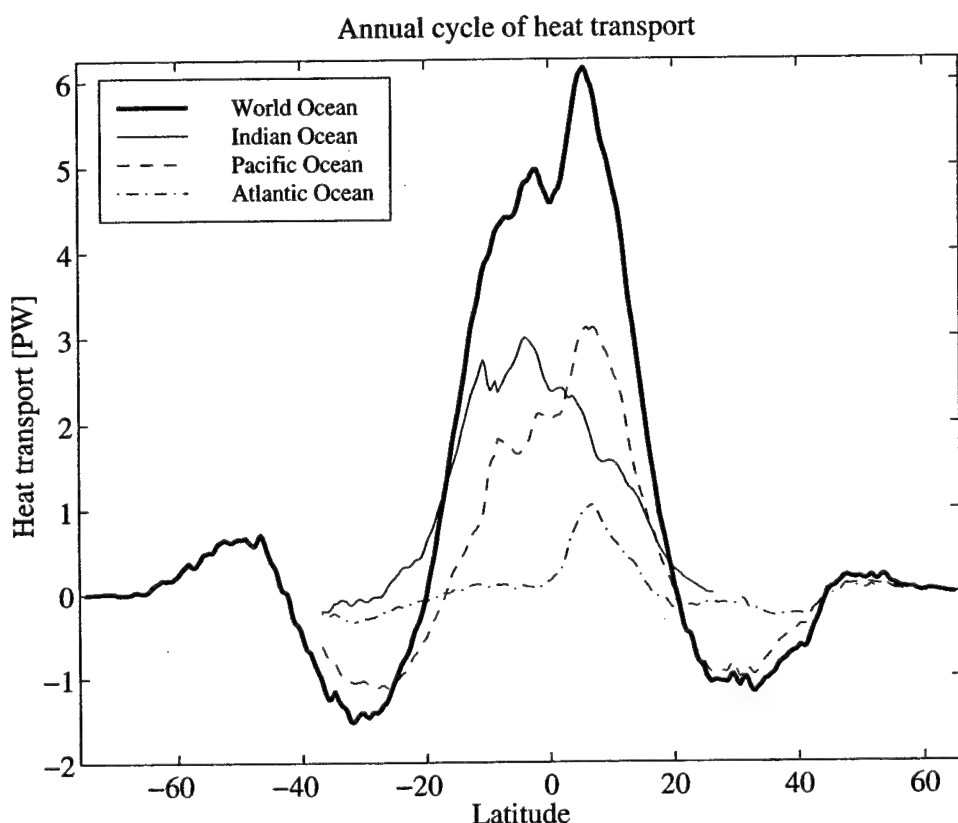
104

Figure 4.6: Annual cycle of heat transport defined as the difference between January and July values for (a) the World Ocean, (b) the Indian Ocean, (c) the Pacific Ocean and (d) the Atlantic Ocean.

total and are shown Fig. 4.8. The spectra were computed using Thompson's multitaper method with a half bandwidth of 2.5 (Thompson 1982; Park et al. 1987; Percival and Walden 1993; Lees and Park 1995). In the Indian and Pacific Oceans the annual cycle is the dominant variability. In the Indian Ocean, at the equator, the spectrum is flat at frequencies higher than the annual period. In the Pacific Ocean the semi-annual cycle significantly contributes, as does the range of periods from 10 days to a month corresponding to synoptic wind-stress fluctuations, with a peak at 10 days. In the Atlantic Ocean, the semi-annual cycle is as important as the annual cycle, with a flat spectrum at higher frequencies. The global total is dominated by the large annual cycles in the Indian and Pacific Oceans, with a strong contribution from the 10 day cycle in the Pacific.

Figure 4.9 shows power spectra of the heat transport at several latitudes in the

105

a World Ocean meridional heat transport anomaly

b Indian Ocean meridional heat transport anomaly
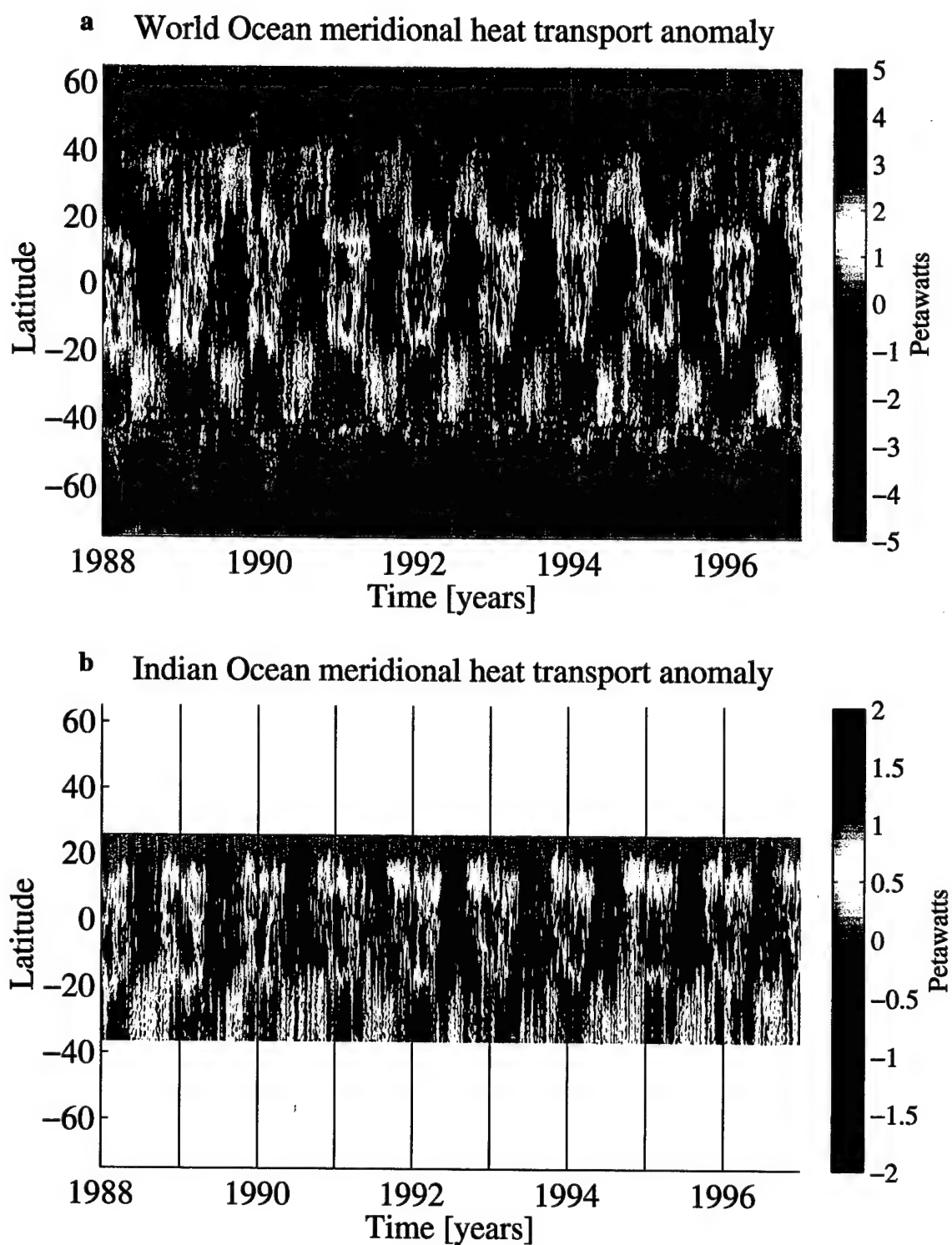
Figure 4.7: (a) Time-dependent heat transport anomaly for the World Ocean. The time mean heat transport has been removed to highlight the variability. (b) Time-dependent heat transport anomaly for the Indian Ocean. Vertical lines mark January 1.

c Pacific Ocean meridional heat transport anomaly

d Atlantic Ocean meridional heat transport anomaly
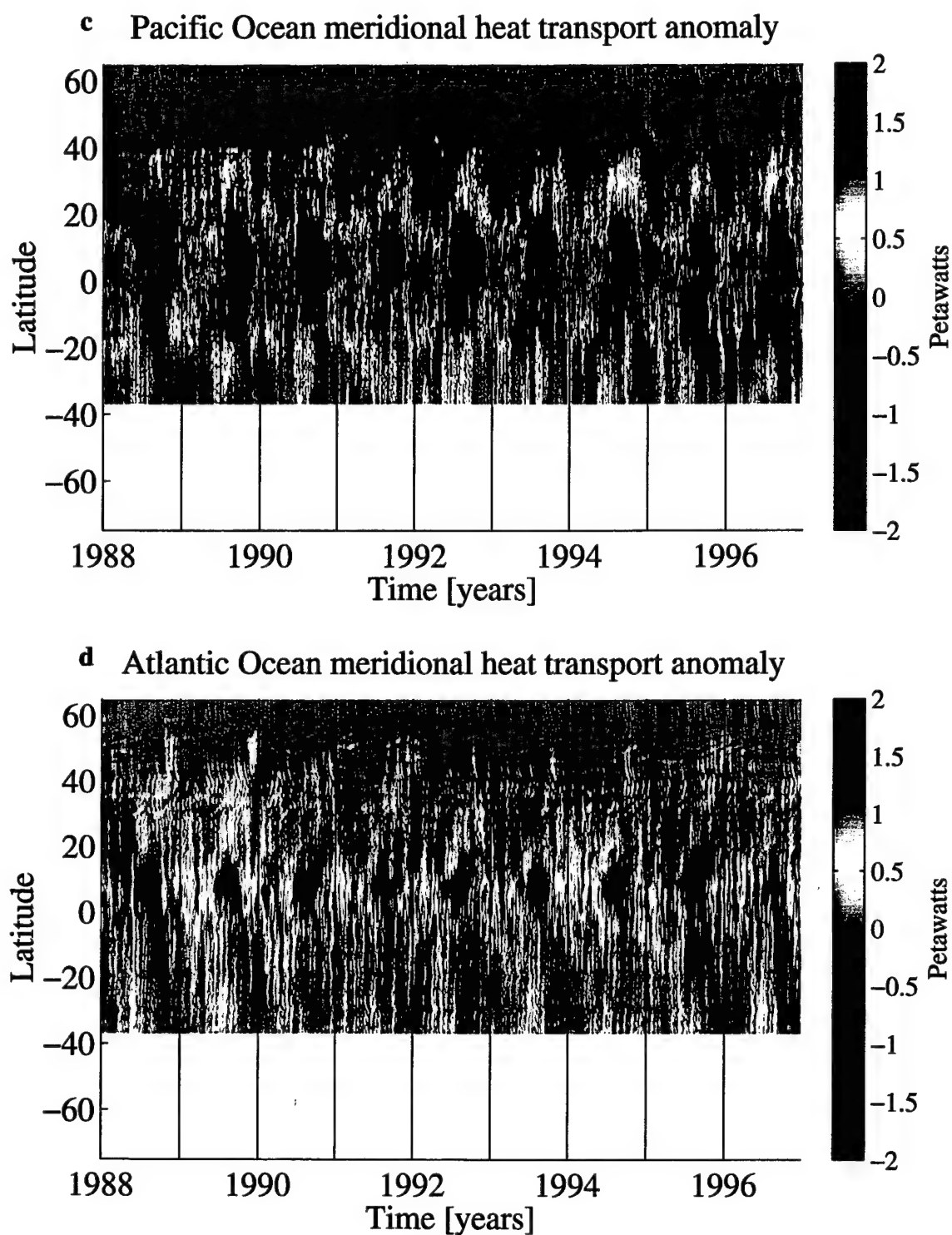
Figure 4.7: cont. (c) Time-dependent heat transport anomaly for the Pacific Ocean. (d) Time-dependent heat transport anomaly for the Atlantic Ocean. Vertical lines mark January 1.
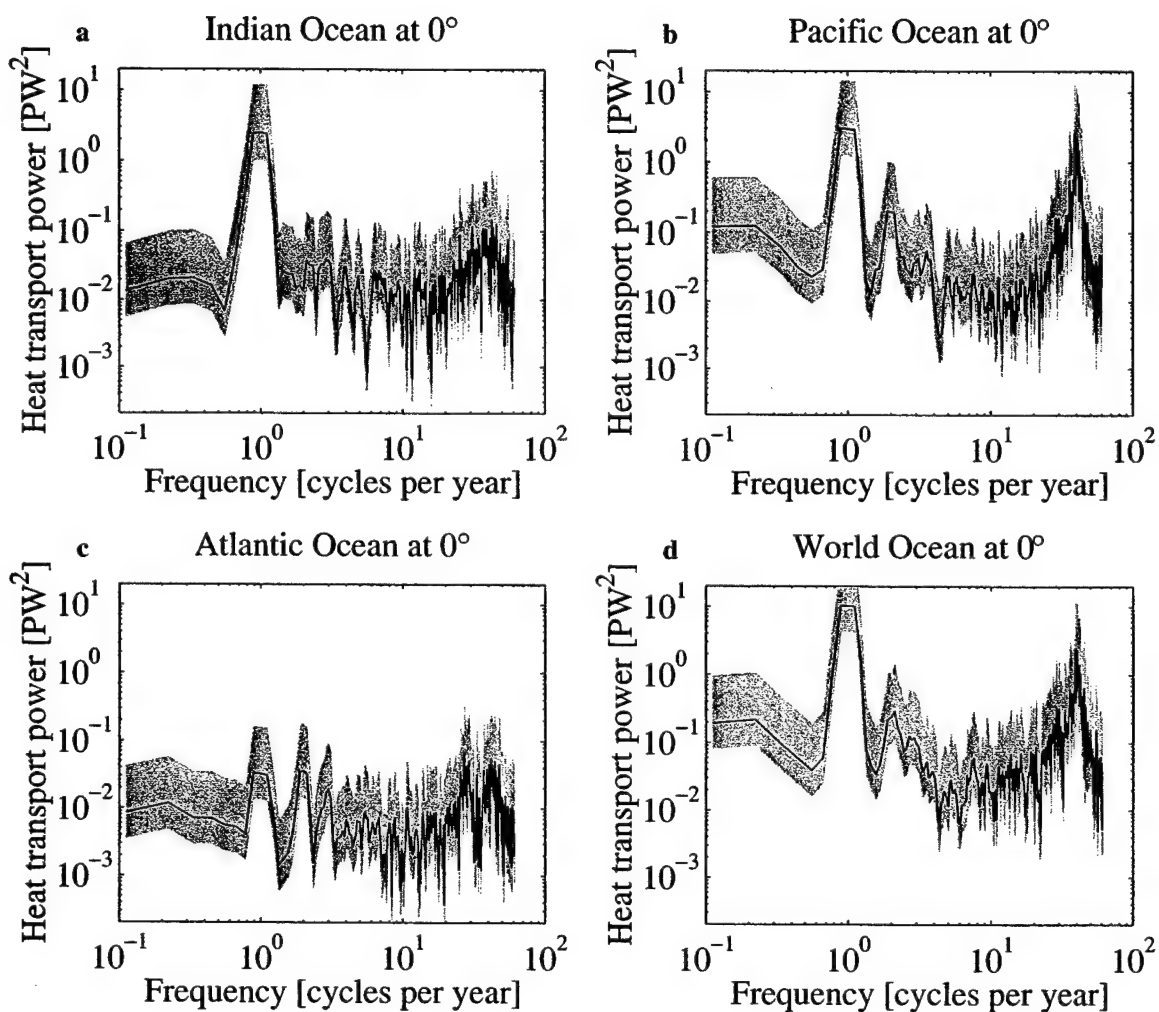
Figure 4.8: Power spectra of heat transport from individual basins at the equator, (a) the Indian Ocean, (b) the Pacific Ocean and (c) the Atlantic Ocean and (d) the three ocean basins combined. The gray shading indicates the 95% confidence interval.

Figure 4.9: Power spectra of heat transport for selected latitudes in the Atlantic Ocean at (a) 11°N, (b) 24°N, (c) 36°N and (d) 48°N. The gray shading indicates the 95% confidence interval.

Atlantic Ocean. At 11°N, the spectrum is red with large peaks at the annual and semi-annual periods. This is in contrast to the 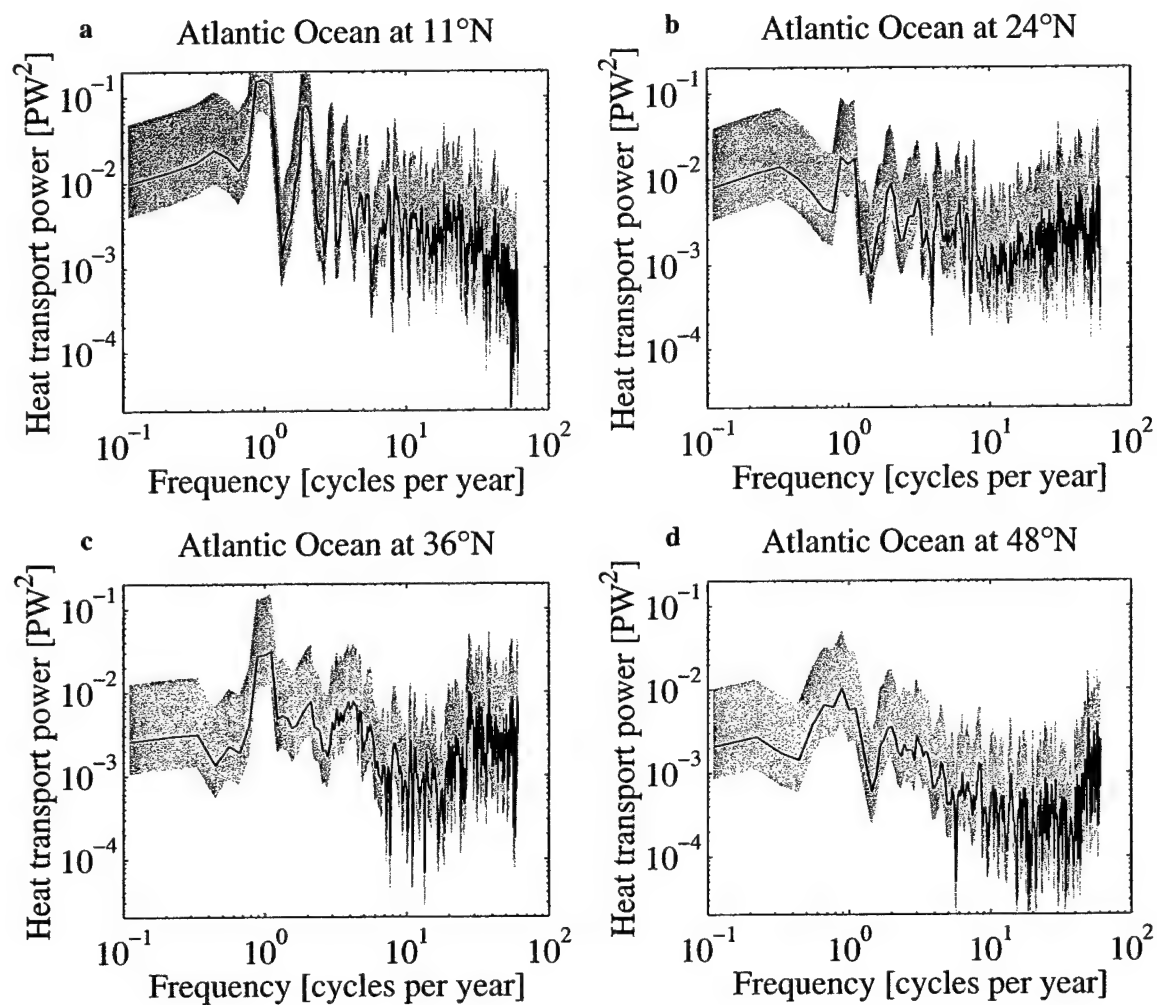equatorial Atlantic where the spectrum is white. At 24°N the annual peak is much less pronounced and the spectrum is flatter at the higher frequencies. Here, however, the highest frequencies are contaminated by the folding in of energy from the inertial frequency due to improper model sampling (Jayne and Tokmakian 1997; and Chapter 2). At 36°N the annual peak is strong, as it is at 48°N as well. The highest frequency energy at both latitudes is again contaminated by aliased inertial oscillations.

4.5 Temporal decomposition

To gain another perspective of what is driving the heat transport variability, the contributions to the heat transport by time-mean and time-varying circulations and thermal fields are examined. For the time-mean and time varying components, the heat transport can be considered as:

$$
F(t) = \int\int_{-H(x)}^{0} \overline{v}\,\overline{\theta}\,dz\,dx + \int\int_{-H(x)}^{0} v'\,\overline{\theta}\,dz\,dx
$$
$$
+ \int\int_{-H(x)}^{0} \overline{v}\,\theta'\,dz\,dx + \int\int_{-H(x)}^{0} v'\,\theta'\,dz\,dx \qquad (4.1)
$$

where $\overline{\{\ \}}$ represents the time-mean of the quantity and $\{\ \}'$ the deviations from it. The first term on the left hand side of (4.1) corresponds to the time-mean velocity field advecting the time-mean temperature field; this is generally the heat transport owing to the steady ocean general circulation and its associated heat transport. The second term is related to the variations in the velocity field acting on the time-mean temperature field. The third term represents the time-mean velocity field advecting variations in the temperature field. Finally, the fourth term of (4.1) is the result of both variations in velocity and temperature. Since by definition, $\int\{\ \}'\,dt = 0$, the second and third terms of (4.1) do not contribute to the time-mean heat transport. However, the time-mean of the fourth term is not zero, and this is the rectified eddy heat transport which will be discussed in Section 4.8.

110

First, the heat transport variability due to velocity variations alone is considered. This corresponds to the second term on the right hand side of (4.1) and comprises the majority of the total variability (Fig. 4.10). Overall, its character is coherent over large spatial scales and is driven by the velocity variations in the Ekman layer and associated deep return flows.

Next, the heat transport fluctuations due to temperature variations are shown in Fig. 4.10c. Its character is different from that of the velocity variability as it shows much less high-frequency variability than the fluctuations due to the velocity fluctuations. In the tropical regions the annual cycle completely dominates the variability in the temperature, whereas the velocity has contributions from higher frequencies. In the tropics, the time-mean Ekman mass transport is away from the equator. Therefore, in the tropics south of the equator, the seasonal cycle of the surface temperature results in a southward heat transport anomaly during the austral summer when the upper layers warm and a northward anomaly in the austral winter as they cool. The same line of argument holds for the tropics north of the equator, where in the time-mean the surface waters flow north, there is a southward heat transport anomaly in boreal winter resulting from the cooling of the surface layers, and northward anomaly in boreal summer due to their warming. The strongest signal in the temperature-variability driven heat transport fluctuations comes in the Antarctic Circumpolar Current region. This signal is again related to the Ekman heat transport. The northward transport anomaly during the austral summer reaches 1 PW and is consistent with a warming of the northward flowing Ekman transport. The northern high latitudes do not show a similar strong seasonal cycle because of the much smaller area covered by the northern subpolar oceans.

Finally, the heat transport variability due to covarying temperature and velocity is considered. For now, the time-mean part of the heat transport due to rectification of covariations in the temperature and velocity will not be considered; it will be discussed in Section 4.8. The global zonal integral of the fourth term in (4.1), with its time-mean removed, is shown in Fig. 4.10d. The semi-annual cycle dominates, particularly in the tropics. This would result from the covariance of two out-of-phase annual cycles. Overall, however, it is a more complicated picture. At 40°S there is

111

a   Total meridional heat transport anomaly

b   Heat transport anomaly, velocity fluctuations

Figure 4.10: (a) Time-dependent heat transport anomaly for the World Ocean due to all variability. (b) Time-dependent heat transport anomaly for the World Ocean due to velocity variability. Vertical lines mark January 1.

112

c   Heat transport anomaly, temperature fluctuations

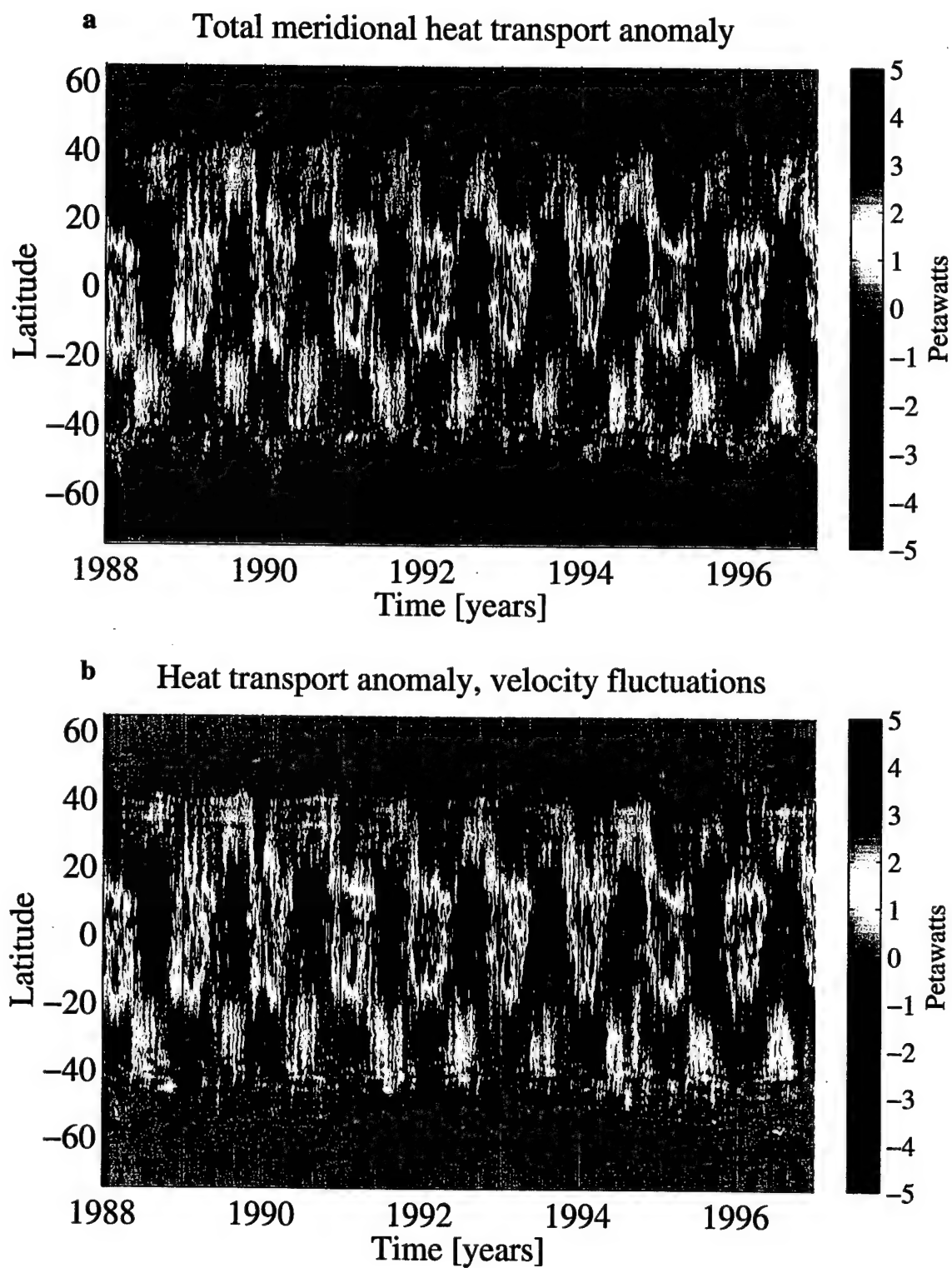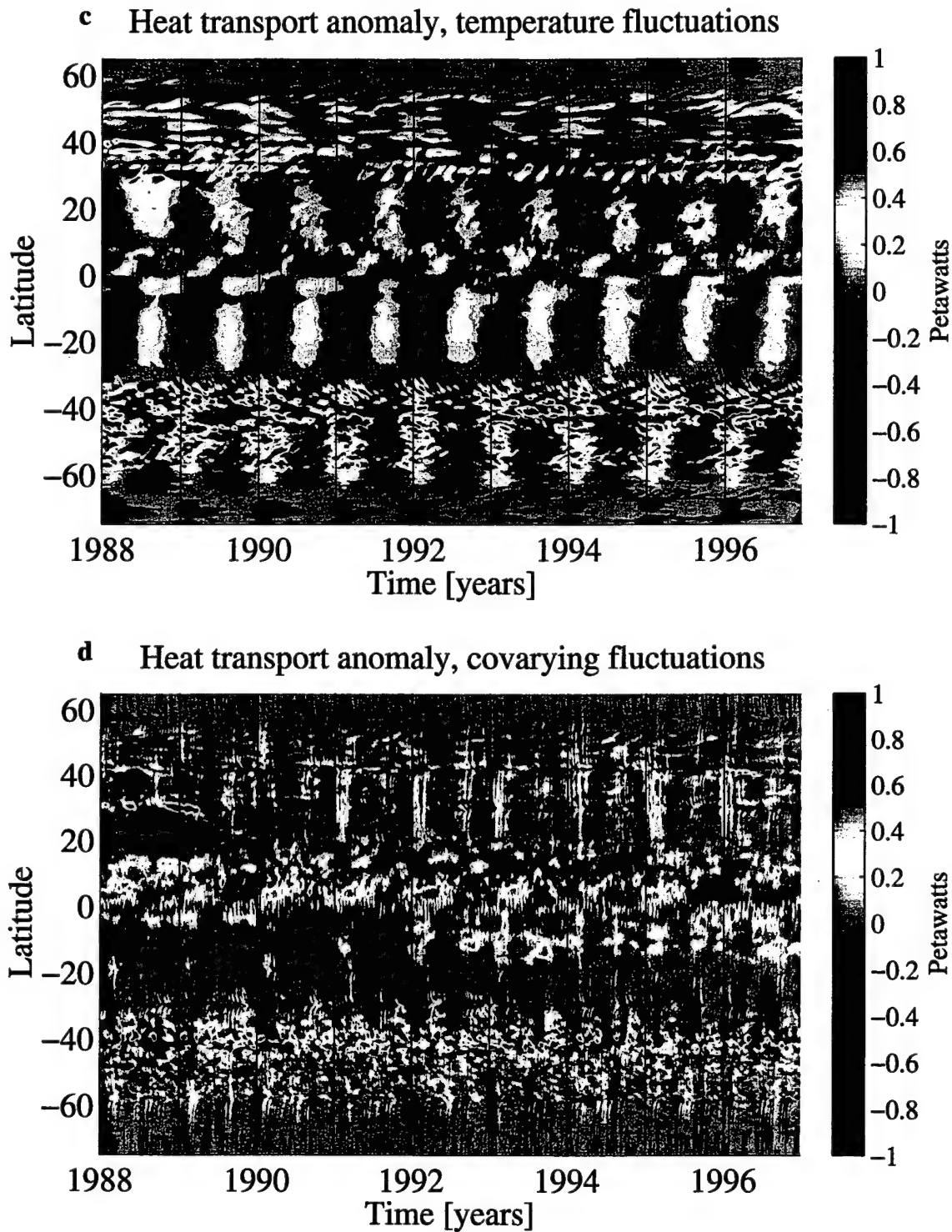**d**   Heat transport anomaly, covarying fluctuations

Figure 4.10: cont. (c) Time-dependent heat transport anomaly for the World Ocean due to temperature variability. (d) Time-dependent heat transport anomaly for the World Ocean due to co-varying velocity and temperature. Vertical lines mark January 1.

small band of high-frequency (around 5 cycles per year) of covarying temperature and velocity anomalies that is associated with Agulhas ring shedding events.

In summary, the time-dependent heat transport appears to be dominated by velocity variations in the surface Ekman layer. The temperature variability in the Ekman layer plays a weaker, but still significant role. The heat transport variations due to covarying Ekman layer transports and temperatures have the smallest contribution. The overall strengths of the individual contributions of the time varying components to the total time variation of the heat transport can be considered in terms of their fractional covariance. Given a signal composed of the three components:

$$F(t) = A(t) + B(t) + C(t) \qquad (4.2)$$

where each component has had its time-mean removed, the correlation is computed by:

$$\rho_A = \frac{\int F(t)A(t)\,dt}{\int F(t)^2\,dt}. \qquad (4.3)$$

It is trivial to show that $\rho_A + \rho_B + \rho_C = 1$. The correlations of three components of the heat transport variability given in (4.1) to the total heat transport variability are computed as a function of latitude and the result is shown in Fig. 4.11. The velocity variations alone account for a majority of the variability over most latitudes. The exception to this are the latitudes between $45° - 60°$S, where the temperature variations dominate; suggesting that the seasonal cycle of the thermal forcing is very important in determining the cycle of the heat transport in the Southern Ocean. Overall, the covarying velocity and temperature variations only weakly contribute to the total.

4.6 Dynamical decomposition

The heat transport can be decomposed into contributions associated with different dynamical regimes. Following Lee and Marotzke (1998), the meridional velocity as

114

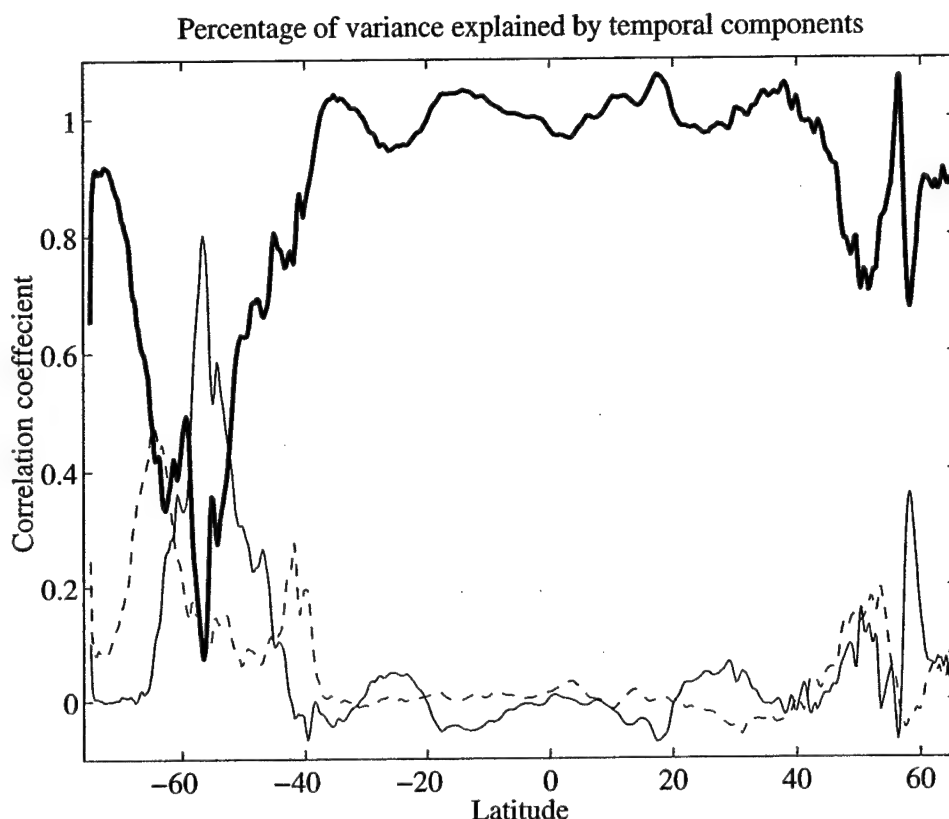Percentage of variance explained by temporal components

Figure 4.11: Correlation of each component of the heat transport variability with the total variability; the velocity variations with the time mean temperature (heavy solid line), the temperature variations with the time mean velocity (thin solid line) and the covarying velocity and temperature (dashed line). All three components sum to 1.

a function of depth is computed using (3.9) (see Section 3.6 for details). The heat transport associated with the dynamical components are equivalent to the "barotropic", "Ekman" and "baroclinic" components of Hall and Bryden (1982). The annual cycle associated with each of these components is shown in Fig. 4.12. The Ekman mode dominates the total variability, with the same characteristics as were discussed in the previous section. The contribution from the barotropic circulation is small everywhere. Interestingly, there is a region of strong compensation between the baroclinic heat transport and Ekman heat transport in the area around 10°N in the Indian Ocean that is related to the strong monsoonal cycle there. This feature can also be seen in the analysis of the Indian Ocean by Lee and Marotzke (1998).

The dynamical decomposition permits the separation of the Ekman heat trans-
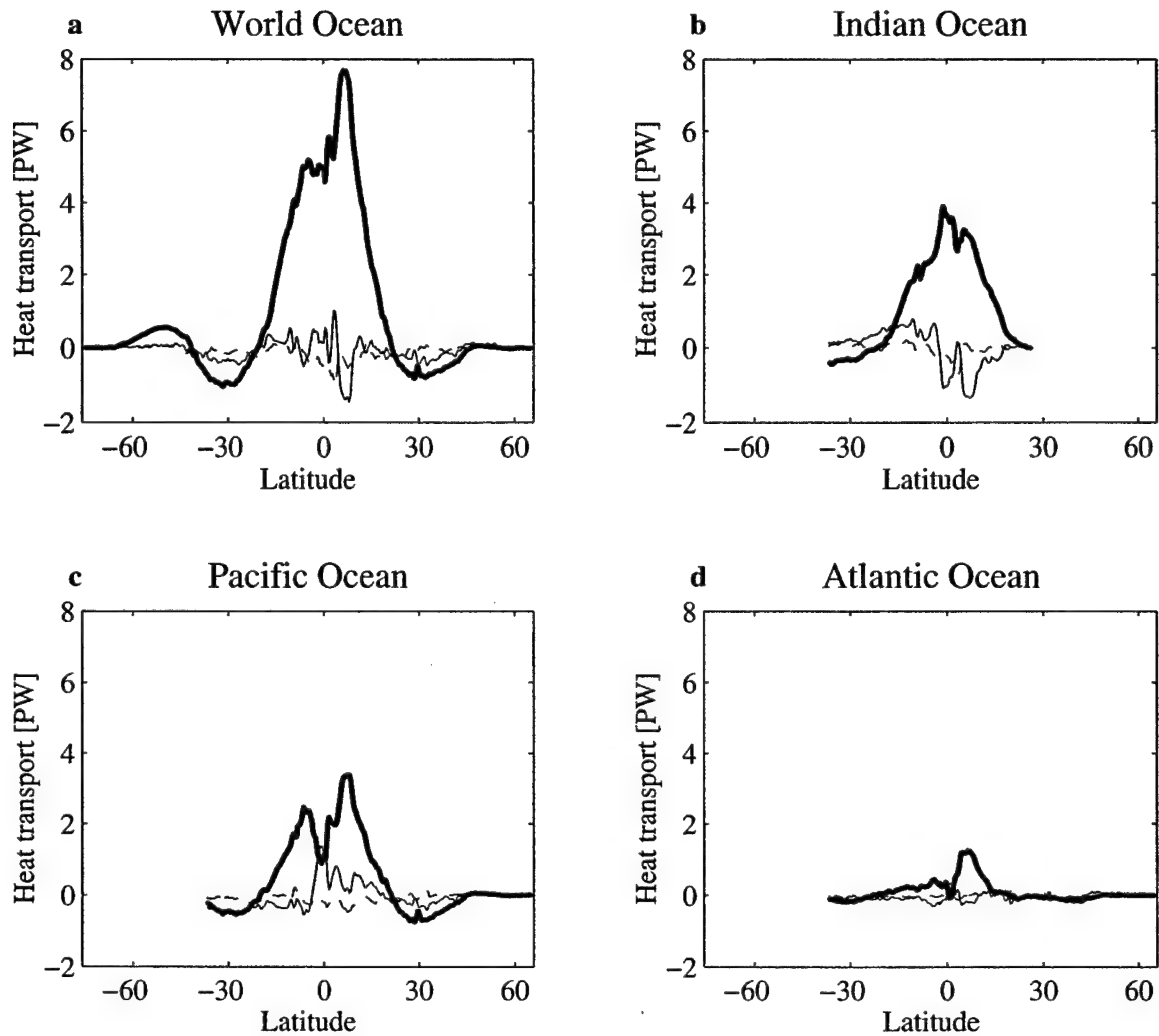
Figure 4.12: Annual cycle of heat transport associated with gyre circulation (dashed line), Ekman circulation (heavy solid line) and baroclinic shear flow (thin solid line) for the World Ocean, and the 3 ocean basins.

port from the rest of the time varying transport. The variance of the barotropic and baroclinic heat transport terms are calculated to investigate how well one-time hydrographic sections can measure the time-mean heat transport. The spacing between hydrographic stations is generally around 150 to 200 km for the IGY sections. The mesoscale eddy field is well-resolved neither in space nor in time by such sampling. The WOCE program was designed to have higher resolution sampling so that the mesoscale eddies would not be aliased in space. Fig. 4.13 shows the variance of the

non-Ekman (or barotropic plus baroclinic) heat transport. In the Atlantic Ocean, away from the equator, it is about 0.2 PW. The Pacific Ocean's mid-latitude variations are large, around 0.3 – 0.4 PW, as are those in the southern Indian Ocean. This suggests that the heat transport estimates made from hydrography using Hall and Bryden's (1982) method are good to within 0.2 – 0.4 PW.

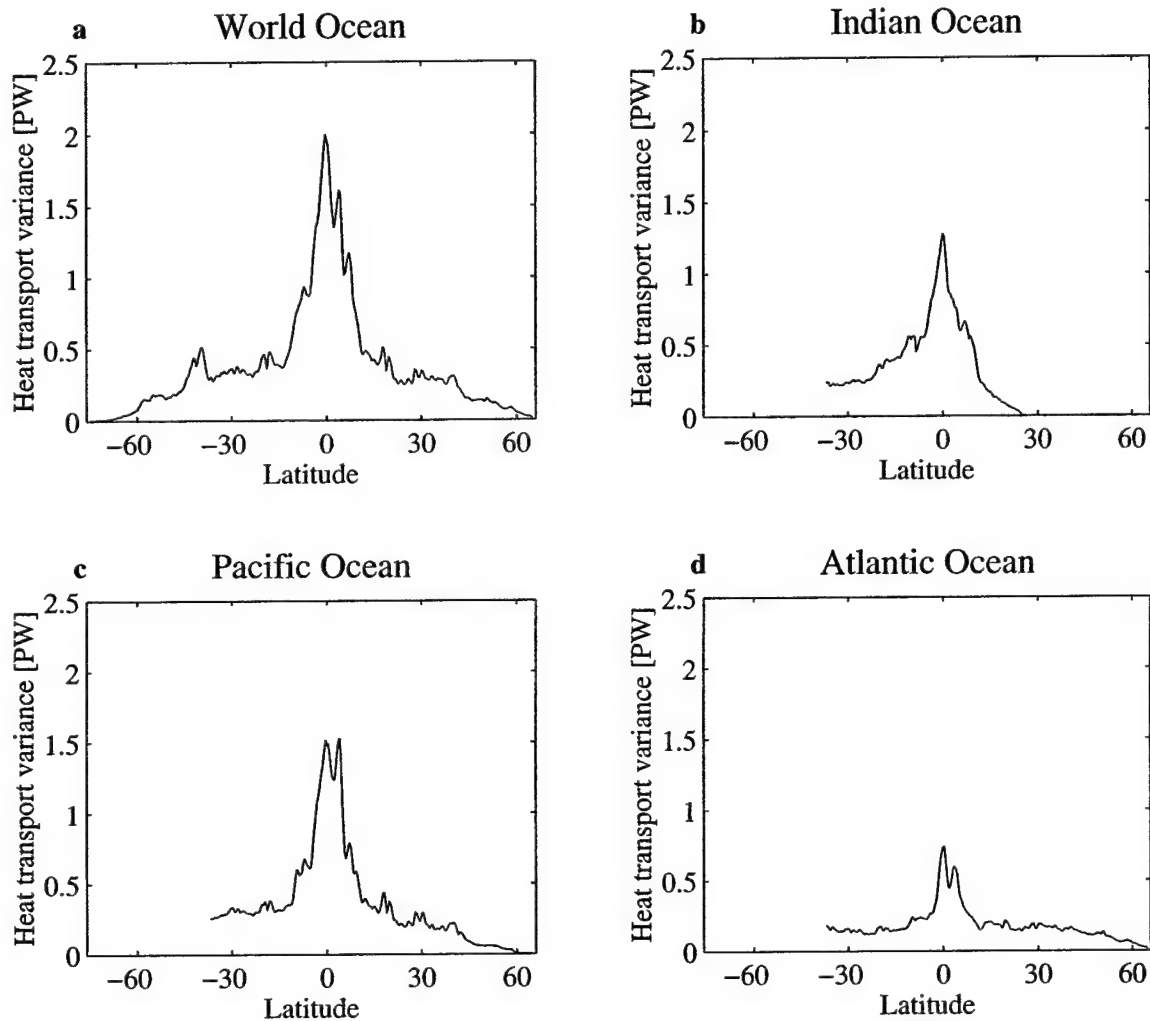Figure 4.13: Root-mean-square variability of heat transport due non-Ekman fluctuations for (a) the World Ocean, (b) the Indian Ocean, (c) the Pacific Ocean and (d) the Atlantic Ocean. The square root of the variance is in units of petawatts.

The contribution to the heat transport by the mesoscale eddy field can be estimated by the integral of the correlations in the deviations from the zonal mean

117

velocity and zonal mean temperature. Hall and Bryden (1982) further decomposed the baroclinic heat transport associated with the shear flow into the transport by the zonal mean of the shear flow and deviations away from it. Let v_{sh} be the baroclinic velocity at each point and be composed of the zonal average, $[v_{sh}]$, and deviations from that v_{sh}^*.

$$\iint v_{sh}\theta \, dx \, dz = \iint [v_{sh}][\theta] \, dx \, dz + \iint v_{sh}^* \theta^* \, dx \, dz, \qquad (4.4)$$

because the zonal integrals of v_{sh}^* and θ^* are zero. This is equivalent to what Hall and Bryden (1982) termed the "eddy contribution" to the heat transport. It is the smallness of the temporal variations in the eddy contribution to the heat transport that is essential to our ability to estimate the annual-mean ocean heat transport from compilations of one time hydrographic sections. If the temporal variability of the heat transport due to the the zonal structure of the section is large, then hydrographic surveys would be heavily aliased by the variability and hence be of limited usefulness. This is not the case however, as is shown in Fig. 4.14. The root-mean-square of the temporal fluctuations is small, of order 0.1 petawatts over the mid-latitude oceans. Its magnitude does increase in the tropics to 0.4 petawatts for the World Ocean. It is also about 0.4 petawatts in the Antarctic Circumpolar Current, centered around 40°S.

At 25°N in the Atlantic Ocean, Hall and Bryden (1982) found that the the eddy contribution to the heat transport was very small, 0.016 PW, compared to the total of 1.2 PW and that most of the baroclinic heat transport was carried by the large scale shear. However, the value of the eddy contribution was not a stable quantity, and they estimated that the term could be up to 15 times larger, or about 0.24 PW, which was 25% of the total heat transport. A more recent estimate by Baringer and Molinari (1999) finds a similar uncertainty of 0.26 PW for the same section. Here, this term has been considered in a different manner. Its temporal variability has been computed to estimate how reliable one time hydrographic sections are. At 25°N in the Atlantic, it has a root-mean-square variability of 0.05 PW, indicating that it is a very minor contributor to the time dependency of the heat transport. Away from the equator and Antarctic Circumpolar current, the eddy field appears to have little

118
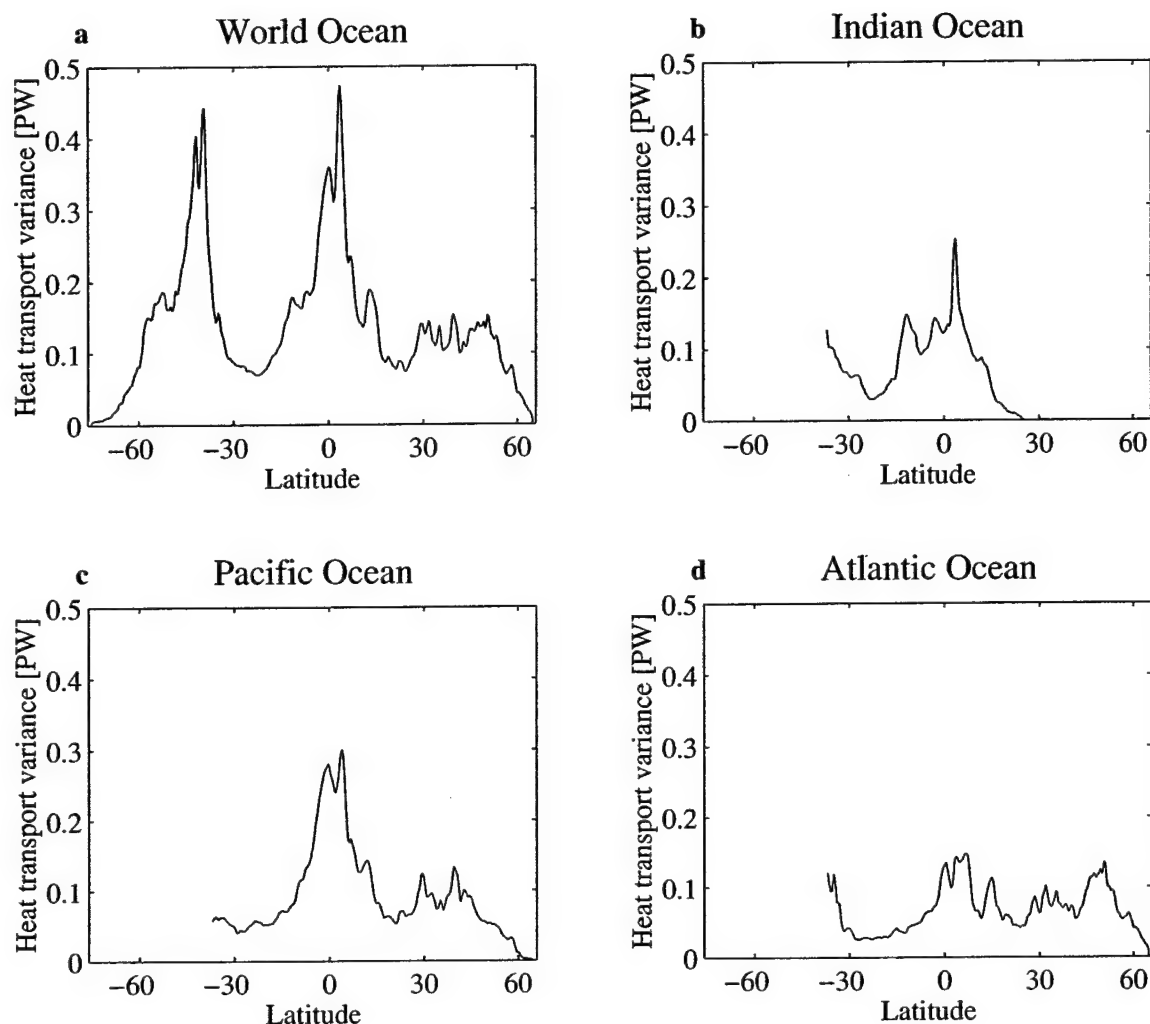
Figure 4.14: Root-mean-square variability of heat transport due to temporal changes in internal structure for (a) the World Ocean, (b) the Indian Ocean, (c) the Pacific Ocean and (d) the Atlantic Ocean. The square root of the variance is in units of petawatts.

impact on the time-dependency of the ocean heat transport. Further, it suggests that hydrographic sections do an adequate job of sampling the heat transport due to the baroclinic shear. It is important to bear in mind however, that the model is not adequately resolving the mesoscale eddy field, and therefore this result should be confirmed with a higher resolution model.

In summary, the temporal variability in the ocean heat transport is dominated by the Ekman heat transport. The deep compensating return flows have little shear

associated with them and therefore would not affect estimates of the heat transport from hydrographic surveys in any of the ocean basins, in agreement with the findings for the Atlantic Ocean of Böning and Herrmann (1994). The time-dependency of the heat transport associated with the barotropic and baroclinic structures is of order 0.2 – 0.4 PW away from the equatorial regions and the Antarctic Circumpolar Current. Therefore, this source of variability could cause temporal aliasing and is probably the largest uncertainty in the error budget for hydrographic surveys. It is concluded that while there is a large time-dependent signal in the ocean's transport of heat, it does not strongly contaminate estimates of the time-mean ocean heat transports made by hydrographic surveys.

4.7   The seasonal heat balance

Since the sources of the heat transport variability have been discussed, where the transported energy goes should be also considered by examining the seasonal heat budget. In addition to the heat transport terms discussed above, the change in ocean heat storage and the time-dependent surface heat flux were also computed from the model fields, so that the total heat balance could be examined. The surface boundary condition on temperature represents the thermal forcing in the model and is given by:

$$\frac{\partial T}{\partial t} = \frac{Q(t)}{\rho_0 c_p h} + \gamma^{-1}(T_{Lev}(t) - T), \qquad (4.5)$$

where T is the model's surface layer temperature, t is time, $Q(t)$ is the surface heat flux from the Barnier et al. (1995) climatology, ρ_0 is the reference density, c_p is the specific heat of sea water, h is the first model level thickness (25 m), γ is the restoring coefficient (30 days) and T_{Lev} is the temperature from the Levitus et al. (1994) climatology.

The overall heat balance for a zonally integrated section can be considered to consist of 4 terms:

$$-\frac{\partial \text{Heat storage}}{\partial t} = \frac{\partial \text{Advection}}{\partial y} + \text{Surface flux} + \text{Diffusive flux} \tag{4.6}$$

It can be readily shown by scaling that the explicit diffusive flux in the model is small compared to the other terms in (4.6). The diffusive flux of heat scales as:

$$\iint A_t \rho_0 c_p \nabla^4 \theta \, dx \, dz \sim \frac{A_t \rho_0 c_p H \Delta\theta}{r^3 (\Delta\phi)^3} \sim 10^7 \text{ W m}^{-1} \tag{4.7}$$

where A_t is the tracer diffusion coefficient, which in the POCM 4_B run is $5 \times 10^{11} \cos^{2.25}(\phi)$ m^4 s^{-1}, ρ_0 is 1025 kg m^{-3}, c_p is 3994 J (kg °C)$^{-1}$, H is the ocean depth, which for this scaling is 4000 m, $\Delta\theta$ is the change in temperature in the meridional direction, which for this discussion is assumed to be of order 0.1°C, r is the radius of the Earth and $\Delta\phi$ is the grid spacing in the meridional direction, which is 0.25°. Therefore, the diffusive flux of heat is order(10^7) W m^{-1} compared to other terms in the heat balance equation which are of order(10^9) W m^{-1}.

The seasonal component of the zonally integrated heat balance in shown in Fig. 4.15. It can be seen that in the tropics out to 20° the change in heat storage is balanced by the divergence of the advection, in agreement with results from the equatorial Atlantic of Merle (1980) and Böning and Herrmann (1994). The seasonal cycle is therefore different from the time-mean where the advective heat transport divergence is largely balanced by the surface flux. In this respect, most of the internal energy is moved around in the ocean, but little moves in and out, and its influence on climate is mollified. In the mid-latitudes the approximate balance is between the surface flux and the change in heat storage as predicted by theory (Gill and Niiler 1973) and confirmed by observations (Hsiung et al. 1989). In the middle-latitudes, the divergence of the heat transport does play a small, but not insignificant role in both hemispheres around 40°, consistent with the results of Hsiung et al. given the uncertainties in their calculation.

As can by seen in (4.5), the model's surface heat flux has two components, one the observed surface heat flux from the ECMWF, and the other a non-physical term
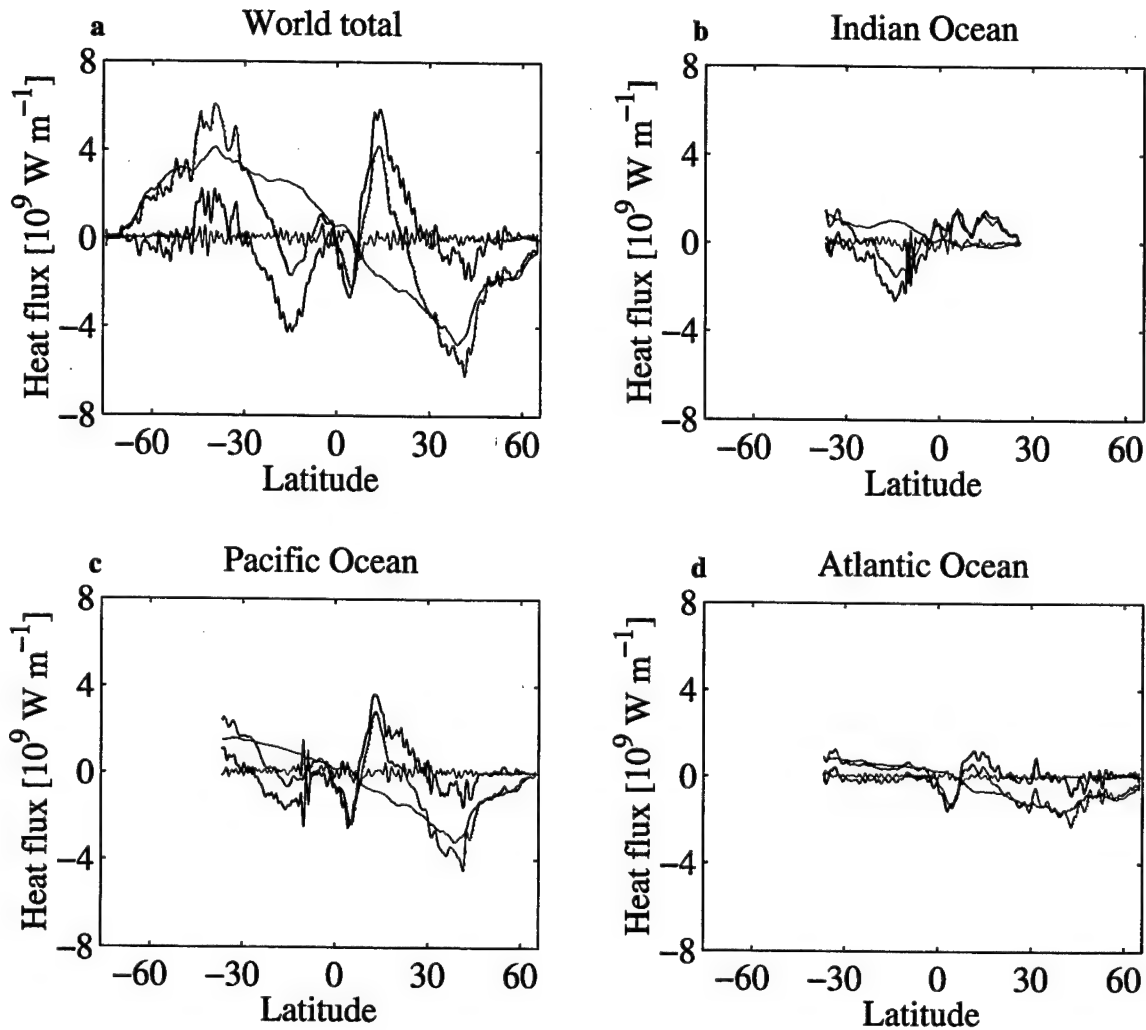
Figure 4.15: Seasonal heat balance for the zonally integrated (a) World Ocean, (b) Indian Ocean, (c) Pacific Ocean and (d) Atlantic Ocean. The blue line is the seasonal change in heat storage, the black line is the divergence of the advective heat transport, the red is the surface flux component, and the green line is the residual of the three terms. They are plotted such that the change in heat storage is equal to the sum of the divergence of the advective heat transport, the surface flux and the residual.

to keep the model realistic by restoring to the temperature climatology of Levitus et al. (1994). Considering their individual magnitudes allows the assessment of their relative importance to the model. Figure 4.16 shows the seasonal component of the surface flux due to forcing by Barnier et al. (1995) derived from ECMWF analyses and the seasonal component due to the restoring to the Levitus et al. (1994) climatology. The surface flux forcing is larger in magnitude than the restoring term, but they are
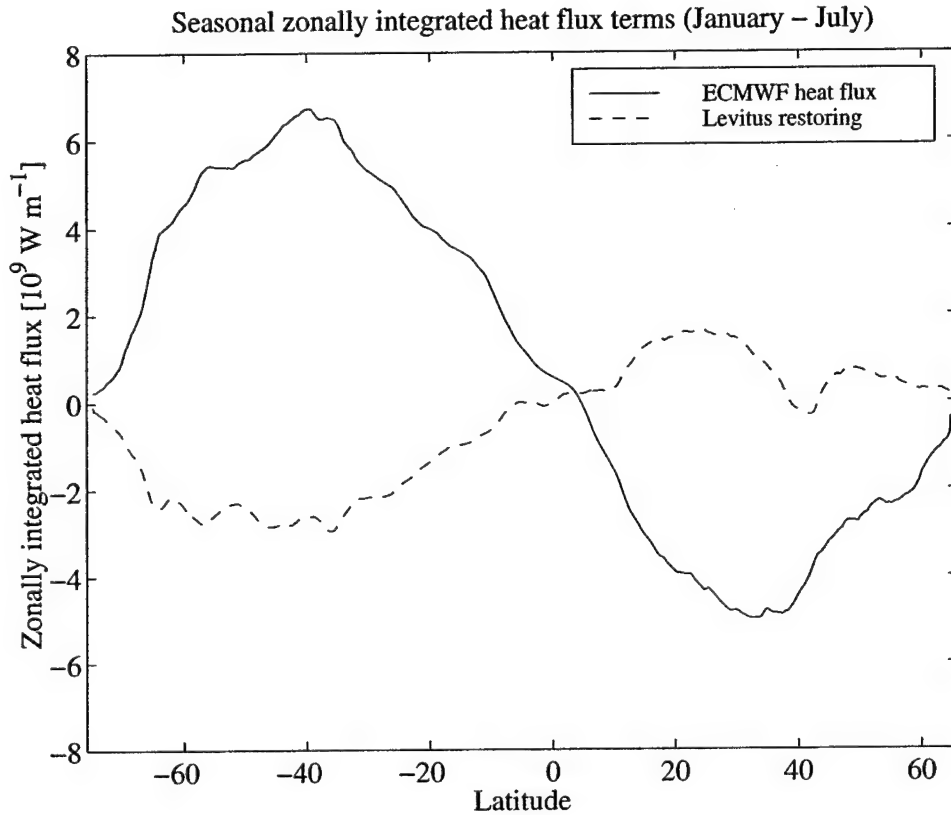
Figure 4.16: Seasonal component of the surface forcing decomposed into the surface heat flux from ECMWF and the restoring to the Levitus et al. (1994) climatology.

working in opposition to each other. Stammer et al. (1996) showed that this model simulation has a heat storage cycle which is too weak compared with observations. That the restoring to climatology opposes the surface heat flux while the seasonal heat storage is too weak indicates that the model is unable to sufficiently mix down into deeper layers the heat put into the surface layer by the surface flux. Presumably, the addition of a mixed layer parameterization to the POCM, would improve this situation and allow a more realistic representation of the heat storage consistent with the observed surface fluxes, with less reliance on the restoring to the Levitus et al. climatology.

4.8 Rectified variability

There exists an important term in the time-mean ocean heat transport which is due to the rectification of velocity and temperature anomalies. It has been the subject of much speculation and theoretical consideration because of the need to include it as a sub-grid scale parameterization in coarse resolution climate models (*e.g.* Gent and McWilliams 1990; Holloway 1992; Griffies 1998). Tests of these parameterizations have met with some success when applied to atmospheric data (Kushner and Held 1998) and ocean models (Böning et al. 1995; Rix and Willebrand 1996); however, little work has been done to date on investigating characteristics of the eddy heat transport. It is a three-dimensional vector quantity in the three spatial directions; latitude, longitude and depth and therefore, a very complicated field to analyze and discuss. It has been shown by previous studies (Stammer et al. 1996; McClean et al. 1997) that this model simulation's eddy energy is too weak but at least a factor of two when compared to the real ocean. It is hoped that while future higher resolution model runs may change the quantitative details presented here, in general the overall qualitative picture would remain similar (Cox 1985; Beckmann et al. 1994). Beckmann et al. found that increasing the resolution of their North Atlantic Ocean model did indeed change the eddy heat transport, but that the heat transport by the mean flow was also affected, however there was very little overall change in the heat transport. Therefore, one might expect that increased resolution might increase the magnitude of the eddy heat transport, but that its overall structure would be qualitatively similar. However, it remains to be seen whether this will be true. This work on the rectified eddy heat transport should be regarded as a demonstration of what analyses could be done on higher resolution, and hopefully more realistic, model runs to understand what the dynamics behind it are.

Unfortunately, the time-mean eddy heat transport is one of the most poorly observed quantities in the ocean. Wunsch (1999) recently compiled a collection of the available current-meter data in an attempt to assess its magnitude in the ocean. In general he found it was significant in the western boundary current regions of the Pacific and Atlantic Oceans. However, it was very small in the interior of the ocean

gyres. Stammer (1998) recently used satellite altimetry data to compute an eddy diffusivity, which he then combined with a temperature climatology to estimate the eddy heat transport. His results were again consistent with the picture that the eddy heat transport is large in the boundary currents and weak in the interior of the gyres. His analysis will be discussed in more detail later. The time-mean eddy heat transport has also been addressed by several regional studies some of which will be discussed later (Bryden 1979; Bryden and Heath 1985; Bryden and Brady 1989; Bower and Hogg 1996; Cronin and Watts 1996).

The time-mean eddy heat transport was calculated using the identity given by:

$$\overline{v'\,\theta'} = \overline{v\,\theta} - \overline{v}\,\overline{\theta} \tag{4.8}$$

where the overbar represents the time-mean and the prime deviations from it. This calculation was performed for both components of the velocity. We will consider the northward eddy heat transport in a few different manners: broken down by basin, by depth, by dynamical components, and finally as a function of longitude and latitude.

To begin, the zonal integral of the northward eddy heat transport for both the World Ocean and the individual ocean basins are compared to the heat transport by the mean circulation in Fig. 4.17, and then plotted together in Fig. 4.18. This is similar to the analysis done by Semtner and Chervin (1992) and McCann et al. (1995) on the 1/2° POCM run. The results are remarkably similar, though the eddy transport in the Antarctic Circumpolar Current is higher in the 1/4° run. Over the World Ocean, the eddy heat transport is a significant contributor to the total time-mean, particularly on either side of the equator, where there is a southward eddy heat transport of 0.9 PW at 5°N and 0.5 PW northward eddy heat transport at 5°S. There is a large convergent eddy heat transport at the equator, consistent with observations from current meter arrays by Bryden and Brady (1989) and Baturin and Niiler (1997) and modeling work by Philander et al. (1986). Farther from the equator there is a second peak in eddy heat transport, which is especially noticeable in the Indian Ocean south of the equator at around 15°S; it will be shown later that this is associated with an area of intense activity in the western half of the Indian Ocean. Another peak is in the Pacific Ocean at 15°N, also concentrated in the western part
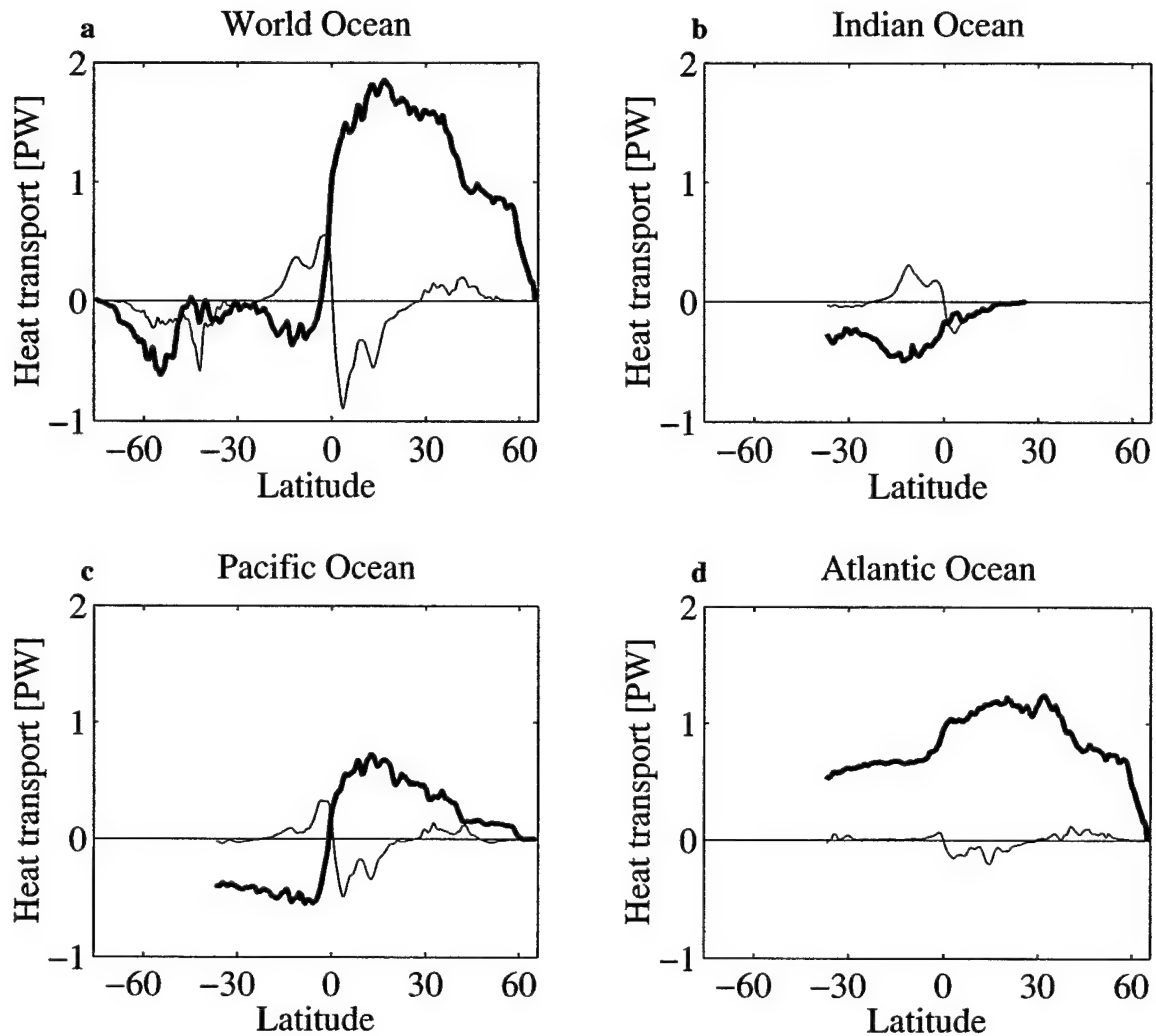
Figure 4.17: Zonally integrated total time-mean northward heat transport (heavy line) and eddy rectified portion of the total (thin line) for (a) the World Ocean, (b) the Indian Ocean, (c) the Pacific Ocean and (d) the Atlantic Ocean.

of the basin. Elsewhere, the eddy transport is large in the Southern Indian Ocean along the Antarctic Circumpolar Current, where approximately 0.6 PW of heat is carried southward by the eddies, which is the same order of magnitude as the time-mean heat transport there (Macdonald and Wunsch 1996). Overall, in the northern mid-latitudes, there is a small eddy heat transport of peak amplitude of 0.2 PW for the World Ocean.

Figure 4.19 shows how the eddy heat transport is distributed over four depth bins;

126

Figure 4.18: Zonally integrated northward eddy heat transport for World Ocean (heavy line), Indian Ocean (dashed-dotted line), Pacific Ocean (dashed line) and Atlantic Ocean (light solid line).
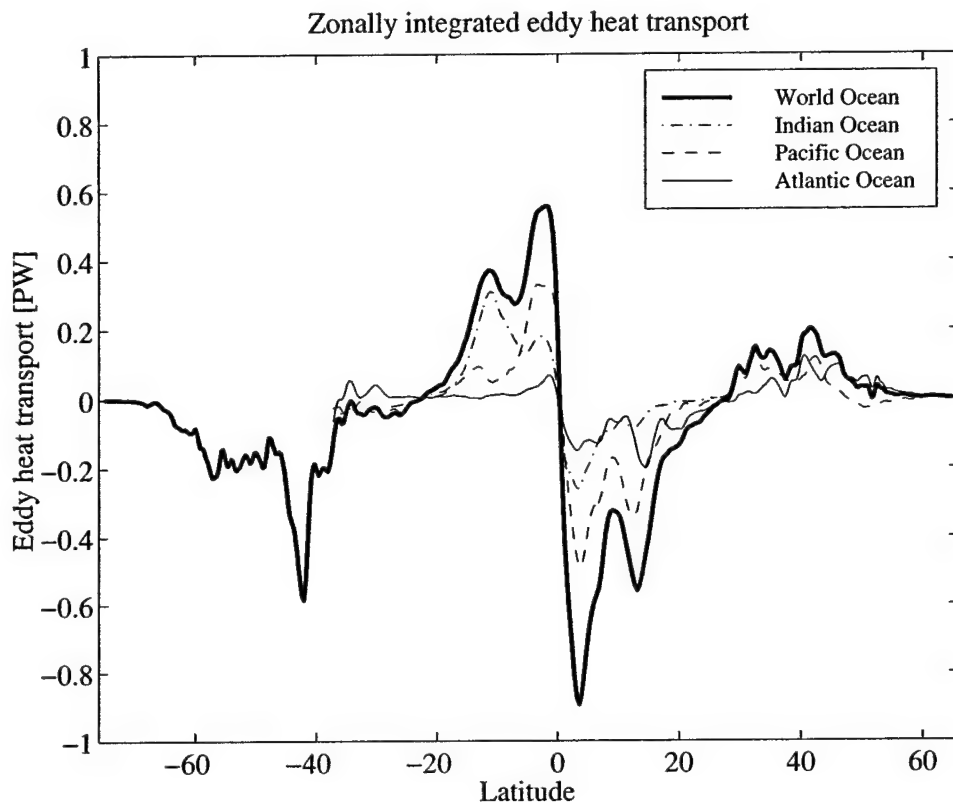
the model surface layer (0 – 25 m), the near surface (25 – 985 m), the mid-depths (985 – 2750 m), and the the deep ocean (2750 – 5200 m). Several features stand out. First, most of the the eddy heat transport is contained in the near surface (0 – 985 m), this is particularly true in the equatorial regions and in the Antarctic Circumpolar Current. Second, there is a broad scale eddy heat transport over the mid-latitudes of both hemispheres in the surface (0 – 25 m) layer of order 0.1 PW. Finally, the two deepest depth bins account for very little of the eddy heat transport despite their covering about 75% of the total ocean depth, the exception being that the mid-depth range (985 – 2750 m) has a small but significant contribution near the equator. Wunsch (1999) in his quasi-global estimate of eddy heat transports from current meter data also found that the majority of the eddy heat transport was confined to the upper 1000 m.
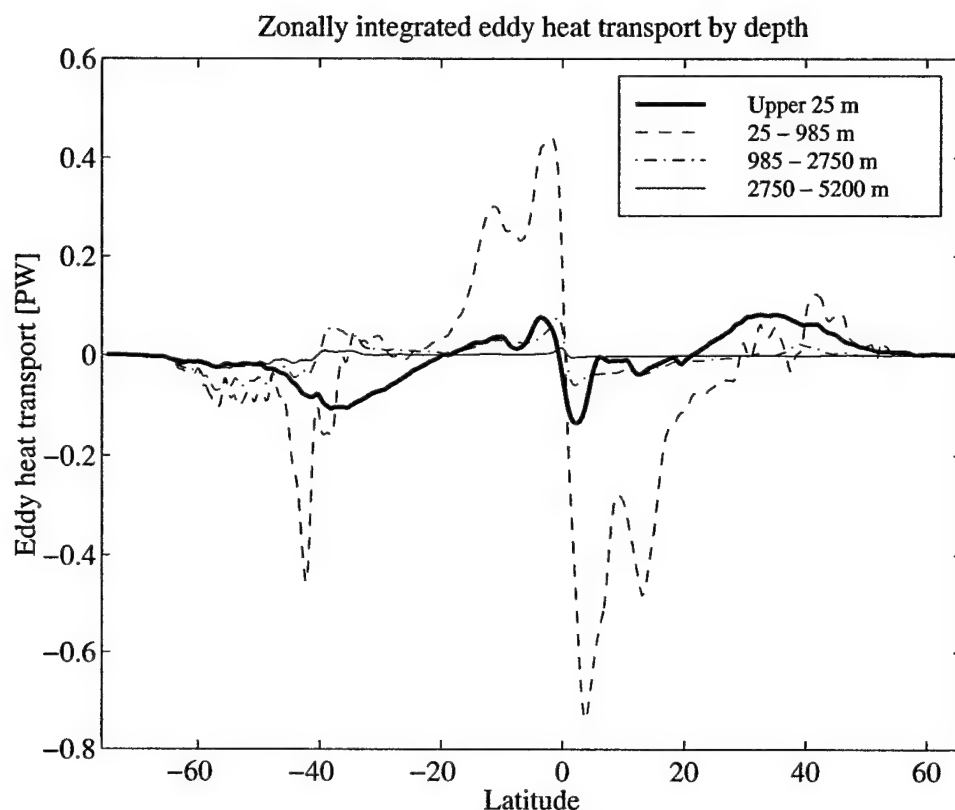
Figure 4.19: Zonally integrated northward eddy heat transport broken down by depth bin, for top 25 m (heavy solid line), 25 – 985 m (dashed line), 985 – 2750 m (dashed-dotted line) and 2750 – 5200 m (light solid line).

Finally, we can consider the eddy heat transports due to each of the dynamical overturning components. Figure 4.20 shows the zonal basin integrals of the eddy heat transport for the 4 components of the overturning decomposition in (3.9) and (4.4). There is an eddy heat transport associated with the Ekman component that is about 0.1 PW in the mid-latitudes and looks remarkably similar to the eddy heat transport in the upper 25 m of the ocean. This distribution suggests two important conclusions: The first is that there is a small, order 0.1 PW, rectified eddy heat transport due to covarying Ekman layer transports and temperature fluctuations not being fully in quadrature. The second is that the majority of the eddy heat transport is associated with the deviations from the zonal mean in the baroclinic shear term. The confinement of the eddy heat transport to the upper 1000 m and its association with the deviations in the baroclinic shear intimate that baroclinic processes are the

dominant process. The barotropic component also contributes strongly to the eddy heat transport in the Antarctic Circumpolar Current, implying that barotropic eddies interacting with topography may also play a role there.

Eddy heat transport associated with dynamical components
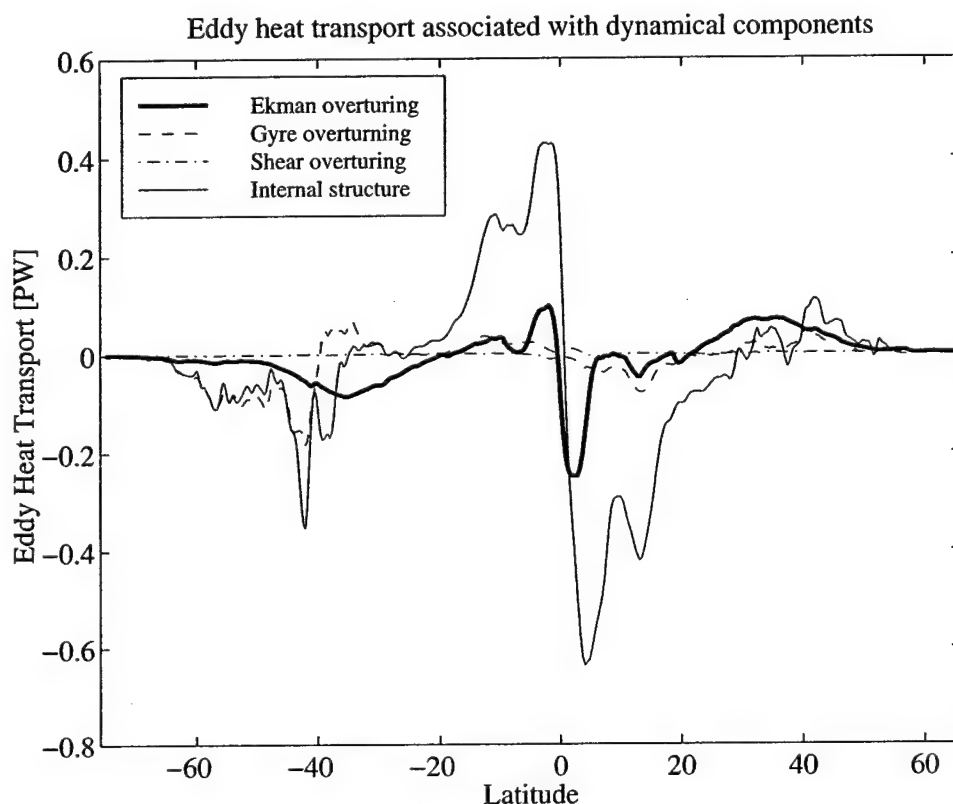
Figure 4.20: Eddy transport decomposed by dynamical component, for the Ekman over-turning (heavy solid line), the barotropic component (dashed line), the zonal mean shear (dashed-dotted line) and the internal shear structure (thin solid line).

4.8.1 A meandering jet

So far only the zonal integral of the northward component of the eddy heat transport has been considered; however, the depth-integrated eddy heat transport is a two-dimensional vector quantity in space. Figure 4.21 shows the depth integrated vector eddy transport for the region of the Gulf Stream off the eastern coast of the United States. This particular region was chosen for its general interest as well as its historical current-meter coverage. While there are obvious model deficiencies in

129

this area, notably that the Gulf Stream tends to follow the coast too tightly and it separates too far north of Cape Hatteras, there are some qualitative conclusions that can be drawn by comparing the eddy-heat-transport field to observations. The SYNOP arrays which were located in the Gulf Stream at 55°W, the data from which were discussed by Bower and Hogg (1996), and, at 68°W, analyzed by Cronin and Watts (1996). Both these studies found significant eastward (downstream) eddy heat transport with small meridional (cross-stream) eddy heat transports, consistent with the overall behavior of the model.

As was discussed by Marshall and Shutts (1981), the eddy heat transport is composed of two different dynamical components; the rotational and the divergent. The rotational component does not contribute to the globally-integrated poleward transport of heat by the oceans. Therefore, to examine the eddy heat transport in more detail, it was broken into its two parts. The distribution of the rotational flux and divergent flux must be determined globally, they are not locally defined. This was done numerically by taking the divergence of the eddy heat transport, inverting the divergence with a Laplacian inverter with Neumann boundary conditions (no heat transport through the lateral boundaries) to find a potential function, and then taking the gradient to recover the vector quantities for the divergent part of the eddy heat transport. This is summarized in the following relations:

$$\overline{\mathbf{v}'\theta'} = (\overline{\mathbf{v}'\theta'})_D + (\overline{\mathbf{v}'\theta'})_R \tag{4.9}$$

$$(\overline{\mathbf{v}'\theta'})_D = \nabla\nabla^{-2}(\nabla \cdot \overline{\mathbf{v}'\theta'}), \tag{4.10}$$

or

$$\nabla^2\phi = \nabla \cdot \overline{\mathbf{v}'\theta'} \tag{4.11}$$

and

$$\overline{\mathbf{v}'\theta'}_D = \nabla\phi, \tag{4.12}$$

since by definition:

$$\nabla \cdot (\overline{v'\theta'})_R = 0, \tag{4.13}$$

where $(\overline{v'T})$ is the depth integrated, vector eddy heat transport, $(\overline{v'\theta'})_D$ is the divergent component of the eddy heat transport and $(\overline{v'\theta'})_R$ is the rotational component. The rotational component was calculated independently from the following:

$$(\overline{v'\theta'})_R = \hat{k} \times \nabla\nabla^{-2}(\hat{k} \cdot \nabla \times \overline{v'\theta'}), \tag{4.14}$$

or

$$\nabla^2 \psi = \hat{k} \cdot \nabla \times \overline{v'\theta'} \tag{4.15}$$

and

$$\overline{v'\theta'}_R = \hat{k} \times \nabla\psi, \tag{4.16}$$

given that:

$$\nabla \times (\overline{v'\theta'})_D = 0. \tag{4.17}$$

As can be seen in Fig. 4.21, the rotational component dominates the total in the Gulf Stream region. There appears to be a southward eddy heat transport to the south of the jet axis which is consistent with a down-gradient transport as the meridional temperature gradient reverse sign south of the Gulf Stream in the model, and is consistent with the eddy driving mechanism in the southern recirculation gyre of the Gulf Stream proposed by Bryden (1982).

The strength of the rotational eddy transport compared to the divergent eddy transport requires explanation. Consider a coherent meandering jet, *e.g.* the Gulf Stream or the Antarctic Circumpolar Current. In such jets, the meandering mode of the jet can dominate the eddy energy. Indeed, in the Gulf Stream, more than 2/3 of the eddy kinetic and potential energy is due to the meandering of the jet (Rossby 1987; Hogg 1994). If the temperature and velocity have distributions which are set by the following relations, as they would in a geostrophic jet:
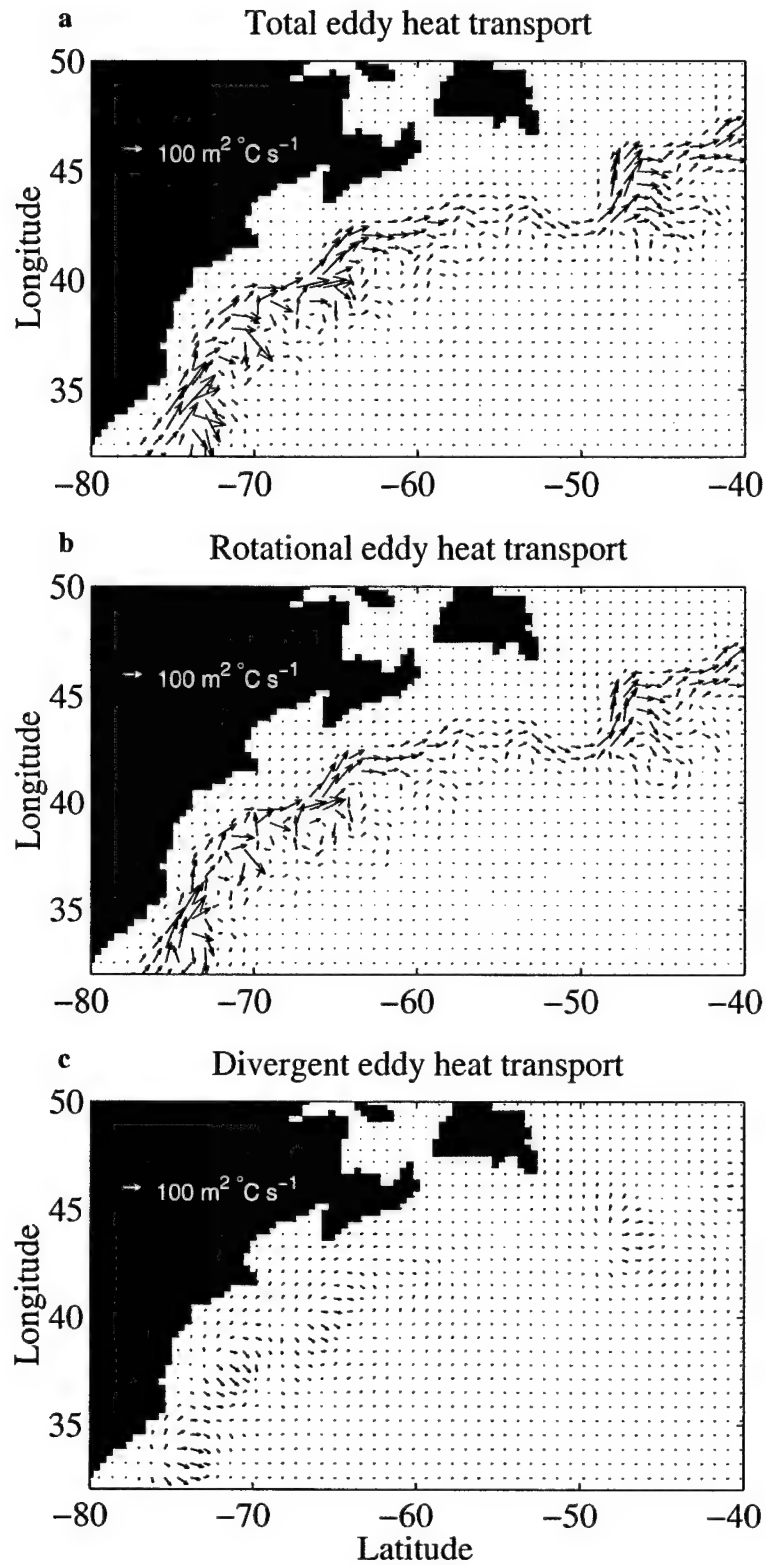
131

Figure 4.21: Vector eddy transport for the Gulf Stream region, for (a) the total vector eddy transport, (b) the rotational component and (c) the divergent component. Shown at 1/2 resolution.

132

$$u = -\frac{\partial \psi(\xi)}{\partial y} \qquad v = \frac{\partial \psi(\xi)}{\partial x} \qquad \theta = \theta(\xi) \tag{4.18}$$

$$\psi = \psi_0 \mathcal{F}(\xi) \qquad \theta = \theta_0 \mathcal{F}(\xi) \tag{4.19}$$

where θ is the temperature, u, v are the eastward and northward velocities given by the streamfunction, ψ. $\mathcal{F}$ is an arbitrary function, and ξ is the spatial and temporal distribution function for the jet. For example, the "Bickley" jet with a standing wave in it would have a streamfunction with the form:

$$\psi(\xi) = \psi_0 \tanh\left[\frac{y}{L} + \frac{\lambda}{L}\sin\left(\frac{2\pi x}{l}\right)\sin\left(\frac{2\pi t}{\tau}\right)\right] \tag{4.20}$$

where:

$$\xi = \xi(x, y, t) = \frac{y}{L} + \frac{\lambda}{L}\sin\left(\frac{2\pi x}{l}\right)\sin\left(\frac{2\pi t}{\tau}\right) \tag{4.21}$$

with the variables x, y, t describing space and time, L being the half-width of the jet, λ the meander amplitude, l the meander wave length and τ the meander period.

The rectified eddy heat transports can then be written as the temporal average over a eddy period:

$$\overline{u'\theta'} = \frac{1}{\tau}\int_0^\tau u\,\theta\,dt - \frac{1}{\tau^2}\int_0^\tau u\,dt\int_0^\tau \theta\,dt$$
$$\overline{v'\theta'} = \frac{1}{\tau}\int_0^\tau v\,\theta\,dt - \frac{1}{\tau^2}\int_0^\tau v\,dt\int_0^\tau \theta\,dt \tag{4.22}$$

or, in terms of the functional forms:

133

$$\overline{u'\theta'} = \frac{1}{\tau}\int_0^\tau -\frac{\partial\psi}{\partial y}\,\theta\,dt - \frac{1}{\tau^2}\int_0^\tau -\frac{\partial\psi}{\partial y}\,dt\int_0^\tau \theta\,dt$$

$$\overline{v'\theta'} = \frac{1}{\tau}\int_0^\tau \frac{\partial\psi}{\partial x}\,\theta\,dt - \frac{1}{\tau^2}\int_0^\tau \frac{\partial\psi}{\partial x}\,dt\int_0^\tau \theta\,dt \tag{4.23}$$

The divergence of the rectified eddy heat flux is given by:

$$\nabla\cdot\overline{\mathbf{v}'\theta'} = \frac{\partial\overline{u'\theta'}}{\partial x} + \frac{\partial\overline{v'\theta'}}{\partial y} \tag{4.24}$$

which, when written in terms of the functional forms, gives:

$$\nabla\cdot\overline{\mathbf{v}'\theta'} = \frac{\partial}{\partial x}\left[\frac{1}{\tau}\int_0^\tau -\frac{\partial\psi}{\partial y}\,\theta\,dt - \frac{1}{\tau^2}\int_0^\tau -\frac{\partial\psi}{\partial y}\,dt\int_0^\tau \theta\,dt\right]$$

$$+ \frac{\partial}{\partial y}\left[\frac{1}{\tau}\int_0^\tau \frac{\partial\psi}{\partial x}\,\theta\,dt - \frac{1}{\tau^2}\int_0^\tau \frac{\partial\psi}{\partial x}\,dt\int_0^\tau \theta\,dt\right] \tag{4.25}$$

Applying Leibniz's rule and the product rule:

$$\nabla\cdot\overline{\mathbf{v}'\theta'} = \frac{1}{\tau}\int_0^\tau -\frac{\partial^2\psi}{\partial x\partial y}\,\theta\,dt + \frac{1}{\tau}\int_0^\tau -\frac{\partial\psi}{\partial y}\frac{\partial\theta}{\partial x}\,dt$$

$$- \frac{1}{\tau^2}\int_0^\tau -\frac{\partial^2\psi}{\partial x\partial y}\,dt\int_0^\tau \theta\,dt - \frac{1}{\tau^2}\int_0^\tau -\frac{\partial\psi}{\partial y}\,dt\int_0^\tau \frac{\partial\theta}{\partial x}\,dt$$

$$+ \frac{1}{\tau}\int_0^\tau \frac{\partial^2\psi}{\partial y\partial x}\,\theta\,dt + \frac{1}{\tau}\int_0^\tau \frac{\partial\psi}{\partial x}\frac{\partial\theta}{\partial y}\,dt$$

$$- \frac{1}{\tau^2}\int_0^\tau \frac{\partial^2\psi}{\partial y\partial x}\,dt\int_0^\tau \theta\,dt - \frac{1}{\tau^2}\int_0^\tau \frac{\partial\psi}{\partial x}\,dt\int_0^\tau \frac{\partial\theta}{\partial y}\,dt \tag{4.26}$$

Canceling like terms leaves:

$$\nabla\cdot\overline{\mathbf{v}'\theta'} = \frac{1}{\tau}\int_0^\tau -\frac{\partial\psi}{\partial y}\frac{\partial\theta}{\partial x}\,dt - \frac{1}{\tau^2}\int_0^\tau -\frac{\partial\psi}{\partial y}\,dt\int_0^\tau \frac{\partial\theta}{\partial x}\,dt$$

$$+ \frac{1}{\tau}\int_0^\tau \frac{\partial\psi}{\partial x}\frac{\partial\theta}{\partial y}\,dt - \frac{1}{\tau^2}\int_0^\tau \frac{\partial\psi}{\partial x}\,dt\int_0^\tau \frac{\partial\theta}{\partial y}\,dt \tag{4.27}$$

Using the chain rule, *i.e.* $\frac{\partial \psi}{\partial x} = \frac{\partial \xi}{\partial x} \frac{\partial \psi}{\partial \xi}$, etc., yields:

$$
\begin{aligned}
\nabla \cdot \overline{\mathbf{v}' \theta'} &= \frac{1}{\tau} \int_0^\tau -\frac{\partial \xi}{\partial y} \frac{\partial \psi}{\partial \xi} \frac{\partial \xi}{\partial x} \frac{\partial \theta}{\partial \xi} \, \mathrm{d}t - \frac{1}{\tau^2} \int_0^\tau -\frac{\partial \psi}{\partial y} \, \mathrm{d}t \int_0^\tau \frac{\partial \theta}{\partial x} \, \mathrm{d}t \\
&+ \frac{1}{\tau} \int_0^\tau \frac{\partial \xi}{\partial x} \frac{\partial \psi}{\partial \xi} \frac{\partial \xi}{\partial y} \frac{\partial \theta}{\partial \xi} \, \mathrm{d}t - \frac{1}{\tau^2} \int_0^\tau \frac{\partial \psi}{\partial x} \, \mathrm{d}t \int_0^\tau \frac{\partial \theta}{\partial y} \, \mathrm{d}t
\end{aligned} \tag{4.28}
$$

Canceling the first and third terms:

$$
\nabla \cdot \overline{\mathbf{v}' \theta'} = -\frac{1}{\tau^2} \int_0^\tau -\frac{\partial \psi}{\partial y} \, \mathrm{d}t \int_0^\tau \frac{\partial \theta}{\partial x} \, \mathrm{d}t - \frac{1}{\tau^2} \int_0^\tau \frac{\partial \psi}{\partial x} \, \mathrm{d}t \int_0^\tau \frac{\partial \theta}{\partial y} \, \mathrm{d}t \tag{4.29}
$$

Expanding the functional forms for the temperature and streamfunction:

$$
\begin{aligned}
\nabla \cdot \overline{\mathbf{v}' \theta'} &= \frac{\theta_0 \psi_0}{\tau^2} \int_0^\tau \frac{\partial \mathcal{F}}{\partial y} \, \mathrm{d}t \int_0^\tau \frac{\partial \mathcal{F}}{\partial x} \, \mathrm{d}t - \frac{\theta_0 \psi_0}{\tau^2} \int_0^\tau \frac{\partial \mathcal{F}}{\partial x} \, \mathrm{d}t \int_0^\tau \frac{\partial \mathcal{F}}{\partial y} \, \mathrm{d}t \\
&= 0.
\end{aligned} \tag{4.30}
$$

Therefore, it is shown that there is no divergent part of the rectified eddy heat transport due to a meandering jet, regardless of its relative functional form and irrespective of its meander mode. All of the rectified eddy heat transport due to a coherent meandering structure is therefore rotational. To illustrate this, consider the eddy heat transport for two examples of meandering. The first is a standing wave pattern in a jet, and the second is a traveling wave structure that grows in amplitude and then decays. The standing wave pattern is given by (4.21) and is shown in Fig. 4.22. The meandering jet which has a standing wave in it has an eddy heat transport that is a series of highs and lows. While the temperature gradient is directed in only one direction across the jet, the cross-stream eddy heat transport varies in direction along the jet. It can be said that the eddy heat transport is not directly associated with the cross-stream temperature gradient.
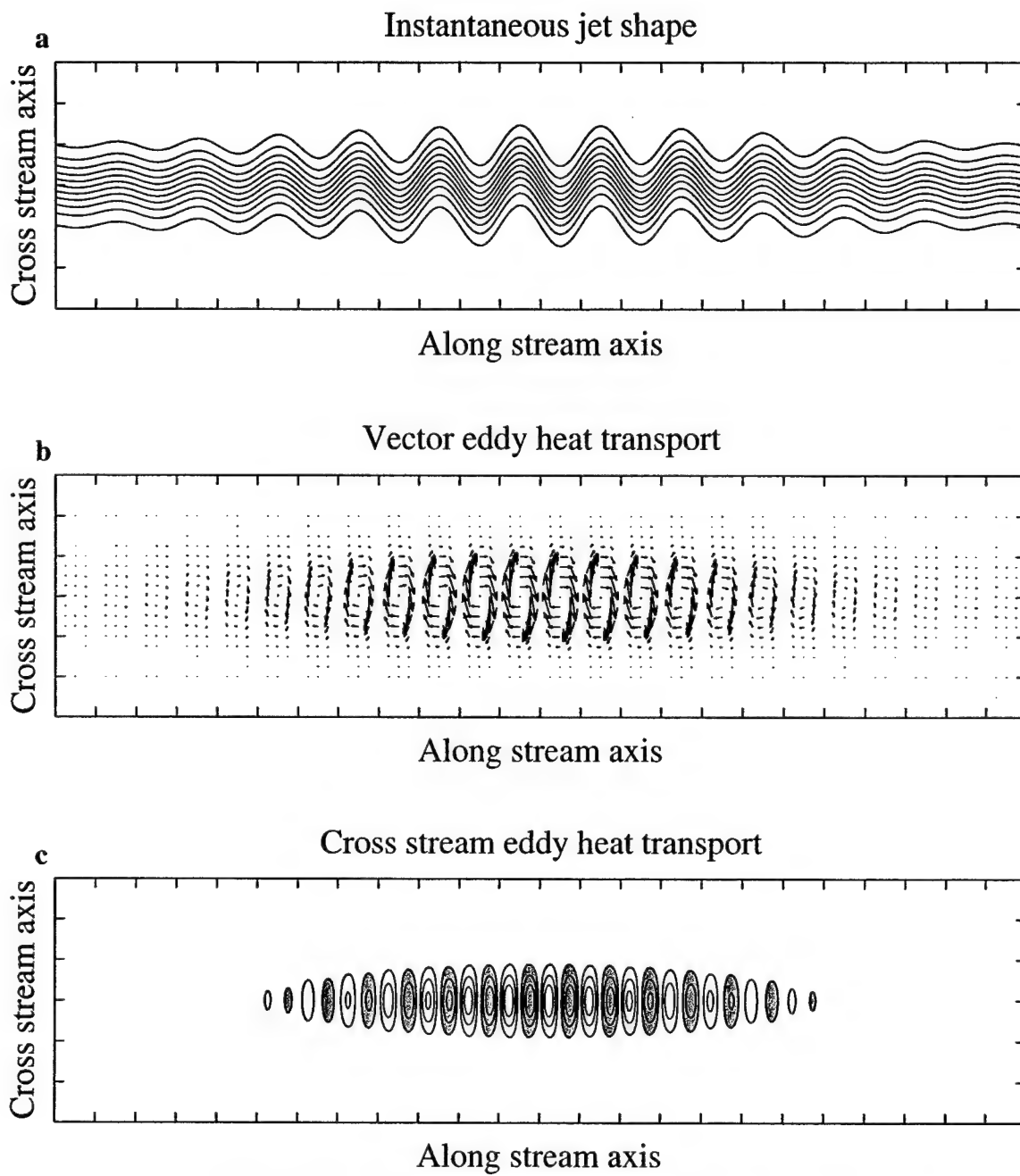
Figure 4.22: (a) Instantaneous streamfunction and temperature for jet with standing wave pattern in it. (b) Eddy heat transport vectors. (c) Cross-stream heat transport magnitude, black contours indicate heat transport in the positive cross-stream direction, gray-shaded contours indicate opposite direction.

Instantaneous jet shape

Cross stream axis

Along stream axis

Vector eddy heat transport

Cross stream axis

Along stream axis

Cross stream eddy heat transport
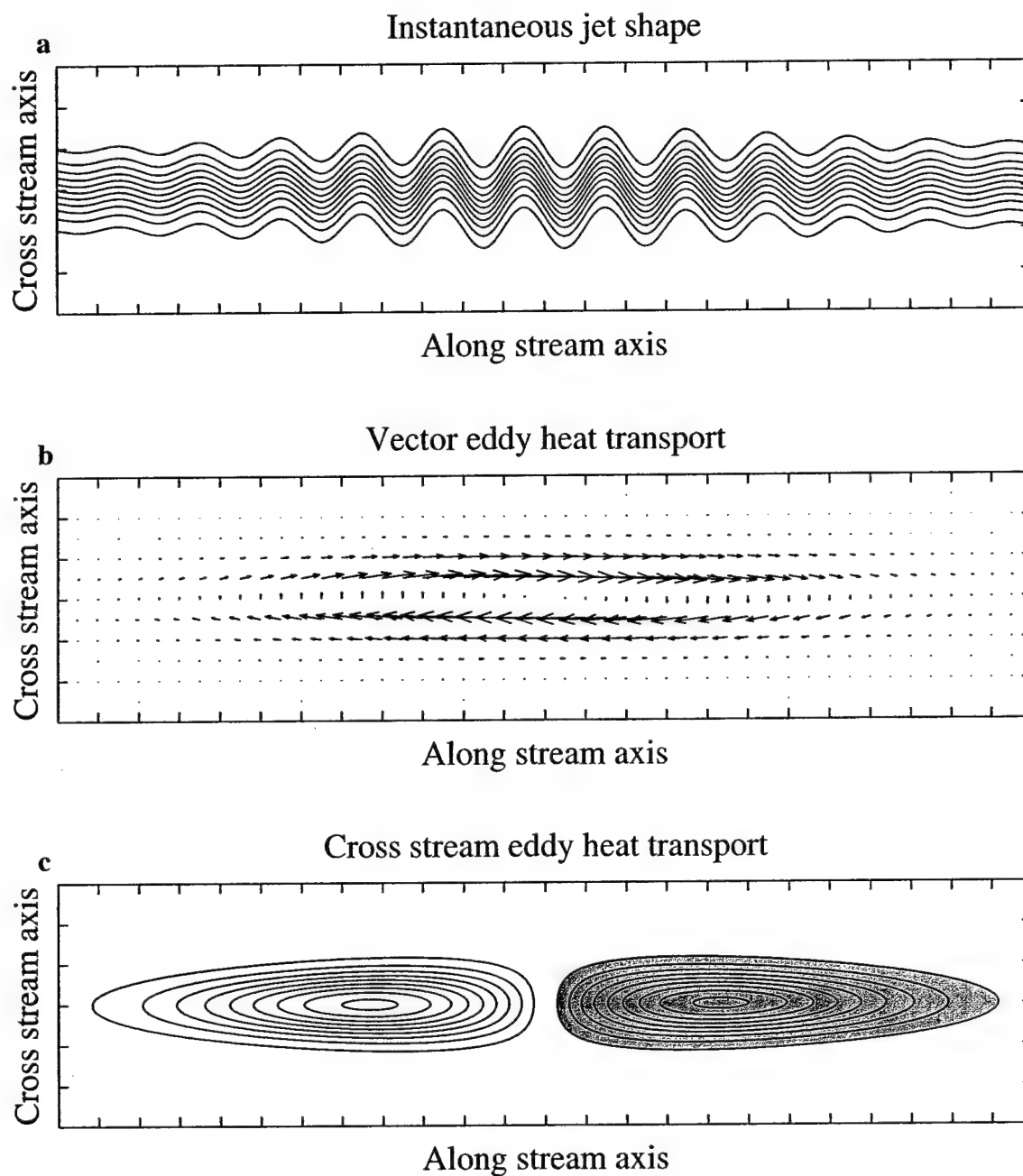
Cross stream axis

Along stream axis

Figure 4.23: (a) Instantaneous streamfunction for jet with growing and decaying translating waves in it. (b) Eddy heat transport vectors. (c) Cross-stream heat transport magnitude, black contours indicate heat transport in the positive cross-stream direction, gray-shaded contours indicate opposite direction.

137

The second example is jet structure in which a traveling wave grows and then decays. This was the behavior discussed by Marshall and Shutts (1981). Its meander spatial and temporal form could be given by a function like:

$$\xi(x, y, t) = \frac{y}{L} + \frac{\lambda}{L} e^{-x^2/\Lambda^2} \sin\left(\frac{2\pi x}{l} - \frac{2\pi t}{\tau}\right)$$ (4.31)

As can be seen by comparing Fig. 4.23 with Fig. 4.22, despite the jets having very similar instantaneous jet shapes, their eddy statistics are very different. In Fig. 4.23, the series of highs and lows are replaced by a single dipole. Again the heat transport is only rotational. Contrasting Fig. 4.22 and Fig. 4.23, it can be seen that the rotational component of the eddy transport can make analyses of the eddy heat transport using scattered current meters very difficult.

4.8.2   The global distribution of eddy transport

The global picture of the eddy heat transport is now considered. The POCM's total eddy heat transport is shown with its rotational and divergent components in Fig. 4.24a–c. For clarity only the northward component is drawn. The model's eddy heat transport can be compared to an estimate of the eddy heat transport made using an eddy diffusivity derived from altimetry data by Stammer (1998) in Fig. 4.24d. The zonal basin integrals of the eddy heat transports for POCM and Stammer's (1998) estimates are shown in Fig. 4.25. Stammer's (1998) analysis is derived from an eddy transfer of temperature, for which the eddy diffusivity was derived from TOPEX/POSEIDON measurements and combined with a climatological temperature field (Levitus et al. 1994) to compute the eddy transport. This analysis assumes that temperature is fluxed down-gradient by Fickian-like processes. The eddy heat transport is given by:

$$\overline{v'\theta'} = -\kappa \nabla_h \overline{\theta}$$ (4.32)

138

where $\overline{\theta}$ is the time-mean temperature from Levitus et al.'s (1994) climatology averaged over the upper 1000 m. The eddy transfer coefficient, κ, was calculated from:

$$\kappa(x, y) = 2 \ \alpha \ K_E(x, y) \ T_{alt}(x, y). \tag{4.33}$$

where the eddy kinetic energy, K_E, and the eddy mixing timescale, T_{alt}, were calculated from TOPEX/POSEIDON observations and α, the mixing efficiency, was deduced from current meter observations to be 0.005.

Stammer's (1998) estimate should be considered to be a calculation of only the divergent eddy heat transport, and as such should be compared to the divergent part of the POCM eddy heat transport. If κ were constant, there would be only a divergent component. However, the rotational part of Stammer's (1998) estimate is still minor, since the curl of a diffusive flux is small according the following:

$$\begin{aligned} \nabla \times \overline{\mathbf{v}'\theta'} &= -\nabla \times \kappa\nabla\overline{\theta} \\ &= \kappa\nabla \times \nabla\overline{\theta} + \nabla\kappa \times \nabla\overline{\theta}. \end{aligned} \tag{4.34}$$

The first term of the right hand side of (4.34) is by definition zero, and the second term of (4.34) is small since $\nabla\kappa$ and $\nabla\overline{\theta}$ tend to be oriented in the same direction. This is opposed to the divergent part of the diffusive flux, given by:

$$\begin{aligned} \nabla \cdot \overline{\mathbf{v}'\theta'} &= -\nabla \cdot \kappa\nabla\overline{\theta} \\ &= \kappa\nabla^2\overline{\theta} + \nabla\kappa \cdot \nabla\overline{\theta}. \end{aligned} \tag{4.35}$$

where the $\kappa\nabla^2\overline{\theta}$ term dominates since κ and $\nabla^2\overline{\theta}$ are both maximum in magnitude along the baroclinic fronts.

a Total meridional depth integrated eddy heat transport
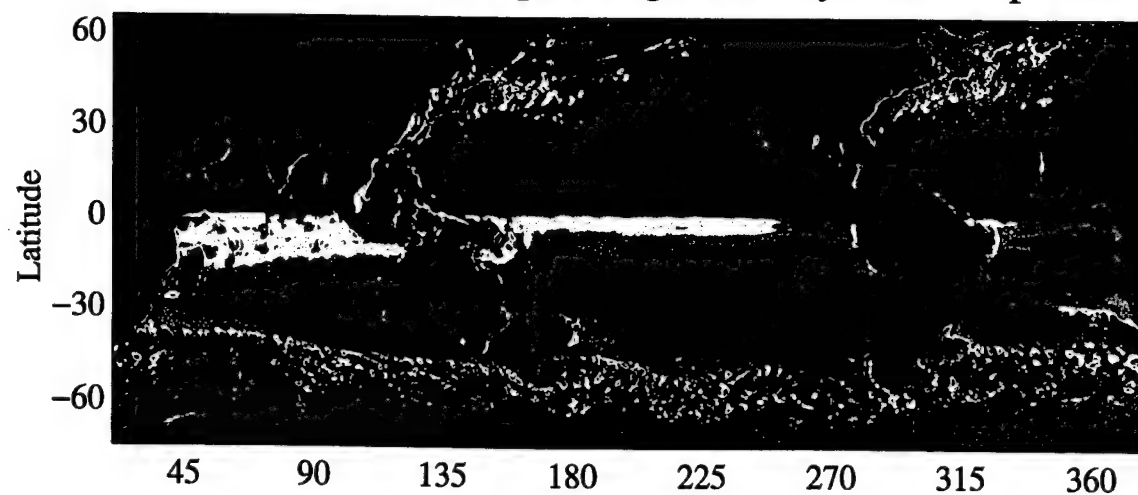
b Rotational meridional depth integrated eddy heat transport
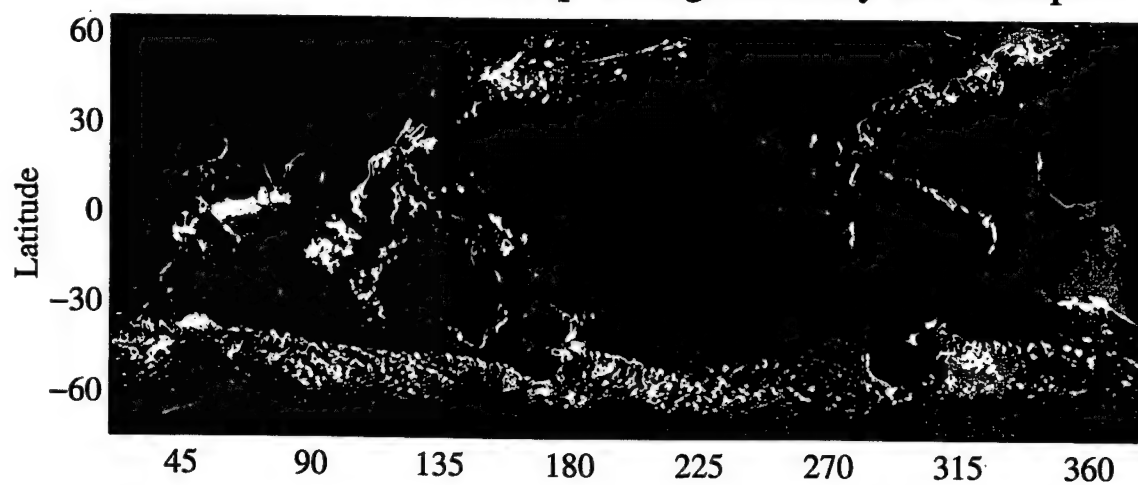
c Divergent meridional depth integrated eddy heat transport
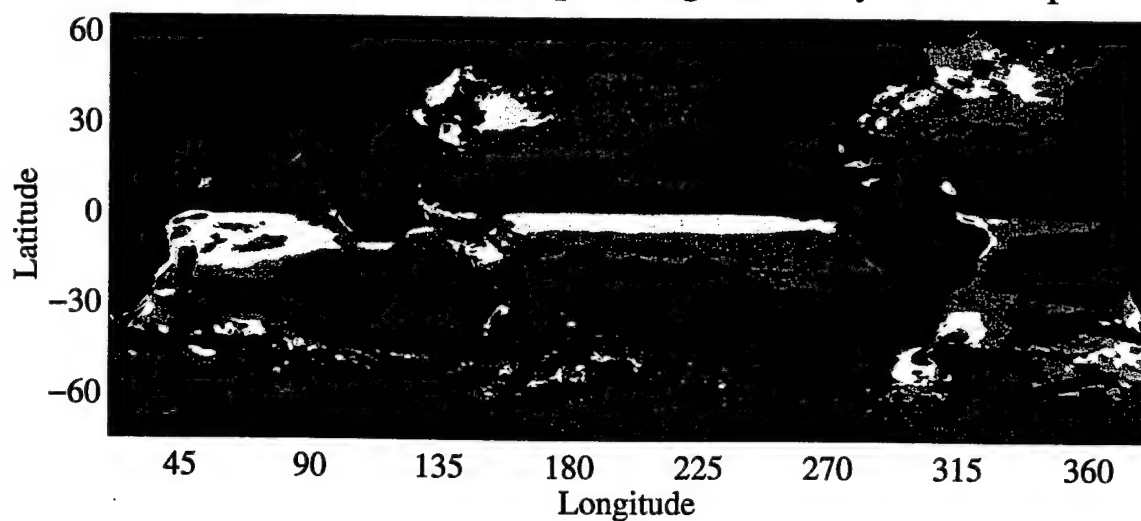
Longitude

d   Stammer (1998) eddy heat transport from TOPEX/POSEIDON
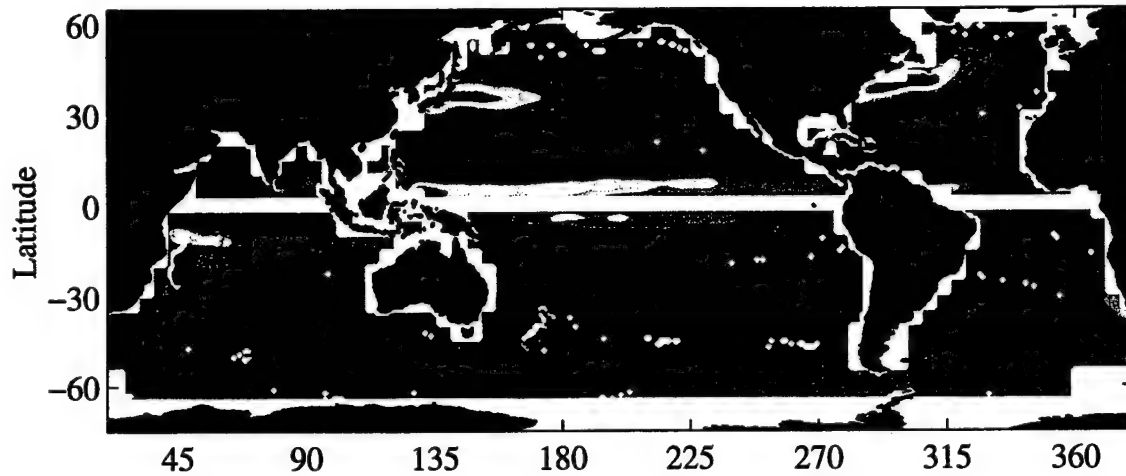
e   POCM eddy-diffusivity derived eddy heat transport
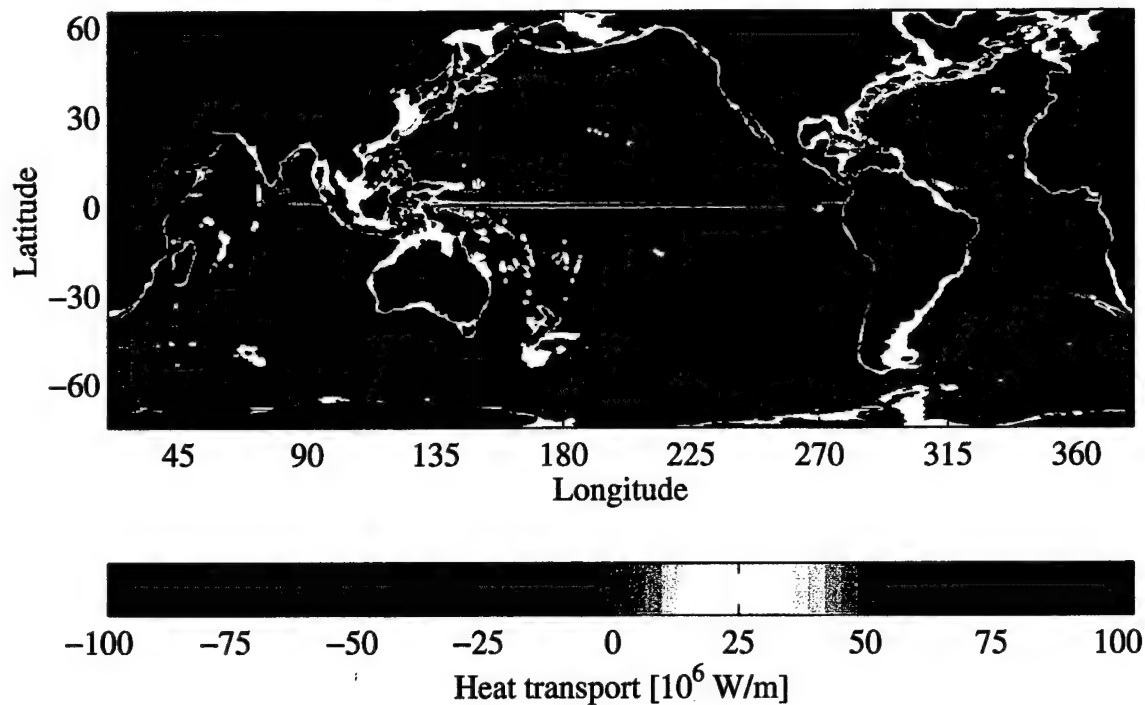
Figure 4.24: (a) Total, depth integrated, northward eddy heat transport as a function of latitude and longitude. (b) Rotational component of depth integrated eddy heat transport. (c) Divergent component of depth integrated eddy heat transport. (d) Estimate of eddy heat transport by Stammer (1998) using TOPEX/POSEIDON data. (e) Estimate of eddy heat transport using Stammer's (1998) method with POCM. Colorbar extends from -1×10^8 to 1×10^8 W m^{-1}.
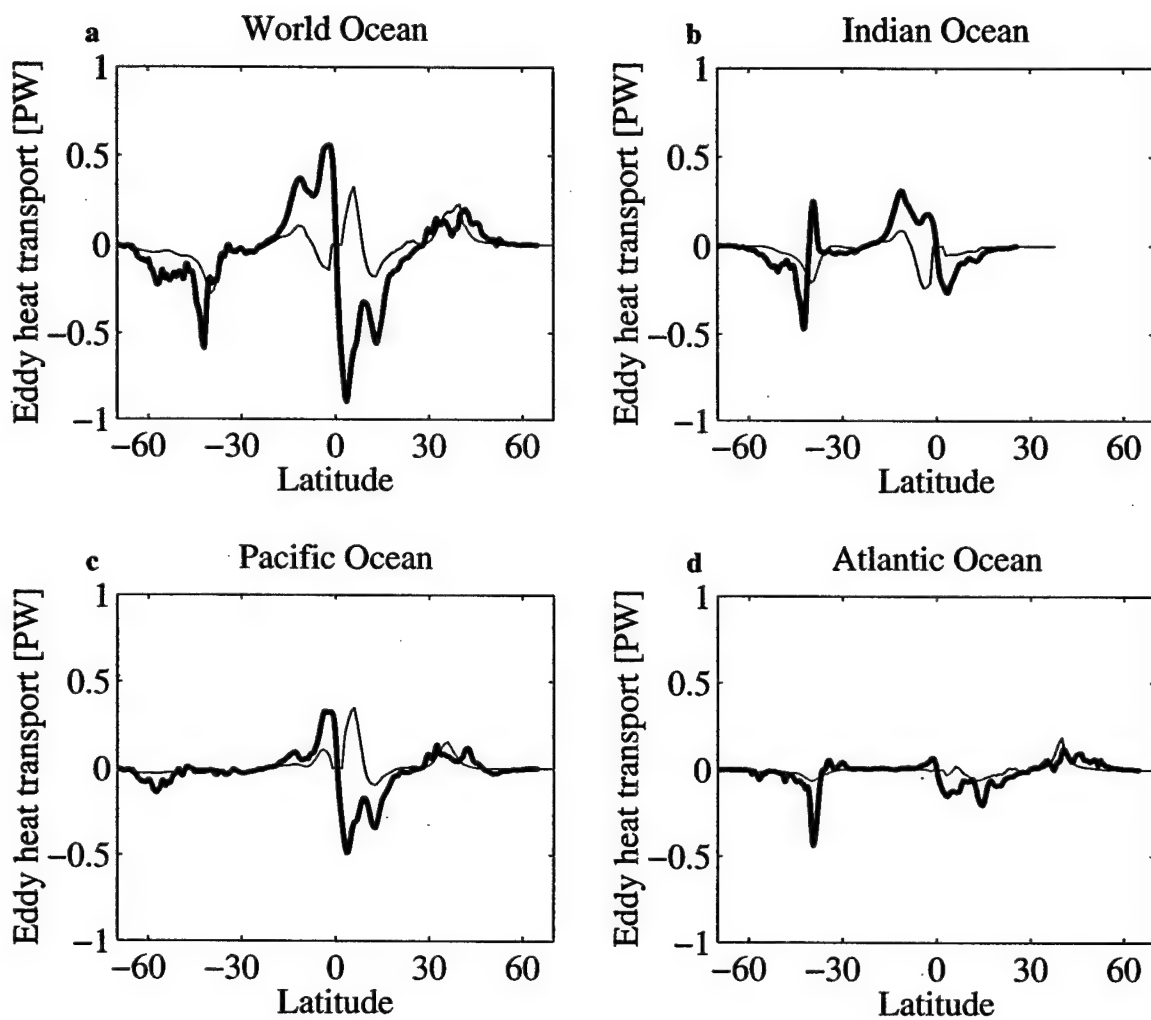
Figure 4.25: (a) Zonally integrated eddy heat transport over the World Ocean for POCM (heavy line) and Stammer (1998) (light line). (b) Same but for Indian Ocean, (c) Pacific Ocean and (d) Atlantic Ocean. The heat transport scale is in petawatts.

A preliminary examination of the POCM's eddy heat transport compared to Stammer's (1998) estimate shows some distinct similarities and differences between the two. First, the POCM shows a convergent eddy heat transport along the equator which is completely lacking in the Stammer (1998) calculation. Second, the Antarctic Circumpolar Current shows a significant southward eddy heat transport in both estimates, though there is some discrepancy in its magnitude. Third, Stammer (1998) found a strong and widespread northward eddy heat transport across both the Gulf Stream and the Kuroshio, that is not observed in the model. Despite all the differences there are some general similarities; in particular the weak eddy heat transports in the centers of the ocean gyres seems to be robust and is supported by Wunsch's (1999) current meter compilation. On a final note, Stammer's (1998) analysis does not include the eddy heat transport due to rectification of Ekman layer variability, but it is a small contribution (order 0.1 PW) to the total and can be computed separately from the wind stress and Ekman layer temperature from climatologies.

To understand the differences between Stammer's (1998) estimate of the eddy heat transport and the POCM's eddy heat transport, his method is applied to the POCM's time-varying sea-surface height field and time-mean temperature field. If the result of this calculation agrees well with the model's directly estimated eddy heat transport, then it would indicate that Stammer's (1998) method is a robust way to calculate the eddy heat transport. If it does not, then it suggests that his method may not correctly predict the eddy transports. The resulting estimate (Fig. 4.24e) is very similar in character to Stammer's (1998) estimate and is very unlike the model's actual eddy heat transport in many parts of the ocean, and it implies that the method used by Stammer (1998) is not appropriate. Additionally, this can be considered a test of the model's simulation of the ocean's eddy field. The model, at least qualitatively, appears to be reproducing the large-scale eddy patterns observed by TOPEX/POSEIDON, as it gives nearly the same result for the eddy diffusivity derived using Stammer's (1998) method. Some possible reasons for the differences in the two eddy heat transports will be discussed below.

There are three regimes to where the model's eddy heat transport will be compared to Stammer's (1998) estimate in detail. The first is in the Southern Ocean.

The two estimates of the eddy heat transport in the Antarctic Circumpolar Current (ACC) region are generally consistent, though the model estimate is larger there, 0.6 PW in the POCM versus what Stammer (1998) considers to be a lower bound for the ACC of 0.3 PW. The amplitude of the eddy heat transport across the ACC is consistent with the estimate of 0.45 ± 0.3 PW from de Szoeke and Levin (1981), but is somewhat larger than the values of 0.3 PW from Gordon and Owens (1987) and 0.2 PW from Thompson's (1993) analysis of the Fine Resolution Antarctic Model. The current meter data from the ACC are inconclusive. Bryden (1979) found a significant southward eddy heat transport in the Drake Passage, and, by extrapolation to the rest of the ACC, thought that it was sufficient to balance the atmospheric heat loss to the south of 60°. However, Bryden's (1979) results were not corrected for mooring blow-over which could have over-estimated the eddy heat transport by as much as 20% (Nowlin et al. 1985). Bryden and Heath (1985) measured the ACC west-southwest of New Zealand and found that the eddy heat transport there was too weak to account for the expected loss of heat to the atmosphere, but their measured transports were not statistically significant. It appears from analysis of the POCM that the extrapolation from either of these two locations is not appropriate, as the strongest southward heat transports in the model are in the the southwestern Indian Ocean sector of the ACC, an area of no current meter coverage. The eddy heat transport is very inhomogeneous, increasing the difficulty of using scattered current meters to extrapolate the eddy heat transport for the rest of the ACC.

The second regime is the area around the western boundary currents. In Stammer's (1998) estimate the Gulf Stream and Kuroshio both have a large northward eddy heat transport that is somewhat smaller in the model. There are, of course, numerous model deficiencies that could play a role in the discrepancies, chief among them being the general weakness of the model temporal and spatial variability, and the failure of the model to reproduce the extension of eddy kinetic energy east of the Kuroshio and Gulf Stream as was pointed out by Stammer et al. (1996). In fact, comparing the model's along-stream eddy heat transport to current meter data from the Gulf Stream at 55°W (Bower and Hogg 1996) and 64°W (Cronin and Watts 1996) shows that model under-estimates the eddy heat transport by a factor of about

4. At 55°W, Bower and Hogg (1996) found that the along-stream eddy heat transport was about 150 °C m^2 s^{-1}, while the model only produces about 40 °C m^2 s^{-1} in the axis of the stream at 55°W. Upstream at 68°W, Cronin and Watts (1996) found a stronger eddy heat transport of 900 °C m^2 s^{-1} compared to the model's 200 °C m^2 s^{-1} there. Therefore, the lack of strong northward eddy heat transport in the Kuroshio extension and the Gulf Stream recirculation region seen by Stammer (1998) may result from the overall weakness of the model's variability. On the other hand, neither Bower and Hogg (1996) nor Cronin and Watts (1996) observed the widespread strong cross-stream eddy heat transport that Stammer (1998) estimates for the Gulf Stream. Wunsch (1999) found strong southward eddy heat transports in a few locations in both the Gulf Stream and the Kuroshio. In the Kuroshio, he found one location with a southward eddy heat transport of 190 °C m^2 s^{-1}, compared to a weaker, but still southward eddy heat transport of 70 °C m^2 s^{-1} in POCM. These southward heat transports are simply not seen in Stammer's (1998) estimate. However, as was argued in the previous section, it is difficult to know exactly what the current-meter observations are showing in the meandering jets, given the dominance of the rotational eddy heat transports.

The third area is the equatorial region where the model shows a convergent eddy heat transport along the equator in all three of the ocean basins, which is different from the Stammer's (1998) southward eddy transport along the equator in the Indian Ocean and the northward transport in the Pacific Ocean. In the equatorial region the POCM is thought to simulate the ocean well, and the convergent eddy heat transport along the equator is supported by previous modeling studies (*i.e.* Semtner and Holland 1980; Cox 1980; Philander et al. 1986). Furthermore, the POCM's eddy heat transport in the Equatorial Pacific is consistent with the observational evidence from the region. The POCM finds a convergent eddy heat transport along the equator of 190 W m^{-2} over the region between 110°W and 140°W. Using data from current meters, Bryden and Brady (1989) found a convergent eddy heat transport along the equator between 110°W and 152°W of about 245 W m^{-2}. Two studies using drifters also found a convergent eddy heat transport along the equator of 180 W m^{-2} between 105°W and 120°W (Hansen and Paul 1984), and 100 W m^{-2} between 110°W

145

and 140°W (Baturin and Niiler 1997). So the model appears to be within the range of eddy heat convergence suggested from the observational work. All three of the observational studies, as well as the modeling studies mentioned above, pointed to the importance of tropical instability waves as the energetic fluctuations responsible for the convergent heat transport. These waves have a wavelength of about 1000 km and periods of 3 – 4 weeks. They occur within about 5° of the equator and derive their energy from the barotropic velocity shear between the South Equatorial Current and the North Equatorial Countercurrent.

Some resolution to the discrepancies between Stammer's (1998) estimate and the model's directly calculated eddy heat transport is required. The disparity of the results, particularly in the equatorial regions suggests that eddy heat transports from the POCM and mixing length arguments are not just quantitatively different, but qualitatively different as well. One way of examining why Stammer's (1998) method may fail is to examine the baroclinic energy conversion term from the turbulent energy equation. This term which has the following form:

$$-\frac{g}{|\partial\bar{\rho}/\partial z|}\left(\overline{u'\rho'}\frac{\partial\bar{\rho}}{\partial x} + \overline{v'\rho'}\frac{\partial\bar{\rho}}{\partial y}\right),\tag{4.36}$$

and is a measure of the conversion of eddy potential energy to other energies such as eddy kinetic energy, mean flow potential energy and mean flow kinetic energy. Where this quantity is negative there is a conversion of energy from the mean flow to the eddy potential energy and where it is positive there is a conversion of energy from the eddy potential energy back to the mean flow. If the effects of salinity are neglected and the stratification is reasonably constant over the depth range of interest, as was assumed by Hansen and Paul (1984), then the tendency of the baroclinic energy conversion due to temperature can be approximated by:

$$\overline{u'\theta'}\frac{\partial\bar{\theta}}{\partial x} + \overline{v'\theta'}\frac{\partial\bar{\theta}}{\partial y}.\tag{4.37}$$

146

If Stammer's (1998) methods were used to calculate the eddy heat transport then (4.37) would assume the form:

$$-\kappa \, |\nabla\bar\theta|^2. \tag{4.38}$$

Hence, using Stammer's (1998) method, the conversion of eddy potential energy would always be negative since both κ and $|\nabla\bar\theta|^2$ are positive, and there would always be a net conversion from the mean flow's energy to eddy potential energy. However, Hansen and Paul (1984) found positive values for the conversion of eddy potential energy due to temperature south of the equator in the Pacific Ocean, indicating a conversion of energy back from the eddy field to the mean flow there. In the POCM the values of $\overline{\mathbf{v}'\theta'} \cdot \nabla\bar\theta$ are consistent with Hansen and Paul's (1984) measurements. In particular, they are of the same magnitude, and are negative north of the equator and, more importantly, positive south of the equator (Fig. 4.26). These positive values indicate that there is a tendency to take energy from the eddy potential energy field and give it to the mean flow there. This is indicative of an up-gradient transport of temperature and is consistent with the findings of Baturin and Niiler (1997) who concluded from their drifter data that a simple down-gradient temperature flux would not work in the Equatorial Pacific since the eddy coefficient of diffusion changed sign depending on location. They went on to state that climate models would need to explicitly resolve tropical instability waves in order to represent their effects. Bryden and Brady (1989) reached similar conclusions from their current-meter observation.

The conversion of eddy potential energy may then provide diagnostic to test when and where eddy parameterizations based on down-gradient fluxes will fail in the ocean; they will fail where there is a baroclinic energy conversion form the eddy field to the mean flow. In essence, Stammer's (1998) eddy parameterization fails to work in the model for the same reason it probably fails to work in the ocean; there are regions in the Equatorial Pacific where the eddy heat transport is up-gradient associated with a net conversion of energy from the eddy field to the mean flow. It would be nice to find a unified argument why the mixing length scalings fail in some locations and work
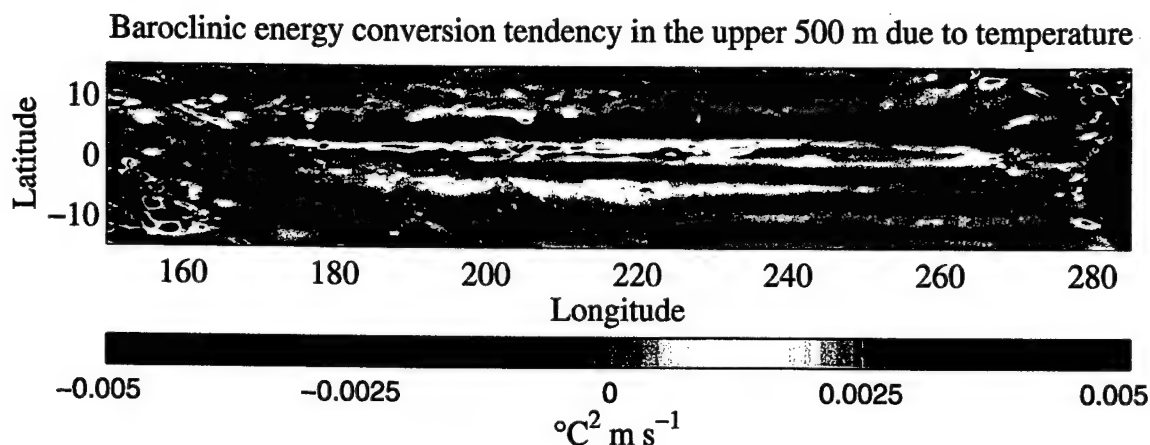
Baroclinic energy conversion tendency in the upper 500 m due to temperature

Figure 4.26: Eddy potential energy conversion tendency due to temperature, estimated by the depth integral of $\overline{v'\theta'} \cdot \nabla\overline{\theta}$ over the upper 500 meters. Negative values correspond to a conversion of mean flow energy to eddy potential energy, and positive values indicate a conversion of eddy potential energy to the mean flow energy.

elsewhere. But it appears as of now that they may fail for different reasons. In the western boundary currents, the meandering jet gives a large apparent eddy diffusivity, even though there is not necessarily any mixing taking place. In the equatorial regions the apparent up-gradient transport of temperature by the tropical instability waves plays a significant dynamical role. It should be noted that these two regimes are both places where there are narrow, barotropically-unstable jets, and the solution to the problem may ultimately come from including it in the parameterizations. In the Antarctic Circumpolar Current, in contrast to these other two regimes, baroclinic instability is dominant and the parameterization gives a consistent estimate, however it remains possible that they agree for different reasons.

4.8.3 Frequency distribution

One final analysis can be made of the rectified eddy heat transport, that is, a decomposition in the frequency domain. The contribution to the time-mean heat transport by rectification of time-varying processes can be thought of as the integral in the frequency domain of the cospectra of the temperature and velocity (*e.g.* Bryden 1979):

$$\overline{v'\theta'} \;=\; \frac{1}{\tau} \int_{-H}^{0} \int \left[v'(t,z)\; \theta'(t,z) \right] dt\, dz$$

$$\;=\; \frac{1}{\tau} \int_{-H}^{0} \int \mathrm{Real}[\hat{v}(f,z)\; \hat{\theta}^{*}(f,z)] \, df\, dz. \tag{4.39}$$

where $\hat{v}(f)$ is the Fourier transform of the velocity time-series, $v'(t)$, and $\hat{\theta}^{*}(f)$ is the complex conjugate of the Fourier transform of the temperature time-series, $\theta'(t)$, and τ is the averaging period.

The cospectra for 4 locations are shown in Fig. 4.27. The cospectra have been multiplied by the frequency to emphasize the lower frequency range while making sure that the area under the curve is proportional to the heat transport at that frequency. The frequency distribution of the eddy heat transport is widely variable around the global ocean. In the equatorial Pacific, most of the covariance is in the frequency band of $20 - 50$ days, consistent with the hypothesis that the tropical instability waves by Hansen and Paul (1984) and Baturin and Niiler (1997) are responsible for the eddy heat transport there. This is to be contrasted with the tropical Indian Ocean location where the covariance is spread over a much broader range of frequencies from $50 - 500$ days, and the Kuroshio where periods around the annual cycle appear to dominate. The ACC location, which is south of Madagascar, is perhaps the most difficult to understand. The co-spectra there are noisy, which could be due to the variability from the strong meandering current there, and it appears that even very long fluctuations with periods of a 1000 days contribute significantly. One of the weaknesses of this analysis is its inability to distinguish the rotational eddy heat transport from the divergent eddy heat transport which is strong in the ACC. Surely the two must have different frequency distribution, but it is not obvious how to compute the separated cospectra.

4.9 Discussion and conclusions

A high-resolution ocean general circulation model, shows large variability in the ocean heat transport. The seasonal cycle of the heat transport has an amplitude of about
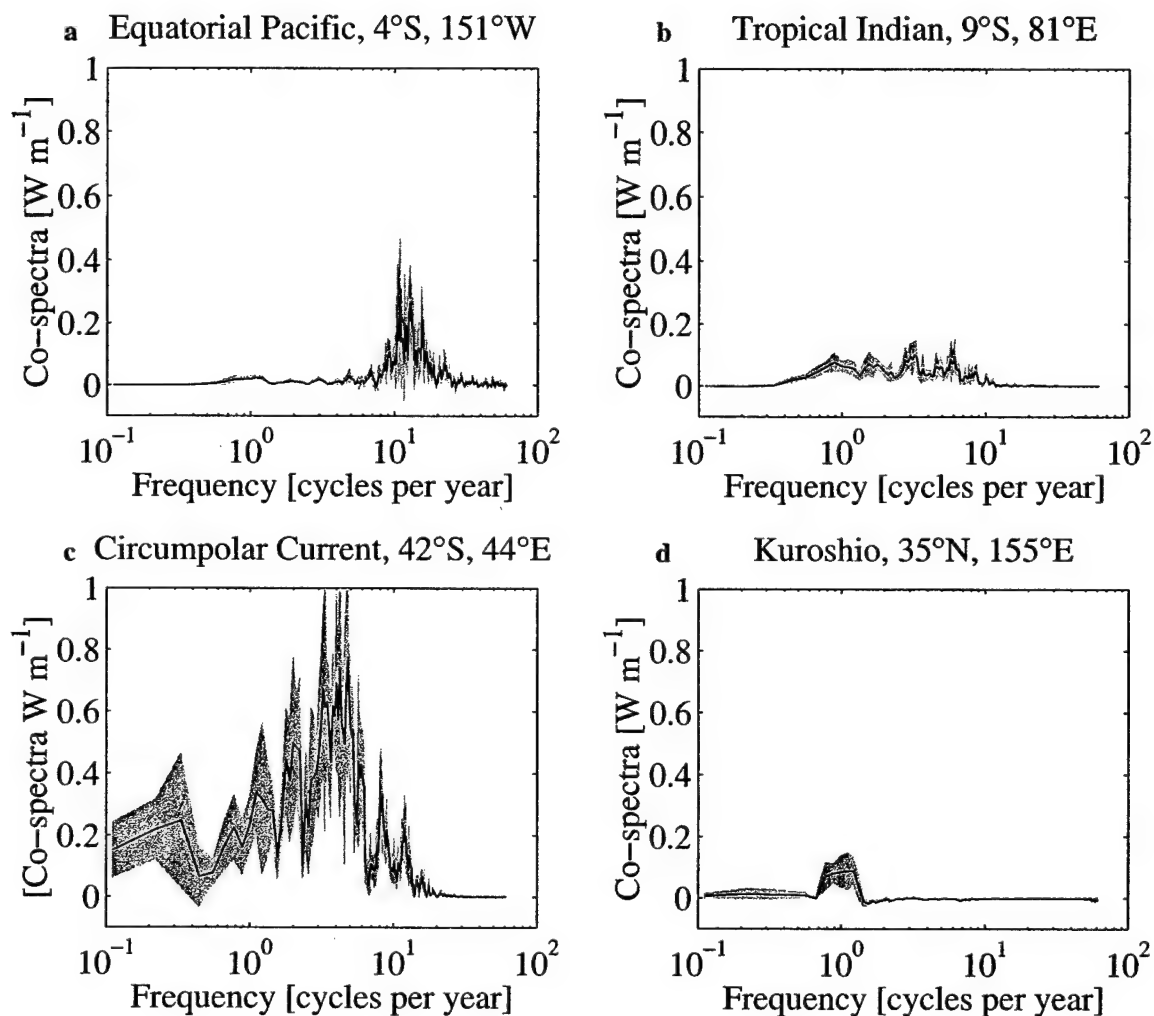
Figure 4.27: Co-spectra of temperature and velocity at 4 selected locations: (a) Equatorial Pacific Ocean, (b) Tropical Indian Ocean, (c) Antarctic Circumpolar Current, and (d) the Kuroshio Current.

150

4.5 PW peak-to-peak near the equator. This finding confirms previous studies from lower-resolution numerical models (Bryan 1982) and is consistent with oceanic and atmospheric data reductions (Hsiung et al. 1989). The dominant mechanism for the heat transport variability is direct forcing by the wind stress, confirming the previous model analyses performed either at low resolution (Bryan and Lewis 1979; Bryan 1982) or confined to single ocean basins (Böning and Herrmann 1994; Wacongne and Pacanowski 1996; Garternicht and Schott 1997; Lee and Marotzke 1998). This directly wind driven variability would also occur for any of the other ocean tracers, such as salt, CO_2 or chlorofluorocarbons (CFC's), whose average Ekman layer concentration is different from the section average. Smaller, but significant, contributions to the heat transport variability come from temperature variations in the surface layer interacting with the Ekman mass transport.

The time-mean ocean heat transport as measured by hydrographic surveys will not be strongly affected by the temporal variability observed in the model. The dominant source of variability is the seasonal cycle of the Ekman heat transport. The deep flows associated with this are barotropic and therefore would not appear in geostrophic calculations of the heat transport from hydrography. Away from the tropics, the heat transport variability associated with the gyre and baroclinic circulations, which are much weaker than the Ekman variability, can amount to a 0.2 – 0.4 PW uncertainty in the heat transport measured by a one-time hydrographic survey.

Globally, internal oceanic instabilities (eddies) play only a minor role in the time-dependent heat transport. They do, however, contribute to the time-mean heat transport in a number of locations. The rectified eddy heat transport was examined in a number of ways. The interiors of the ocean gyres have little eddy heat transport in agreement with analyses of current meter data (Wunsch 1999) and an estimate derived from mixing length arguments (Stammer 1998). The most significant eddy heat transport activity was found in western boundary currents, equatorial regions, and the Antarctic Circumpolar Current. For zonal averages the eddy heat transport makes a significant contribution to the total time-mean heat transport in the tropics and the Antarctic Circumpolar Current. There is a global zonally-integrated eddy heat transport of about 0.1 PW at its maximum due to rectification effects in the

Ekman layer and the majority of the eddy heat transport is concentrated in the upper 1000 m of ocean depth.

The POCM's eddy heat transport differs from the estimate constructed by Stammer (1998) from a mixing length argument using altimetry data and a temperature climatology. Stammer's (1998) method was tested by applying it to the model fields and it was shown that it does not reproduce the model's directly computed heat transport, bringing into question the validity of his eddy parameterization. The differences between the model's directly calculated eddy heat transport and Stammer's (1998) estimate where discussed. In the western boundary currents it was found that there is a large rotational component to the eddy heat transport which results from the meandering of the jets and that it obscures the dynamically important divergent component. An analytical argument shows that for a coherent meandering jet there can be a large rotational eddy heat transport, which is not necessarily down-gradient. This rotational eddy heat transport may make analyses of scattered current-meter records difficult to interpret. Furthermore, the meandering jet has associated with it high levels of eddy kinetic energy which using Stammer's (1998) method would imply high levels of eddy diffusion where none necessarily exist. Along the equator the rotational component is weak, but there is a convergent eddy heat transport which comes from tropical instability waves with periods from 20 – 50 days, in agreement with results from current-meter observations (Bryden and Brady 1989), mixed-layer drifters (Hansen and Paul 1984; Baturin and Niiler 1997) and previous modeling work (Semtner and Holland 1980; Cox 1980; Philander et al. 1986). In some locations the eddy heat transport is up-gradient and is associated with areas of conversion of eddy potential energy to the mean flow energy. In the Antarctic Circumpolar Current, the model's eddy heat transport agrees well with the Stammer's (1998) estimate probably because baroclinic instability dominates there. Finally, in the interiors of the gyres the eddy heat transport is very weak and the mixing length argument (Stammer 1998), the evidence from current meters (Wunsch 1999) and the model are all in agreement.

Chapter 5

Summary and Conclusions

5.1 Summary of results

Driven by a desire to understand the time-dependency of the ocean's heat transport, this thesis has explored and explained some of the dynamics that are responsible for its variability. In particular, the seasonal cycle and higher frequency variations have been explained as the result of wind stress fluctuations, and where a dynamical explanation for it was previously lacking, one has been put forward to describe it. Of equal importance, the model's rectified eddy heat transport was analyzed and compared to an estimate derived by a mixing length argument, showing serious deficiencies with the eddy parameterization.

Consideration has been given to the numerical issues surrounding the appropriate sampling and forcing methods to be used in an ocean general circulation model when high-frequency motions are present. It was shown that inertial oscillations can present significant difficulties in the analysis of model output when they are aliased in time by improper sampling. These high-frequency variations are shifted into longer period motions whose frequency depends on the latitude and sampling rate. At some specific combinations of latitude and sampling rate, they are aliased into the mean fields. For studies of the general circulation of the ocean, it is recommended that some type of filtering prior to saving fields for later analysis be incorporated in the model runs to remove the inertial oscillations. The method used to perform the temporal interpolation of the wind stress fields can cause the high-frequency power spectrum

to be distorted. It is suggested that the model forcing fields be interpolated to every model time step to remove step functions in the forcing of the model.

The role of variable wind stress in forcing ocean heat transport fluctuations was discussed and its dynamics explained. For the first time, a cohesive dynamical explanation for the seasonal Ekman overturning circulation was put forward by combining and extending the work of Schopf (1980), Willebrand et al. (1980) and Bryan (1982). It was found that the seasonal cycle of the meridional overturning streamfunction is governed by a relatively simple set of dynamics compared to the time-mean meridional overturning. In particular, there is a high degree of compensation between the zonal integral of the Ekman mass transport and the barotropic transport. It can be summarized in the following argument: An oscillation in the zonal integral over the basin width of the zonal wind stress drives a corresponding change in the integrated northward Ekman mass transport across that section. The change in the mass transport across the zonal section creates a pressure imbalance which through geostrophy and a series of gravity waves drives a barotropic flow back across the section, balancing the initial change in the Ekman transport. Hence, there is little net flow across the section. The response is essentially a shallow Ekman layer due to the wind stress together with a compensating flow governed by barotropic dynamics. The adjustment to the change in the wind is fast, as the Ekman layer adjusts in an inertial period and the barotropic transport is set up by external gravity waves which can traverse the basin in under a day. A homogeneous shallow-water model using the same wind stress forcing, model grid and topography as the ocean general circulation model was employed to demonstrate that the dominant balances for the seasonal overturning circulation are in fact well represented by Ekman and barotropic dynamics. Temperature fluctuations play a less significant role in the overall heat transport variability.

An interesting feature of the seasonal cycle of the zonal wind was found in the course of this thesis work. That is, that the seasonal cycle of the zonally-integrated zonal wind was found to be anti-symmetric about the equator. The model of the thermally-driven tropical atmospheric circulation (Hadley cell) of Gill (1980) was examined and it was shown that it explains this phenomenon well. The anti-symmetry

154

of the zonal wind drives an Ekman flow field which is unidirectional and together with continuity and direct pressure forcing drives the flow across the equator. While this result was anticipated by Gill's (1980) model, this appears to be the first time it has been discussed, especially in the context of its impact on the ocean's meridional heat transport.

The seasonal cycle of meridional heat transport can be well described by a simple equation relating the zonal integral of the wind stress to the Ekman layer temperature and the section averaged potential temperature. This equation is similar to the one first used by Kraus and Levitus (1986), but it is shown that it only applies to the time-varying component of the Ekman heat transport, not the total (time-mean plus time-varying) as was previously assumed. The arguments presented give a new, sound dynamical foundation for understanding the time-varying Ekman heat transport. The seasonal heat transport across the equator is directed from the summer hemisphere into the winter hemisphere, reinforcing the atmospheric energy transport by the Hadley circulation. In the traditional time-mean picture, the ocean and atmosphere transport heat from the tropics towards the poles tempering the equator to pole temperature difference. With this work, it is now understood how the ocean on the seasonal timescale, in conjunction with the atmosphere, transports energy from the summer hemisphere to the winter hemisphere, moderating the seasonal cycle of ocean and atmospheric temperatures than would otherwise occur.

In the POCM, at the equator, the global ocean's seasonal heat transport has a peak-to-peak amplitude of about 4.5 PW, nearly identical to the seasonal cycle of energy transport of the atmosphere. The seasonal cycle of the ocean's heat transport is larger than the amplitude of the time-mean ocean heat transport, particularly in the tropics. At 7°N, the Atlantic and Pacific Oceans have their maximum amplitude in the seasonal cycle of 1 PW and 3 PW, respectively. The Indian Ocean has its maximum peak-to-peak seasonal cycle of 2.6 PW at 5°S. At about 20° from the equator, the seasonal cycle of the Ekman heat transport reverses sign, leading to a maximum convergence (divergence) of heat in the latitudes around 15° in the winter (summer) hemisphere. In the tropics, the advected energy produces the seasonal cycle in storage of heat that is out of phase with the surface heat flux. In the mid-

latitudes, the surface heat flux is largely in balance with storage in agreement with the theory by Gill and Niiler (1973), however in the Pacific Ocean the divergence of Ekman heat transport plays small, but not insignificant role. At high latitudes, the seasonal heating and cooling of the Ekman layer drives the time-dependency of the heat transport there. The model's seasonal heat transport cycle was shown to be consistent with observational estimates (Hsiung et al. 1989).

It is one of the major conclusions of this thesis that despite the Ekman transport's strong impact on the time-dependent heat transport, the largely depth-independent character of its associated meridional overturning streamfunction means that it does not affect estimates of the time-mean heat transport made by one-time hydrographic surveys, provided that the Ekman layer contribution is estimated from the time-mean wind stress. The dynamical arguments presented here do not support the assumptions made by Bryden et al. (1991) that the ocean's response to the seasonal wind cycle is confined to the upper 700 m. These results extend the study of Böning and Herrmann (1994), which were limited to the North Atlantic, to all the ocean basins. Away from the tropics, the heat transport variability associated with the barotropic gyre and baroclinic circulations, are much weaker than the Ekman variability, and can amount to a 0.2 − 0.4 PW variance in the heat transport measured by a one-time hydrographic survey. Hence estimates of the time-mean heat transport made from one-time hydrographic surveys using the method of Hall and Bryden (1982) are fundamentally sound.

The rectified eddy heat transport from the model was computed and several novel aspects of it were discussed. It was found that the model shows areas of concentrated eddy heat transport in the western boundary currents, the equatorial region, and the Antarctic Circumpolar Current. The interiors of the ocean gyres have little eddy heat transport. In the zonal integral the eddy heat transport makes a significant contribution to the total time-mean heat transport in the tropics and the Antarctic Circumpolar Current and the majority of the transport is concentrated in the upper 1000 m of ocean depth. It was also found that there is a large rotational component of the total eddy transport, especially in the western boundary currents and the Antarctic Circumpolar Current, which obscures the dynamically important divergent

156

component. From an analytical argument it was found that for a coherent meandering jet there can be a large rotational eddy heat transport, which is not necessarily associated with the time-mean temperature gradient. This rotational eddy heat transport may make analyses of scattered current-meter records difficult to interpret. More importantly, it implies that not all oceanic variability necessarily leads to mixing and that the eddy diffusivity is not directly proportional to the bulk eddy kinetic energy, at least in meandering jets. Along the equator the rotational component is weak, but there is a convergent eddy heat transport which comes from tropical instability waves with periods from 20 – 50 days, in agreement with current meter observations (Bryden and Brady 1989), float observations (Hansen and Paul 1984; Baturin and Niiler 1997) and previous modeling work (Philander et al. 1986).

The model's eddy heat transport differs from the estimate derived by Stammer (1998) using altimetry data and a temperature climatology. In his method, a mixing length hypothesis is invoked to calculate the eddy heat transport as a down-gradient temperature transfer, as would be theoretically accomplished by small spatial-scale eddies stirring a large spatial-scale background temperature gradient. The eddy transfer coefficient is set by the eddy timescale and eddy kinetic energy calculated from TOPEX/POSEIDON data. As a test, Stammer's method was applied to the model fields and it was shown that it does not reproduce the model's directly computed heat transport, questioning the validity of calculating the eddy heat transport using a simple mixing length argument.

There are several reasons why Stammer's (1998) method does not work in the model and may not be applicable to the ocean. In the western boundary currents, where Stammer (1998) found large eddy transports, the eddy dynamics are dominated by the meandering of the jet. However, Stammer's (1998) method for calculating the eddy diffusivity using the eddy kinetic energy measured from TOPEX/POSEIDON does not account for variability associated with the meandering jet and over-estimates the eddy heat transport across them. It is not obvious how to adjust his method to compensate for the meandering of oceanic jets. In the equatorial regions of the ocean other dynamics, such as tropical instability waves, dominate over baroclinic instability. Observational evidence from the tropics strongly suggest an up-gradient

transfer of temperature by the eddies associated with the conversion of eddy potential energy to the mean flow, ruling out a simple eddy induced diffusion of temperature. In the Antarctic Circumpolar Current, Stammer's (1998) method and the model appear to agree, perhaps not a surprising result, since it is a largely zonal baroclinic jet and the mixing length theories have been developed around zonal flows (*e.g.* Green 1970; Stone 1972; Visbeck et al. 1997). Finally, in the interiors of the gyres the eddy heat transport is very weak and the mixing length argument (Stammer 1998), the evidence from current meters (Wunsch 1999) and the model are all in agreement.

5.2 Concluding remarks

The ocean's role in the transport of heat is complex. No one study can hope to answer all the questions about it, and it is inevitable that other questions are raised. For fluctuations in the zonally-integrated heat transport on the seasonal and shorter time scales, the Ekman and barotropic dynamics presented here work well. Now that this relatively simple model of the seasonal heat transport has been set in a sound theoretical framework by this thesis, an interesting study would be to construct a seasonal ocean heat budget. This could be done using TOPEX/POSEIDON data to calculate energy storage from steric height changes, as was done in Stammer (1997), and the advective heat transports could be calculated from the time-varying Ekman heat transport from temperature and wind stress climatologies, leaving the surface heat flux as the residual. This surface heat flux could be compared to those estimated from atmospheric analyses (*i.e.* Barnier et al. 1995), as well as those derived from bulk formulae, as a consistency check.

At longer timescales the dynamics of the ocean's heat transport variability are not so clear. On timescales longer than a year, it is likely that the barotropic response discussed in this thesis is replaced by a baroclinic response as the return flow for the Ekman becomes shallower (Willebrand et al. 1980). Additionally, the horizontal gyre circulations and boundary currents will likely fluctuate and cause changes in the ocean's heat transport that feedback into changes in the atmosphere. The coupling to the atmosphere makes the ocean's role in long-term heat transport variations compli-

cated indeed as the atmosphere and ocean are entwined in a game of push-me pull-me. It remains to be established by future work what the exact dynamics of low-frequency (*i.e.* decadal–centennial) heat transport fluctuations are, but the limited duration of eddy-resolving OGCM runs handicaps our ability to investigate the ocean's role in long-term climate variability. It has not yet been shown what the effects of mesoscale eddies are on long-term variability, but simply assuming they are negligible cannot be justified, and they will need to be studied with long eddy-resolving runs when computational resources are adequate. The alternative of using a coarser models coupled to atmospheric and sea ice models, and with questionable sub-gridscale parameterizations leaves any conclusions drawn from such models open to criticism on the failings of the parameterizations. However, it is the only reasonable way to proceed as of now to extend our understanding of the ocean's role in climate at longer timescales.

Perhaps the most important question raised by this thesis is the conflict between the model's rectified eddy heat transport and the estimate of it made by Stammer (1998) based on mixing length arguments. It remains to be shown if a unified mixing length argument can be applied to the whole ocean or whether they are doomed to work only in a few select locations. The work done here implies that they do not work well over the whole ocean. Eddies in the ocean's turbulent circulation are almost certainly dynamically active, especially in boundary currents where it has long been known that they can flux potential vorticity up the mean gradient, and better parameterizations will need to take into account places in the ocean where there is a conversion of energy from the eddy field back to the mean flow field. Eddy transports due to more diverse phenomena, such as non-local wave propagation transporting and dissipating energy away from the generation region, as well as barotropic shear instability and tropical instability waves need to be understood and taken into consideration. Studies need to be undertaken that concentrate on heat and momentum, in addition to potential vorticity. Even though potential vorticity is the usual framework in which eddy-mean flow interactions are cast, it is unlikely that the eddy heat transport can be generalized from the potential vorticity flux. Process studies combined with numerical modeling to examine the eddy-mean flow interactions in all of the major oceanic regimes will ultimately be required to understand and parameterize

the effects of eddies. It is questionable whether all the oceanic regimes can even be included into a single parameterization, but if they can, it will be more complex than a simple down-gradient temperature transport. This will be surely a major undertaking since there is not even a demonstrably correct parameterization for eddies in the Gulf Stream, arguably the most extensively surveyed and modeled current in the ocean. While it may be alluring to believe that eddies simply stir the ocean and that baroclinic instability reigns supreme, the ocean is probably not so simple.

Bibliography

Adamec, D., M. M. Rienecker, and J. M. Vukovich, 1993: The time-varying characteristics of the meridional Ekman heat transport for the World Ocean. *J. Phys. Oceanogr.*, **23**, 2704–2716.

Anderson, D. L. T., K. Bryan, A. E. Gill and R. C. Pacanowski, 1979: The transient response of the North Atlantic: Some model studies. *J. Geophys. Res.*, **84**, 4795–4815.

Anderson, D. L. T., and R. A. Corry, 1985: Ocean response to low frequency wind forcing with application to the seasonal variation in the Florida Straits-Gulf Stream transport. *Prog. Oceanog.*, **14**, 7–40.

Baringer, M. O., and R. Molinari, 1999: Atlantic Ocean baroclinic heat flux at 24 to 26°N. *Geophys. Res. Lett.*, in press.

Barnier, B., L. Siefridt, and P. Marchesiello, 1995: Thermal forcing for a global ocean circulation model using a 3–year climatology of ECMWF analyses. *J. Mar. Syst.*, **6**, 363–380.

Baturin, N. G., and P. P. Niiler, 1997: Effects of instability waves in the mixed layer of the equatorial Pacific. *J. Geophys. Res.*, **102**, 27 771–27 793.

Beckmann, A., C. W. Böning, C. Köberle, and J. Willebrand, 1994: Effects of increased horizontal resolution in a simulation of the North Atlantic Ocean. *J. Phys. Oceanogr.*, **24**, 326–344.

Böning, C. W., and P. Herrmann, 1994: Annual cycle of poleward heat transport in the ocean: results from high-resolution modeling of the North and Equatorial Atlantic. *J. Phys. Oceanogr.*, **24**, 91–107.

Böning, C. W., W. R. Holland, F. O. Bryan, G. Danabasoglu, and J. C. McWilliams, 1995: An overlooked problem in model simulations of the thermohaline circulation and heat transport in the Atlantic Ocean. *J. Climate*, **8**, 515–523.

Bower, A. S., and N. G. Hogg, 1996: Structure of the Gulf Stream and its recirculations at 55° W. *J. Phys. Oceanogr.*, **26**, 1002–1022.

Bracewell, R. N., 1986: *The Fourier Transform and Its Applications.* McGraw-Hill, 444 pp.

Brink, K. H., 1989: Evidence for wind-driven current fluctuations in the western North Atlantic. *J. Geophys. Res.*, **94**, 2029–2044.

Broecker, W. S., 1991: The great global conveyor belt. *Oceanography*, **4**, 79–89.

Bryan, F. O., 1997: The axial angular momentum balance of a global ocean general circulation model. *Dyn. Atmos. Oceans*, **25**, 191–216.

Bryan, K., 1962: Measurements of meridional heat transport by ocean currents. *J. Geophys. Res.*, **67**, 3403–3414.

Bryan, K., and L. J. Lewis, 1979: A water mass model of the World Ocean. *J. Geophys. Res.*, **84**, 2503–2517.

Bryan, K., 1982: Seasonal variation in meridional overturning and poleward heat transport in the Atlantic and Pacific Oceans: a model study. *J. Mar. Res.*, **40**, Supplement, 39–53.

Bryan, K., 1991: Poleward heat transport in the ocean: A review of a hierarchy of models of increasing resolution. *Tellus*, **43 AB**, 104–115.

Bryden, H. L., 1979: Poleward heat flux and conversion of available potential energy in Drake Passage. *J. Mar. Res.*, **37**, 1–22.

Bryden, H. L., and R. A. Heath, 1985: Energetic eddies at the northern edge of the Antarctic Circumpolar Current in the Southwest Pacific. *Prog. Oceanog.*, **14**, 65–87.

Bryden, H. L., and E. C. Brady, 1989: Eddy momentum and heat fluxes and their effects on the circulation of the equatorial Pacific Ocean. *J. Mar. Res.*, **47**, 55–79.

Bryden, H. L., D. H. Roemmich, and J. A. Church, 1991: Ocean heat transport across 24°N in the Pacific. *Deep-Sea Res.*, **38**, 297–324.

Carissimo, B. C., A. H. Oort, and T. H. Vonder Haar, 1985: Estimating the meridional energy transports in the atmosphere and ocean. *J. Phys. Oceanogr.*, **15**, 82–91.

Chao, Y., and L.–L. Fu, 1995: A comparison between the TOPEX/POSEIDON data and a global ocean general circulation model during 1992–1993. *J. Geophys. Res.*, **100**, 24 965–24 976.

Chave, A. D., D. S. Luther, and J. H. Filloux, 1992: The Barotropic Electromagnetic and Pressure Experiment, 1, Barotropic current response to atmospheric forcing. *J. Geophys. Res.*, **97**, 9565–9593.

Cox, M. D., 1985: An eddy-resolving numerical model of the ventilated thermocline. *J. Phys. Oceanogr.*, **15**, 1312–1324.

Cronin, M., and D. R. Watts, 1996: Eddy-mean flow interaction in the Gulf Stream at 68°W. Part I: Eddy energetics. *J. Phys. Oceanogr.*, **26**, 2107–2131.

Cox, M. D., 1980: Generation and propagation of 30-day waves in a numerical model of the Pacific. *J. Phys. Oceanogr.*, **10**, 1168–1186.

de Szoeke, R. A., and M. D. Levine, 1981: The advective flux of heat by mean geostrophic motions in the Southern Ocean. *Deep-Sea Res.*, **28A**, 1057–1085.

Dukowicz, J., and R. D. Smith, 1994: Implicit free-surface method for the Bryan-Cox-Semtner ocean model. *J. Geophys. Res.*, **99**, 7991–8014.

Fu, L.-L., 1981: Observations and models of inertial waves in the deep ocean. *Rev. Geophys. Space Phys.*, **19**, 141–170.

Fu, L.-L., and R. A. Davidson, 1995: A note on the barotropic response of sea level to time-dependent wind forcing. *J. Geophys. Res.*, **100**, 24 955–24 963.

Fu, L.-L., and R. D. Smith, 1996: Global ocean circulation from satellite altimetry and high-resolution computer simulation. *Bull. Amer. Meteor. Soc.*, **77**, 2625–2636.

Fukumori, I., R. Raghunath, and L.-L. Fu, 1998: Nature of global large-scale sea level variability in relation to atmospheric forcing: A modeling study. *J. Geophys. Res.*, **103**, 5493–5512.

Garternicht, U., and F. Schott, 1997: Heat fluxes of the Indian Ocean from a global eddy-resolving model. *J. Geophys. Res.*, **102**, 21 147–21 159.

Gent, P. R., and J. C. McWilliams, 1990: Isopycnal mixing in ocean circulation models. *J. Phys. Oceanogr.*, **20**, 150–155.

Ghirardelli, J. E., M. M. Rienecker, and D. Adamec, 1995: Meridional Ekman heat transport: Estimates from satellite data. *J. Phys. Oceanogr.*, **25**, 2741–2755.

Gill, A. E., and P. P. Niiler, 1973: The theory of the seasonal variability in the ocean. *Deep-Sea Res.*, **20**, 141–178.

Gill, A. E., 1980: Some simple solutions for heat-induced tropical circulation. *Quart. J. Roy. Met. Soc.*, **106**, 447-462.

Gill, A. E., 1982: *Atmosphere-Ocean Dynamics.* Academic Press, 662 pp.

Godfrey, J. S., 1996: The effect of the Indonesian throughflow on ocean circulation and heat exchange with the atmosphere: A review. *J. Geophys. Res.*, **101**, 12 217–12 237.

Gordon, A. L., and W. B. Owens, 1987: Polar Oceans. *Rev. Geophys.*, **25**, 227–233.

Gordon, A. L., and J. L. McClean, 1999: Thermohaline stratification of the Indonesian Seas: Model and observations. *J. Phys. Oceanogr.*, **29**, 198–216.

Green, J. S. A., 1970: Transfer properties of the large-scale eddies and the general circulation of the atmosphere. *Quart. J. Roy. Met. Soc.*, **96**, 157–185.

Griffies, S. M., 1998: The Gent-McWilliams skew flux. *J. Phys. Oceanogr.*, **28**, 831–841.

Hadley, G., 1735: Concerning the cause of the general trade-winds. *Philos. Trans. R. Soc. London*, **39**, 58-62.

Hall, M. M., and H. L. Bryden, 1982: Direct estimates and mechanisms of ocean heat transport. *Deep-Sea Res.*, **29**, 339–359.

Halley, E., 1686: An historical account of the trade winds, and monsoons, observable in the seas between and near the tropicks, with an attempt to assign the phisical cause of the said winds. *Philos. Trans. R. Soc. London*, **16**, 153-168.

Haney, R. L., 1971: Surface thermal boundary condition for ocean climate models. *J. Phys. Oceanogr.*, **1**, 241–248.

Hansen, D. V., and C. A. Paul, 1984: Genesis and effects of long waves in the Equatorial Pacific. *J. Geophys. Res.*, **89** 10 431–10 440.

Hellerman, S., 1967: An updated estimate of the wind stress on the world ocean. *Mon. Wea. Rev.*, **95**, 607–626; see also corrigendum (1968), **96**, 63–74.

Hellerman, S., and M. Rosenstein, 1983: Normal monthly wind stress over the world ocean with error estimates. *J. Phys. Oceanogr.*, **24**, 1093–1104.

Hirst, A. C., and J. S. Godfrey, 1993: The role of Indonesian throughflow in a global ocean GCM. *J. Phys. Oceanogr.*, **23**, 1057–1085.

Holloway, G., 1992: Representing topographic stress for large-scale ocean models. *J. Phys. Oceanogr.*, **22**, 1033–1046.

Hogg, N. G., 1994: Observations of Gulf Stream meander-induced disturbances. *J. Phys. Oceanogr.*, **24**, 2534–2545.

Hsiung, J., R. E. Newell, and T. Houghtby, 1989: The annual cycle of oceanic heat storage and oceanic meridional heat transport. *Quart. J. Roy. Met. Soc.*, **115**, 1–28.

Jayne, S. R., and R. Tokmakian, 1997: Forcing and sampling of ocean general circulation models: Impact of high-frequency motions. *J. Phys. Oceanogr.*, **27**, 1173–1179.

Keith, D. W., 1995: Meridional energy transport: uncertainty in zonal means. *Tellus*, **47A**, 30–44.

Killworth, P. D., D. Stainforth, D. J. Webb, and S. M. Paterson, 1991: The development of a free-surface Bryan-Cox-Semtner ocean model. *J. Phys. Oceanogr.*, **21**, 1333–1348.

Killworth, P. D., 1996: Time interpolation of forcing fields in ocean models. *J. Phys. Oceanogr.*, **26**, 136–143.

Klinger, B. A., and J. Marotzke, 1999: Meridional heat transport by the subtropical cell. *J. Phys. Oceanogr.*, submitted.

Kobayashi, T., and N. Imasato, 1998: Seasonal variability of heat transport derived from hydrographic and wind stress data. *J. Geophys. Res.*, **103**, 24 663–24 674.

Koblinsky, C. J., and P. P. Niiler, 1982: The relationship between deep ocean currents and winds east of Barbados. *J. Phys. Oceanogr.*, **12**, 144–153.

Koblinsky, C. J., P. P. Niiler, and W. J. Schmitz, Jr., 1989: Observations of wind-forced deep ocean currents in the North Pacific. *J. Geophys. Res.*, **94**, 10 773–10 790.

Kraus, E. B., and S. Levitus, 1986: Annual heat flux variations across the tropic circles. *J. Phys. Oceanogr.*, **16**, 1479–1486.

Kushner, P. J., and I. M. Held, 1998: A test, using atmospheric data, of a method for estimating oceanic eddy diffusivity. *Geophys. Res. Lett.*, **25**, 4213–4216.

Large, W. G., J. C. McWilliams, and S. C. Doney, 1994: Oceanic vertical mixing: A review and a model with nonlocal boundary layer parameterization. *Rev. Geophys.*, **32**, 363–403.

Lamb, P. J., and A. F. Bunker, 1982: The annual march of the heat budget of the North and Tropical Atlantic Oceans. *J. Phys. Oceanogr.*, **12**, 1388–1410.

Lau, K. M. W., 1978: Experiment with a simple ocean-atmosphere climate model: The role of the ocean in the global climate. *J. Atmos. Sci.*, **35**, 1144–1163.

Lee, T., and J. Marotzke, 1998: Seasonal cycles of meridional overturning and heat transport of the Indian Ocean. *J. Phys. Oceanogr.*, **28**, 923–943.

Lees, J. M., and J. Park, 1995: Multiple-taper spectral analysis: A stand-alone C-subroutine. *Comput. & Geosci.*, **21**, 199–236.

Levitus, S., and A. H. Oort, 1977: Global analysis of oceanographic data. *Bull. Amer. Meteor. Soc.*, **58**, 1270–1284.

Levitus, S., 1982: Climatological atlas of the World Ocean. NOAA Prof. Pap. No. 13, [U.S. Govt. Printing Office] 173 pp.

Levitus, S., 1987: Meridional Ekman heat fluxes for the World Ocean and individual ocean basins. *J. Phys. Oceanogr.*, **17**, 1484–1492.

Levitus, S., R. Burgett, and T. Boyer, 1994: *World Ocean atlas 1994*, vol. 3, *Salinity*, and vol. 4, *Temperature. NOAA Atlas NESDIS 3 & 4*, U.S. Department of Commerce, Washington, D.C., 1994.

Luther, D. S., A. D. Chave, J. H. Filloux, and P. F. Spain, 1990: Evidence for local and nonlocal barotropic responses to atmospheric forcing during BEMPEX. *Geophys. Res. Lett.*, **17**, 949–952.

Macdonald, A. M., 1995: Oceanic fluxes of mass, heat and freshwater: A global estimate and perspective. Ph.D. thesis, 326 pp. Mass. Inst. of Technol./Woods Hole Oceanogr. Inst. Joint Program, Cambridge, Mass.

Macdonald, A. M., and C. Wunsch, 1996: An estimate of global ocean circulation and heat fluxes. *Nature*, **382**, 436–439.

Marcus, S. L., Y. Chao, J. O. Dickey, and P. Gegout, 1998: Detection and modeling of nontidal oceanic effect on Earth's rotation rate. *Science*, **281**, 1656–1659.

Marshall, J., and G. Shutts, 1981: A note on rotational and divergent eddy fluxes. *J. Phys. Oceanogr.*, **11**, 1677–1680.

Marshall, J., C. Hill, L. Perelman, and A. Adcroft, 1997a: Hydrostatic, quasi-hydrostatic and non-hydrostatic ocean modeling. *J. Geophys. Res.*, **102**, 5733–5752.

Marshall, J., A. Adcroft, C. Hill, L. Perelman, and C. Heisey, 1997b: A finite-volume, incompressible Navier Stokes model for studies of the ocean on parallel computers. *J. Geophys. Res.*, **102**, 5753–5766.

McCann, M. P., A. J. Semtner, and R. M. Chervin, 1994: Transports and budgets of volume, heat, and salt from a global eddy-resolving ocean model. *Clim. Dyn.*, **10**, 59–80.

McClean, J. L., A. J. Semtner, and V. Zlotnicki, 1997: Comparisons of mesoscale variability in the Semtner-Chervin 1/4° model, the Los Alamos Parallel Ocean Program 1/6° model, and TOPEX/POSEIDON data. *J. Geophys. Res.*, **102**, 25 203–25 226.

McCreary, J. P., Jr., P. K. Kundu, and R. L. Molinari, 1993: A numerical investigation of dynamics, thermodynamics and mixed-layer processes in the Indian Ocean. *Prog. Oceanog.*, **31**, 181–244.

Meehl, G. A., W. M. Washington, and A. J. Semtner, Jr., 1982: Experiments with a global ocean model driven by observed atmospheric forcing. *J. Phys. Oceanogr.*, **12**, 301–312.

Merle, J., 1980: Seasonal heat budget in the Equatorial Atlantic Ocean. *J. Phys. Oceanogr.*, **10**, 464–469.

Mestas-Nuñez, A. M., D. B. Chelton, M. H. Freilich, and J. G. Richman, 1994: An evaluation of the ECMWF-based climatological wind-stress fields. *J. Phys. Oceanogr.*, **24**, 1532-1549.

Molinari, R. L., E. Johns, and J. F. Festa, 1990: The annual cycle of meridional heat flux in the Atlantic Ocean at 26.5°N. *J. Phys. Oceanogr.*, **20**, 476–482.

Munk, W. H., and G. J. F. MacDonald, 1960: *The rotation of the Earth.* Cambridge University Press, 323 pp.

Niiler, P. P., and C. J. Koblinsky, 1985: A local time-dependent Sverdrup balance in the eastern North Pacific Ocean. *Science*, **229**, 754–756.

Niiler, P. P., J. Filloux, W. T. Liu, R. M. Samelson, J. D. Paduan, and C. A. Paulson, 1993: Wind-forced variability of the deep eastern North Pacific: Observations of seafloor pressure and abyssal currents. *J. Geophys. Res.*, **98**, 22 589–22 602.

Nowlin, W. D., Jr., S. J. Worley, and T. Whitworth III, 1985: Methods for making point estimates of eddy heat flux as applied to the Antarctic Circumpolar Current. *J. Geophys. Res.*, **90**, 3305–3324.

Oort, A. H., and T. H. Vonder Harr, 1976: On the observed annual cycle in the ocean-atmosphere heat balance over the Northern Hemisphere. *J. Phys. Oceanogr.*, **6**, 781–800.

Park, J., C. R. Lindberg, and F. L. Vernon, 1987: Multitaper spectral analysis of high-frequency seismograms. *J. Geophys. Res.*, **92**, 12 675–12 684.

Peixoto, J. P., and A. H. Oort, 1992: *Physics of Climate.* American Institute of Physics, 520 pp.

Percival, D. B., and A. T. Walden, 1993: *Spectral Analysis for Physical Applications.* Camridge University Press, 583 pp.

Philander, S. G. H., 1978: Forced oceanic waves. *Rev. Geophys.*, **16**, 15–46.

Philander, S. G. H., W. J. Hurlin, and R. C. Pacanowski, 1986: Properties of long equatorial waves in models of the seasonal cycle in the Tropical Atlantic and Pacific Oceans. *J. Geophys. Res.*, **91**, 14 207–14 211.

Philander, S. G. H., and R. C. Pacanowski, 1986: The mass and heat budget in a model of the tropical Atlantic Ocean. *J. Geophys. Res.*, **91**, 14 212–14 220.

Ponte, R. M., 1990: Barotropic motions and the exchange on angular momentum between the oceans and solid earth. *J. Geophys. Res.*, **95**, 11 369–11 374.

167

Ponte, R. M., and R. D. Rosen, 1994: Oceanic angular momentum and torques in a general circulation model. *J. Phys. Oceanogr.*, **24**, 1966–1977.

Ponte, R. M., D. Stammer, and J. Marshall, 1998: Oceanic signals in observed motions of the Earth's pole of rotation. *Nature*, **391**, 476–479.

Priestley, M. B., 1981: *Spectral Analysis and Time Series.* Vol. 1: *Univariate Series*; Vol. 2: *Multivariate Series, Prediction and Control.* Academic Press, 890 pp plus appendices (combined edition).

Rix, N. H., and J. Willebrand, 1996: Parameterization of mesoscale eddies as inferred from a high-resolution circulation model. *J. Phys. Oceanogr.*, **26**, 2281–2285.

Robbins, P. E., and J. M. Toole, 1997: The dissolved silica budget as a constraint on the meridional overturning circulation of the Indian Ocean. *Deep-Sea Res. I*, **44**, 879–906.

Rosen, R. D., D. A. Salstein, and T. M. Wood, 1990: Discrepancies in the Earth-atmosphere angular momentum budget. *J. Geophys. Res.*, **95**. 265–279.

Rossby, T., 1987: On the energetics of the Gulf Stream at 73W. *J. Mar. Res.*, **45**, 59–82.

Samelson, R. M., 1990: Evidence for wind-driven current fluctuations in the eastern North Atlantic. *J. Geophys. Res.*, **95**, 11 359–11 368.

Schopf, P. S., 1980: The role of Ekman flow and planetary waves in the oceanic cross-equatorial heat transport. *J. Phys. Oceanogr.*, **10**, 330–341.

Semtner, A. J., and R. M. Chervin, 1988: A simulation of the global ocean circulation with resolved eddies. *J. Geophys. Res.*, **93**, 15 502–15 522, 15 767–15 775.

Semtner, A. J., and R. M. Chervin, 1992: Ocean general circulation from a global eddy-resolving model. *J. Geophys. Res.*, **97**, 5493–5550.

Semtner, A. J., and W. R. Holland, 1980: Numerical simulation of equatorial ocean circulation. Part I: A basic case in turbulent equilibrium. *J. Phys. Oceanogr.*, **10**, 667–693.

Stammer, D., R. Tokmakian, A. J. Semtner, and C. Wunsch, 1996: How well does a 1/4° global circulation model simulate large-scale oceanic observations? *J. Geophys. Res.*, **101**, 25 779–25 811.

Stammer, D., 1997: Steric and wind-induced changes in TOPEX/POSEIDON large-scale sea surface topography observations. *J. Geophys. Res.*, **102**, 20 987– 21 009.

Stammer, D., 1998: On eddy characteristics, eddy transports, and mean flow properties. *J. Phys. Oceanogr.*, **28**, 727–739.

Stone, P., 1972: A simplified radiative-dynamical model for the static stability of the rotating atmosphere. *J. Atmos. Sci.*, **29**, 405–418.

Thompson, D. J., 1982: Spectrum estimation and harmonic analysis. *IEEE Proc.*, **70**, 1055–1096.

Thompson, S. R., 1993: Estimation of the transport of heat in the Southern Ocean using a fine-resolution numerical model. *J. Phys. Oceanogr.*, **23**, 2493–2497.

Toole, J. M., and B. A. Warren, 1993: A hydrographic section across the subtropical South Indian Ocean. *Deep-Sea Res. I*, **40**, 1973–2019.

Trenberth, K. E., and A. Solomon, 1994: The global heat balance: heat transports in the atmosphere and ocean. *Clim. Dyn.*, **10**, 107–134.

Vinnichenko, N. K., 1970: The kinetic energy spectrum in the free atmosphere — 1 second to 5 years. *Tellus*, **22**, 158–166.

Visbeck, M., J. Marshall, T. Haine, and M. A. Spall, 1997: On the specification of eddy transfer coefficients in coarse resolution ocean circulation models. *J. Phys. Oceanogr.*, **27**, 381–402.

Vonder Harr, T. H., and A. H. Oort, 1973: New estimate of annual poleward energy transport by northern hemisphere oceans. *J. Phys. Oceanogr.*, **3**, 169–172.

Wacongne, S., and R. Pacanowski, 1996: Seasonal heat transport in a primitive equation model of the Tropical Indian Ocean. *J. Phys. Oceanogr.*, **26**, 2666–2699.

Warren, B. A., 1999: Approximating the energy transport across oceanic sections. *J. Geophys. Res.*, in press.

Wilkin, J. L., J. V. Mansbridge, and J. S. Godfrey, 1995: Pacific Ocean heat transport at 24°N in a high-resolution global model. *J. Phys. Oceanogr.*, **25**, 2204–2214.

Willebrand, J., 1978: Temporal and spatial scales of the wind field over the North Pacific and North Atlantic. *J. Phys. Oceanogr.*, **8**, 1080–1094.

Willebrand, J., S. G. H. Philander, and R. C. Pacanowski, 1980: The oceanic response to large-scale atmospheric disturbances. *J. Phys. Oceanogr.*, **10**, 411–429.

Wunsch, C., 1999: Where do ocean eddy heat fluxes matter? *J. Geophys. Res.*, in press.

Yu, L., and P. Malanotte-Rizzoli, 1998: Inverse modeling of seasonal variations in the North Atlantic Ocean. *J. Phys. Oceanogr.*, **28**, 902-922.

Zhang, Q., and J. Marotzke, 1999: The importance of open-boundary estimation for an Indian Ocean GCM-data synthesis. *J. Mar. Res.*, in press.

50272-101

REPORT DOCUMENTATION PAGE	1. REPORT NO. MIT/WHOI 99-05	2.	3. Recipient's Accession No.

4. Title and Subtitle

Dynamics of Global Ocean Heat Transport Variability

5. Report Date
June 1999

6.

7. Author(s) Steven Robert Jayne

8. Performing Organization Rept. No.

9. Performing Organization Name and Address

MIT/WHOI Joint Program in Oceanography/Applied Ocean Science & Engineering

10. Project/Task/Work Unit No.
MIT/WHOI 99-05

11. Contract(C) or Grant(G) No.
(C) OCE-9617570
(G) OCE-9730071

12. Sponsoring Organization Name and Address

Department of Defense
National Science Foundation
TEPCO/MIT Environmental Research Program

13. Type of Report & Period Covered
Sc.D. Thesis

14.

15. Supplementary Notes

This thesis should be cited as: Steven Robert Jayne, 1999. Dynamics of Global Ocean Heat Transport Variability. Sc.D. Thesis. MIT/WHOI, 99-05.

16. Abstract (Limit: 200 words)

A state-of-the-art, high-resolution ocean general circulation model is used to estimate the time-dependent global ocean heat transport and investigate its dynamics. Globally, the cross-equatorial, seasonal heat transport fluctuations are close to $\pm 4.5 \times 10^{15}$ watts, the same amplitude as the seasonal, cross-equatorial atmospheric energy transport. The majority of it is due to wind-induced current fluctuations in which the time-varying wind drives Ekman layer mass transports that are compensated by depth-independent return flows. The temperature difference between the mass transports gives rise to the time-dependent heat transport.

The rectified eddy heat transport is calculated from the model. It is weak in the central gyres, and strong in the western boundary currents, the Antarctic Circumpolar Current, and the equatorial region. It is largely confined to the upper 1000 meters of the ocean. The rotational component of the eddy heat transport is strong in the oceanic jets, while the divergent component is strongest in the equatorial region and Antarctic Circumpolar Current. The method of estimating the eddy heat transport from an eddy diffusivity derived from mixing length arguments and altimetry data, and the climatological temperature field, is tested and shown not to reproduce the model's directly evaluated eddy heat transport.

17. Document Analysis   a. Descriptors

ocean
heat
transport

b. Identifiers/Open-Ended Terms

c. COSATI Field/Group

18. Availability Statement	19. Security Class (This Report) UNCLASSIFIED	21. No. of Pages 169
Approved for publication; distribution unlimited.	20. Security Class (This Page)	22. Price

(See ANSI-Z39.18)   *See Instructions on Reverse*   OPTIONAL FORM 272 (4-77)
(Formerly NTIS-35)
Department of Commerce